UNIVERSITEIT VAN PRETORIA
UNIVERSITY OF PRETORIA
YUNIBESITHI YA PRETORIA

Optimisation of the heat treatment cycles of CSIR semi-solid metal processed Al-7Si-Mg alloys A356/7

by

Heinrich Möller

Submitted for the

Degree of Philosophiae Doctor (Metallurgical Engineering)

in the

Faculty of Engineering, Built Environment and Information Technology

UNIVERSITY OF PRETORIA

Pretoria, South Africa

2011

Submission date: 25 March 2011

SUMMARY

Title: Optimisation of the heat treatment cycles of CSIR semi-solid metal processed Al-7Si-Mg alloys A356/7

Candidate: Heinrich Möller

Supervisor: Professor Waldo E. Stumpf

Department: Materials Science and Metallurgical Engineering, University of Pretoria

Degree: Philosophiae Doctor (Metallurgical Engineering)

Conventional casting alloys Al-7Si-Mg A356/7 contain between 6.5 and 7.5% Si, together with 0.25-0.7% Mg and are used for critical castings in the automotive and aerospace industries. These alloys are also the most popular alloys used for semi-solid metal (SSM) forming due to good castability and fluidity imparted by the large volumes of the Al-Si eutectic. Despite their industrial importance, there is a lack of detailed research work revealing precipitate micro- and nanostructural evolution during aging of these alloys compared with the Al-Mg-Si 6000 series wrought alloys. This study characterises the heat treatment response of SSM-processed Al-7Si-Mg alloys in comparison with conventionally liquid cast alloys (investment casting and gravity die casting). It is shown that, provided that the maximum quantity of the alloy's Mg is placed into solid solution during solution treatment, and that the alloy's Fe content is within specification, the response to age hardening of Al-7Si-Mg alloys is independent of the processing technique used. The nanostructural evolution of Al-7Si-Mg alloys after artificial aging with and without natural pre-aging has been characterized using transmission electron microscopy and atom probe tomography and correlated with hardness and mechanical tensile properties. The number densities and Mg:Si ratios of solute clusters, GP zones and β″-needles were determined. The heat treatment response of SSM-processed casting alloys A356/7 alloys are also compared with SSM-processed Al-Mg-Si 6000 series wrought alloys, with the advantage of having similar globular microstructures. The high Si-content of the casting alloys compared to the wrought alloys offers several advantages, including a faster artificial aging response (shorter T6 aging cycles), higher strength for comparable Mg contents and less sensitivity to prior natural aging on peak strength. Finally, an age-hardening model was developed for the Al-7Si-Mg alloys, including a method of incorporating the effects of changes in Mg-content on the aging curves.

Keywords: Al-Si-Mg alloys, heat treatment, natural aging, artificial aging, temper, semi-solid metal, rheocasting, high pressure die casting, transmission electron microscopy, atom probe tomography.

9. ACKNOWLEDGEMENTS

The following contributions are gratefully acknowledged:

- Professor Waldo Stumpf, my supervisor at the University of Pretoria, South Africa.
- Dr Sagren Govender, Research Group Leader of the Advanced Casting Technologies group at the CSIR.
- Dr Willie du Preez, Competency Area Manager of Metals and Metals Processes and Dr Liesbeth Botha, Director of Materials Science and Manufacturing at the CSIR.
- My colleagues at the CSIR who have contributed to the successful completion of this particular work: Ulyate Curle, Pierre Rossouw, Prudence Masuku, Danie Wilkins, Marius Grobler, Andre Grobler, Chris McDuling, Erich Guldenpfennig, Dr Lillian Ivanchev, Martin Williams, Peter Malesa, Sam Papo, Mary Mojalefa and Duncan Hope.
- Adrian Paine from SimLogic for assistance with ProCAST.
- Professor Rob Knutsen from the University of Cape Town, South Africa (impact testing) and Professor Chris Pistorius from Carnegie-Mellon University in Pittsburgh, United States of America (Thermo-Calc).
- The Department of Science and Technology (DST) in South Africa is acknowledged for co-funding under the Advanced Metals Initiative (AMI) Program.
- Funding from the CSIR Strategic Research Panel (SRP) “Young Researcher Establishment Fund” (YREF) is gratefully acknowledged.
- The technical, scientific and financial assistance from the AMMRF (Australian Microscopy and Microanalysis Research Facility) and specifically Dr Gang Sha, Dr Junhai Xia and Prof Simon Ringer from the University of Sydney, Australia.
- My family, the Möllers and the Roose for their continuing support.
- My wonderful wife Lida and our two gorgeous daughters Christia and Celicia for their love and support.

- Soli Deo Gloria -

TABLE OF CONTENTS

1. INTRODUCTION

1.1. Historical perspective

The casting of metals is a prehistoric technology. Even though it is not exactly known when casting began, archeologists give the name “chalcolithic” to the period in which the making and use of metals were first being mastered in the Near East and date this period to approximately between 5000 and 3000 BC (i.e. immediately preceding the Bronze Age). The first metal used for casting was native copper as was deduced from chemical analyses of the earliest cast axes and other objects. The fuel employed was charcoal, which supplied a reducing atmosphere when the fire was enclosed in an attempt to reduce the loss of heat and the molds were made of stone of a smooth texture such as steatite or andesite [1].

In the early 1970’s, thixotropic behaviour was discovered in semi-solid metal alloys which lead to the development of thixocasting and rheocasting (collectively called semi-solid metal processing) [2]. Given the long history of metal casting, it can be seen that this new processing technique is a modern technology.

1.2. Heat treatment and age hardening of Al-alloys

Alfred Wilm accidentally discovered age hardening in an Al-Cu-Mg alloy only approximately 100 years ago and thereby paved the way for using Al-alloys as engineering materials [3]. It took another 30 years before the mechanism of age-hardening could be explained, when in 1938, Guinier and Preston postulated that small precipitates were responsible for the effect [4,5].

1.2.1. Al-Si-Mg alloys

The commercial attraction of Al-Si cast alloys is based on the discovery of modification of the Al-Si eutectic around 1920 by Aladar Pacz [6]. He discovered that the brittle Al-Si eutectic changed its morphology from long plates to fine acicular fibres when small quantities of alkali fluoride or sodium or potassium were added to the melt. In 1921, Al-Si alloys containing up to 15% silicon were introduced in the United States under the trade name "ALPAX" [7]. After World War I, Germany could not afford to use copper in its aluminium alloys and the Al-Si castings provided an alternative for example in the motor blocks of the Daimler cars. The alloy was also used in France in streetcars and railways [6].

The addition of magnesium to Al-Si alloys makes them age-hardenable and these alloys were also developed in the 1920's [8]. The yield strengths of Al-Si-Mg alloys in the T6 condition are more than double that of the binary Al-Si alloys containing the same quantity of Si. They also exhibit good corrosion resistance and are used in the aerospace and automotive industries [9]. With the advent of semi-solid metal (SSM) processing, the Al-7Si-Mg alloys soon became the most popular alloys for study [10]. This is due to their good castability and fluidity imparted by the large volumes of the Al-Si eutectic, with the additional advantage of the castings being age-hardenable to improve strength.

1.3. Heat treatment of Al-7Si-Mg alloys

1.3.1. Conventional liquid cast Al-7Si-Mg alloys

Rinderer and co-workers [11] lamented the lack of detailed research work revealing precipitate micro- and nanostructural evolution during aging of the Al-Si-Mg casting alloys as recently as 2010. They attributed this situation to difficulties the eutectic component causes in preparing high-quality samples for transmission electron microscopy (TEM) and atom probe tomography (APT).

1.3.2. SSM-processed Al-7Si-Mg alloys

Dewhirst [12] stated that: "Due to the differences in thermal history and rheological character between semi solid material and liquid metal, the necessary processing steps are not the same as they have been for thousands of years of foundry experience. The intuition of foundrymen, developed as the trade itself did over the millennia, is not necessarily correct when it comes to semi solid metallurgy. Although knowledge of the mechanisms behind heat treatment of metals is not nearly as old as metal casting itself, those mechanisms have been around for almost 100 years. Through forging, heat treatments have been around in one fashion or another for much longer. As with all new processes, after the mechanisms for SSM heat treatment were commercialised, the first heat treatments applied to it were essentially those already in use for dendritic (liquid cast) materials. These treatment regimes are not necessarily the optimal ones, as the differing microstructure and solidification history of SSM components changes a number of factors." He continued that: "The heat treatment principles for conventionally cast aluminum alloys are well understood, but the different microstructure and solidification history of SSM components indicate that heat

treatment conditions which were optimised for conventionally cast materials do not apply to SSM components."

However, Birol [13,14] postulated that the morphology of the primary α-Al, whether dendritic or globular, has no effect on the artificial aging response of Al-7Si-Mg alloys. He suggested that the favourable impact of the globular structure is most likely offset by the relatively coarser structure in SSM-processed alloys. There is, therefore, disagreement regarding the effects of SSM-processing on the subsequent heat treatment response of these alloys.

1.4. Objective

The objective of this study is to characterise the heat treatment response of SSM-processed Al-7Si-Mg alloys in comparison with conventionally liquid cast alloys (investment casting and gravity die casting). The heat treatment parameters that are specified for conventionally liquid cast alloys are critically analysed to determine whether they are applicable to SSM-processed components and if they are still the same optimised parameters for dendritic castings in a world where energy and environmental features have changed since these cycles were originally developed.

The investigated heat treatment cycles include parameters that affect the T4, T5 and T6 temper conditions i.e. the effects of solution heat treatment, quenching, natural aging and artificial aging on hardness, tensile properties and impact properties are considered. Chemical composition variations within specification (especially Mg) also constitute a major part of this study. Techniques such as optical microscopy, scanning electron microscopy, transmission electron microscopy and atom probe tomography were employed to obtain an in-depth understanding of the processes that occur during heat treatment of these alloys. In addition, commercially available software packages Thermo-Calc and ProCAST were used to supplement the experimental observations. Finally, an age-hardening model was developed based on the Shercliff and Ashby methodology [15], including a method of incorporating the effects of changes in Mg-content on the aging curves.

1.5. Publications

During the course of this study, a number of papers relating to the investigation have been authored or co-authored by Heinrich Möller. These papers are distinguished from other papers by including “HM” in front of the number in the reference list [HM1-HM15].

2. LITERATURE SURVEY

2.1. Semi-solid metal processing

2.1.1. History and introduction

Thixotropy can be derived from the Greek words for “contact, touch”, and “change, modification” [6]. Thixotropic materials flow when sheared, but when allowed to stand they thicken up again. Common materials that display this behaviour are mascara, honey and certain kinds of paint [16]. Thixotropic behaviour in metallic alloys was first discovered by Spencer and co-workers in the early 1970’s while they worked on hot tearing in the lead-tin system [2]. It was found that stirring the metal alloys continuously during cooling from the fully liquid state to the semi-solid state lowered the viscosity significantly compared to when the alloy was cooled into the semi-solid state without stirring. Stirring breaks up the dendrites which would be present in conventionally liquid cast alloys and results in a microstructure in the semi-solid state consisting of spheroids or globules of solids surrounded by liquid (Fig. 2.1 [17]).

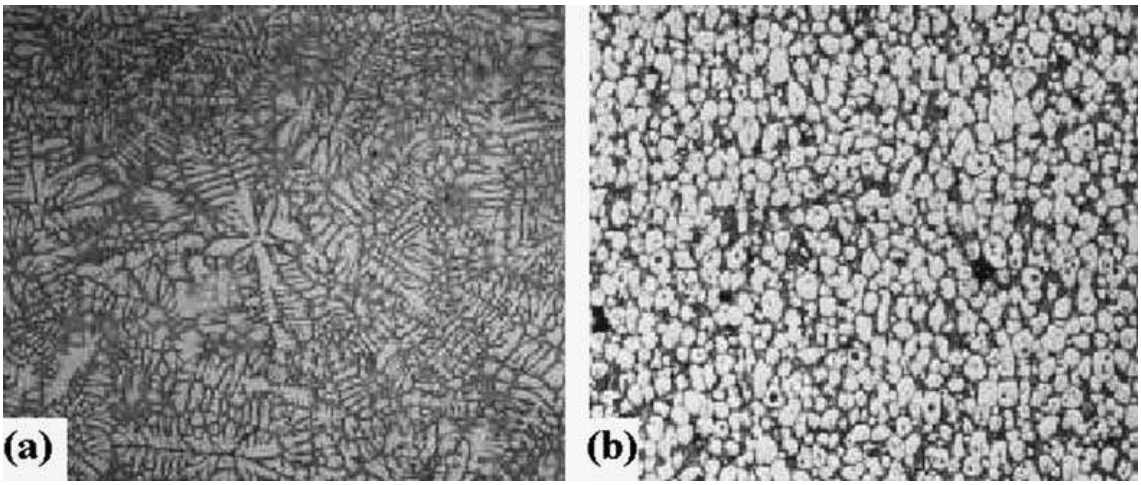

Figure 2.1: Micrograph of a typical (a) dendritic microstructure in an as-cast sample and (b) globular microstructure in a semi-solid alloy sample [16].

This globular microstructure is a prerequisite for thixotropic behaviour and when such a semi-solid microstructure is allowed to stand, the globules/spheroids agglomerate and the viscosity increases with time [16]. If the material is sheared, the agglomerates are broken up and the viscosity decreases. In the semi-solid state (with ~ 30-50% liquid), the alloy will support its own weight when allowed to stand and can be handled as a solid. However, as soon as it is sheared, it flows with a viscosity similar to that of heavy machine oil. The cutting test, in which the alloy can be cut and spread

like butter, demonstrates the thixotropic behaviour of semi-solid alloy slugs in Figure 2.2 [16].

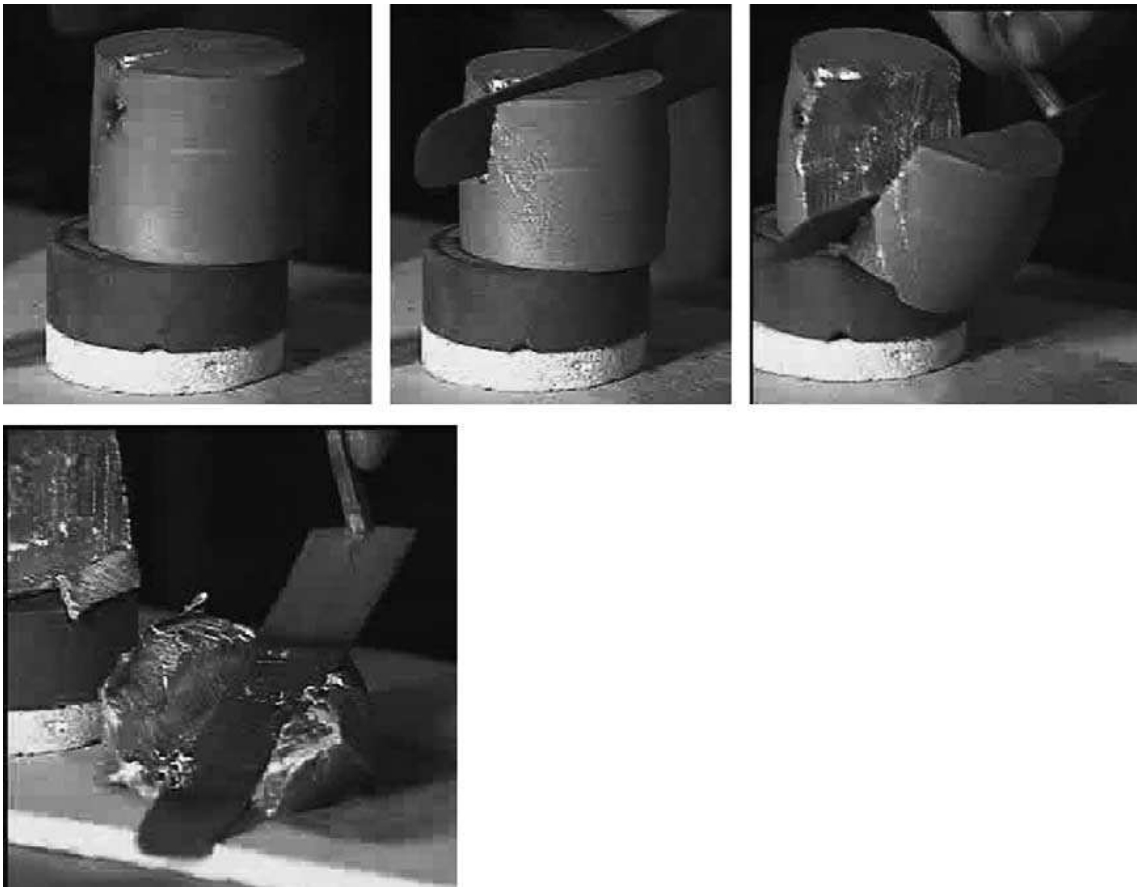

Figure 2.2: A photographic sequence illustrating the thixotropic behaviour of semi-solid alloy slugs [16].

More than 30 years of research has been invested in the field of SSM-processing and the interest in the field is highlighted by eleven international conferences [17-27] with a twelfth planned in South Africa in 2012. SSM-processing presents an alternative manufacturing route for aerospace, military and especially automotive components [16,28]. Suspension parts, engine brackets and fuel rails for automotives are being produced in Europe, whereas examples from the USA include mechanical parts for snowmobiles and mountain bikes. Asia has focused more on the production of electronic components such as electrical housing components and notebook cases with emphasis on magnesium alloys [16]. Two main routes have subsequently been developed for producing semi-solid parts, namely thixoforming and rheocasting.

2.1.2. Thixoforming

Thixoforming is a general term used to describe the near-net shape forming processes from a partially melted, non-dendritic alloy slug within a metal die. If the component shaping is performed in a closed die, it is referred to as thixocasting, while if the shaping is achieved in an open die, it is called thixoforging [6,16]. There are two separate stages involved in the thixoforming process namely reheating and forming. Reheating to the semi-solid state is a particularly important phase in the thixoforming process and is mainly achieved by induction heating, which guarantees exact and rapid heating. The increased costs associated with thixocasting (for example recycling of thixocast scrap and the necessity of an outside manufacturer for billet production) have resulted in rheocasting becoming the preferred semi-solid process [16].

2.1.3. Rheocasting

Rheocasting involves preparation of a SSM slurry directly from the liquid, followed by a forming process such as high pressure die casting (HPDC). Component shaping directly from SSM slurries is inherently attractive due to its characteristics, such as overall efficiency in production and energy management [6]. The distinctions between thixocasting, thixoforging and rheocasting are illustrated graphically in Figure 2.3 [29].

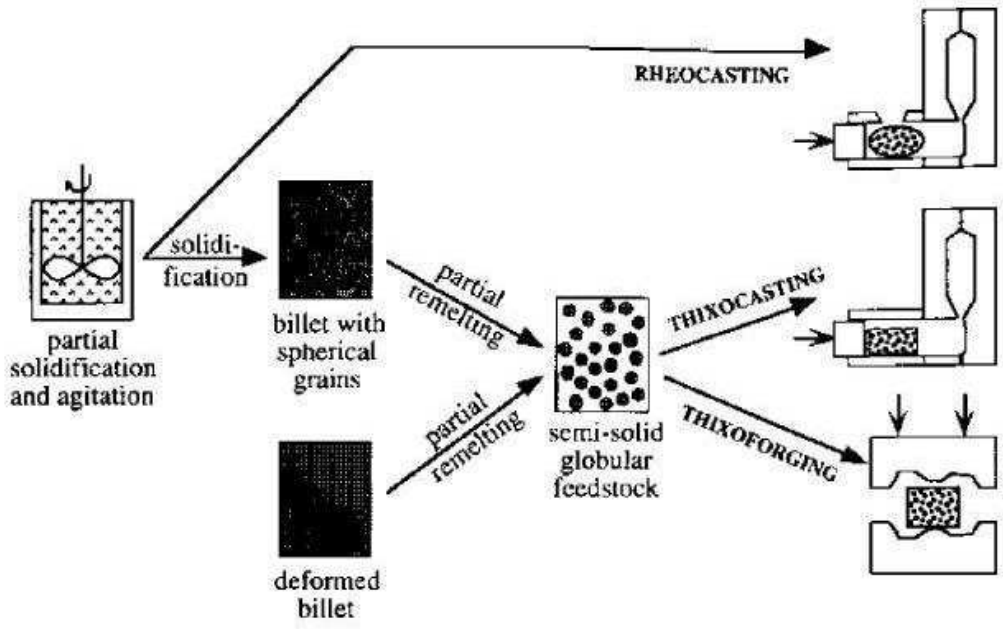

Figure 2.3: Schematic illustration of different routes for SSM-processing [29].

2.1.3.1. CSIR rheocasting system (CSIR-RCS)

The Council for Scientific and Industrial Research (CSIR) in South Africa has developed and patented a rheoprocessing system which uses combined coils for induction stirring and simultaneous forced air cooling, named the CSIR RheoCasting System (CSIR-RCS) [30,31]. One of the features of the equipment and process required that it be flexible so that it could be used on both horizontal and vertical injection high pressure die casting equipment and be implemented in most existing HPDC foundries without significant capital investment. It also has to be able to produce a billet per minute with the ability to vary the cycle time as needed. Using these requirements, the equipment for treatment of light metal alloys from liquid state to semi-solid slurry (Figure 2.4) was developed. Cups filled with metal move in a vertical direction upwards and stepwise through three conditioning units. Each conditioning unit consists of an induction coil and air-cooling. The equipment can be operated as units of a single coil, two coils or three coils depending on the production requirements and material being processed. After rheoprocessing the semi-solid billet is transferred to a HPDC machine for casting.

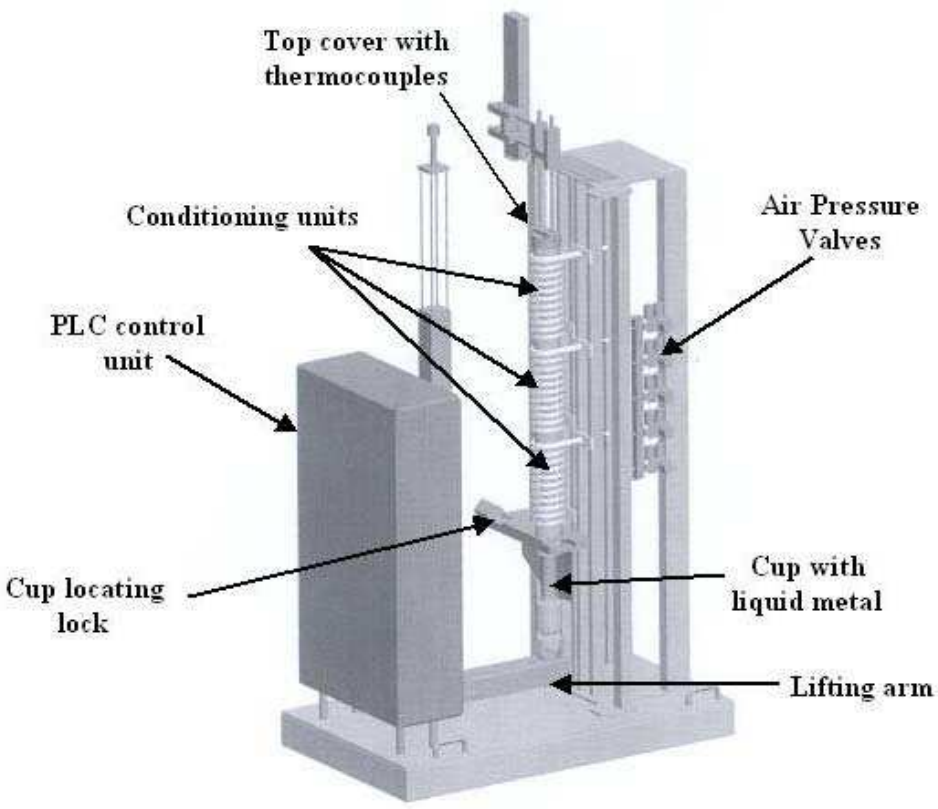

Figure 2.4: The CSIR Rheoprocessing slurry maker for continuous delivery of SSM billets [31].

2.1.4. Advantages and disadvantages of SSM-processing

The main advantages and disadvantages of semi-solid processing (relative to die casting) have been summarised by Atkinson [16] to be as follows:

Advantages

- Energy efficiency: metal is not being held in the liquid state over long periods of time;
- Production rates are similar to pressure die casting or better;
- Smooth filling of the die with no air entrapment and low shrinkage porosity gives parts of high integrity (including thin-walled sections) and allows application of the process to higher-strength heat-treatable alloys;
- Lower processing temperatures reduce the thermal shock on the die, promoting die life and allowing the use of non-traditional die materials;
- Fine, uniform microstructures give enhanced properties;

- Reduced solidification shrinkage gives dimensions closer to near net shape and justifies the elimination of machining steps; and
- Surface quality is suitable for plating.

Disadvantages

- The cost of raw material for thixoforming can be high and the number of suppliers small;
- Process knowledge and experience has to be continually built up in order to facilitate application of the process to new components;
- Initially at least, personnel require a higher level of training and skill than with more traditional processes;
- Temperature control: the fraction solid and viscosity in the semi-solid state are very dependent on temperature. Alloys with a narrow temperature range in the semi-solid region require accurate control of the temperature; and
- Liquid segregation due to non-uniform heating can result in non-uniform composition in the component.

2.2. Al-7Si-Mg alloys

The Al-Si binary alloy system is an eutectic system with the eutectic composition at 12.6wt% Si (Fig. 2.5 [32]).

Conventional casting alloys Al-7Si-Mg A356/7 contain between 6.5 and 7.5% Si, together with 0.25-0.7% Mg and are used for critical castings in aircraft such as the engine support pylons, while automotive components include wheels and cylinder heads [9]. These alloys are probably the most popular alloys used for semi-solid metal forming due to good castability and fluidity imparted by the large volumes of the Al-Si eutectic [10].

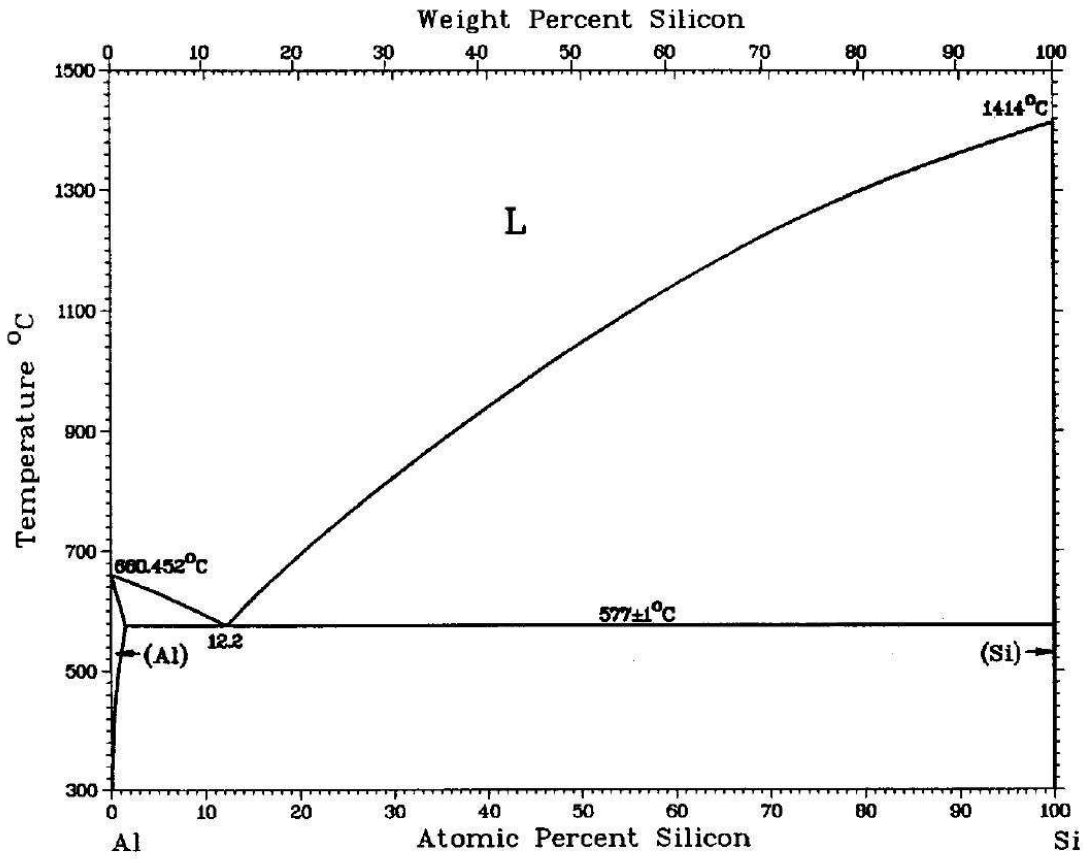

Figure 2.5: The Al-Si binary phase diagram [32].

The chemical composition limits for alloys A356, as well as A357 to F357 are shown in Table 2.1 [33]. International standards for aluminium alloys often permit significant fluctuations in the content of alloying elements. The main difference between alloy A356 and the F357 alloy lies in the magnesium content, whereas the main difference between alloys F357 and A357 is their beryllium content (Table 2.1). The addition of beryllium to this alloy system (e.g. alloy A357) leads to a change in the morphology of the iron-rich intermetallics, which results in slightly better ductility [34] – see section 2.2.1.4. The Be-containing alloys are gradually being phased out in many applications due to the carcinogenic effects of beryllium, particularly at higher concentrations used during make-up of the alloys. The beryllium-free alloy F357 is frequently incorrectly labelled as A357, especially in semi-solid metal research [35,36].

Table 2.1: Chemical composition limits (in wt%) for alloys A356, A357, B357, C357, D357, E357 and F357 [33].

		Si	Mg	Fe	Cu	Mn	Ti	Be
A356	Min	6.5	0.25	-	-	-	-	-
	Max	7.5	0.45	0.20	0.20	0.10	0.20	-
A357	Min	6.5	0.40	-	-	-	0.10	0.04
	Max	7.5	0.70	0.20	0.20	0.10	0.20	0.07
B357	Min	6.5	0.40	-	-	-	0.04	-
	Max	7.5	0.60	0.09	0.05	0.05	0.20	-
C357	Min	6.5	0.45	-	-	-	0.04	0.04
	Max	7.5	0.70	0.09	0.05	0.05	0.20	0.07
D357	Min	6.5	0.55	-	-	-	0.10	0.04
	Max	7.5	0.60	0.20	-	0.10	0.20	0.07
E357	Min	6.5	0.55	-	-	-	0.10	-
	Max	7.5	0.60	0.10	-	0.10	0.20	0.002
F357	Min	6.5	0.40	-	-	-	0.04	-
	Max	7.5	0.70	0.10	0.20	0.10	0.20	0.002

2.2.1. Influence of important alloying elements in modified Al-7Si-Mg alloys

2.2.1.1. Silicon

Silicon promotes castability because of the high fluidity imparted by the presence of large volumes of the Al-Si eutectic and together with magnesium it forms strengthening precipitates during heat treatment [9]. Silicon is a faceted phase and makes the Al-Si eutectic an irregular eutectic. Silicon also reduces the thermal expansion coefficient and increases corrosion and wear resistance. At room temperature, hypoeutectic alloys such as A356/7 consist of a soft and ductile primary α-Al phase and a hard and brittle eutectic phase containing secondary α-Al and silicon (Fig. 2.6 [37]). Silicon has the strongest influence on the ratio of solid to liquid fraction of all alloying elements in A356/7 and a fluctuation of 1 wt% silicon in aluminium (as is allowed according to Table 2.1) results in a solid fraction change of almost 9% if the casting temperature is held constant [38].

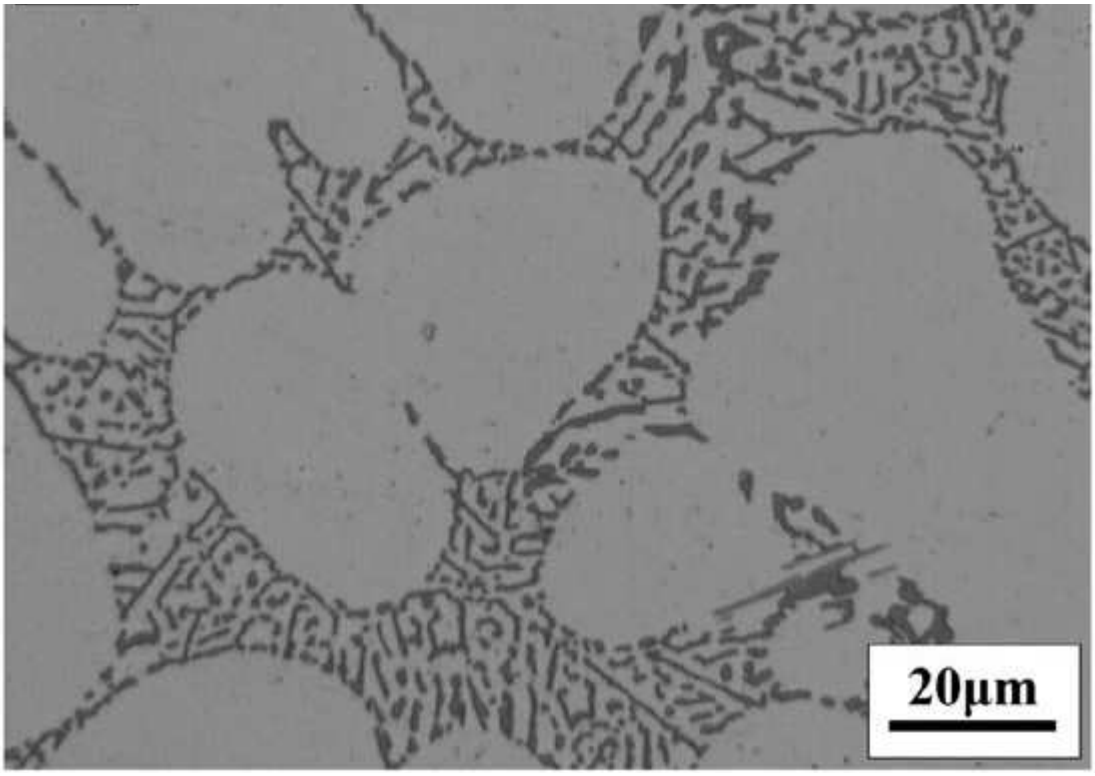

Figure 2.6: Microstructure of alloy A356 showing primary α-Al and the α-Al/Si eutectic [37].

2.2.1.2. Magnesium

Small additions of magnesium induce significant age hardening and the yield strength in the T6 condition has been shown to be more than double that of the binary alloy containing the same amount of silicon [9]. The complete precipitation process in Al-Si-Mg alloys is acknowledged as possibly being the most complex of all age-hardened aluminium alloys [9]. For these alloys in general, the decomposition of the supersaturated solid solution (SSS) is believed to occur as shown in equation 2.1 [39-42]:

$$\mathbf{SSS \rightarrow (Mg + Si)_{clusters} / GP\text{-}I_{spherical} \rightarrow \beta'' / GP\text{-}II_{needles} \rightarrow \beta_{rods}' \rightarrow \beta_{plates} \ (+ Si)} \qquad \mathbf{(2.1)}$$

- GP = Guinier-Preston zones which are spherical with structures that are not well defined [9]. A high resolution transmission electron micrograph (HRTEM) of a naturally aged Si-excess wrought Al-Mg-Si alloy displays a uniform fringe contrast as shown in Fig. 2.7(a) [43]. No contrast attributed to precipitate

particles is observed. On the other hand, the contrast arising from the precipitate particles is observed in the Si-excess alloy that was pre-aged at 70°C for 16 h. The HRTEM image indicates that the precipitates are approximately 2 nm in size and are coherent with the matrix, and the precipitates were therefore designated as GP zones [43].

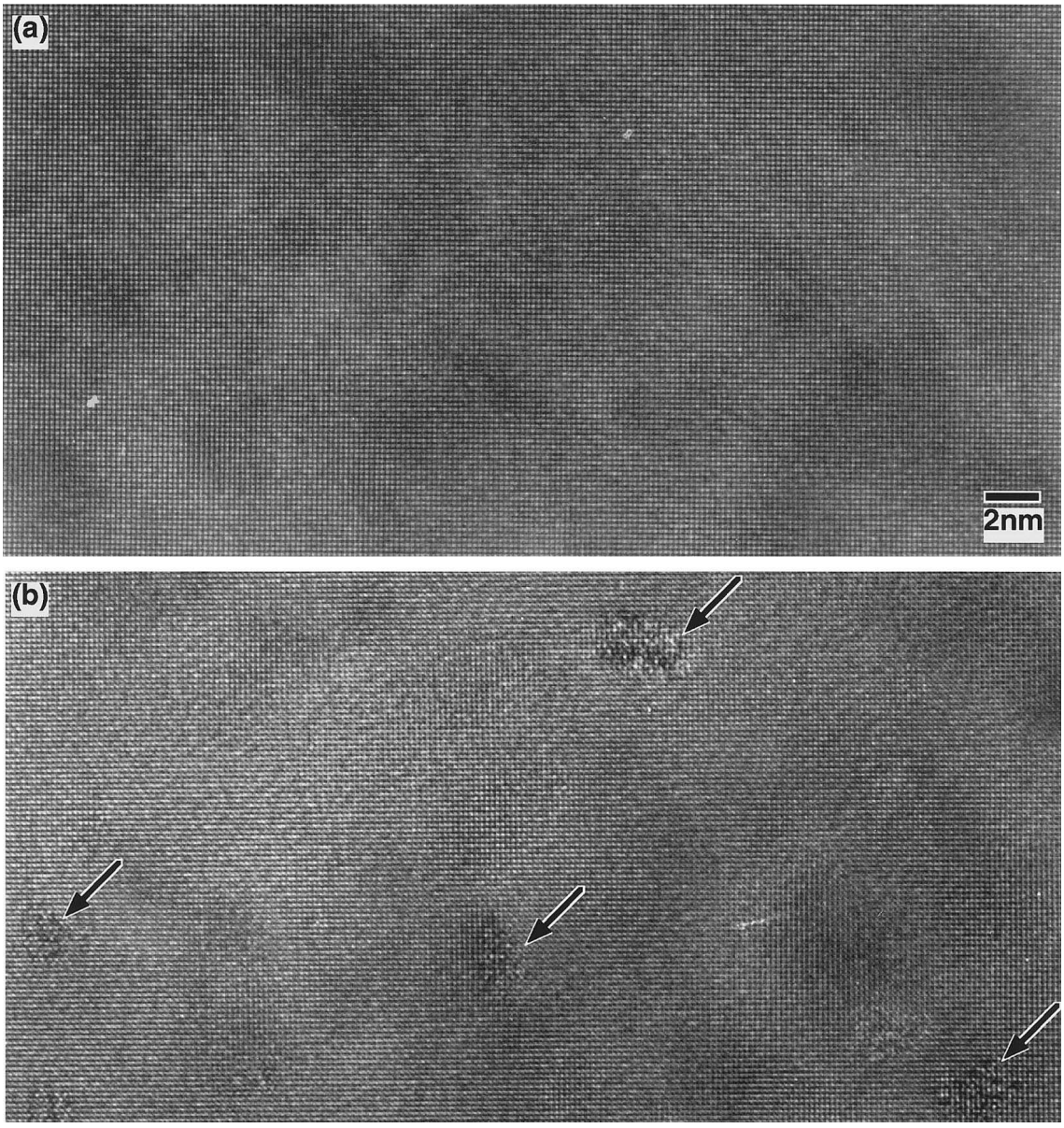

Figure 2.7: HRTEM images taken at the [001]Al zone axis of Al-0.65Mg-0.70Si (Si-excess) alloy after (a) natural aging and (b) 70°C pre-aging [43].

- β″ is a metastable precursor of first β′ and then the stable β. It is monoclinic (three unequal axes with the angles between the axes $\alpha = \gamma = 90^{o} \neq \beta$) with a = 1.534 nm, b = 0.405 nm, c = 0.683 nm and $\beta = 106^{o}$ [9,44]. The β″ precipitates

as coherent needles and lies along $<100>_{\alpha}.(010)_{\beta''}//(001)_{\alpha};[001]_{\beta''}//[310]_{\alpha}$. β″–needles precipitated in alloy A356 aged at 180°C for 2 h are shown in Figure 2.8 [11].

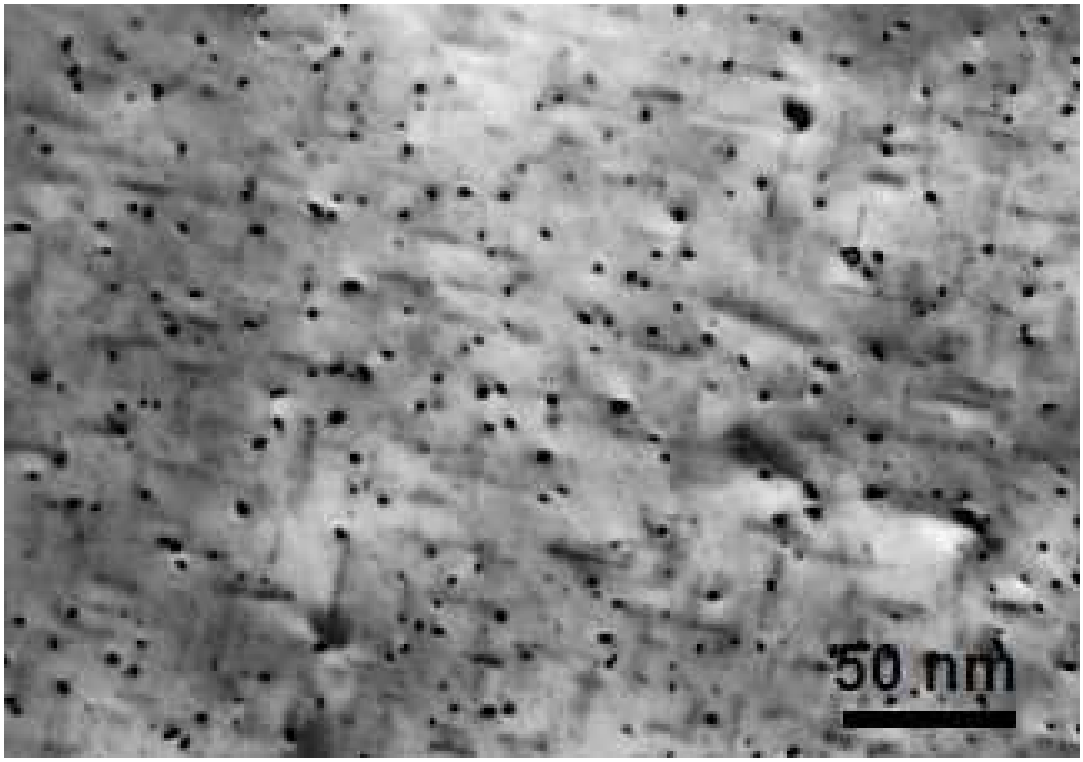

Figure 2.8: TEM image showing β″–needles in an A356 alloy artificially aged at 180°C for 2 h [11].

The β″ precipitate is the main strengthening precipitate in Al-Mg-Si alloys and the composition is thought to be Mg_5Si_6 [45]. However, Buha and co-workers [42] have detected ~ 75 at% Al in these precipitates in the wrought Al-Mg-Si alloy 6061-T6.

- β′ is also a metastable precursor to β with a hexagonal crystal structure with a = 0.705 nm, c = 0.405 nm [9,39]. They precipitate as semi-coherent rods which lie along $<100>_{\alpha}.(001)_{\beta'}//(100)_{\alpha};[100]_{\beta'}//[011]_{\alpha}$ (Fig 2.9 [39]). The composition is believed to be close to $Mg_{1.7}Si$ [9].

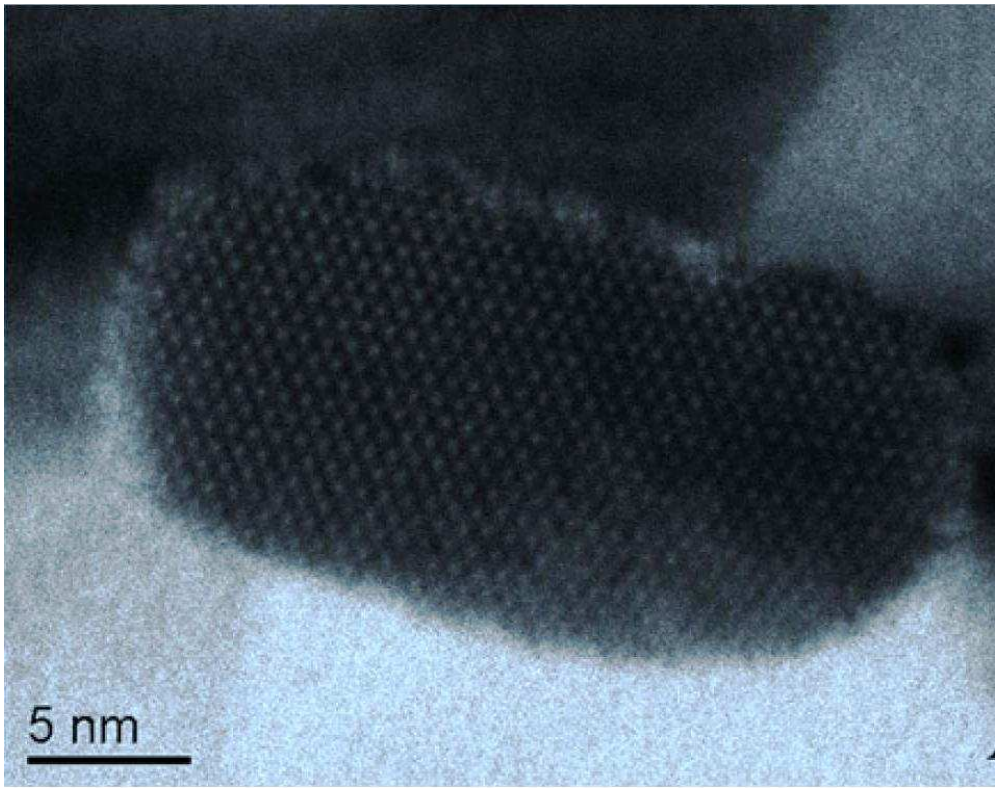

Figure 2.9: HRTEM image showing a β′–rod in a wrought 6082 alloy artificially aged at 260°C for 8 h [39].

- β = Equilibrium Mg_2Si which is face-centred cubic with a = 0.639 nm [9]. The plates or cubes are formed on $\{100\}_\alpha$. They may transform directly from β′ with $(100)_\beta$// $(100)_\alpha$; $[110]_\beta$//$[100]_\alpha$. Figure 2.10 [46] shows typical morphologies of primary Mg_2Si particles at different growth stages in an Al-15%Mg_2Si alloy.

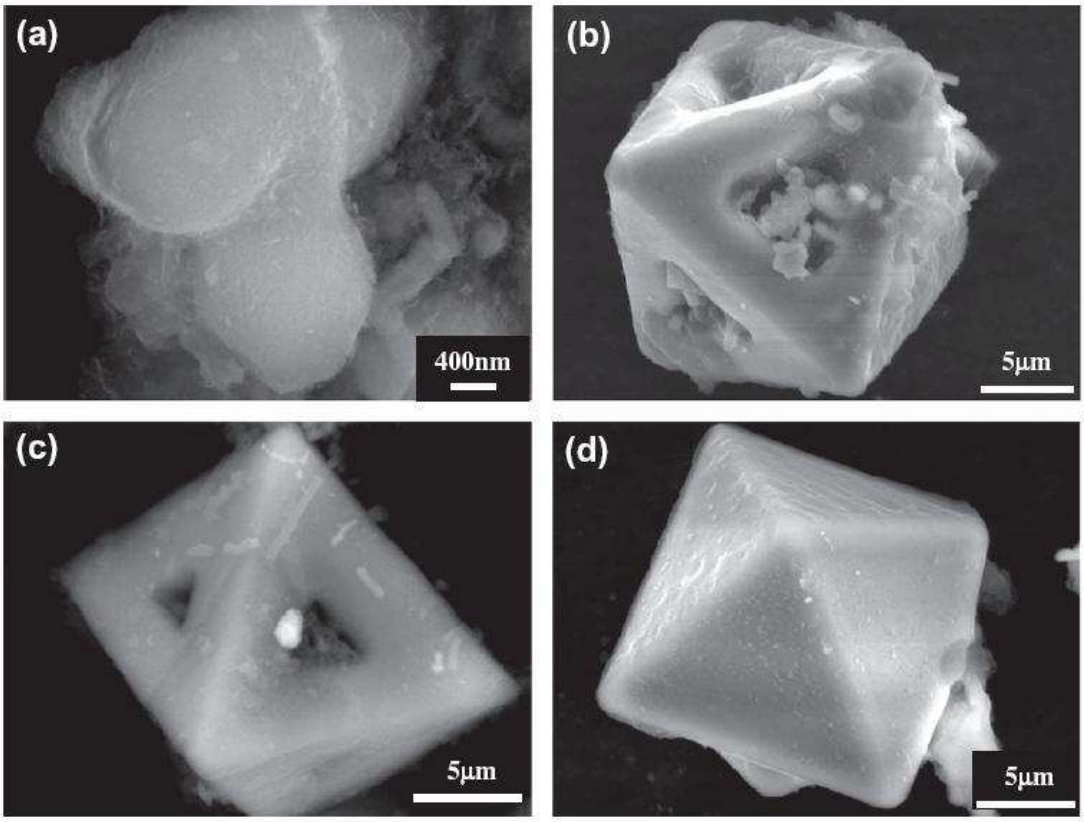

Figure 2.10: Typical morphologies of primary Mg_2Si particles at different growth stages in an Al-15%Mg_2Si alloy [46].

2.2.1.3. Iron

Iron is the most common impurity found in aluminium. It has a high solubility in molten aluminium, but only a maximum of ~ 0.05% in the solid state. Iron, therefore, occurs mainly as intermetallic second phases in combination with aluminium and other elements [33]. Figure 2.11 shows a SEM micrograph of π-$Al_8FeMg_3Si_6$ and β–Al_5FeSi particles in a Be-free alloy F357 [34]. The plate-like phase (indicated as arrow 1) was identified as β–Al_5FeSi, whereas the Chinese script phase (indicated as arrow 2) was identified as π-$Al_8FeMg_3Si_6$. Taylor and co-workers [47,48] have studied the influence of solution treatment on the changes to the relative proportions of iron-containing intermetallic particles in Al-7Si-Mg alloys. They showed that solution treatment caused a substantial transformation of the π-phase ($Al_8FeMg_3Si_6$) to the Mg-free β-phase (Al_5FeSi) in low Mg alloys (0.3-0.4 % or A356). However, this transformation does not occur at higher Mg levels (0.6-0.7% or F357). The transformation of Mg-containing π to β–Al_5FeSi is accompanied by a release of Mg

into the aluminium matrix, which should have an influence on the subsequent aging response of the alloy (equation 2.1).

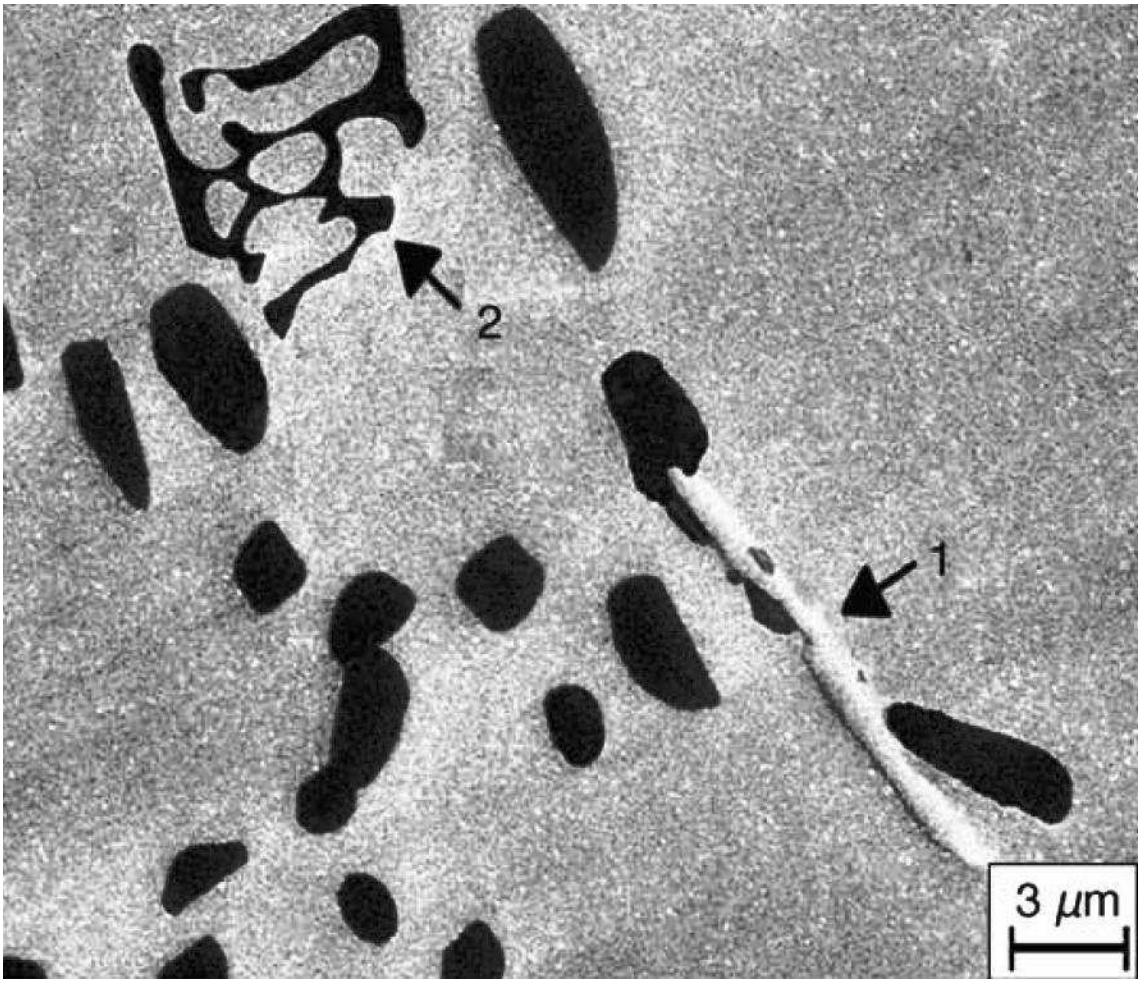

Figure 2.11: SEM micrograph showing the presence of plate-like β–Al_5FeSi (arrow 1) and Chinese-script π-$Al_8FeMg_3Si_6$ (arrow 2) in a Be-free alloy F357 [34].

2.2.1.4. Beryllium

The addition of beryllium to this alloy system leads to a change in the morphology of the iron-rich intermetallics, which results in a slightly better ductility [34]. Figure 2.12 shows that adding Be to the alloy changes the plate-like β–Al_5FeSi phase (Fig. 2.11) to a spherical shape [34].

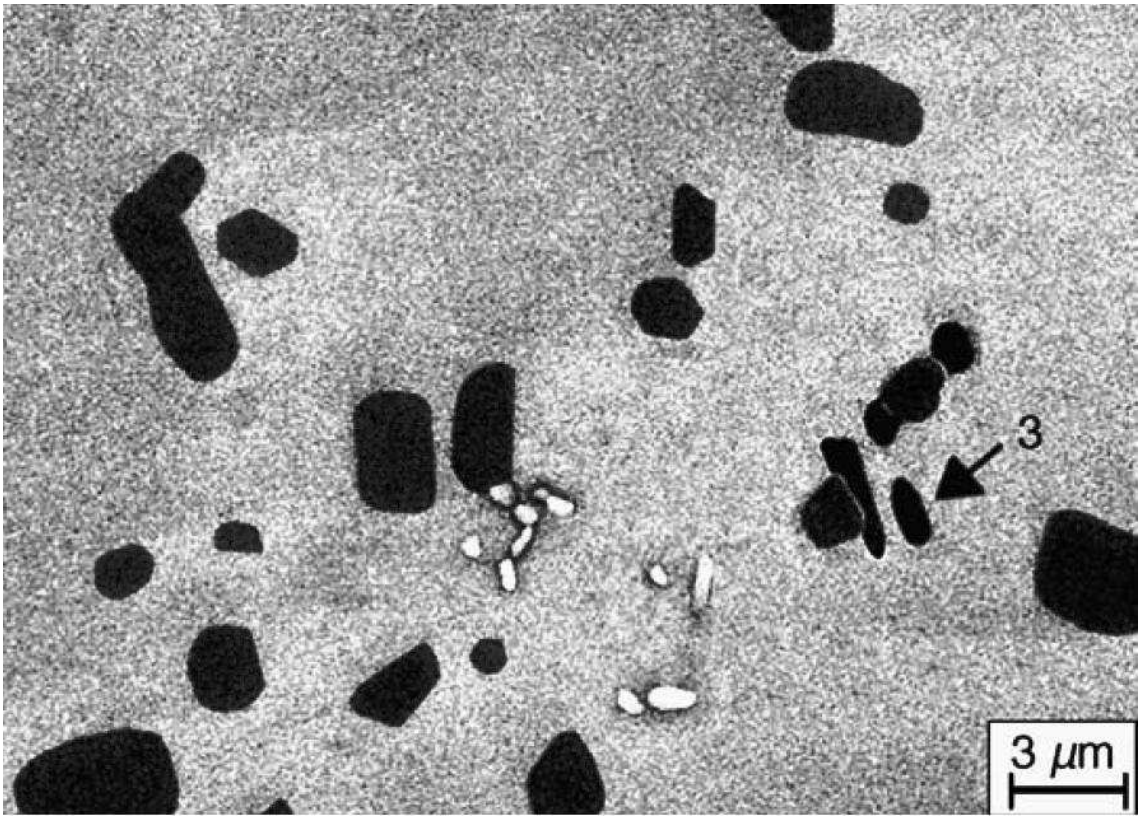

Figure 2.12: SEM micrograph showing the presence of nodular β–Al_5FeSi (arrow 3) in a 0.04wt% Be-containing alloy A357 [34].

Exposure to beryllium is associated with two pulmonary diseases, namely acute berylliosis and a granulomatous lung disease known as chronic beryllium disease (CBD) [49]. Be-containing alloys A357, C357 and D357 (Table 2.1) are therefore gradually being phased out in many applications.

2.2.1.5. Copper

Copper is limited to a maximum of 0.2% in Al-7Si-Mg alloys (Table 2.1). The addition of Cu has been claimed to lead to a higher nucleation rate and refinement of GP zones and β″-precipitates in Al-Mg-Si alloys [50,51]. However, a study of an Al-Si-Mg alloy modified with Sr found that a Cu-content higher than 0.2% resulted in a 7-fold increase of the dispersed microporosity [52]. It was postulated that copper forms interdendritic Cu-rich phases which solidify at a lower temperature. The relationship between the porosity fraction and Cu-content is shown in Fig. 2.13 [53].

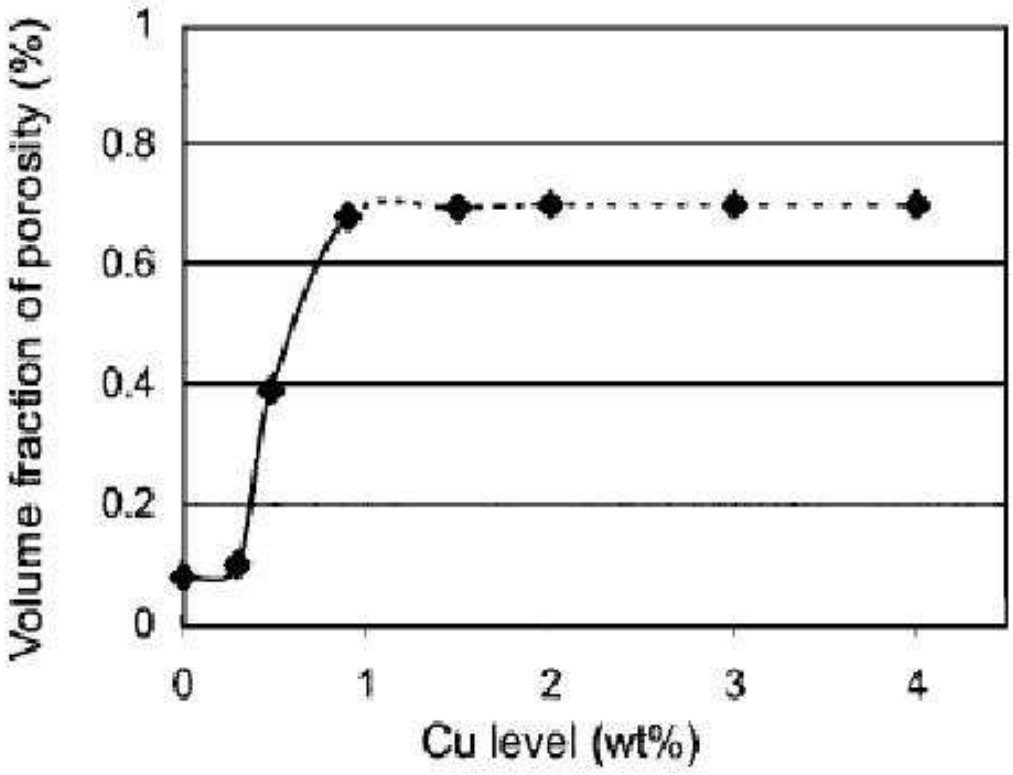

Figure 2.13: The effects of Cu content on porosity fraction in Al-Si alloy [53].

2.2.1.6. Manganese

Manganese is a common impurity in aluminium alloys and has a very limited solid solubility in aluminium in the presence of other impurities [33]. As with beryllium, manganese additions to A356/7 have been shown to modify the morphology of β-Al_5FeSi to improve the ductility of the alloy [54]. When manganese is used as a modifier, it replaces the acicular β-Al_5FeSi with a granular α-Al(Mn,Fe)Si, as shown in Figure 2.14 [54]. The combined addition of Mn and Cr has been shown to be especially effective in this regard [54]. However, the combined content of manganese, iron, chromium and other transition metals must be limited to control the formation of large fractions of coarse and brittle constituents which act as crack initiators and reduce the fracture toughness of the material [55].

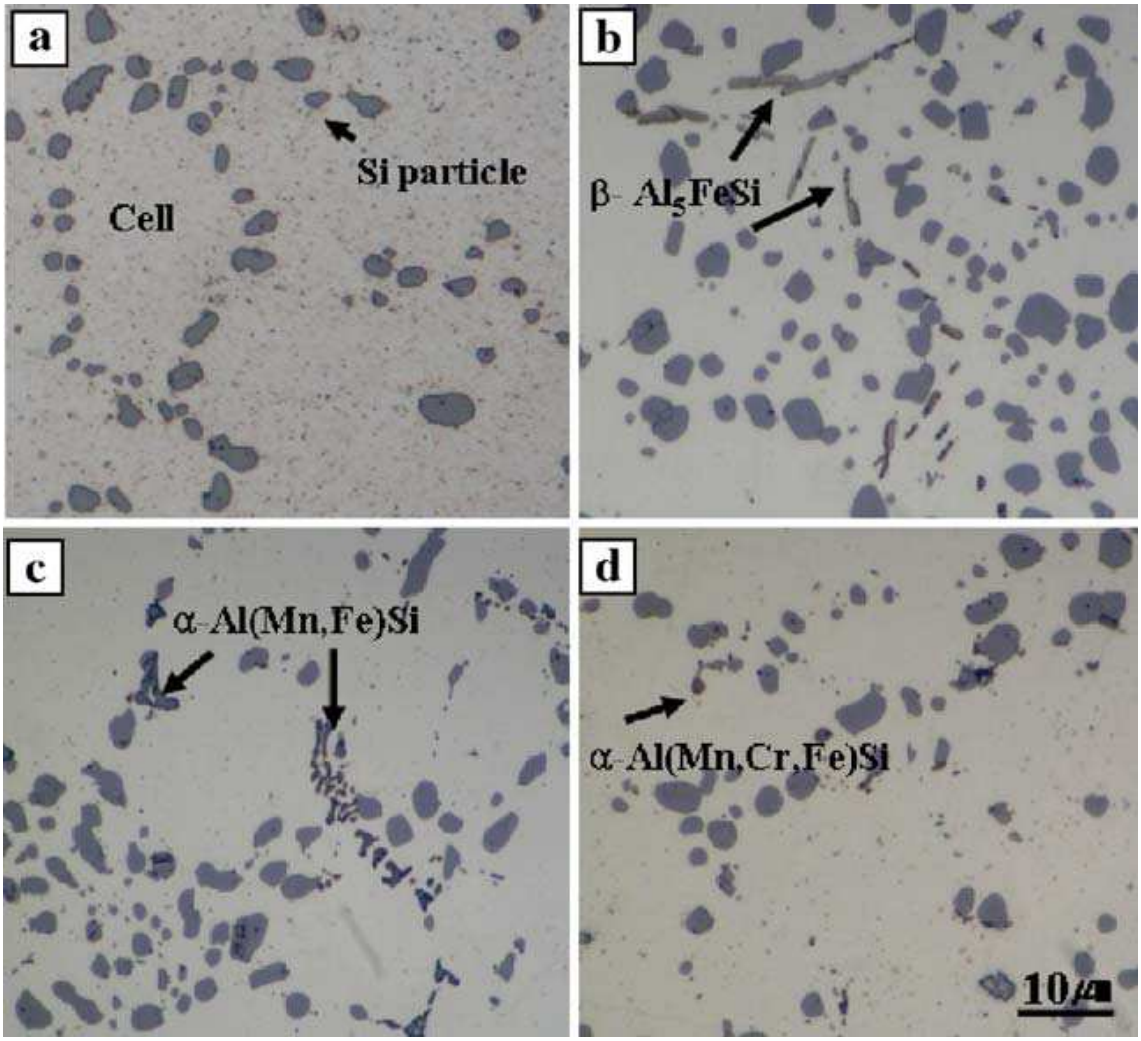

Figure 2.14: Typical solidification microstructures of (a) A356 with ~ 0% Fe, (b) A356–0.20Fe, (c) A356–0.20Fe–0.20Mn and (d) A356–0.20Fe–0.13Mn–0.13Cr [54].

2.2.1.7. Titanium

Titanium is used primarily as a grain refiner of aluminium alloy castings and ingots. When used alone, the effect of titanium decreases with time of holding in the molten state and with repeated remelting. The grain-refining effect is enhanced if boron is also present in the melt or if it is added as a master alloy containing boron combined as TiB_2 [33]. However, Figure 2.15 shows that the grain refining effect of Ti and B addition to SSM-processed alloy A356 is not very successful - an average globule circular diameter of 81μm in the A356 without Ti and B was found, with an average globule circular diameter of 78μm in the A356 with Ti and B [56].

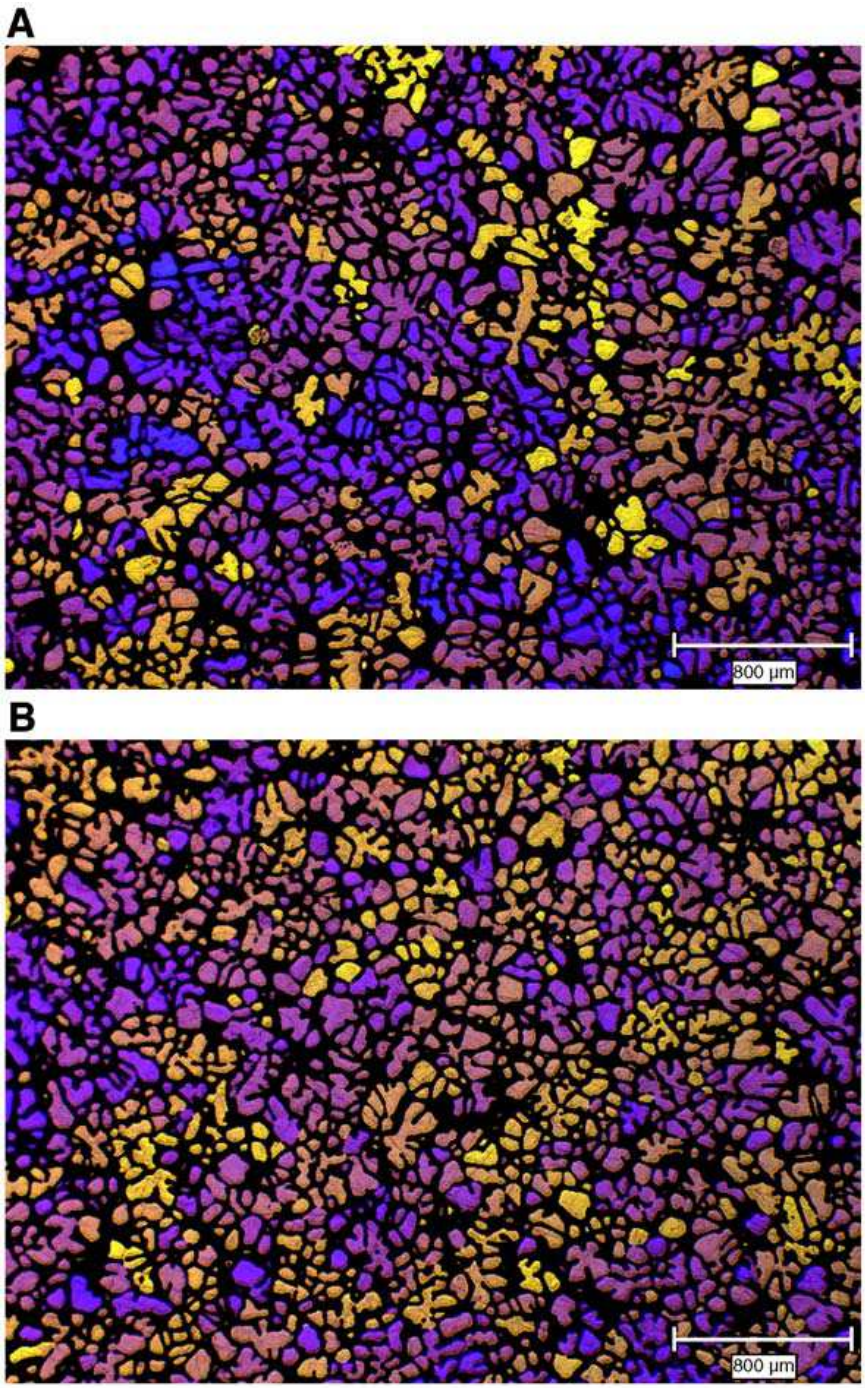

Figure 2.15: Polarised light micrographs showing the effect of Ti, B addition: (A) SSM-processed base alloy A356 without any additions; (B) SSM processed alloy A356 with the addition of 580 ppm Ti and 98 ppm B [56].

2.2.1.8. Strontium, Sodium and Antimony

The size and shape of the eutectic silicon particles can be modified with the addition of strontium, sodium or antimony [6,9]. The use of sodium as the modifying agent causes foundry problems because the fluidity of the melt is reduced. The major

difficulty is however its rapid and uncertain loss through evaporation or oxidation [9]. Additions of antimony at ~ 0.2% can also cause modification but result in a lamellar rather than a fibrous eutectic [9]. Attention has therefore been directed at an alternative method and modification is currently carried out mostly by using additions of strontium (Fig. 2.16 [57]. The amounts of strontium needed range from 0.015 to 0.02% for hypoeutectic castings, but high cooling rates during solidification reduces the amounts needed (Fig. 2.16(b)). Loss of strontium through volatilisation during melting is less than sodium and the modified microstructure can be retained if the alloys are remelted. Over-modification is not a significant problem, because excess amounts are taken into compounds such as Al_3SrSi_3, Al_2SiSr_2 and Al_4Si_2Sr [9,57]. A modification rating (MR) system classifies the eutectic Si structures commonly observed in commercial Al-Si castings by a number from one to six [58]. Table 2.2 describes the MR system in more detail [59].

Table 2.2: Modification rating (MR) system for classification of eutectic Si structures [59].

MR number	Structure	Description
1	Fully unmodified	Si is present in the form of large plates as well as in acicular form.
2	Lamellar	A finer lamellar structure, though some acicular Si may be present (but not large plates).
3	Partially modified	The lamellar structure starts to break up into smaller pieces.
4	Absence of lamellae	Complete disappearance of lamellar phase. Some acicular phase may still be present.
5	Fibrous Si eutectic (Fully modified)	The acicular phase is completely absent.
6	Very fine eutectic (Super modified)	The fibrous Si becomes so small that individual particles cannot be resolved with optical microscopy.

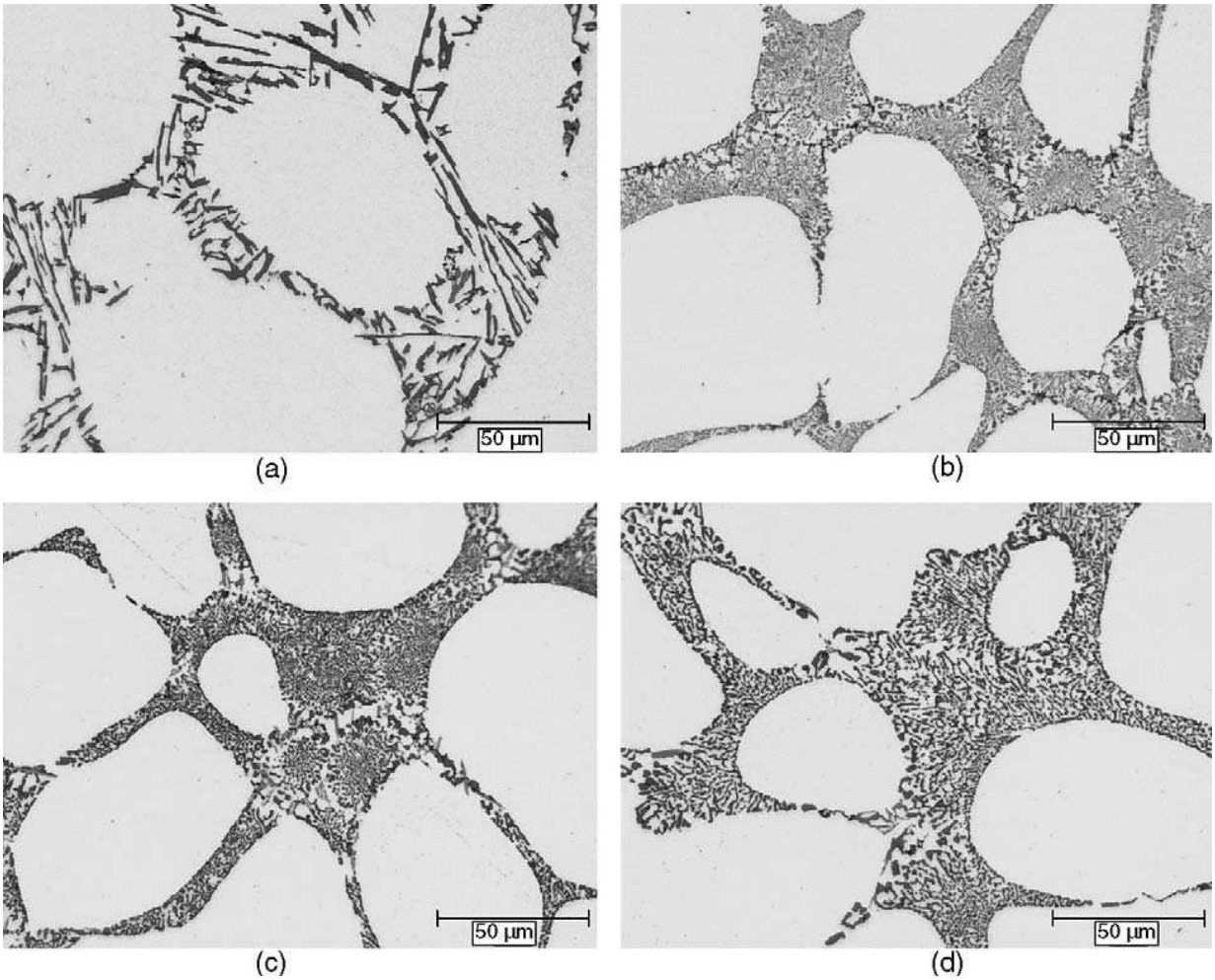

Figure 2.16: Optical micrographs showing the effect of Sr addition in SSM-processed A356 (a) non-modified with MR = 2, (b) 47 ppm Sr with MR = 5, (c) 156 ppm Sr with MR = 5, and (d) 392 ppm Sr with MR = 5 [57].

2.3. Heat Treatment

Aluminium alloys used for high-pressure die casting are mostly those based on the systems Al-Si-Mg and Al-Si-Cu, each of which has the capacity to respond to age hardening [60]. However, conventional liquid HPDC components cannot be given traditional solution heat treatments due to surface blistering and dimensional instability as a result of gas entrapment during casting [60]. Lumley and co-workers [61] have shown that liquid HPDC components can be partially solution heat treated to achieve an adequate supersaturated solid solution of the solute elements if the solution treatment stage is carried out at lower than normal temperatures (e.g. 440-490^{o}C) and for much shorter times (Fig. 2.17 [61]).

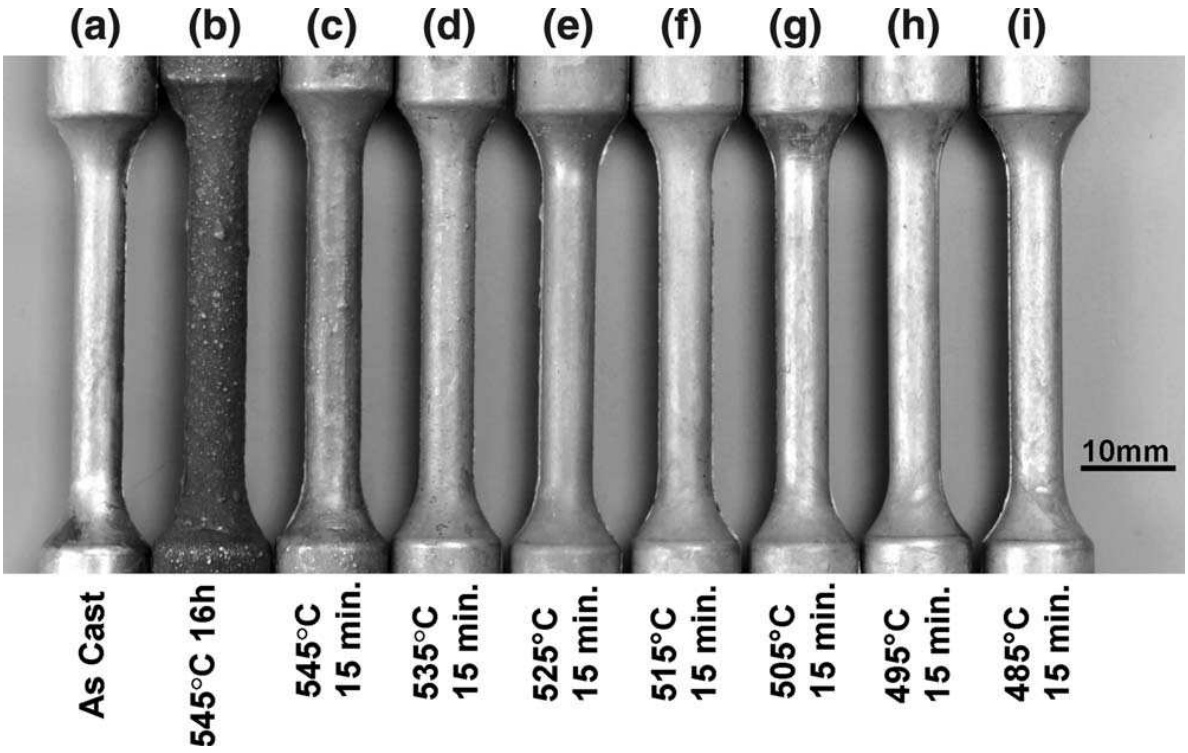

Figure 2.17: Surface appearances of Al alloy 360 in the conventionally cast HPDC as-cast condition and after different solution-treatment schedules [61].

However, one of the advantages of SSM-processing is that the laminar flow during die-fill avoids the problems of oxide and gas entrapment and also reduces the shrinkage problems during solidification [28]. Blistering during heat treatment of SSM-HPDC components can, therefore, be prevented and traditional solution heat treatments can be performed to achieve complete supersaturated solid solutions.

Heat treatment is a critical process to improve mechanical properties of certain alloy components. Heat treatment technology is currently facing numerous challenges such as energy conservation, environmental impact and the more strict market needs such as reliability, higher performance and production costs [6,62]. Additionally, heat treatment standards presently being used in foundries were developed several years ago and have to be amended to suit current foundry practices [63]. Controlled heat treatment of aluminium alloys can significantly influence properties such as strength, ductility, fracture toughness, thermal stability, residual stresses, dimensional stability, and resistance to corrosion and stress corrosion cracking [6]. The main heat treatment procedures are homogenisation, annealing, and precipitation hardening involving solution heat treatment, quenching and aging [64]. A heat treatment and temper

designation system has been developed by the Aluminium Association to describe the processing of wrought and cast aluminium alloys (Table 2.3 [6,64]).

Table 2.3: Heat treatment and temper designation system for aluminium alloys [6,64].

Suffix		Treatment
F		As-fabricated
O		Annealed
H		Strain hardened by cold work
T		Heat treated to a stable condition, excluding annealing (O)
	T1	Cooled from an elevated temperature forming process (partial solution) followed by natural aging
	T2	Cooled from an elevated temperature forming process, cold worked and naturally aged
	T3	Solution heat treated, quenched, cold worked and naturally aged
	T4	Solution heat treated, quenched and naturally aged
	T5	Rapidly cooled from elevated forming temperature and then artificially aged
	T6	Solution heat treated, quenched and then artificially aged
	T7	Solution heat treated, quenched and overaged
	T8	Solution heat treated, quenched, cold worked and then artificially aged (amount of cold work in % indicated by subsequent digit)
	T9	Solution heat treated, quenched, artificially aged and then cold worked
	T10	Cooled from an elevated temperature forming process, cold worked and then artificially aged
W		Unstable temper applied for alloys which age spontaneously at room temperature after solution heat treatment. Only specific if followed by the time of natural aging

2.3.1. Solution heat treatment

A solution heat treatment is carried out at a sufficiently high temperature for sufficiently long times to produce a nearly homogeneous solid solution [6]. The temperature is determined based on the maximum solid solubility and composition and is usually attained by heat treating near, but below, the eutectic temperature. Temperature variations within ± 6°C are allowed in most cases, but may be even stricter for some high-strength aluminium alloys [6]. Underheating can result in incomplete solution and might reduce the strengthening potential of the alloy, but is sometimes necessary for instance to avoid distortion and blistering in liquid HPDC components [60,61]. Overheating can lead to incipient melting of low-melting point phases (Fig. 2.13). The extent to which Mg and Si can be present in solid solution in alloys A356/7 depends on the actual solution treatment temperature and alloy chemistry. Fig. 2.18 shows the equilibrium concentrations of Mg and Si versus temperature in Al-Si-Mg ternary alloys in which both Si and Mg_2Si phases are present [48]. Figure 2.19 shows the 7% Si vertical section (as found in alloys A356/7) of the Al-Si-Mg equilibrium phase diagram [48]. This shows that the maximum solubility of Mg in this ternary alloy system is 0.68% at 555^{o}C. This corresponds closely to the maximum specification for alloy F357 of 0.70% in Table 2.1. Ohnishi and co-workers [65] illustrated an increase in the extent of solutionizing (with a corresponding higher strengthening potential of alloy A356) with an increase of solution treatment temperature from 500 to 570^{o}C. However, the most popular solution treatment temperature employed for Al-7Si-Mg alloys is 540^{o}C, which is 15^{o}C below the eutectic temperature [48]. From Fig. 2.18 it can be seen that the maximum solute content of Mg and Si at 540^{o}C should be 0.62 and 0.90% respectively. Using Fig. 2.19, it is seen that a 540^{o}C solution treatment temperature would result in a maximum Mg solute content of approximately 0.6% (dashed line).

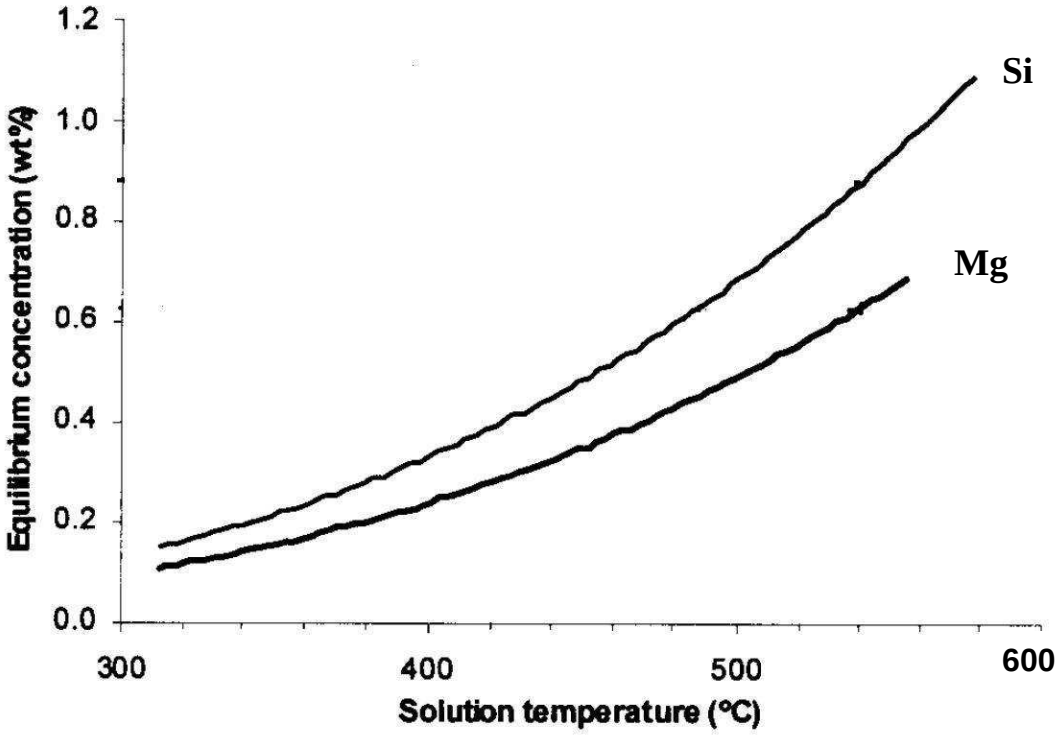

Figure 2.18: Equilibrium solute concentrations of Mg and Si in Al-Si-Mg ternary alloy system at various temperatures [48].

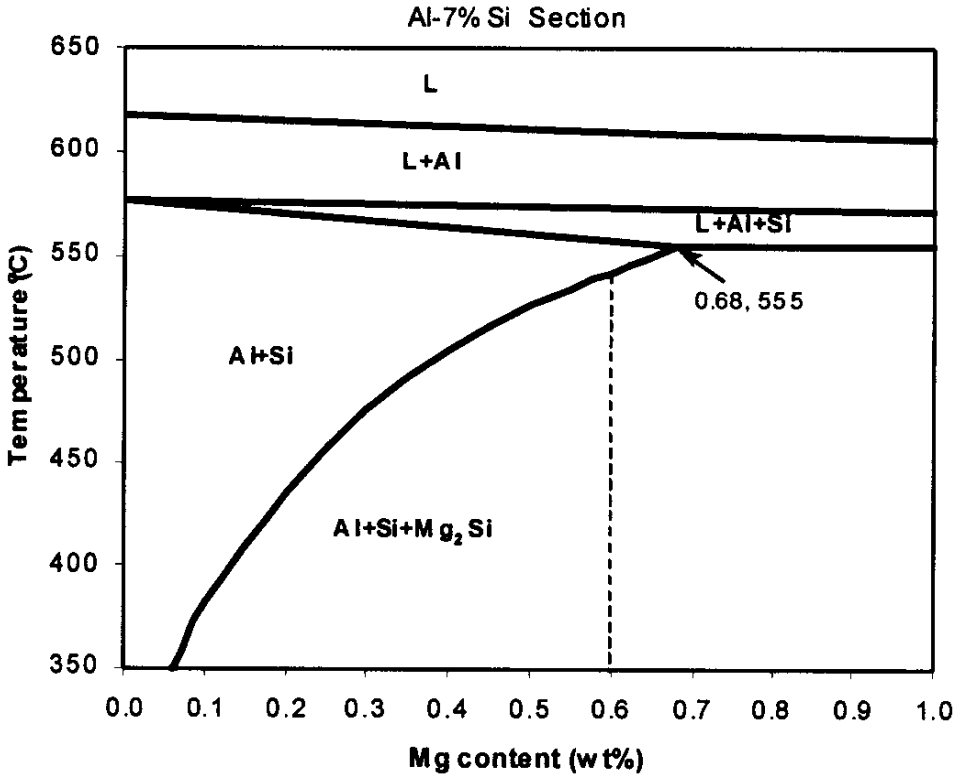

Figure 2.19: Vertical section of the Al-Si-Mg equilibrium phase diagram at 7% Si [48].

Commercial Al-7Si-Mg alloys are not pure ternary alloys and contain various impurities of which the typical ~ 0.1% Fe influences the solution treatment response the most [47,48]. Taylor and co-workers [47,48] showed that solution treatment caused a considerable transformation of the Mg-containing π-$Al_8FeMg_3Si_6$ phase to the Mg-free β-Al_5FeSi phase in alloy A356, but that this transformation did not occur in alloy F357. They found that full dissolution of the bulk Mg-content of the alloy in the matrix was possible up to 0.4%. Above 0.4% Mg, the stability of the π-$Al_8FeMg_3Si_6$ phase resulted in only partial dissolution of the bulk Mg-content of the alloy (Fig. 2.20 [48]). It can be seen from Fig. 2.20 that an F357 alloy containing 0.70% Mg and 0.12% Fe will only have 0.52% Mg in solid solution after solution heat treatment at 540°C.

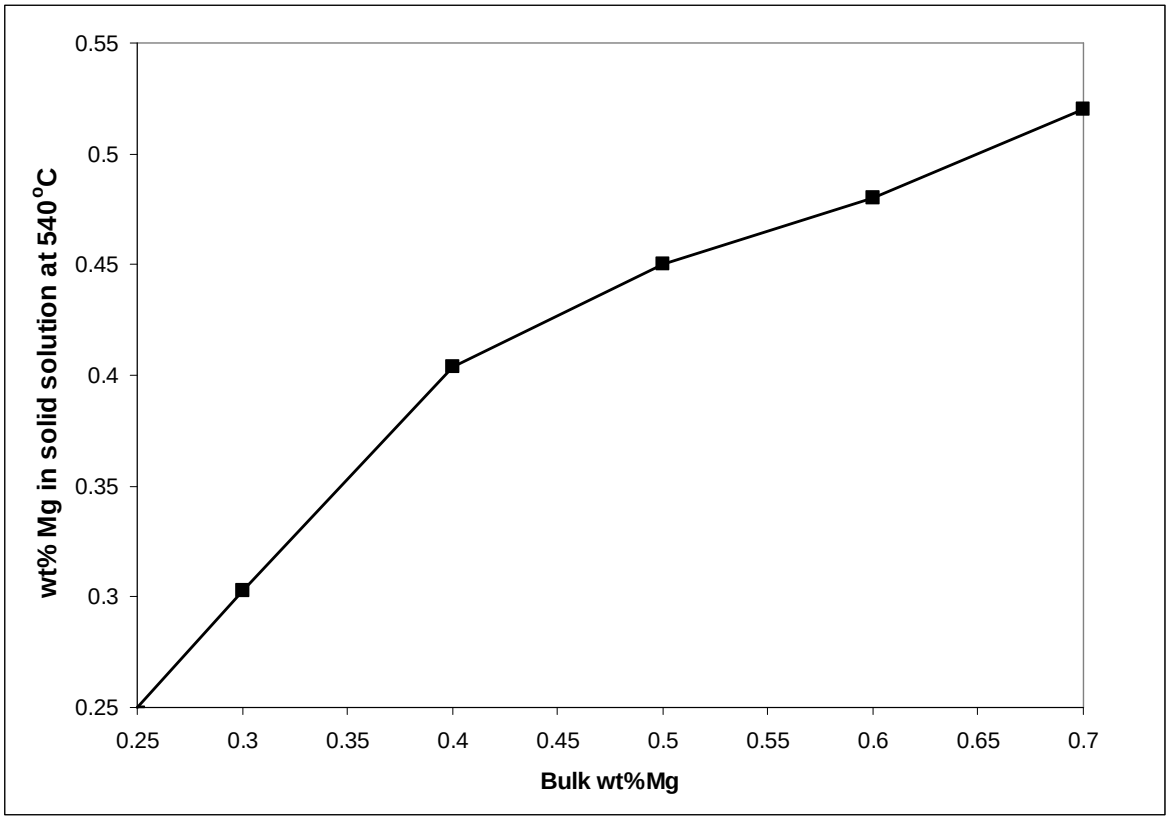

Figure 2.20: Mg-concentration in solid solution (after solution treatment at 540°C) as a function of bulk Mg-concentration in Al-7Si-Mg alloys [48].

The solution treatment time depends on the casting method, the extent of modification and the desired level of spheroidisation and coarsening of the silicon particles. Table 2.4 illustrates the differences in solution heat treatment parameters for liquid cast A356 as a function of the casting method [33].

Table 2.4: Solution heat treatment parameters for Sr-modified A356 [33].

Casting Method	Microstructural Features	Solution treatment
Sand	Large dendrite arm spacing (DAS) and globular Si particles	540^{o}C for 12 h
Permanent Mould	Fine DAS and small globular Si particles	540^{o}C for 4-12 h

Shivkumar et al [66] showed that, for permanent mould cast test bars of alloy A356, a solution treatment of only 50 minutes at 540^{o}C was sufficient to produce more than 90% of the maximum yield strength, more than 95% of the ultimate tensile strength (UTS) and nearly 90% of the maximum elongation for a given aging condition. They also demonstrated that the magnesium and silicon contents in the α-Al dendrites reached the maximum equilibrium level according to the alloy composition and that the distribution of silicon and magnesium became homogeneous within 50 minutes at 540^{o}C. Zhang et al [67] studied the possibility of using even shorter solution treatment times with A356 cast by low pressure die casting. Compared with a "traditional" 6 h solution treatment at 540^{o}C, a solution treatment of 30 minutes was sufficient to achieve more than 90% of the maximum yield strength, more than 95% of the maximum UTS and the maximum % elongation. However, only 80% of the maximum impact energy was achieved, which was attributed to a smaller silicon interparticle spacing. According to Taylor et al [48], the Mg_2Si dissolves within 5 minutes for alloy A356 and about 40 minutes for A357 during solution treatment at 540^{o}C. Homogenisation of the concentration profiles also occur rapidly – approximately 8-15 minutes for A356 and about 40-50 minutes for A357 [49]. Rometsch et al [68] performed mathematical modelling of the dissolution of Mg_2Si and homogenisation in Al-7Si-Mg alloys. The model predicts that dissolution and homogenisation are complete after solution treatment times of less than one hour at 540^{o}C for both A356 and A357. They also suggested that, from a yield strength point of view, the main objective of the solution treatment is not to dissolve the Mg_2Si particles, but rather to diffuse Mg from the eutectic matrix into the dendritic matrix. The numerical model predictions of the time required to complete Mg_2Si dissolution and alloy homogenisation at 540^{o}C for both A356 and A357 as a function of the DAS are

shown in Fig. 2.21. It can be seen that the alloy Mg content (i.e. the increase in Mg-content from alloy A356 to A357) and DAS have significant effects on the times required for dissolution and homogenisation. However, in general, less than an hour is required in all instances in Fig. 2.21.

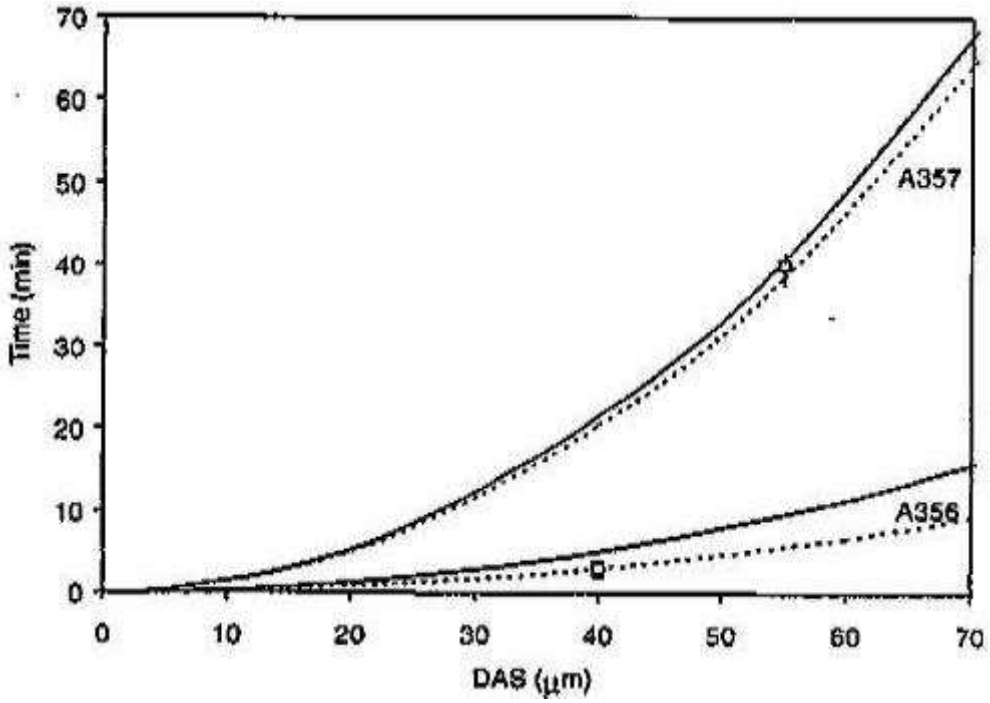

Figure 2.21: Numerical model predictions of the time required to complete Mg_2Si dissolution (dotted curves) and alloy homogenisation (solid curves) at 540°C for both A356 and A357. The vol% of Mg_2Si was kept constant in each alloy as the DAS was increased [68].

In Al-Si casting alloys, the solution treatment is also applied to cause spheroidisation of the eutectic silicon particles, which leads to improved ductility and fracture toughness (Fig. 2.22 [6]). Aluminium-silicon casting alloys, in which the eutectic silicon is modified, undergo rapid spheroidisation of the silicon particles, while complete spheroidisation is never achieved in unmodified alloys [6,69].

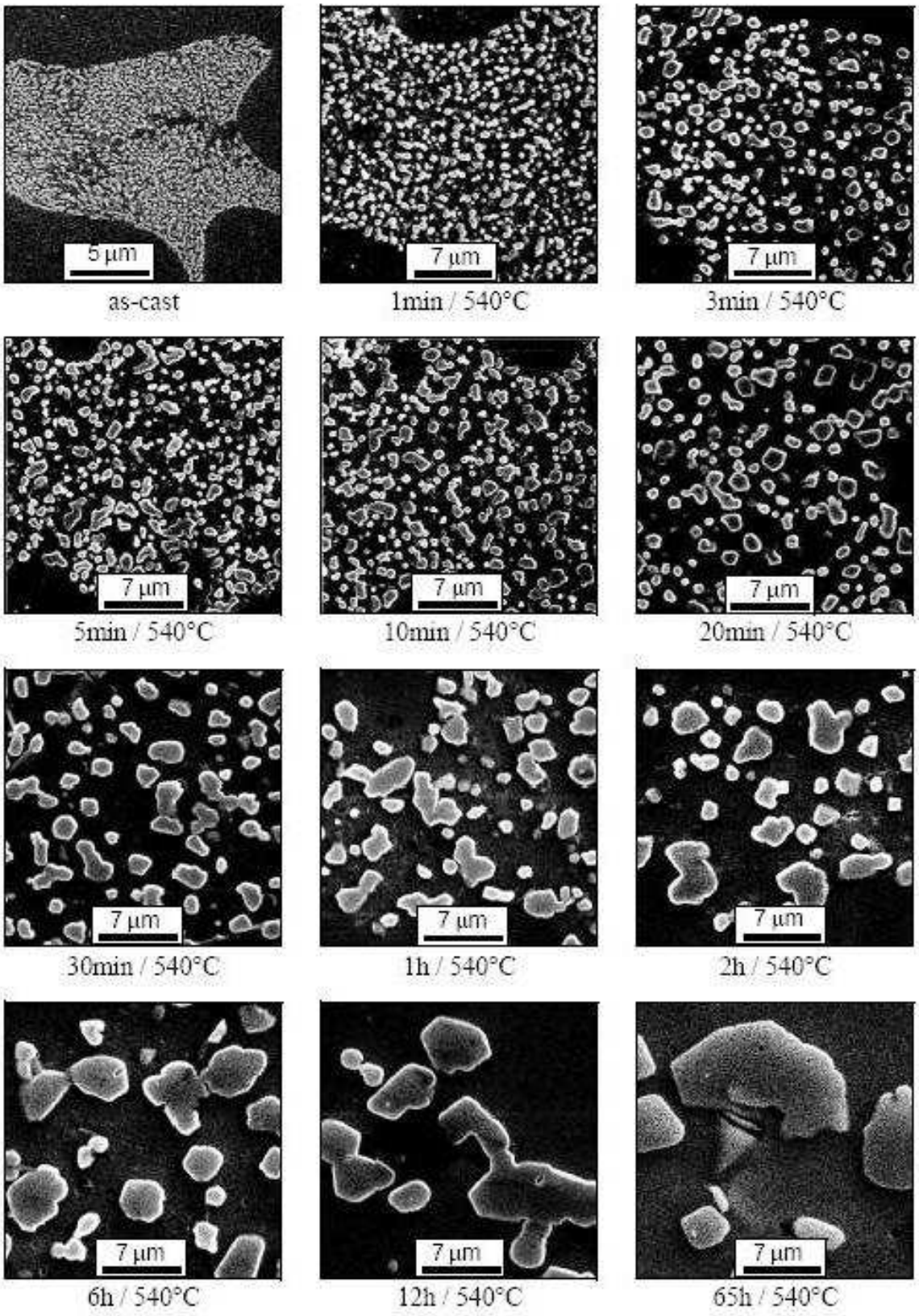

Figure 2.22: Chronology of Si spheroidisation of Sr-modified A356 at 540°C [6].

Detailed investigations on silicon spheroidisation in Sr-modified A356 by Ogris [6] have shown that the disintegration and spheroidisation of the silicon coral branches is complete within 3 minutes of soaking time between 500°C and 540°C (Fig. 2.22). This is supported by the observation by Parker and co-workers [69] that spheroidisation is complete in less than 10 minutes at 540^{o}C.

It should be noted that, apart from chemical modification by additions of Sr, Na or Sb, modification of eutectic Si-particles can also be achieved by high cooling rates during solidification [57,59,70]. It is well known that the solidification rate during HPDC is high [71] and lower levels of Sr are expected to be required to achieve modification during SSM-HPDC of Al-7Si-Mg alloys (also see Fig. 2.16).

From the above discussion, it appears as if the frequently specified solution treatment time of $\geq$ 6 h at 540^{o}C is very conservative in terms of the times actually required to achieve solute dissolution and Si-spheroidisation.

2.3.2. Quenching

Subsequent to solution heat treatment, the alloy must be cooled at a sufficiently high rate to retain the solute in solid solution and to retain a high number of vacancies at room temperature. High cooling rates associated with water quenching result in the generation of thermal stresses leading to distortion and residual stresses, especially in large castings with complex geometries [72]. Conversely, low cooling rates that provide reduced levels of thermal stress, produce non-strengthening quench precipitates (such as β′ and β in the Al-Mg-Si system), which ultimately reduce the strength attainable after aging. An optimum balance between strength and thermal stresses during quenching is therefore desired. Slower quenching rates can be achieved by using water at 65-80°C, boiling water, polyalkylene glycol, forced air or mist [72]. The average quench rates corresponding to different quench conditions, as found by Zhang and Zheng [73], are listed in Table 2.5.

Table 2.5: The average quench rates in the temperature range of 450°C to 200°C corresponding to different quenching conditions [73].

Quenching condition	25°C Water	60°C Water	95°C Water	Air Cool
Quench rate (°C/s)	250	110	20	0.5

The sensitivity of alloys to quench rate and the allowable delay between solution heat treatment and quenching is determined from quench factor analysis which is based on avoiding the tip of the nose of the Continuous Cooling Transformation (CCT) diagram. The 95% iso-yield strength contours for unmodified alloy A357 and wrought alloy 6082 are presented in Figure 2.23 [74]. Alloy 6082, with almost the same β-Mg_2Si content as A357, is much less quench sensitive than A357. The relatively high quench sensitivity of cast Al-7Si-Mg alloys is mainly due to the presence of Si particles in the structure, which affects quench sensitivity in three ways: (1) Si in solid solution diffuses to these particles, (2) particles serve as heterogeneous nucleation sites for β-Mg_2Si and (3) dislocation densities in dendrites of Al-7Si alloys are expected to be high due to localised plastic strain from the mismatch of the coefficient of thermal expansion (CTE) between Si and Al. Large differences in CTE between the Al matrix and Si particles result in the generation of compressive residual stresses in the particles and tensile residual stresses in the matrix during cooling from high temperatures. Some of the CTE mismatch is accommodated by plastic relaxation in the matrix, increasing its dislocation density, which provides more nucleation sites for quench precipitates [74].

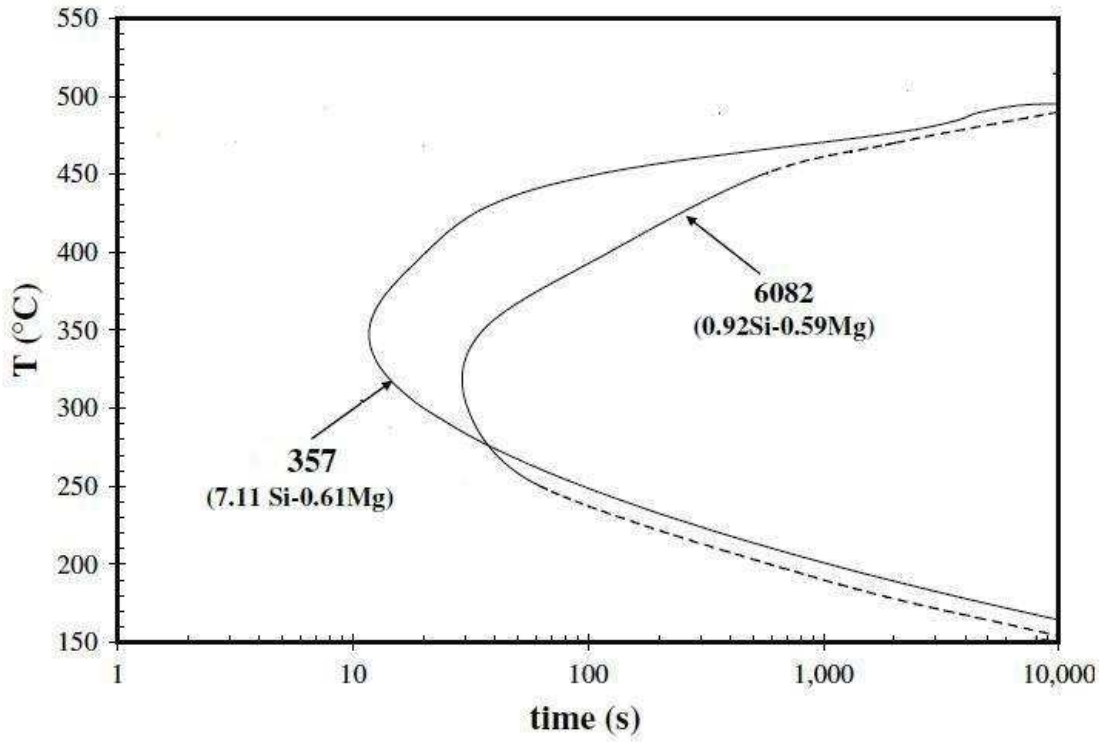

Figure 2.23: 95% iso-yield strength contours in casting alloy A357 and wrought alloy 6082 [74].

Zhang and Zheng [73] showed that the yield strength and ultimate tensile strength (UTS) of alloy A356 artificially aged at 170^{o}C for 6 h decreased significantly with decreasing quench rate (Figure 2.24). With a decrease in quench rate from 250^{o}C/s to 0.5^{o}C/s (Table 2.5), the UTS decreased from 330 to 242 MPa, i.e. by 27%, while the yield strength decreased from 274 to 184 MPa, i.e. by 33 %.

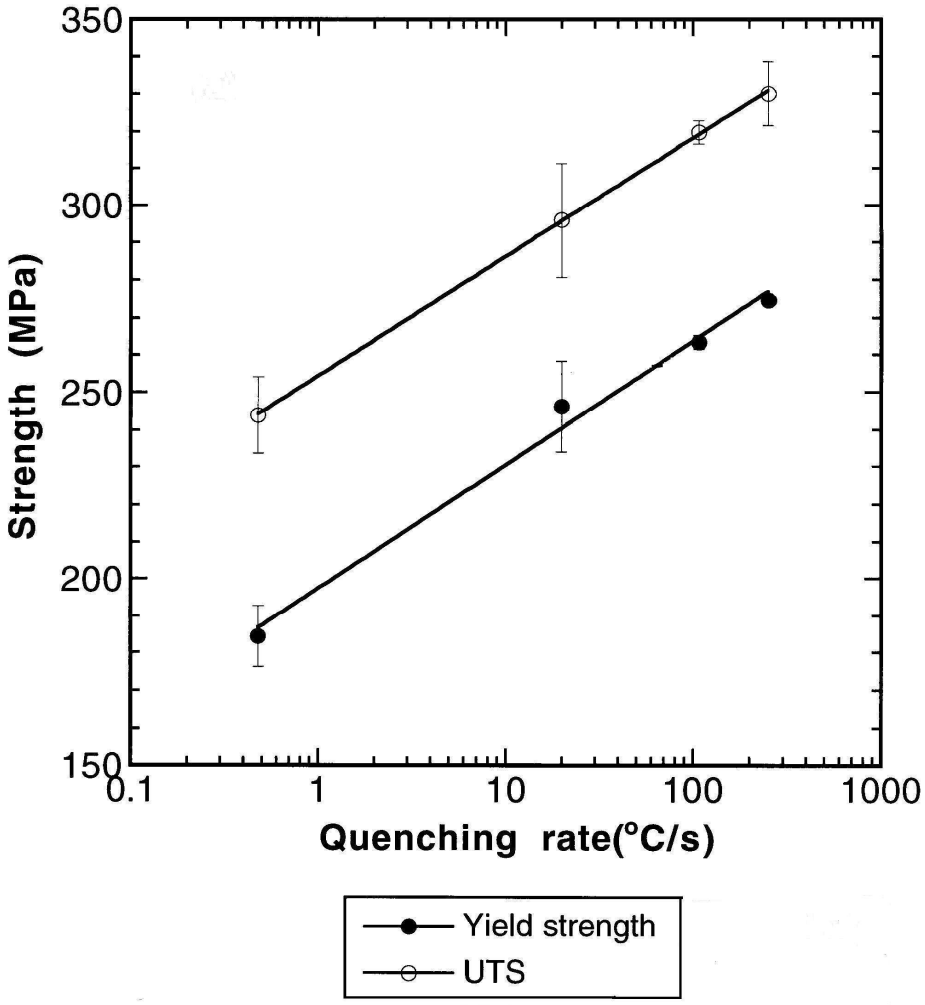

Figure 2.24: Strength of peak-aged alloy A356 as a function of the average quench rate - the quenching conditions listed in Table 2.5 were applied [73].

2.3.3. Aging

Aging is the controlled decomposition of the supersaturated solid solution to form finely dispersed precipitates in heat-treatable alloys, usually by soaking for convenient times at one or sometimes two temperature levels. Aging takes place at room temperature (natural aging) or at an elevated temperature in the range of 100–210^{o}C (artificial aging). The objective of aging is to obtain a uniform distribution of small precipitates, which gives a high strength.

The strength of an alloy is derived from the ability of precipitates to impede mobile dislocations. The strength is determined by the size and distribution of the precipitates and by the coherency of the precipitates with the matrix. The interaction with the dislocations can be described by the Friedel effect and by the Orowan mechanism [75]. Small and not too hard precipitates are normally sheared by moving dislocations

(Friedel effect – Fig. 2.25(a) [75]). When the precipitates are larger and harder, the moving dislocations bypass the precipitates by bowing (Orowan mechanism - Fig. 2.25(b) [75]). The strength of the precipitates increases with their size as long as they are sheared by dislocations. Further increase of precipitate size makes the shearing processes more difficult; hence, it is more favourable for the dislocations to pass the precipitates via the Orowan mechanism. This leads to a decrease in strength with further increase in precipitate size (Fig. 2.25(c) [75]). The highest strength is obtained when there is an equal probability for the dislocations to pass the precipitates by shearing and by bowing [75]. Figure 2.25 is used in the process model for age hardening of Al-7Si-Mg alloys (see Chapter 6).

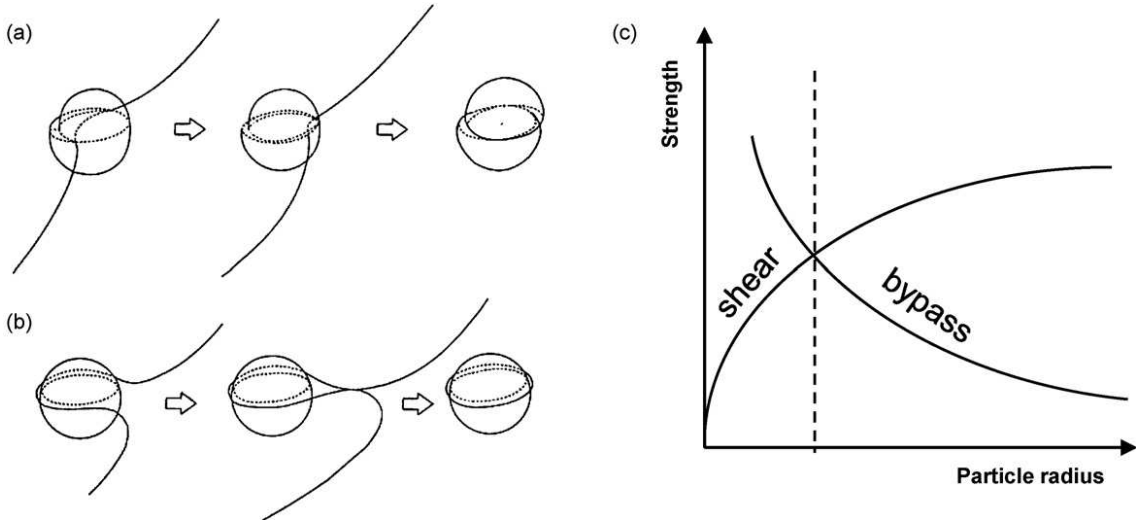

Figure 2.25 [75]: Dislocations pass precipitates either by (a) shearing or (b) bypassing [76]. (c) Relationship between precipitate radius and strength of the particles to resist shearing or bypassing by dislocations [9].

It is often assumed that the precipitation sequence (equation 2.1) and phases in the Al-Mg-Si 300 series casting alloys are similar to those in Al-Mg-Si 6000 series wrought alloys [11]. To date, there is a lack of detailed research work revealing precipitate micro- and nanostructural evolution during aging of the Al-Si-Mg casting alloys. This is due to difficulties the eutectic component causes in preparing high-quality samples for transmission electron microscopy (TEM) and atom probe tomography (APT) [11]. The nanostructural evolution of the Al-Mg-Si 6000 series wrought alloys has been studied much more extensively than the casting alloys [77-79]. The main difference between the 300 series and 6000 series is the Si content, with the casting alloys

containing a significantly higher quantity of this alloying element (Table 2.1). The 6000 series wrought alloys generally contain ≤ 1.5% Si and ≤ 1.2% Mg respectively [80]. The following discussion on the aging characteristics of Al-Si-Mg alloys will therefore also incorporate studies on the precipitation of the 6000 series wrought alloys.

2.3.3.1. Natural aging

Natural aging refers to the decomposition of the solid solution that occurs at room temperature. During natural aging, the high level of supersaturation and the high vacancy concentration from rapid quenching cause quick formation of clusters and hardness and strength increases swiftly (Fig. 2.26) [80]). The change in hardening rate in Fig. 2.26 from fast to slow was attributed to a decrease in the growth rate of the clusters. Initially, silicon dominates cluster formation due to its higher diffusivity and lower solubility in aluminium. Later (i.e. after approximately 50 minutes), the clusters begin to enrich in Mg and hardening occurs at a lower rate due to cluster growth that is limited by Mg diffusion [80].

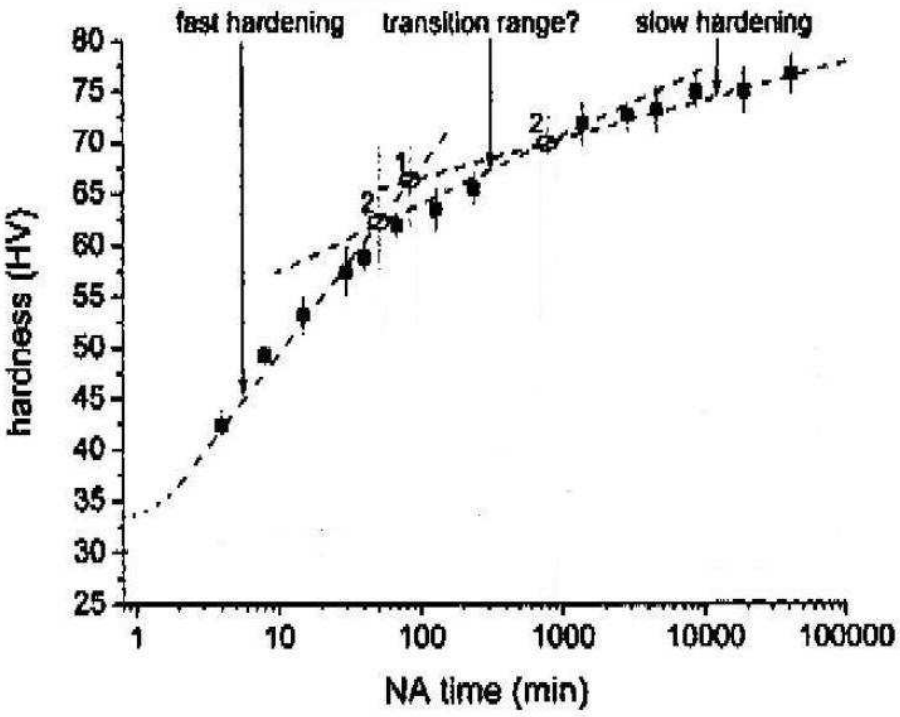

Figure 2.26: Hardness evolution of Al-0.59% Mg-0.82% Si naturally aged at 25°C after solution heat treatment and quench [80].

Nearly maximum stable values are attained in 4 or 5 days for Al-7Si-Mg alloys and the T4 temper is therefore usually specified as material that was naturally aged for 120 hours [81]. The solute clusters that are found in large numbers in Al-Mg-Si alloys in the T4 condition typically contain only a few to tens of solute atoms [78]. They are fully coherent with the matrix and are difficult to resolve even by employing HRTEM (Fig. 2.7(a)) and a technique such as APT is required for their study (Figure 2.27 [78]).

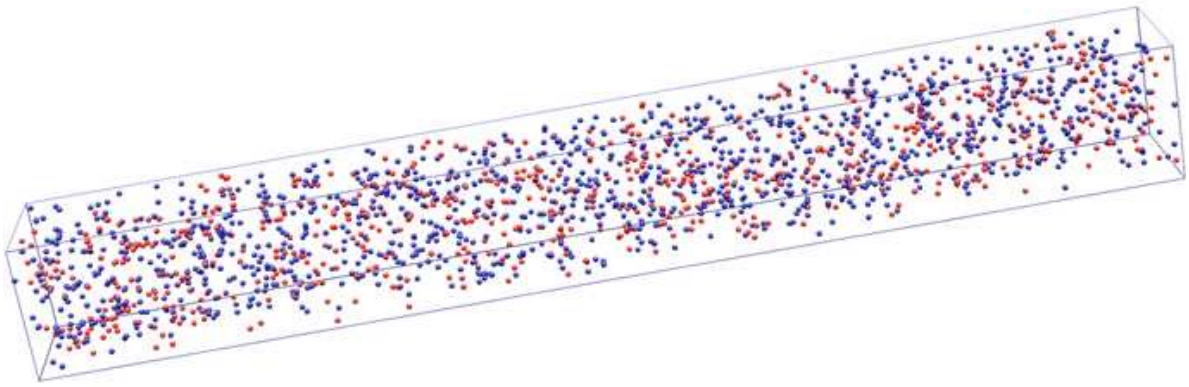

Figure 2.27: 3-dimensional reconstruction of Mg (red spheres) and Si (blue spheres) atom positions in a Al–0.59% Mg–0.82% Si alloy after solution heat treatment with subsequent aging at room temperature (NA) for 1 week. The investigated volume is 8.5x8.5x62 nm^3 [78]

It was postulated that only about 5% of all Si and Mg atoms in the naturally aged specimen in Fig. 2.26 were located in the clusters and that such clusters consisted of only about 4–8 atoms [78].

2.3.3.2. Artificial aging

Artificial aging involves decomposition of the supersaturated solid solution at elevated temperature, normally in the range of 100-210°C for times between 2 h to 48 h [6]. At these temperatures, atoms can move over larger distances and the precipitates formed during artificial aging are normally much larger in size than clusters and GP zones [75]. The artificial aging treatment is designed to produce optimum size, distribution, constitution and morphology of precipitates.

The most comprehensive sets of artificial aging curves for Al-7Si-Mg alloys A356/7 have been determined by Rometsch and Schaffer (Figures 2.28 and 2.29 [82]). These

curves were produced after a solution treatment at 540°C for 75 minutes (A356) and 120 minutes (A357), quenching in room temperature water and artificial aging without delay (i.e. no natural pre-aging).

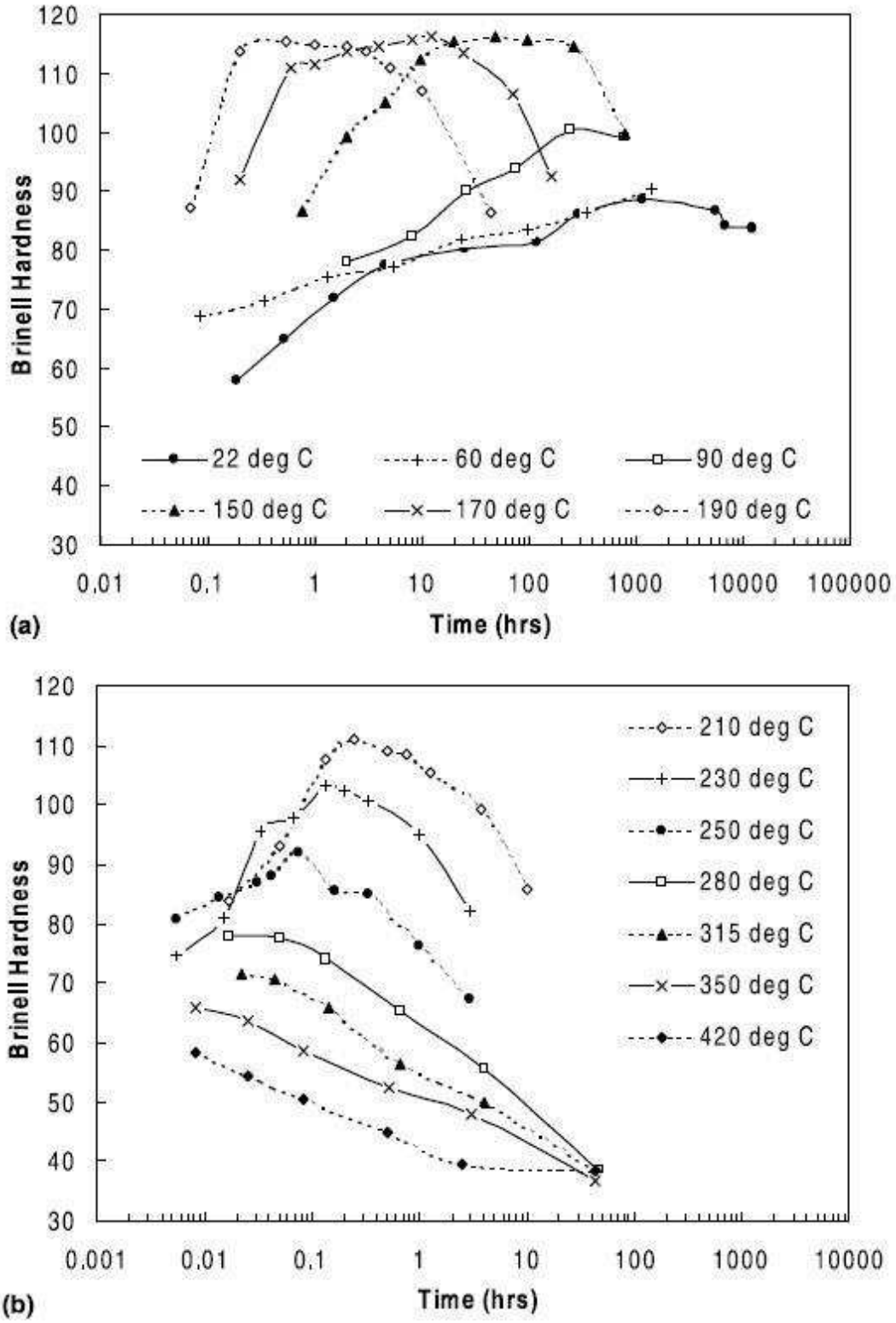

Figure 2.28: HB aging curves for A356 at (a) 22–190°C and (b) 210–420°C [82].

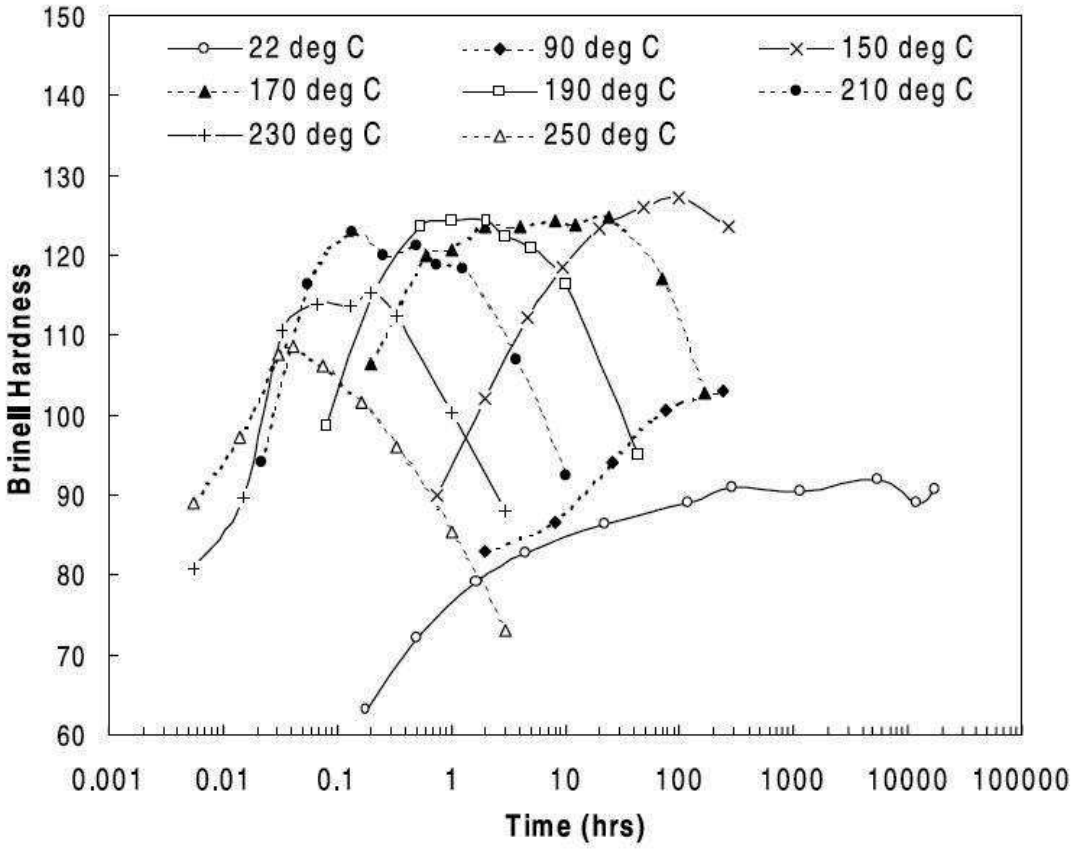

Figure 2.29: HB aging curves for A357 at 22–250°C [82].

When artificial aging temperatures in the range of 170–210°C are used, comparable strength levels are achieved in Figs. 2.28 and 2.29. The time for aging can, however, be shortened if a higher temperature is used - the time to peak hardness is about 10 h at 170°C, while it is only 20 min at 210°C. If the artificial aging temperature is increased above 210°C, a decrease in strength is seen. According to Eskin [83], the β″-phase is substituted by the β′-phase at temperatures above 200°C, which gives a lower contribution to strength.

The precipitation sequence of alloy A356 was recently studied by Rinderer et al by employing TEM and APT [11]. Sample preparation of casting alloys presents more difficulties than the wrought alloys and APT measurements of only ~ 0.5 million atoms were achieved. The success rate for measurement of the A356 alloy was also reduced compared to the 6000 wrought alloys. Castings were studied after solution heat treatment at 540°C for 6h followed by a 60°C water quench. Natural aging was for 2 h prior to artificial aging at 180°C and aging was performed at various times of

0.25 h, 1 h, 2 h, 196 h and 670 h with 2 h representing the peak hardness condition. The TEM sequence of precipitation is shown in Fig. 2.30 [11].

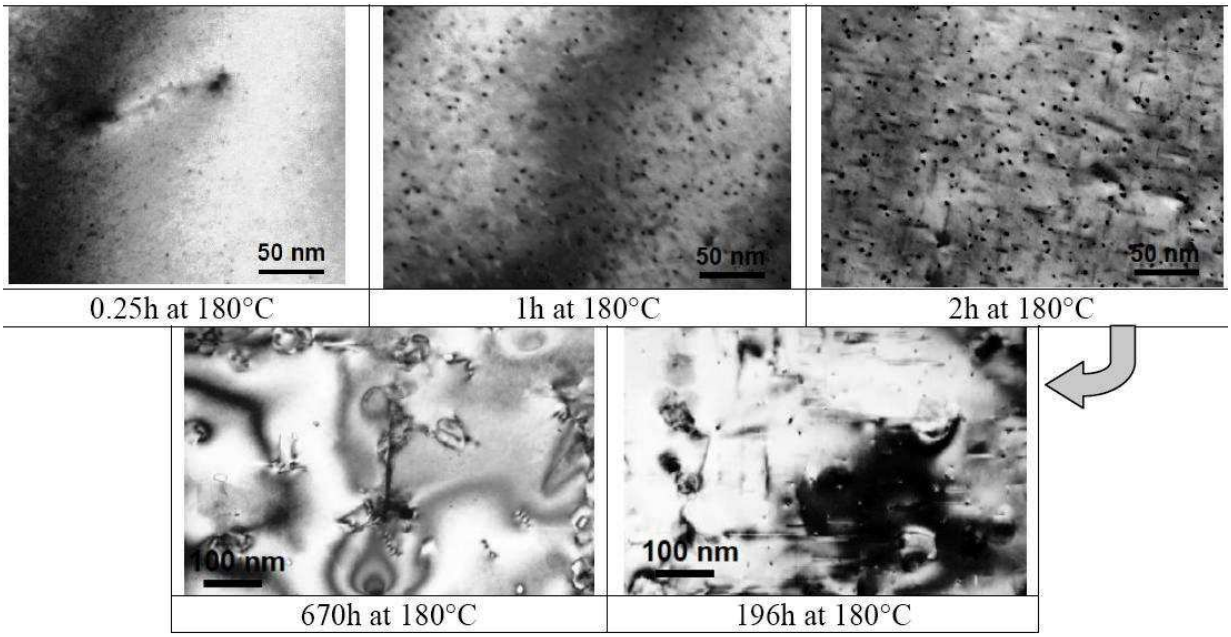

Figure 2.30: TEM bright field micrographs illustrating the precipitation sequence in A356 alloy aged at 180°C for various times [11].

After artificial aging for 0.25h at 180^{o}C, the TEM micrograph shows a microstructure that contains a uniform dispersion of fine spherical particles (i.e. GP zones) and a very small amount of fine needle-like precipitates on dislocations. After aging for 1 h the microstructure includes fine-scale $<100>_{\alpha}$ precipitate needles which are most likely the β″-phase. In the peak aging condition of 2 h, the microstructure shows a higher proportion of β″. Over-aging for 196 h results in a microstructure consisting of a mixture of coarse $<100>_{\alpha}$ rods (most likely the β′-phase). Long-term aging for 670 h at 180°C only led to a significant coarsening of β′ and precipitates of the equilibrium β-phase were not detected.

3D atom probe analysis was performed on A356 samples in the under-aged (0.25 h at 180°C) and peak aged (2 h at 180°C) conditions (Fig. 2.31 [11]).

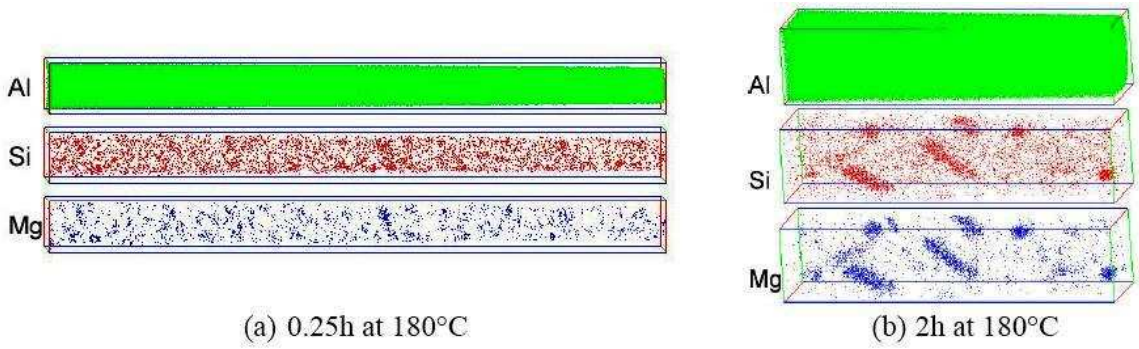

Figure 2.31: 3D-APT results for A356 alloy aged at 180°C. For the under-aged condition (a), the volume shown is 14x14x166 nm^3 and the analysis volume for the peak aged sample (b) is 20x19x88 nm^3 [11].

In the under-aged condition the number density of Mg/Si aggregates was found to be ~ 7 x 10^{23} m^{-3} and, on average, the Mg/Si ratio of the aggregates was ~ 0.7. For the peak aged condition, the composition of the precipitates had an average Mg/Si ratio of ~ 1.2, i.e. the additional aging time resulted in an increase in the Mg associated with the precipitates. The number density of particles decreased to 4 x 10^{23} m^{-3} and this reduction in the number density of particles was accompanied by coarsening of the precipitates compared to the under-aged condition [11].

2.3.3.3. Influence of natural pre-aging on subsequent artificial aging

The influence of prior natural aging time on the subsequent artificial aging response of Al-Mg-Si wrought 6000 series alloys is complex, but has been studied extensively [50,80,84-87]. In the more highly alloyed alloys within the 6000 series it has been suggested that clusters that form during natural aging are “robust” during subsequent artificial aging [9,84]. They proposedly trap the available vacancies or deplete the matrix from solute atoms, while also not being favourable nucleation sites for further in-situ heterogeneous nucleation of β″ [86]. For instance, the number density of β″ precipitates in alloy 6082 has been shown to be almost five times higher in samples that were artificially aged immediately after solution treatment compared to samples that were naturally aged for a week before artificial aging [84], which had an adverse effect on the tensile properties [9,85]. The opposite, however, is believed to occur in the 6000 series alloys that are not as highly alloyed [9,50,85]. Chang and co-workers [50] described the “positive effect” of natural pre-aging on precipitation hardening in a wrought alloy with a composition of Al-0.44at%Mg-0.38at%Si. Artificial aging of

naturally aged samples increased the value of the peak hardness which was attributed to an increase in the number density of β″ needle-like precipitates as compared to samples without prior natural aging. Bichsel and Ried [87] have drawn contour plots for 6000 series wrought alloys showing the effect of 24 h natural aging on the change in UTS (MPa) as a function of the Mg and Si content (Fig. 2.32 [85]). The contour lines indicate the change in UTS after artificial aging at 165^{o}C for 15 h. Figure 2.32 confirms that the negative effect of natural pre-aging is obtained in 6000 series alloys with high Si and Mg contents, whereas the opposite occurs in alloys with low Si and Mg contents.

Gupta et al [88] have used differential scanning calorimetry (DSC) to study precipitation in a naturally pre-aged wrought Al-Mg-Si alloy (Fig. 2.33). The curve shows two exothermic precipitation peaks B and D, and three dissolution troughs, A, C and E. Peak B is a composite peak and was attributed to precipitation of β″/β′, while peak D was attributed to precipitation of β particles. The trough A is consistent with the dissolution of some of the zones and clusters that are typically present in the T4 temper alloys.

The effects of natural pre-aging on artificial aging of 300 series casting alloys have not been studied as comprehensively as for the 6000 series wrought alloys and only mechanical testing studies have been conducted with a lack of microstructural investigations. Emadi et al [72] found that natural pre-aging of A356 was detrimental to yield strength and UTS, although the properties seemed to recover after a delay of 20 h for bars aged at 170^{o}C (Fig. 2.34 [72]. Ductility was improved up to 12 h natural aging and then dropped significantly for 20 h natural aging [Fig. 2.34 [72]). The authors concluded that the reasons for the observed behaviour are not clear. A recent review paper [75] on the heat treatment of Al-Si-Mg-(Cu) casting alloys concluded that the influence of natural pre-aging on the subsequent artificial aging is not yet fully understood and needs to be studied further.

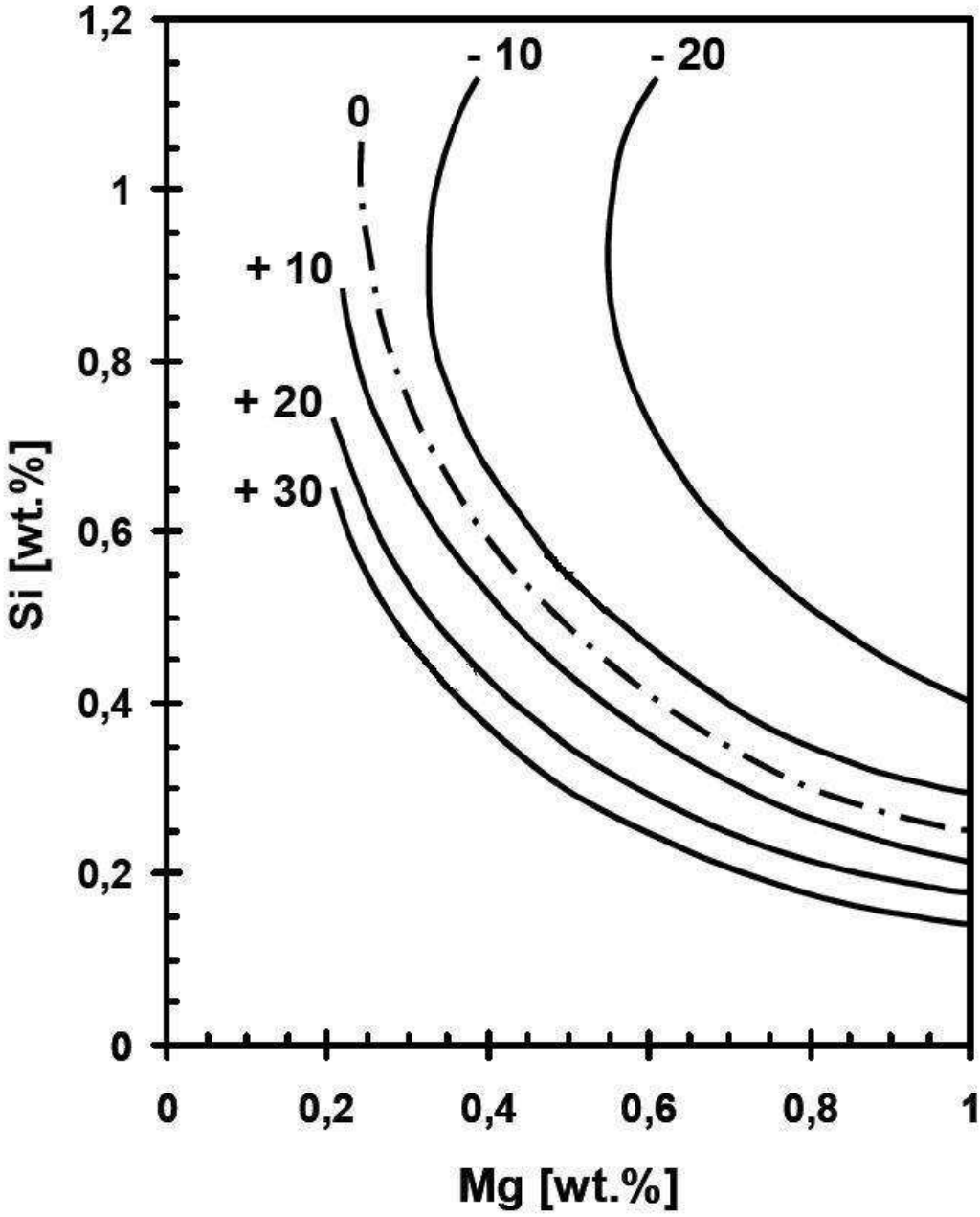

Figure 2.32: Contour plots for 6000 series alloys showing the effect of 24 h natural pre-aging on the change in UTS (MPa) after artificial aging at 165°C for 15 h as a function of the Mg and Si content [85].

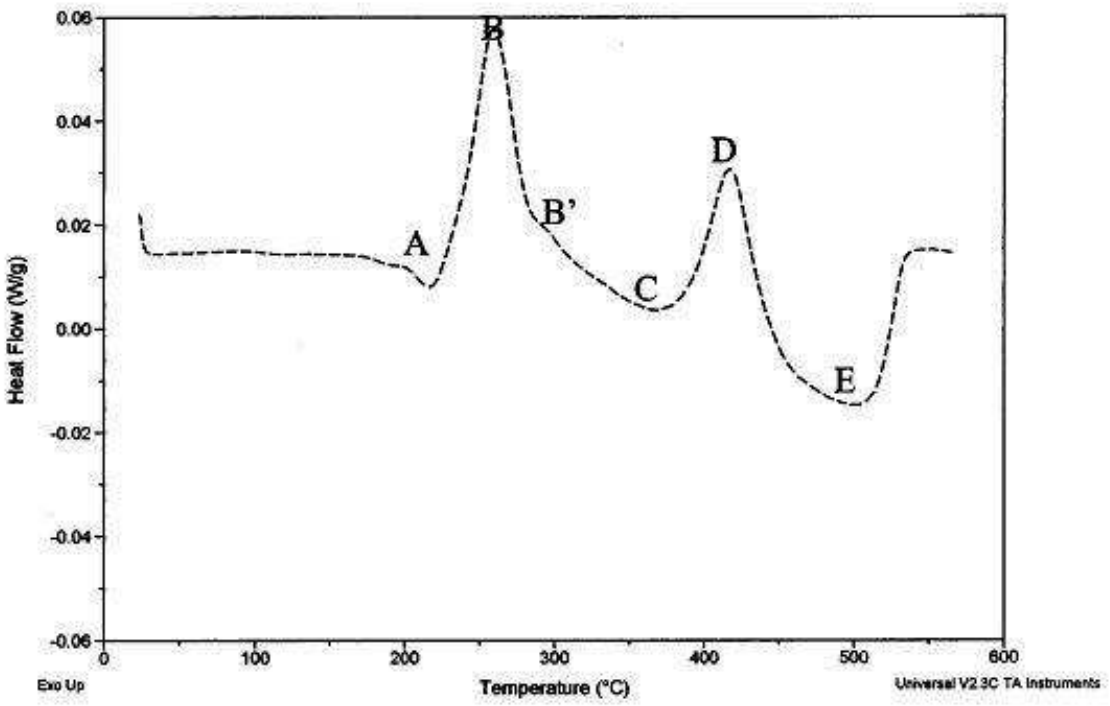

Figure 2.33: DSC curve of a wrought Al–Mg–Si alloy in the T4 condition with 1.26wt% Mg_2Si [88].

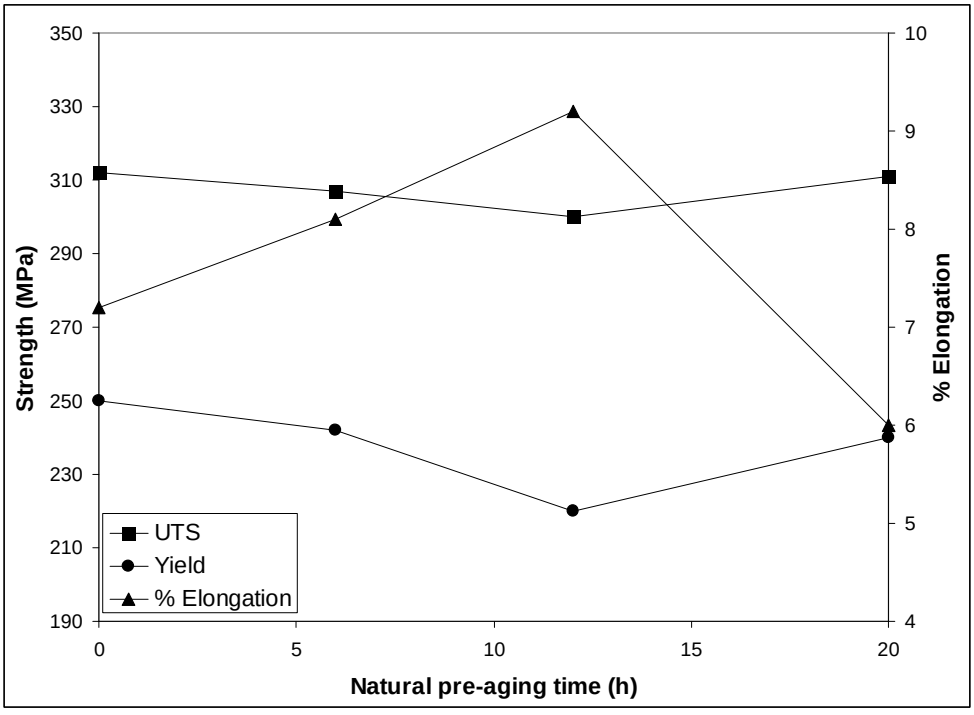

Figure 2.34: Effect of natural pre-aging time on yield strength, UTS and %elongation of A356. Heat treatment consisted of solution treatment at 540°C for 3 h, a room temperature water quench, natural pre-aging and artificial aging at 170°C for 6 h [72].

2.3.3.4. Heat treatment response of SSM-processed Al-7Si-Mg alloys in comparison with conventional liquid cast alloys

According to Dewhirst [12], after the mechanisms for SSM heat treatment were commercialised, the first heat treatments applied to it were essentially those already in use for dendritic materials. These treatment regimes are not necessarily the optimal ones as the different microstructure and solidification history of SSM components should be considered.

The American Society for Testing and Materials (ASTM) Standard B969 from 2010 named "*Standard Specification for Aluminum-Alloy Castings Produced by the Squeeze Casting, Thixocast and Rheocast Semi-Solid Casting Processes*" recommends heat treatment parameters for SSM-cast A356 and A357 as shown in Table 2.6.

Table 2.6: ASTM B969-10 recommended heat treatment parameters for semi-solid thixocast and rheocast castings.

Alloy	Final temper	Solution heat treatment		Precipitation heat treatment	
		Metal temperature ± 5°C	Time at temperature (h)	Metal temperature ± 5°C	Time at temperature (h)
A356	T5	-	-	160	6-12
	T6	540	4-10	160	3-6
A357	T5	-	-	170	6
	T6	540	10	170	6

In this standard it is recommended that the quench after solution treatment should be carried out in water at 65-100°C. Recommendations on natural pre-aging and its influence on subsequent artificial aging are not included.

Only limited work has been performed on the optimisation of the solution heat treatment of SSM processed A356/7. In the casting industry, it is often specified that a dendritic (especially permanent mould cast) A356 component should be solution

treated for 6 hours at 540^{o}C [67]. This has also been the most popular solution heat treatment used for SSM-processed A356 [81,89]. According to Dewhirst [12], the time needed for the solution treatment for semi-solid metal processed A356 should be less than for dendritic A356 due to shorter diffusion paths (due to a globular microstructure) and because the thermal history of SSM-processed components promotes enhanced solutionising before heat treatment commences. Rosso and Actis Grande [90] proposed that a solution heat treatment of 1 hour at 540^{o}C is sufficient to obtain a high level of properties in the T6 temper. A solution treatment of only 30 minutes caused the presence of brittle intermetallic phases due to an incomplete solution process. According to Dewhirst [12], the optimum solution treatment time at 540^{o}C is 4 hours. Birol [13] has recently investigated the effect of solution heat treatment on the age hardening capacity of dendritic and globular alloy F357. The DSC spectra of the dendritic and globular alloy were found to be nearly identical (Fig. 2.35). The peaks on Fig. 2.35 correspond to the following [13]:

1). Formation of clusters.

2). Dissolution of GP zones.

3). Precipitation of β″.

4). Formation of β′.

5). Precipitation of Si.

6). Formation of β.

Note that the DSC curves presented in Fig. 2.35 are for solution treated alloys, in contrast to the DSC curve in Fig. 2.33, which was for a T4 alloy. Fig. 2.35 therefore has a formation-of-clusters peak, whereas Fig. 2.33 has a relatively large dissolution-of clusters peak.

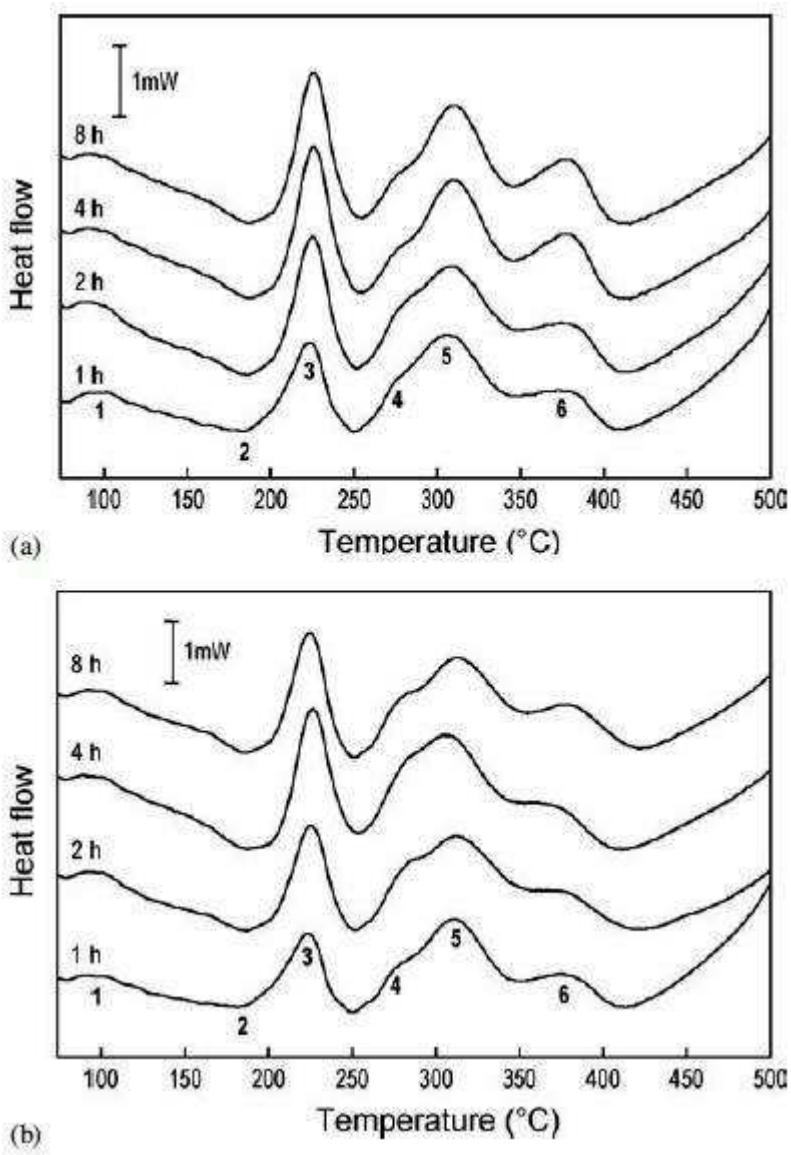

Figure 2.35: DSC scans of (a) dendritic and (b) globular F357 alloy after soaking at 540°C for different times [13].

The response to artificial aging of the dendritic and globular alloys F357 which have been subjected to solution treatment at 540°C for various times is illustrated in Fig. 2.36 [13]). The morphology of the primary α-Al, whether dendritic or globular, apparently has no effect on the artificial aging response of the alloy [13,14]. Birol [13] postulated that the favourable impact of the globular structure is offset by the relatively coarser structure in SSM-processed alloys. It is also seen from Fig. 2.36 that a solution treatment time of at least 2 h at 540°C is required to obtain maximum hardness after artificial aging in this alloy.

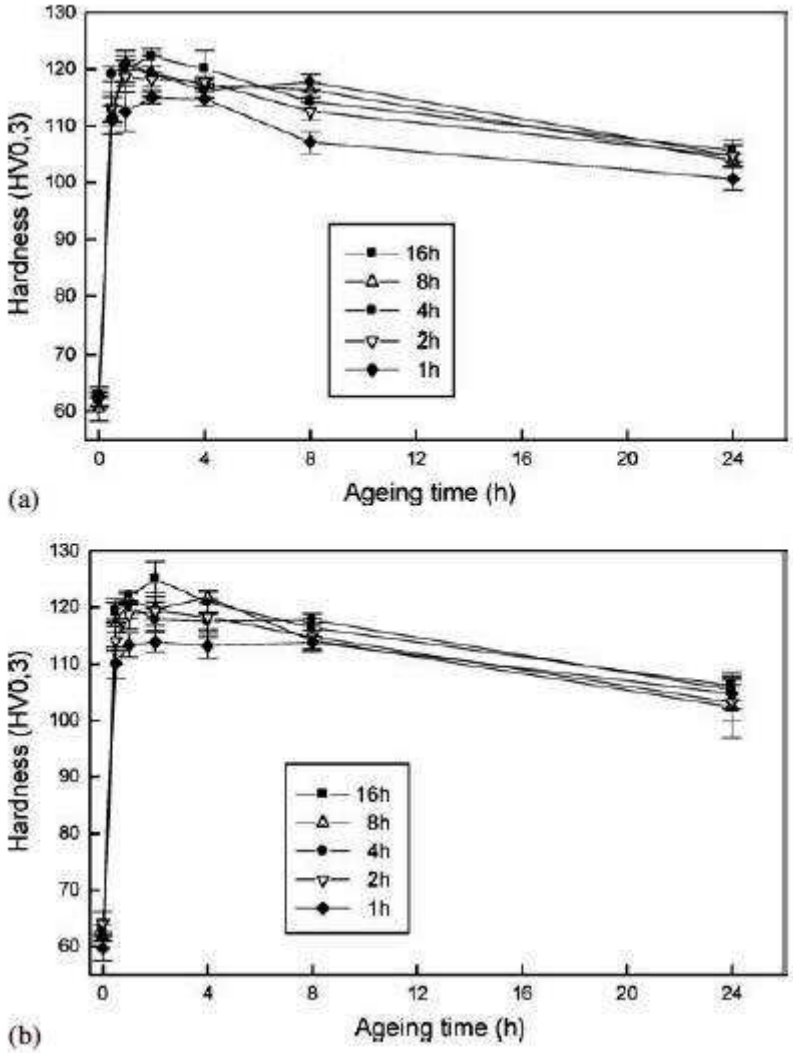

Figure 2.36: Artificial aging curves of (a) dendritic and (b) globular alloy F357 artificially aged at 190°C after solution treatment at 540°C for different times [13].

The influence of natural pre-aging on artificial aging has not received much attention when SSM processed Al-7Si-Mg alloys are heat treated to a T6 temper. According to Dewhirst [12], a natural aging time of eight hours is frequently used to ensure process uniformity. Dewhirst [12] varied the natural pre-aging time of semi-solid processed A356 between 8 and 24 hours and found that increasing the natural aging time beyond 8 hours had a slightly negative effect on the tensile properties of the material. However, it was concluded that artificial aging temperature and time were of much greater importance. Rosso and Actis Grande [90] also studied the optimisation of T6 heat treatment cycles for SSM-processed A356, but did not consider natural pre-aging time as a variable.

The artificial aging parameters of 170^{o}C for 6 hours are probably the most popular for SSM processed A356 [81,89,90]. There have been a few attempts to also shorten this treatment without compromising mechanical properties. Both Dewhirst [12] and Rosso and Actis Grande [90] determined the optimum artificial aging treatment for SSM processed A356 to be 4 h at 180^{o}C, with Birol [13,14] proposing 190^{o}C for 2 h for F357. The tensile properties for SSM-processed A356-T6 using the "traditional" heat treatment cycles, as well as the shorter cycles of 540^{o}C-1h and 180^{o}C-4h as proposed by Rosso and Actis Grande [90] are compared in Table 2.7.

Table 2.7: Brinell hardness (HB), yield strength (YS), UTS and %elongation of SSM-processed A356-T6 [90].

Heat treatment	HB	YS (MPa)	UTS (MPa)	%Elongation
Traditional	112	273	333	11
540^{o}C-1h; 180^{o}C-4h	113	279	332	10

The new, shorter cycles could lead to significant economic and environmental advantages. Temperature control (especially in the solution treatment step) and the performance and reliability of heat treating furnaces would then be of primary importance [90]. A summary of ASTM B969, the traditional and the proposed optimum heat treatment parameters for SSM-processed Al-7Si-Mg alloys is presented in Table 2.8.

Table 2.8: Summary of ASTM B969, the traditional and the proposed optimum heat treatment parameters for SSM-processed Al-7Si-Mg alloys.

	Solution heat treatment	Artificial aging
ASTM B969-10	540°C; 4-10h (A356) 540°C; 10h (A357)	160°C; 3-6h (A356) 170°C; 6h (A357)
"Traditional" [81,89]	540°C; 6h	170°C; 6h
Rosso and Actis Grande [90]	540°C; 1h (A356)	180°C; 4h (A356)
Dewhirst [12]	540°C; 4h (A356)	180°C; 4h (A356)
Birol [13,14]	540°C; 2h (F357)	190°C; 2h (F357)

Typical (or mid-range) mechanical properties for rheocast A356 and A357 in different temper conditions according to ASTM Standard B969-10 are listed in Table 2.9.

Table 2.9: Typical (or mid-range) mechanical properties for rheocast A356 and A357 in different temper conditions: ASTM B969-10.

Alloy	Temper	0.2% YS (MPa)	UTS	% Elongation in 5D
A356	F	110	240	11
	T5	180	270	6
	T6	235	310	11
A357	T6	290	345	6

3. EXPERIMENTAL METHODS

3.1. Semi-solid metal processing

3.1.1. SSM-HPDC of rectangular plates

The SSM-processing of each batch of alloy A356 or F357 commenced by melting a master melt of A356 (with composition of 0.36% Mg in Table 3.1) in a 20 kg resistance heated tilting furnace. Additions of Mg and Al-10Sr were made to the melt to obtain the desired composition and thereafter the melt was degassed with argon. A356 alloys with Mg-contents less than that of the master melt (< 0.36% Mg) were obtained by allowing evaporation of Mg from the melt followed by subsequent addition of Sr to compensate for evaporation losses. A sample was poured from the melt, cooled and the chemical composition analysed by optical emission spectroscopy (Thermo Quantris OES). Table 3.1 shows the chemical compositions for each of the alloys. It can be seen that almost the whole Mg-composition range of these alloys is covered (Table 2.1).

The thermodynamic properties (liquidus and solidus) of the alloys were then calculated with an aluminium thermodynamic database (ProCAST) from the specific OES compositions by employing the Scheil equation (or non-equilibrium lever rule) [91]. The Scheil equation was used since solidification during SSM-HPDC does not occur under equilibrium conditions due to the fast cooling rates that are achieved. These thermodynamic properties were used to determine SSM processing parameters namely pouring temperature and SSM casting temperature. A pouring temperature of approximately 40^{o}C above the liquidus and a SSM processing temperature corresponding to a solid fraction of ~30% were used from experience with this specific SSM processing system. For example, Figure 3.1 shows the solid fraction as a function of temperature for a typical A356 composition of Al-7Si-0.3Mg-0.1Fe-0.03Sr and F357 with composition of Al-7Si-0.6Mg-0.1Fe-0.03Sr. Table 3.2 summarises the calculated thermodynamic properties and derived rheocasting parameters for these compositions. It is seen that the processing parameters do not differ much for A356 and F357. This procedure was used for each of the compositions shown in Table 3.1.

Table 3.1: Chemical composition (wt%) of alloys A356 and F357 used for producing SSM-HPDC plates.

Al	Si	Mg	Fe	Cu	Mn	Ti	Sr
A356							
Balance	7.10	0.25	0.14	0.01	0.01	0.08	0.04
Balance	7.21	0.28	0.13	0.01	0.01	0.12	0.04
Balance	7.02	0.30	0.07	0.01	0.01	0.15	0.0002
Balance	7.15	0.31	0.13	0.01	0.01	0.09	0.02
Balance	7.14	0.34	0.14	0.01	0.01	0.08	0.03
Balance	7.14	0.36	0.10	0.01	0.01	0.07	0.02
Balance	7.08	0.38	0.10	0.01	0.01	0.12	0.02
Balance	7.08	0.40	0.10	0.01	0.01	0.08	0.02
F357							
Balance	6.81	0.45	0.12	0.01	0.01	0.09	0.02
Balance	6.80	0.49	0.13	0.04	0.01	0.13	0.02
Balance	7.20	0.52	0.08	0.02	0.01	0.12	0.0014
Balance	7.01	0.62	0.10	0.01	0.01	0.13	0.02
Balance	7.10	0.63	0.09	0.01	0.01	0.14	0.02
Balance*	7.20	0.67	0.25	0.01	0.01	0.16	0.04

* This alloy also contained 0.04% Ni - an order of magnitude higher than any of the other alloys. This was due to inadvertent contamination of the melt with stainless steel during degassing.

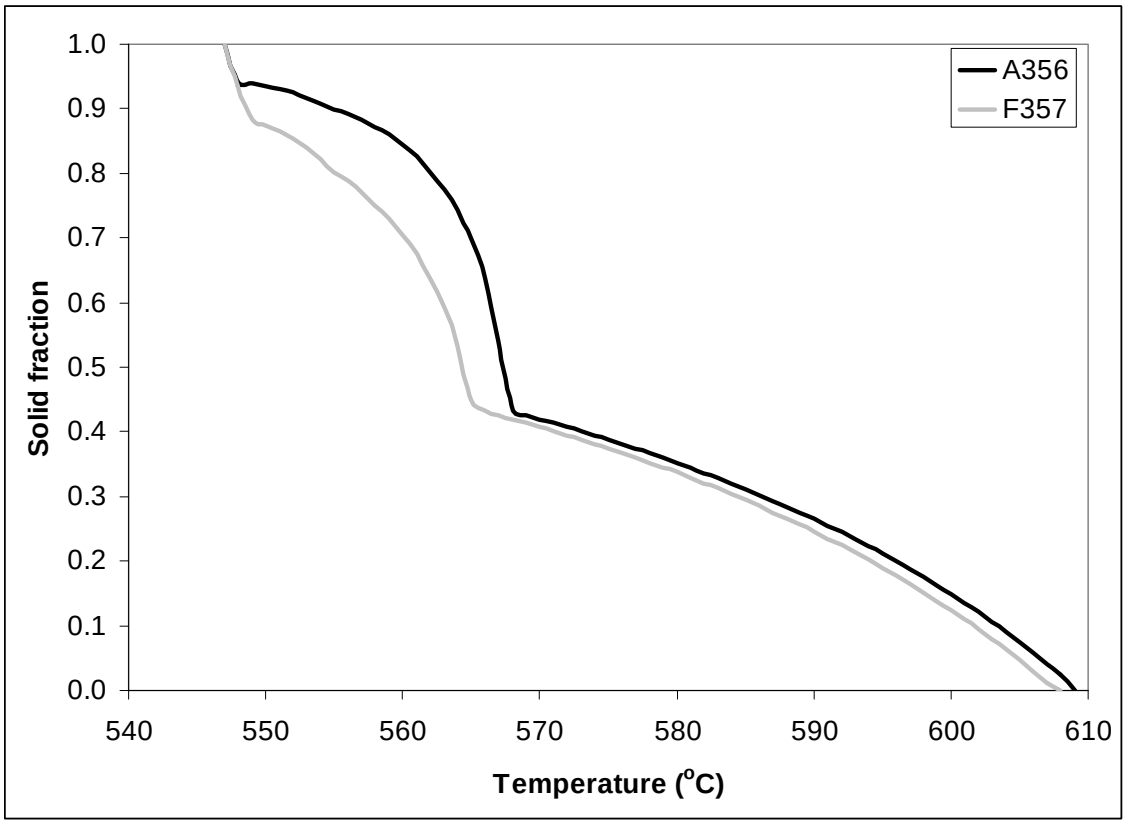

Figure 3.1: Solid fraction as a function of temperature calculated by ProCAST for typical A356 (Al-7Si-0.3Mg-0.1Fe-0.03Sr) and F357 (Al-7Si-0.6Mg-0.1Fe-0.03Sr).

Table 3.2: Calculated thermodynamic and derived rheocasting parameters of typical A356 and F357 (from Fig. 3.1) for the CSIR-RCS-HPDC cell.

Parameter	Property	A356 temperature (°C)	F357 temperature (°C)
Thermodynamic	Liquidus	609	608
	Solidus	548	548
Rheocasting	Pouring	645	645
	SSM	586	584

The sequence for casting was then as follows: liquid metal was poured from the tilting furnace into the stainless steel processing cup (about 400 g), which was then manually transferred to a single coil version of the CSIR-RCS (induction stirring with simultaneous forced air cooling [31]), where processing started once the cup entered the coil (Fig. 3.2).

Figure 3.2: Single coil version of the CSIR rheocasting system.

The semi-solid temperature of the alloy in the cup was measured by a thermocouple. Processing stopped after the thermocouple signal reached the preset SSM temperature calculated as shown in Table 3.2. At this point, the cup was ejected from the coil and manually transferred to the HPDC machine (initially with an Edgewick machine with a 50 ton clamping force, later replaced with an LK machine with a 130 ton clamping force – Fig. 3.3). The injection shot was manually triggered when the SSM billet was in the shot sleeve. The piston followed the set computer controlled injection velocity profile. Plates having dimensions of 4×80×100mm^3 for the Edgewick machine and 6x55x100mm^3 for the LK machine were cast. The dies used to cast the plates are shown in Fig. 3.4 (with the 4×80×100mm^3 plate cavity insert) and Fig. 3.5 (with the 6x55x100mm^3 plate cavity insert).

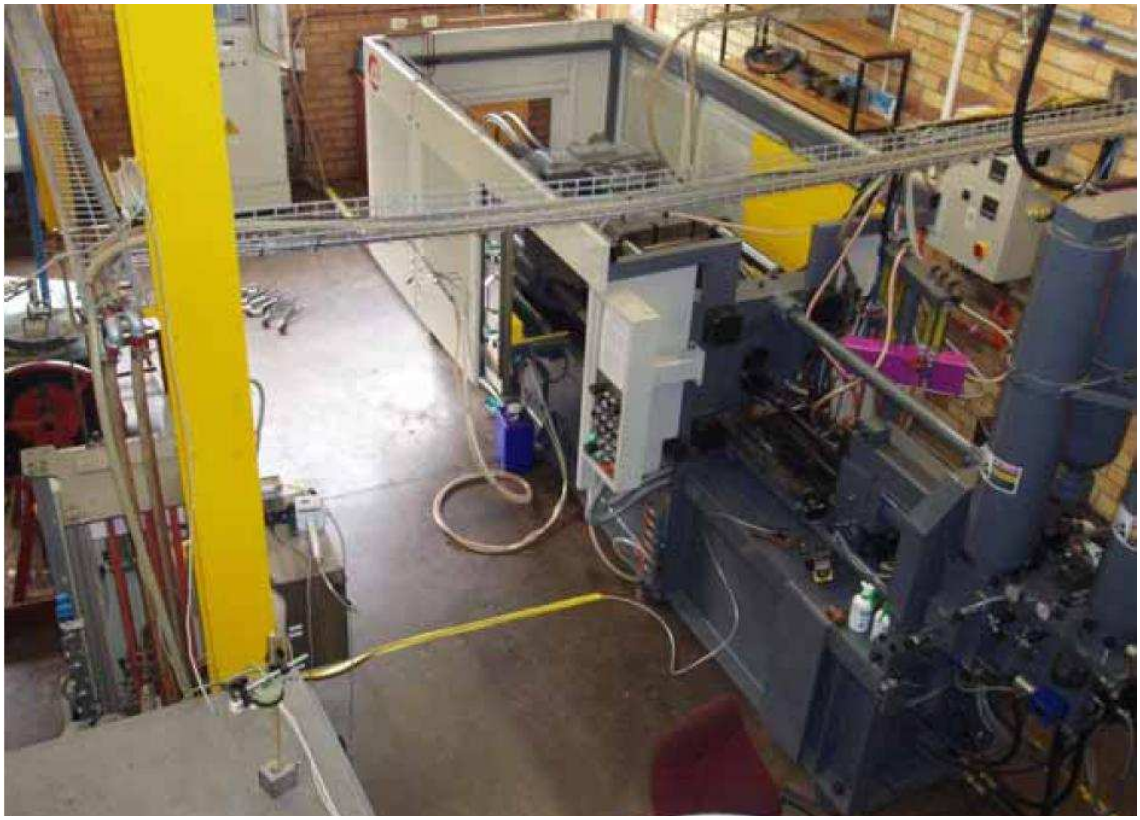

Figure 3.3: LK DCC130 shot controlled high pressure die casting machine.

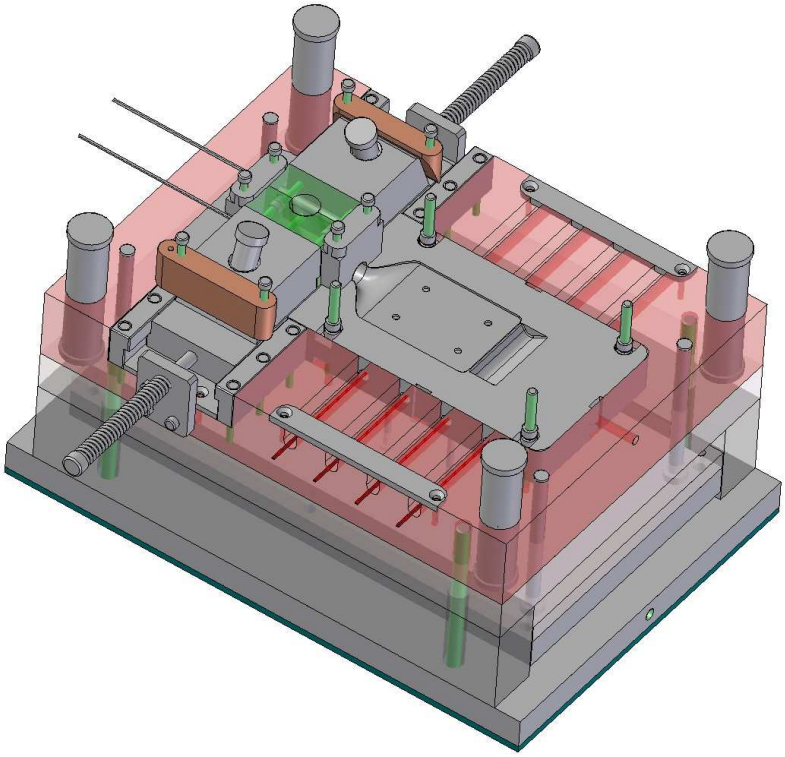

Figure 3.4: Moving half of the plate die (containing the 4×80×100mm^3 cavity insert) used with the 50 t Edgewick HPDC machine.

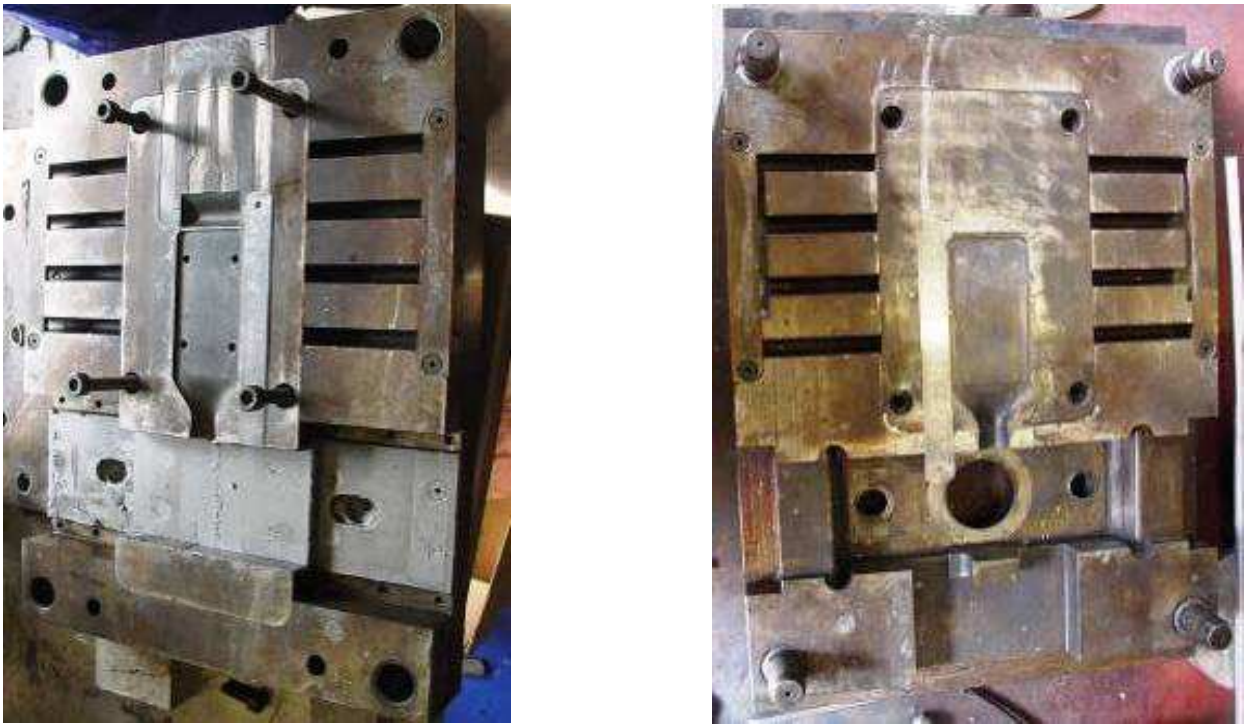

Figure 3.5: Moving half (on the left) and fixed half (on the right) of the plate die (containing the 6×55×100mm^3 cavity insert) used with the LK DCC130 HPDC machine.

The tool material used was W302 (AISI H13, DIN 1.2344) hot working die steel with a hardness of HRC = 46. It was cartridge heated to a temperature of 250^{o}C and lubricated using ISOLAT ENVIRO 911N from Fochem International (Pty) Ltd.

Both the Edgewick and LK DCC130 machines have shot control. However, the Edgewick machine is relatively old and the shot control was not very sophisticated. The shot control system was mainly used to control the injection speed and for multiple step injection profiles. The shot profile was composed of two phases, a low speed of ~ 0.3 m/s and a high speed of ~ 0.5 m/s. In order to achieve the full intensification pressure available, the stroke length was set to a distance longer than that required to achieve intensification after complete filling. A low speed and high speed of ~ 0.45 and 0.85 m/s respectively were used with the LK DCC130 machine. With this machine, intensification could be triggered using a preset back pressure or plunger position. The plunger position was used for the casting of the A356/7 plates. Typical speed and pressure profiles during SSM-HPDC of a F357 plate (6x55x100mm^3) using the LK DCC130 machine are shown in Fig. 3.6.

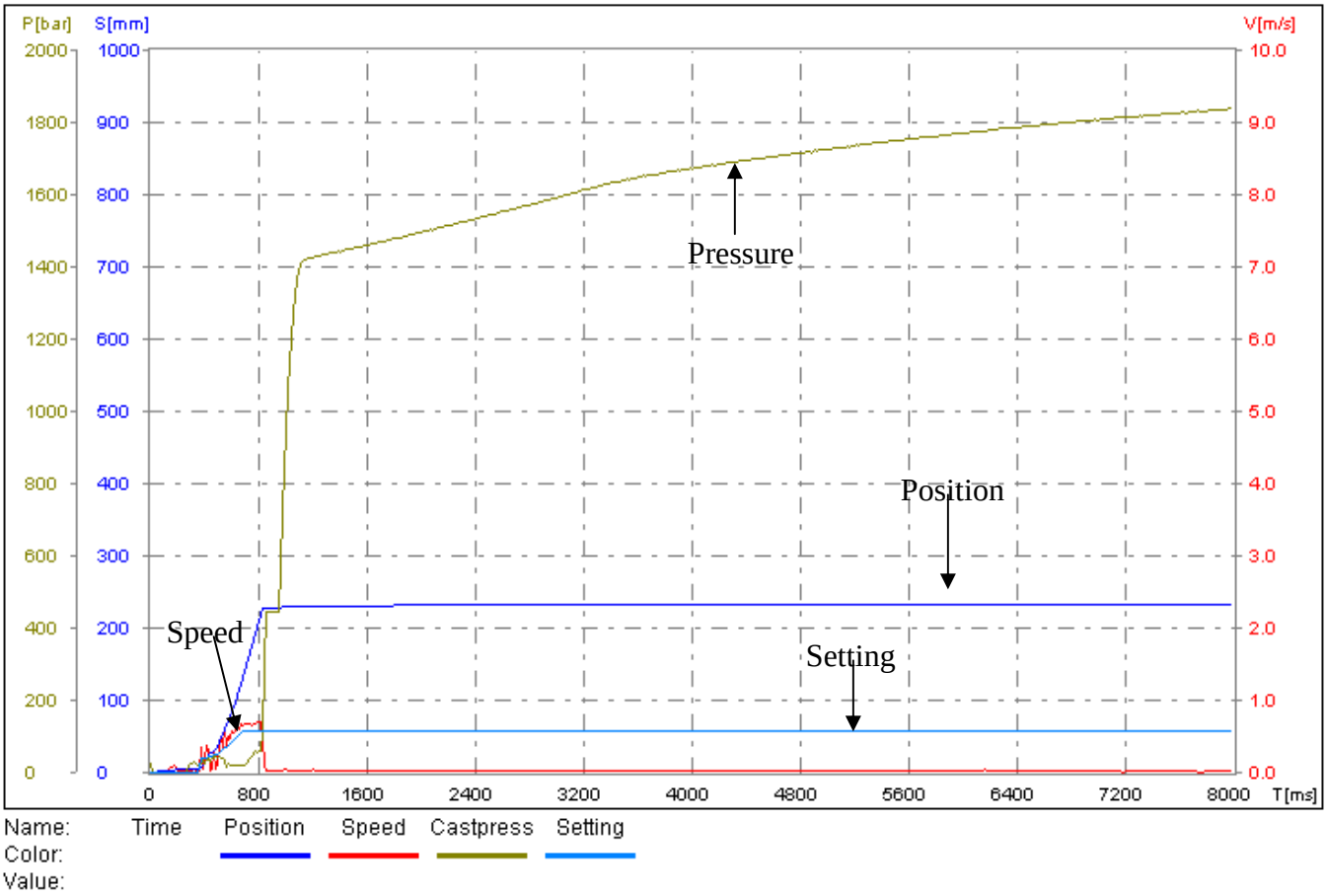

Figure 3.6: Speed and pressure profiles during SSM-HPDC of a F357 plate (6x55x100mm^3) using the LK DCC130 machine.

Figure 3.7 shows the whole casting including the biscuit and the runner of the plate cast using the LK DCC130 machine.

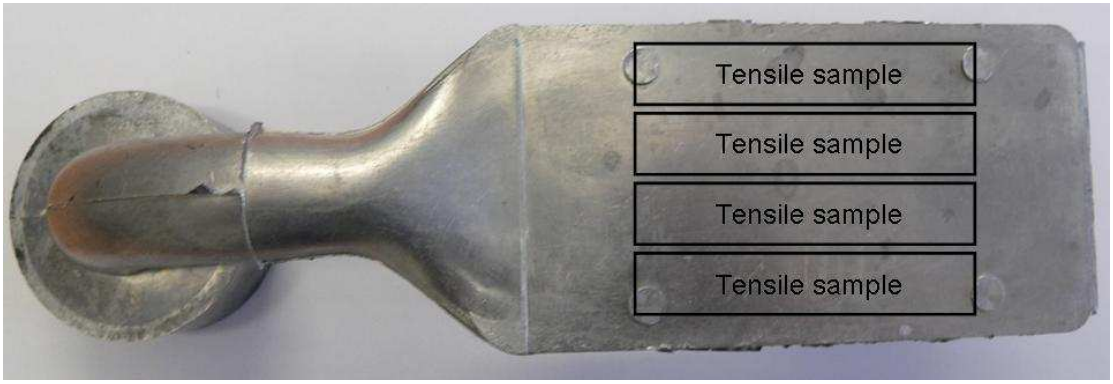

Figure 3.7: SSM-HPDC plate (6x55x100mm^3) including the runner and biscuit, also indicting where the tensile samples were machined from.

3.1.2. SSM-HPDC of automotive brake callipers

Automotive brake callipers were also produced with SSM-HPDC to determine whether the heat treatment cycles that were developed for the small rectangular plates could also be applied successfully to a larger (and more complex) casting. Figure 3.8 shows the brake calliper casting in drawing (including the runner and the biscuit) [92]. The overall dimensions for the casting in Figure 3.8 are 327mm high × 163mm wide × 95mm thick with the biscuit and gate diameters 78mm and 35mm respectively.

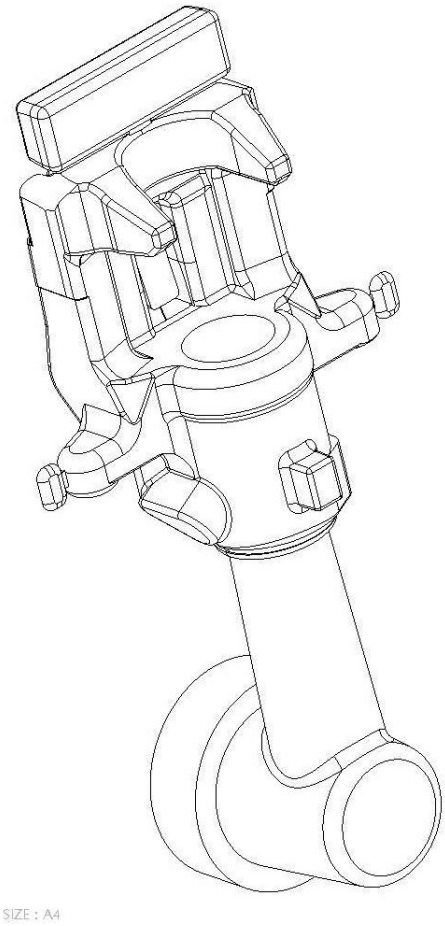

Figure 3.8: Automotive brake calliper including runner and biscuit [92].

To accomplish SSM-HPDC of the automotive brake calliper, the industrial scale version of the CSIR-RCS-HPDC cell was used (Fig. 3.9). The main components that make up the cell are: a 240 kg dosing furnace (WESTOFEN WESTOMAT W25S), an automated robotic arm (FANUC ROBOT M-16iA), a three-coil version of the CSIR-RCS (induction stirring with simultaneous forced air cooling [31]) processing unit and a 630 ton clamping force HPDC machine with full shot control (LK DCC630). The mechanical hardware operation of the cell runs automatically through computer

control software (NATIONAL INSTRUMENTS LABVIEW8.6). The 240 kg dosing furnace was filled by melting commercial aluminium alloy A356 ingots in charges of approximately 40 kg each with a custom-made induction heating ladle furnace. The metal temperature in the dosing furnace was left to equilibrate after the last charge (with additional Sr) was added. A sample was poured into a cup and chilled for chemical analysis by OES. The composition of the aluminium alloy A356 melts are given in Table 3.3 and the pouring temperature and SSM-processing temperature were determined as described before for the plates.

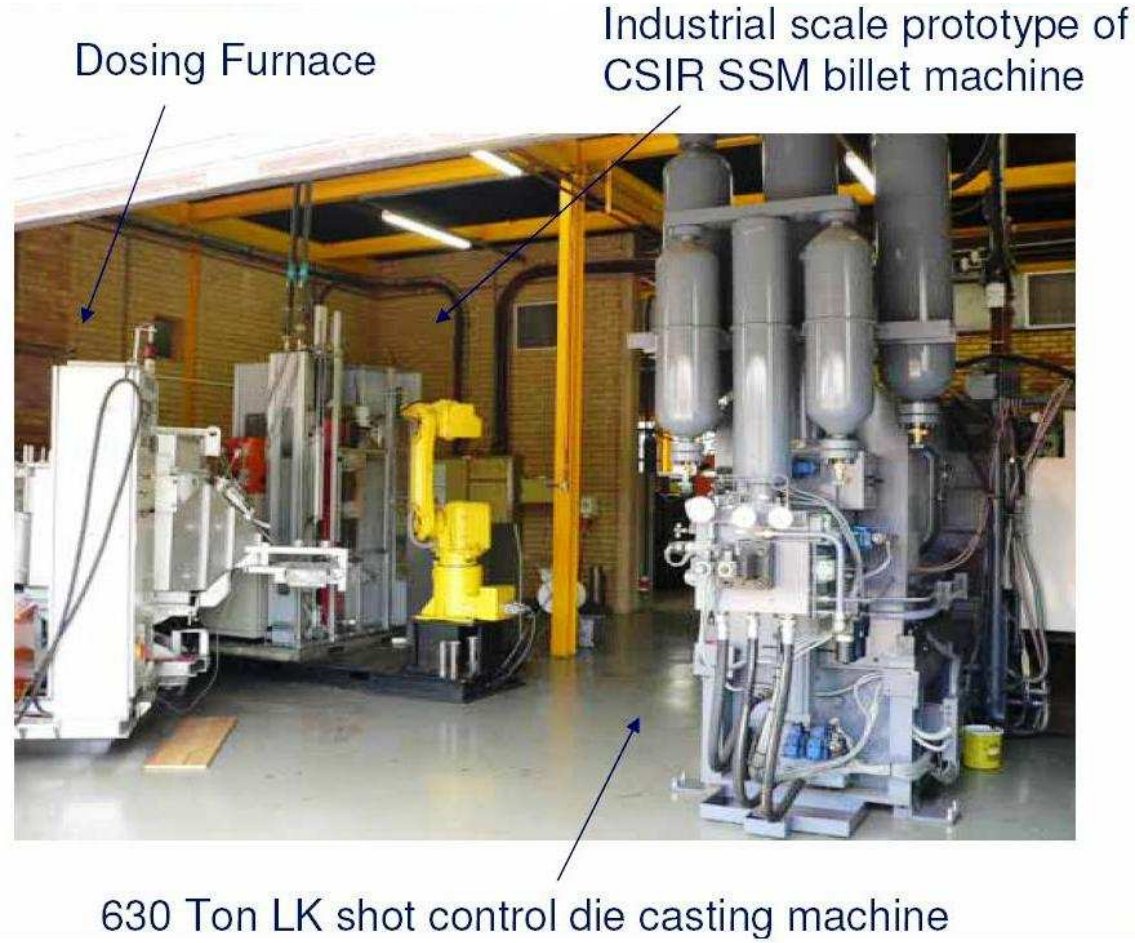

Figure 3.9: Industrial scale version of the CSIR-RCS-HPDC cell with dosing furnace and LK DCC630 HPDC.

Table 3.3: Chemical composition (wt%) of alloy A356 used for producing SSM-HPDC and gravity die cast (GDC) automotive brake callipers.

Method	Al	Si	Mg	Fe	Cu	Mn	Ti	Sr
SSM-HPDC (1)	Balance	7.3	0.31	0.14	0.01	0.01	0.16	0.03
SSM-HPDC (2)	Balance	7.0	0.35	0.14	0.01	0.01	0.14	0.02
GDC	Balance	6.6	0.36	0.27	0.03	0.01	0.06	0.02

The sequence for casting was as follows: liquid metal was poured from the dosing furnace into a stainless steel processing cup (approximately 2 kg) which was then robotically transferred to the CSIR-RCS unit and entered the coil train at the bottom. All three coils in the processing unit were inductive while forced air cooling was only used (manually activated) on the top coil to control the SSM temperature which was measured with a thermocouple in the semi-solid metal contained in the cup. When this cup at the top of the train had been processed after reaching the SSM temperature, it was robotically transferred to the shot sleeve of the HPDC machine and the injection shot was triggered automatically to fill the die. The die temperature was controlled by two oil heaters (REGLOPLAS 300 L), one for each half of the die, and was set at 170^{o}C. The piston followed a set computer-controlled injection velocity profile to achieve the best filling result [92]. To make comparisons between the heat treatment response of globular and dendritic A356, automotive brake callipers of similar composition (Table 3.3) and exact design (shape, size, mass) were cast by a local manufacturer using gravity die casting (GDC).

3.2. Investment casting of rectangular plates

To make further comparisons of the heat treatment response of globular and dendritic A356, rectangular plates (95x30x4mm^{3}) with a composition given in Table 3.4 were cast using investment casting (IC) to obtain a coarser dendritic microstructure than achieved in the brake calliper cast using GDC.

Table 3.4: Chemical composition (wt%) of alloy A356 used for producing investment cast (IC) plates.

Al	Si	Mg	Fe	Cu	Mn	Ti	Sr
Balance	6.70	0.25	0.10	0.01	0.01	0.06	0.03

Wax pattern assemblies consisted of 6 of the plates assembled with 3 plates per opposite side, spaced 40 mm apart. A vertical 25mm x 20mm rectangular runner bar was used (250mm long) as shown in Fig. 3.10. The plates were assembled at an angle of 75 degrees inclined to the runner bar. The runner bar extended below the lowest plate's tip to form a dross trap. A pouring cup was attached to the top of the runner bar. The wax used was Remet 289B green wax. The preferred bottom pouring method for aluminium was not used to simplify the assembly and to ensure symmetry in the mould. Wax assemblies were prepared by washing with Pattern Wash 6 from Remet and rinsed with de-ionised water. The wax assemblies were left for 24 h to dry and to stabilise at the dipping room temperature of 21°C. The primary slurry consisted of Ransom & Randolph Primecote, colloidal silica 30% binder and Zircon flour (Zircon silicate) -325mesh as refractory filler. The secondary slurry consisted of Ransom and Randolph Customcote colloidal silica 25% binder with fused silica (-325mesh) as the refractory filler. The face coat stucco used was Zircon sand P109 (mean 109µm) and the back-up coat stucco was Chamotte (Aluminosilicate). The shell making facility was temperature controlled to 21°C±1°C and the humidity was monitored – the relative humidity was measured as ±60%. The dipping procedure is given in Table 3.5.

Figure 3.10: Wax pattern assembly used for investment casting (IC) of alloy A356.

De-waxing (wax removal) was performed using a standard LBBC steam boilerclave with 200°C steam at 8 bar pressure for 15 min. The moulds were pre-fired in a gas fired furnace with a 5% oxidising atmosphere to a temperature of 800°C, kept for 2 h, and furnace cooled. The mould was inspected and vacuumed to ensure that the mould was clean and preheated to the required casting temperature and soaked for 1 h in an electric kiln furnace. The metal and mould temperature during casting was 720^{o}C to ensure a relatively coarse microstructure. Aluminium alloy A356 was melted in a SiC crucible in an electric furnace. Melting was timed to reach 720°C as the mould reached the 1 h soaking time. This was to reduce metal time at temperature to reduce hydrogen pick-up as no de-gassing was done due to the small volume of the melt. The mould and metal was removed from the furnace at the same time. The mould was

suspended in still air on a mould stand and the metal surface was skimmed to remove dross and slowly poured into the mould. The mould was left to cool to room temperature and mould removal was done by hand.

Table 3.5: The dipping procedure for investment casting of alloy A356.

Coate No:	Slurry	Stucco	Drying Time	Drying Method
Primary 1	Zircon Primary	Zircon Sand	8 hours	Air dry
Primary 2	Zircon Primary	Zircon Sand	8 hours	Air dry
Secondary 1	Customcote	Chamotte 0.25-0.7mm	45 Min	Fan
Secondary 2	Customcote	Chamotte 0.25-0.7mm	45 Min	Fan
Back-up 1	Customcote	Chamotte 0.7-1.2mm	45 Min	Fan
Back-up 2	Customcote	Chamotte 0.7-1.2mm	45 Min	Fan
Back-up 3	Customcote	Chamotte 0.7-1.2mm	45 Min	Fan
Back-up 4	Customcote	Chamotte 0.7-1.2mm	45 Min	Fan
Seal coate	Customcote	----------	24 Hours	Air

3.3. SSM-HPDC of Al-Mg-Si wrought alloys 6082 and 6004

To make direct comparisons of SSM-HPDC Al-7Si-Mg casting alloys with SSM-HPDC Al-Mg-Si wrought alloys, SSM slurries of alloys 6082 and 6004 (chemical compositions of the melts are given in Table 3.6, as well as the upper and lower limit specifications for the different elements [33]) were prepared using the CSIR-RCS single coil version. Rectangular plates ($6\times55\times100mm^3$) were cast in steel moulds with an LK DCC130 HPDC machine (Fig. 3.3). Special emphasis was placed on the effects of prior natural aging on subsequent artificial aging and alloy 6082 was selected as a

reference alloy in which natural aging has a negative influence on artificial aging, whereas a second reference alloy 6004 is expected to show the opposite effect (Fig. 2.32). For microscopy, the 6082 and 6004 were etched using Barker's anodizing method.

Table 3.6: Chemical composition limits for wrought Al-Mg-Si alloys 6082 and 6004 [33], as well as the compositions of the alloys used in this study.

Alloy	Si	Mg	Fe	Mn	Cu	Ti
6082	0.82	0.84	0.22	0.58	0.03	0.02
Spec low	0.70	0.60	-	0.40	-	-
Spec high	1.30	1.20	0.50	1.00	0.10	0.05
6004	0.47	0.45	0.16	0.22	0.02	0.01
Spec low	0.3	0.40	0.10	0.20	-	-
Spec high	0.6	0.70	0.30	0.60	0.10	0.05

3.4. Thermo-Calc

Thermo-Calc (a commercially available software package used to perform thermodynamic and phase diagram calculations for multi-component systems of practical importance) was used to investigate the possible effects of variable compositions on the equilibrium phases in some of the alloys, using the Al-DATA ver. 2 database.

3.5. Heat treatment of castings

3.5.1. Solution treatment

All solution treatments were performed in a CARBOLITE HRF 7/22 air circulating furnace with a fan to ensure a uniform temperature distribution. Solution treatment temperature was not considered as a variable in this study since a temperature of 540^{o}C gives the best compromise between shortening heat treatment time as well as minimising the risk of blistering and distortion [72,90]. However, solution treatment times were varied between 0.5 to 24 h.

3.5.2. Quench after solution treatment

All samples were quenched in room temperature water after the solution heat treatment, except for samples from the batches with 0.36 and 0.40% Mg (Table 3.1), where quenching was also performed in 70^{o}C water.

3.5.3. Natural aging and the T4 temper

Natural aging curves were determined by measuring Vickers hardness (VHN) using a FUTURE-TECH FV-700 Vickers hardness tester by employing a 10 kg load from the average of at least four readings per sample. The average hardness values were reproducible within ± 3 VHN for all samples tested.

3.5.4. Artificial aging and the T5 and T6 tempers

All artificial aging heat treatments were performed in the same furnace as above. The T5 temper condition was investigated using the batch containing 0.63% Mg in Table 3.1. The variables that were used to test the SSM-HPDC F357 in the T5 temper condition are shown in Table 3.7.

Table 3.7: Heat treatment parameters for SSM-HPDC F357-T5.

Quench after SSM-HPDC	Natural pre-aging	Artificial aging
Air (AQ)	25^{o}C-120h	180^{o}C-4h
Water (WQ)	-	180^{o}C-4h
Water (WQ)	25^{o}C-120h	180^{o}C-4h
Water (WQ)	25^{o}C-120h	160^{o}C-28h

The T6 temper condition was studied by determining artificial aging curves at temperatures ranging from 160–190^{o}C, following natural pre-aging periods ranging from 0–120 h. Vickers hardness measurements were done as above. In certain samples, the micro-Vickers hardness of the primary α-Al globules and the eutectic regions were also determined by using a FUTURE-TECH FM-700 Vickers microhardness tester by employing a 50 g load.

Samples used for the aging curves were cut from the plates and were deliberately kept relatively small at ~ 4 x 20 x 20 mm^3 to avoid variations in quench rates achieved after the solution heat treatments.

3.6. Tensile testing

The tensile properties of the alloys were determined using an INSTRON 1342/H1314 with 25 kN load cell capacity and an INSTRON Model 2620-602 extensometer with gauge length of 12.5mm. To determine the 0.2% proof stress, a stress rate of 10MPa/s was used and for the ultimate tensile stress (UTS) determination a displacement rate of 10mm/min. These parameters were selected based on the American Society for Testing and Materials (ASTM) standard E8M-04. The extensometer was removed during tensile testing after reaching the 0.2% plastic strain value (typically after 1-2% strain) to prevent damage to the extensometer in the case of premature fracture. The % elongation after fracture was calculated in accordance with ASTM standard E8M-04, where gauge marks were drawn with ink on the tensile specimens. After fracture, the ends of the fractured specimen were fitted together carefully and the distance between the gauge marks measured. Tensile specimens that were machined from the plates and brake callipers are shown in Figures 3.11 and 3.12 respectively.

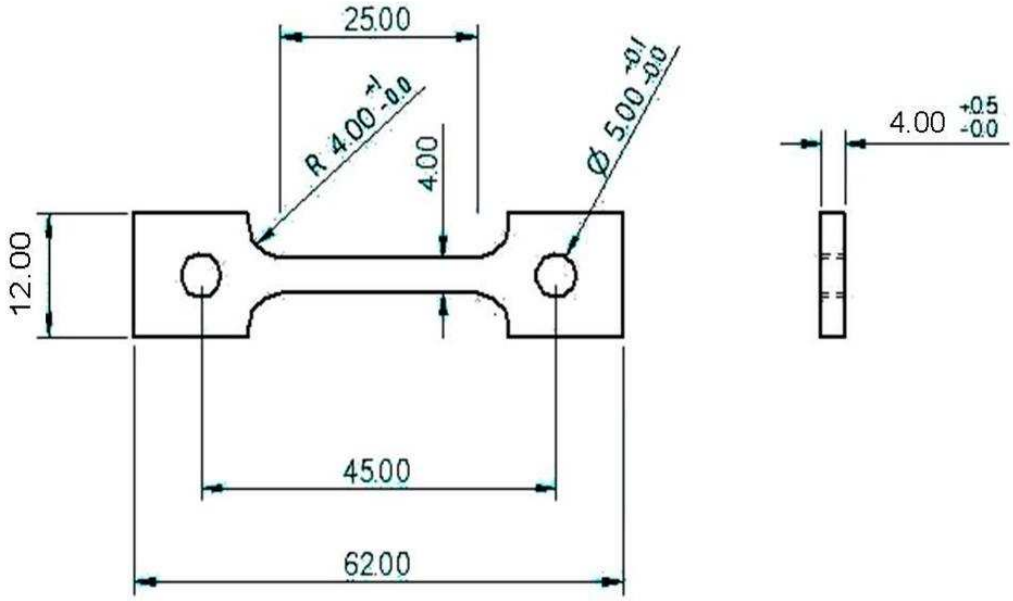

Figure 3.11: Tensile specimens with dimensions in mm machined from plates.

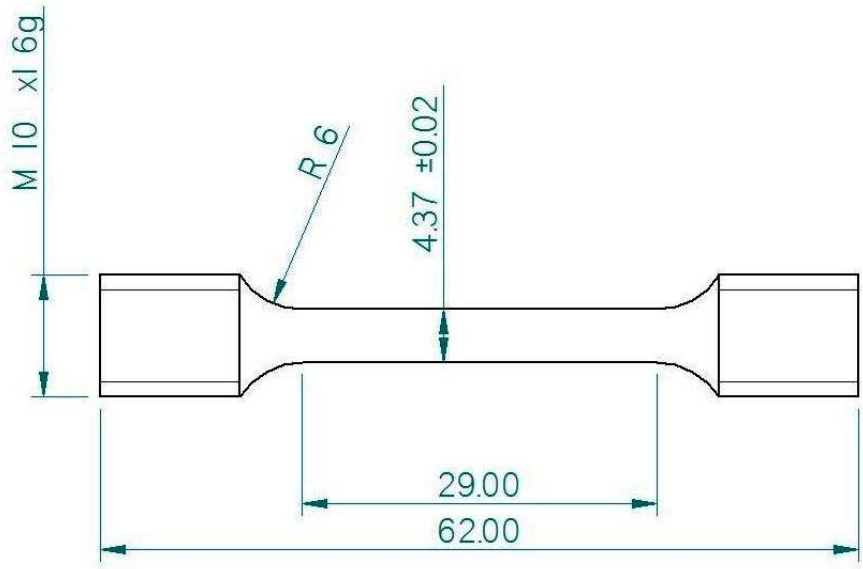

Figure 3.12: Tensile specimens with dimensions in mm machined from brake callipers.

Four tensile samples were machined from each 6x55x100mm^3 plate (Fig. 3.7) and five from each 4×80×100mm^3 plate. The positions in the brake callipers where the tensile samples (Fig. 3.12) were machined from are shown in Fig. 3.13.

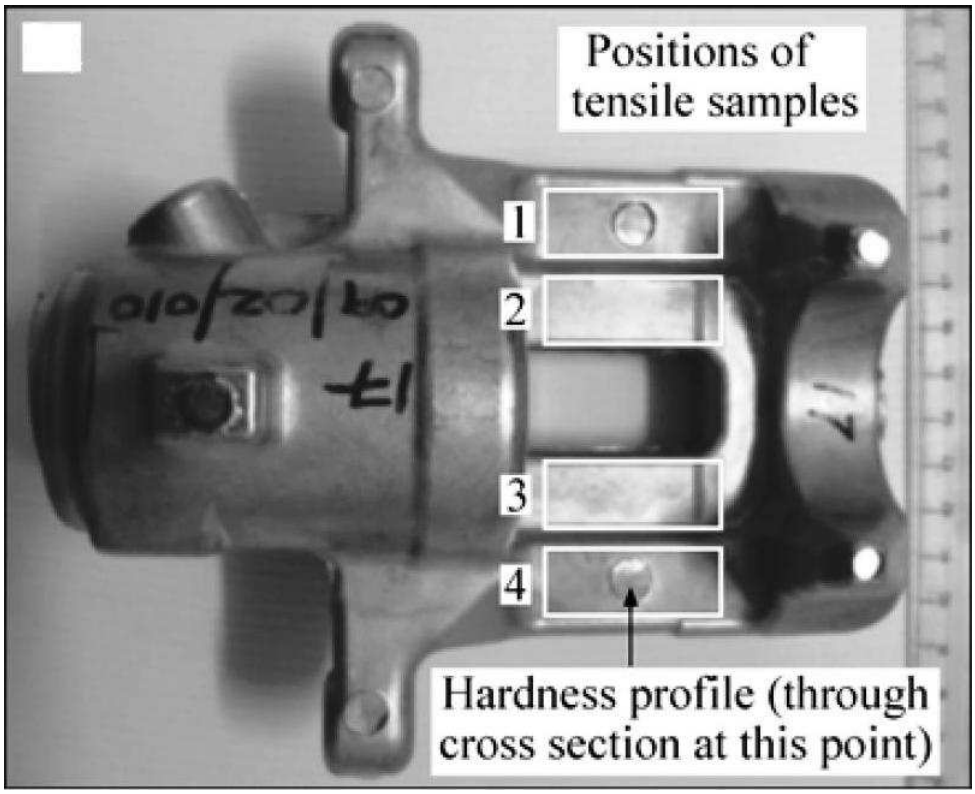

Figure 3.13: Positions where 4 tensile specimens/brake calliper were machined from.

3.6.1. The Quality Index (QI)

The "Quality Index" (QI) was used in this work to allow comparison of different compositions and heat treatments. The quality index relates the ductility (% elongation or %A) and strength (ultimate tensile strength or UTS) into a single term. It was originally developed by Drouzy and co-workers [93]. The quality index (specifically for alloys A356/7) is given by equation 3.1:

$$\mathbf{QI\ (MPa) = UTS\ (MPa) + 150log(\%\ elongation)} \qquad \mathbf{(3.1)}$$

The rationale behind this equation lies in the well known phenomenon that for most mechanisms of strengthening in alloys (except for grain refinement) one has to sacrifice some ductility or toughness and a high QI, therefore, aims to find a combination of high strength and high ductility or toughness in the alloy.

3.7. Impact testing

The impact strengths of samples from batches with 0.25, 0.31 and 0.45% Mg respectively (Table 3.1) were determined using a ZWICK impact tester with a 40 kpcm hammer. Non-standard sized Charpy specimens (55x10x3mm^3 with a 45^o V-notch of 2mm depth) were machined from the plates. Subsequently, the impact properties of samples from the batch with 0.38% Mg (Table 3.1) were determined by an INSTRON DYNATUP 9210 drop weight impact tester using the sub-standard size Charpy specimens for each temper condition (F, T4, T5, T6). The mass of the weight for the drop weight test was 5.5 kg. In order to achieve a total projectile energy of 5 J, a drop height of 9.3 cm was required. This resulted in a speed at impact of 1.35 m/s. Maximum sensitivity was obtained by using a 15 kN load cell.

The validity of using Charpy impact testing to measure the fracture properties of aluminium alloys has been questioned before [94]. Therefore, the impact results in this thesis are considered only as a comparative means to rapidly differentiate between different conditions.

3.8. Optical microscopy and scanning electron microscopy

The samples used for optical microscopy and scanning electron microscopy were mounted in an electro-conductive resin prior to grinding on SiC papers from P120 to

P2400 grit. This was followed by polishing using 9 to 1 μm diamond suspension, finishing with 50 nm colloidal silica. An optical microscope (LEICA DMI5000 M) equipped with a camera (LEICA DFC480) and imaging software (Image–Pro MC v6.0) was used to study the microstructures of the alloys. Scanning electron microscopy (SEM) was performed with a JEOL JSM-6510. Etching was performed using an aqueous solution containing 0.5% HF.

3.9. Transmission electron microscopy (TEM) and Atom probe tomography (APT)

The TEM and APT investigations were conducted at the Australian Centre for Microscopy & Microanalysis (ACMM), The University of Sydney, Australia. Thin foil samples of the alloy from the batch with 0.49% Mg (Table 3.1) were prepared from punched 3 mm discs using electrochemical jet polishing in a solution of 30% nitric acid in methanol at -30^{o}C. TEM studies were performed using a PHILIPS CM120 operated at 120 kV. Needle-like samples with fine tips with radii ~ 50 nm for APT were prepared from blanks with dimensions of 0.3x0.3x15mm^{3} using a two-stage electropolishing technique [95]. The first stage involved electropolishing in a room temperature solution of 25% perchloric acid in acetic acid at 15V, whereas the second stage was conducted in a room temperature solution of 5% perchloric acid in 2-butoxyethanol at 20V. APT analysis was done using a Local Electrode Atom Probe (LEAP®) manufactured by Imago Scientific instruments, under ultrahigh vacuum (~ 1 x 10^{-8} Pa) at a sample temperature of ~ 20 K, with a proven detector efficiency of this instrument of 57% [96]. The pulse fraction or ratio of pulse voltage to DC standing voltage employed was 20% with a pulse repetition rate of 200 kHz. In spite of concerns regarding preparation of APT samples for casting alloys, measurements with more than 8 million atoms were attained, which is significantly more than what has been reported for these alloys before [11]. Reconstruction and visualization of the APT data was done with the Imago Visualization and Analysis Software (IVAS^{TM}) in combination with advanced calibration techniques [96,97]. For quantification of clusters, the maximum separation algorithm was employed [98]. Mg, Si and Cu atoms were identified as clusters if they had a separation distance of less than 0.6 nm. A surrounding distance from these atoms of 0.5 nm was chosen to include all other elements. The smallest solute clusters taken into account were designated to contain at

least n = 10 solute atoms in order to minimise the effect of small solute clusters that exist in the alloy having a random distribution of solutes [99]. Areas within the primary α-Al grains were used for study for both TEM and APT, rather than the eutectic α-Al grains. The rate of nucleation and growth of precipitates has been shown to be different in the eutectic region of Al-Mg-Si alloys, which is a high solute density region of the material, compared to the primary α-Al grains [100].

4. RESULTS

4.1. Semi-solid metal processing

4.1.1. ProCAST simulation of SSM-HPDC of plates

ProCAST (operating in semi-solid mode with "Viscosity" defined with "Power Cut-Off") was used to provide an indication of the flow behaviour and cooling characteristics of the plates during HPDC. Figure 4.1 shows the simulated flow behaviour of the SSM-slurry during HPDC. Complete filling of the die is predicted to occur after only ~ 0.33 s (Fig. 4.1(c)).

To determine how the plates cool down in the die during the intensification step, values of $T_{initial}$ = 580^{o}C (casting temperature) and T_{die} = 250^{o}C were used for the simulation. Complete solidification is predicted to occur within ~ 5.5 s within the plate (Fig. 4.2(a)), whereas it is predicted to occur only after ~ 20 s in the relatively high-volume biscuit (Fig. 4.2(b)).

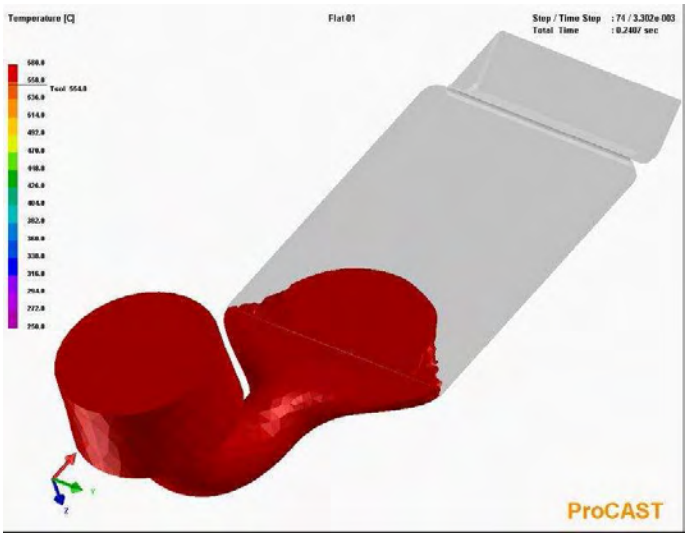

(a)

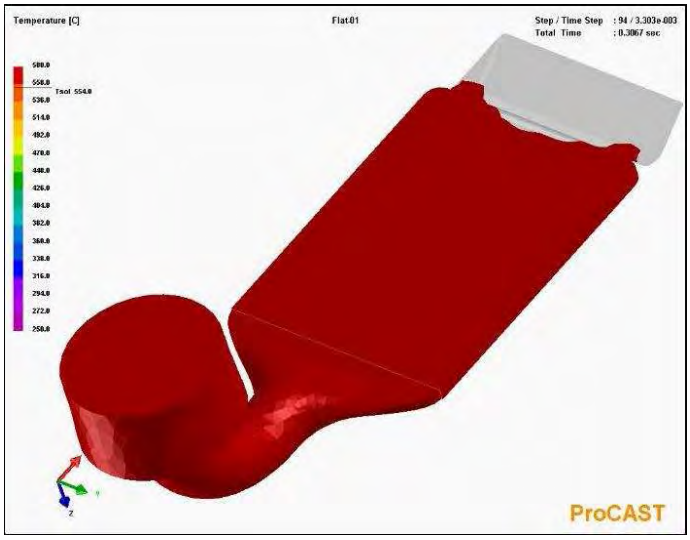

(b)

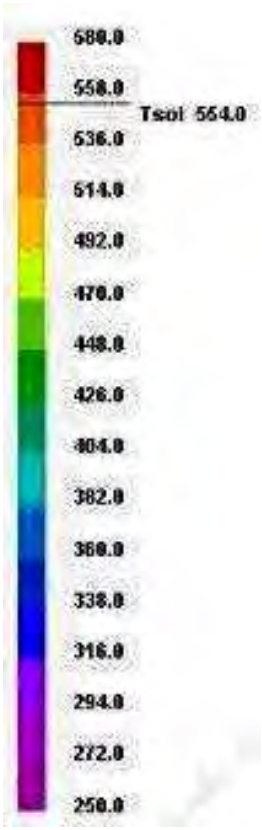

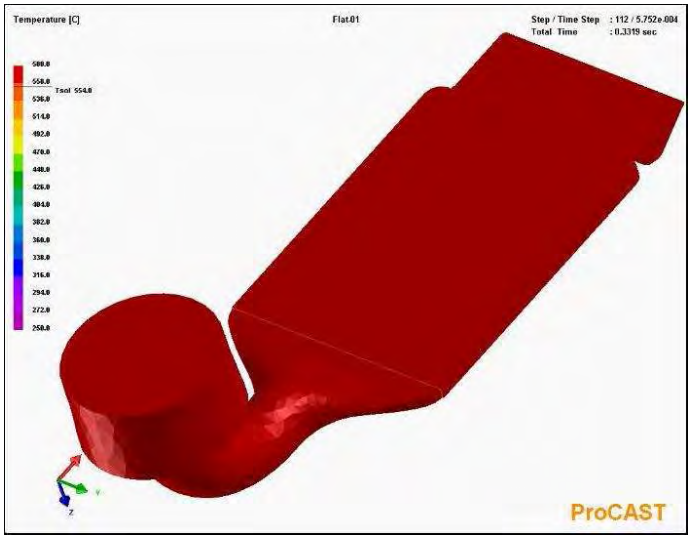

(c)

Figure 4.1: ProCAST simulation of filling of the die during SSM-HPDC after (a) 0.24 s, (b) 0.30 s and (c) 0.33 s.

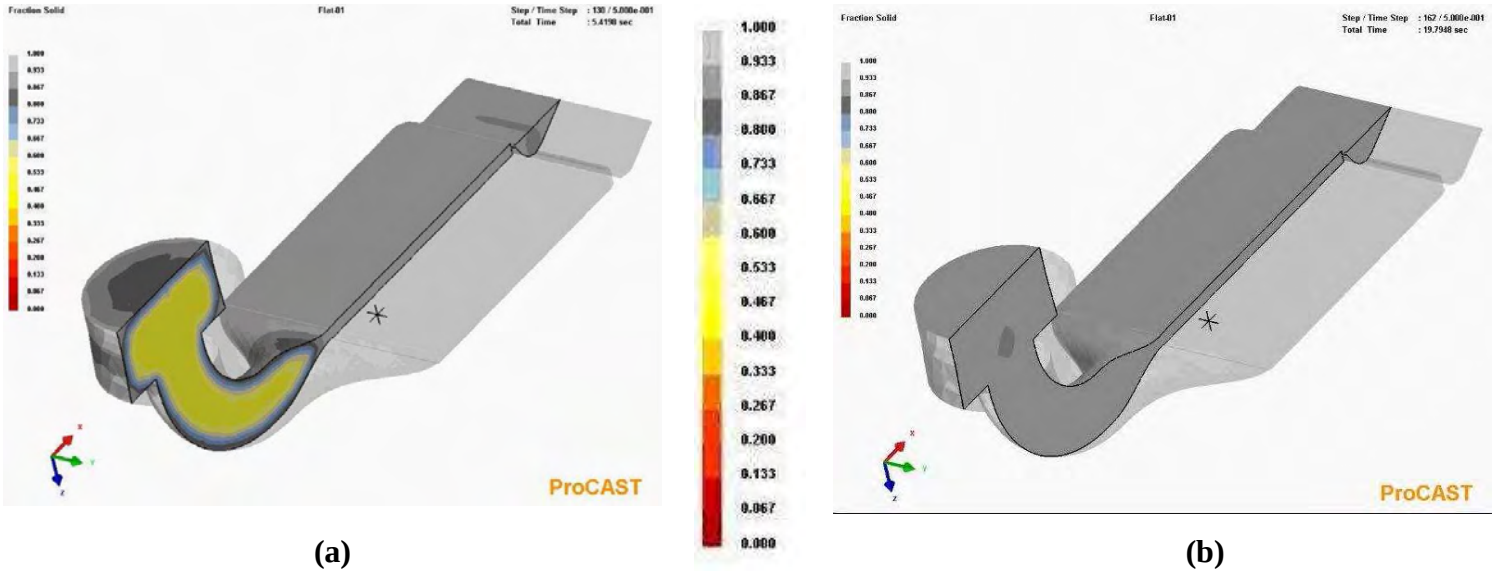

(a) **(b)**

Figure 4.2: ProCAST simulation of the solid fraction as a function of intensification time showing complete solidification in (a) the plate after 5.5 s and (b) the biscuit after 20 s.

The cooling behaviour within different parts of the plate-casting during intensification between 0-10s, 10-20s and 20-30s is compared in Fig. 4.3. The fastest cooling rates within the plates of ~ 18^{o}C/s are shown to occur during the first ten seconds of intensification (Fig. 4.4). Thereafter, the cooling rates drop significantly to ~ 9^{o}C/s between 10-20s and only ~ 2.5^{o}C/s between 20 and 30s. The large (high-volume) biscuit is shown to have a low cooling rate throughout of between 2 and 8^{o}C/s.

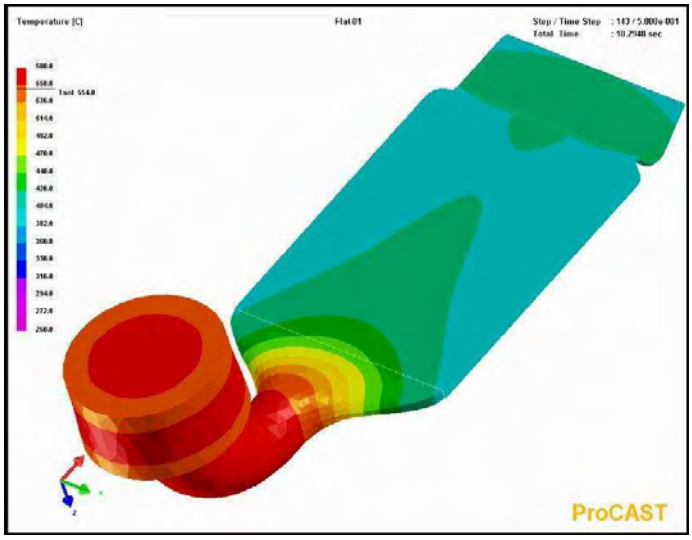

(a)

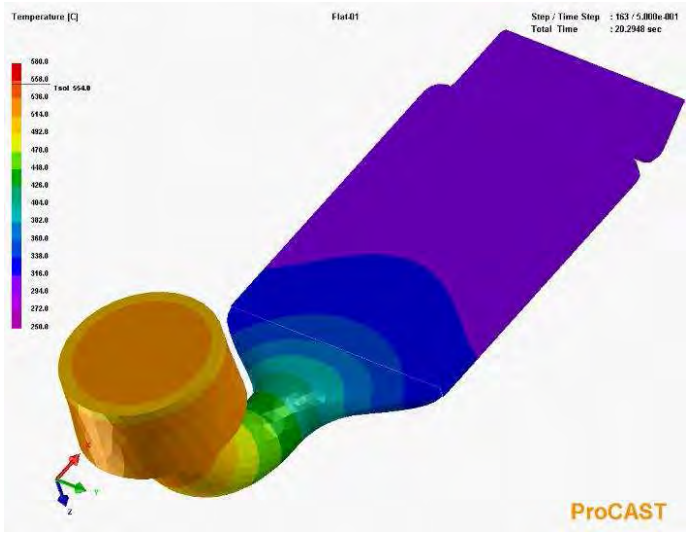

(b)

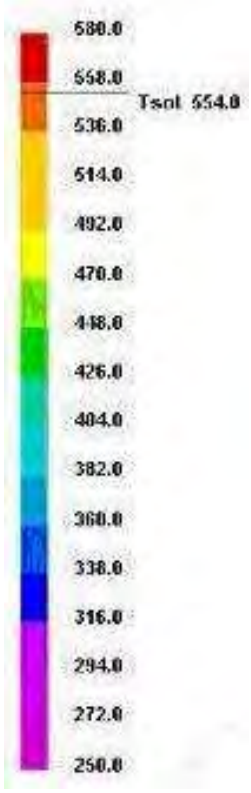

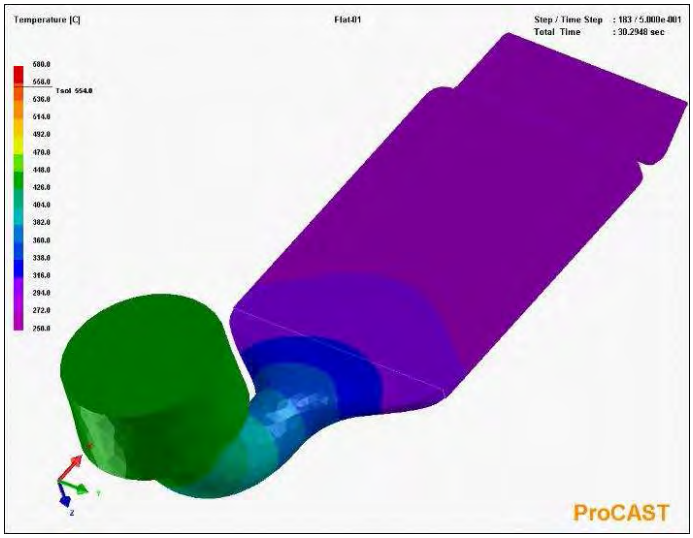

(c)

Figure 4.3: Temperature distribution within the plate during intensification in the die for (a) 10 s, (b) 20 s and (c) 30 s as predicted by ProCAST.

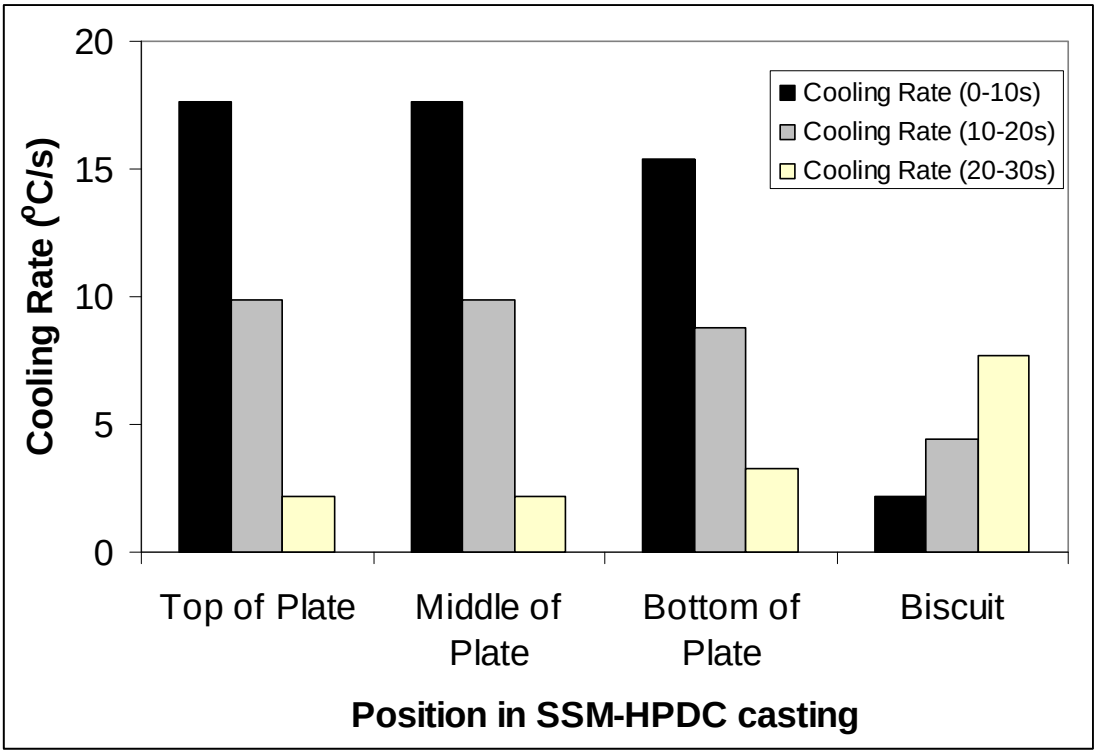

Figure 4.4: The average cooling rates achieved during intensification within different parts of the plate-casting.

4.1.2. Optical microscopy of SSM-HPDC of plates

Optical micrographs of the typical as-cast (F temper) microstructure of SSM-HPDC Al-7Si-Mg alloys are shown in Figure 4.5(a) (low magnification) and Figure 4.5(b) (high magnification). The microstructure consists of globular primary α-Al and a fine eutectic with fibrous silicon particles corresponding to a MR number (Table 2.2) of 5.

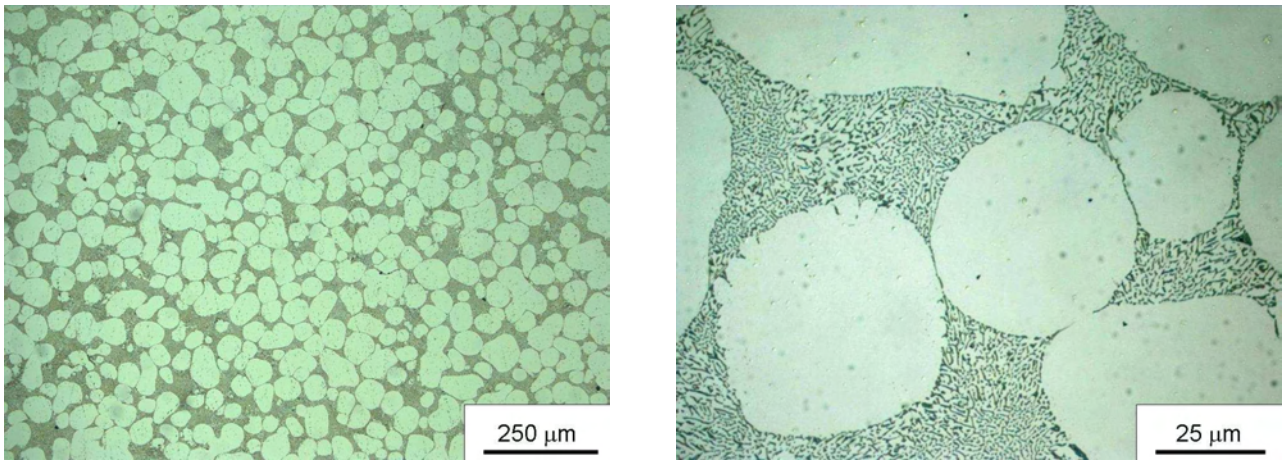

(a) **(b)**

Figure 4.5: Typical as-cast (F temper) microstructure of Al-7Si-Mg alloys after SSM-HPDC at (a) low magnification and (b) high magnification.

Statistical analysis of the microstructures of as–cast SSM-HPDC Al-7Si-Mg alloys shows a typical globule diameter of ~70 µm with roundness (Eq. 4.1) of ~ 1.4 (Table 4.1). Roundness was used as a parameter to describe the primary α-Al globules, since round particles are a prerequisite for SSM-processing.

Table 4.1: Statistical analysis of diameter and roundness of primary α-Al globules in SSM-HPDC Al-7Si-Mg alloys.

	Diameter (µm)	**Roundness**
Mean	69.5	1.43
Std. Dev	26.8	0.38
Samples	587	587

$$\textbf{Roundness} = (\text{Perimeter})^2 / (4\pi \times \text{area}) \qquad (4.1)$$

Perfectly circular areas will have a roundness of 1 and other shapes > 1.

4.2. Solution heat treatment

4.2.1. Spheroidisation of eutectic Si

The size and shape of the eutectic silicon particles in Al-7Si-Mg alloys can be "modified" (refined) either by chemical additions such as Sr or by rapid cooling during solidification (Table 2.2). Figure 4.6 shows optical micrographs of as-cast SSM-HPDC Al-7Si-Mg alloys with varying Sr contents. Statistical analysis of the eutectic Si-particles in these samples is presented in Table 4.2. The aspect ratio (the ratio between the major axis and minor axis of an ellipse equivalent to the object) is used for the eutectic Si-particles, since this parameter has been shown to influence the properties of these alloys [101].

Table 4.2: Statistical analysis of equivalent diameter and aspect ratio of eutectic Si in as-cast SSM-HPDC Al-7Si-Mg alloys with 2, 14 and 200 ppm Sr.

	Diameter (μm)			Aspect ratio		
	2 ppm	**14 ppm**	**200 ppm**	**2 ppm**	**14 ppm**	**200 ppm**
Mean	1.47	0.62	0.86	2.59	2.03	2.13
Std.Dev	1.22	0.57	0.79	2.0	0.95	1.2
Samples	772	1302	792	772	1302	792

The SSM-HPDC processed alloy containing 2 ppm Sr has coarser Si-eutectic particles with a higher aspect ratio (MR = 3) than the 14 ppm Sr and the 200 ppm Sr alloys (Table 4.2). The full modification (MR = 5) of the 14 ppm Sr alloy is due to the high cooling rates that are achieved during HPDC (Fig. 4.4). For comparison, Fig. 4.7 shows the unmodified microstructure (MR = 1) of the 14 ppm Sr alloy that had been rheoprocessed only and left to cool to room temperature in air (no HPDC).

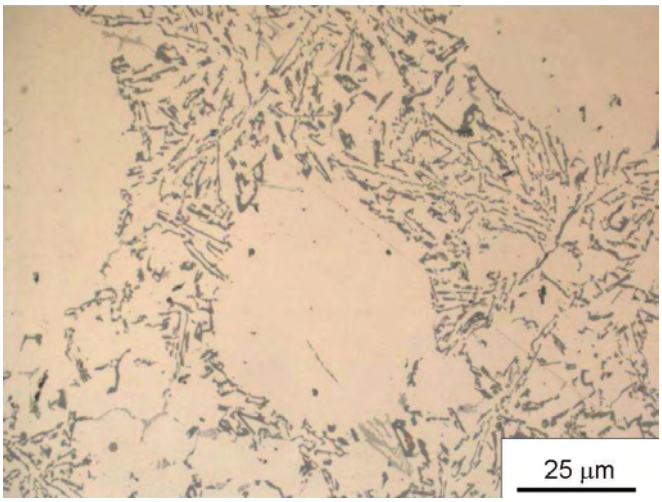

2 ppm Sr (MR = 3)

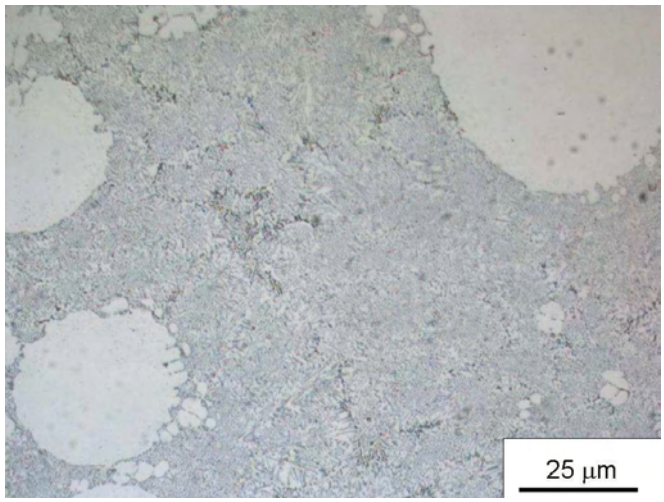

14 ppm Sr (MR = 5)

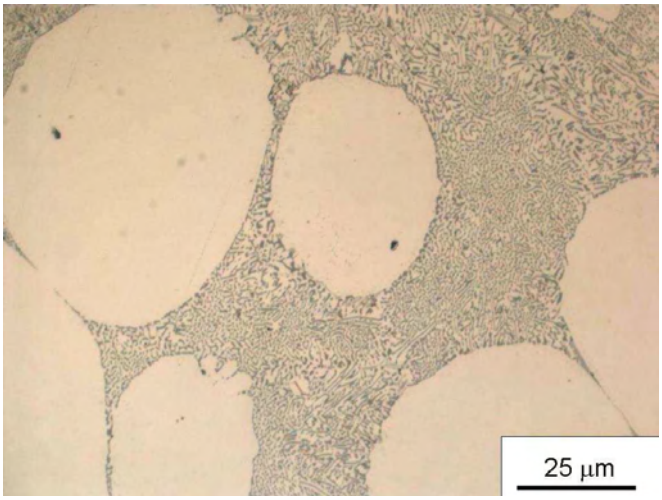

200 ppm Sr (MR = 5)

Figure 4.6: As-cast microstructures (including MR numbers from Table 2.2) of SSM-HPDC Al-7Si-Mg alloys with increasing Sr contents.

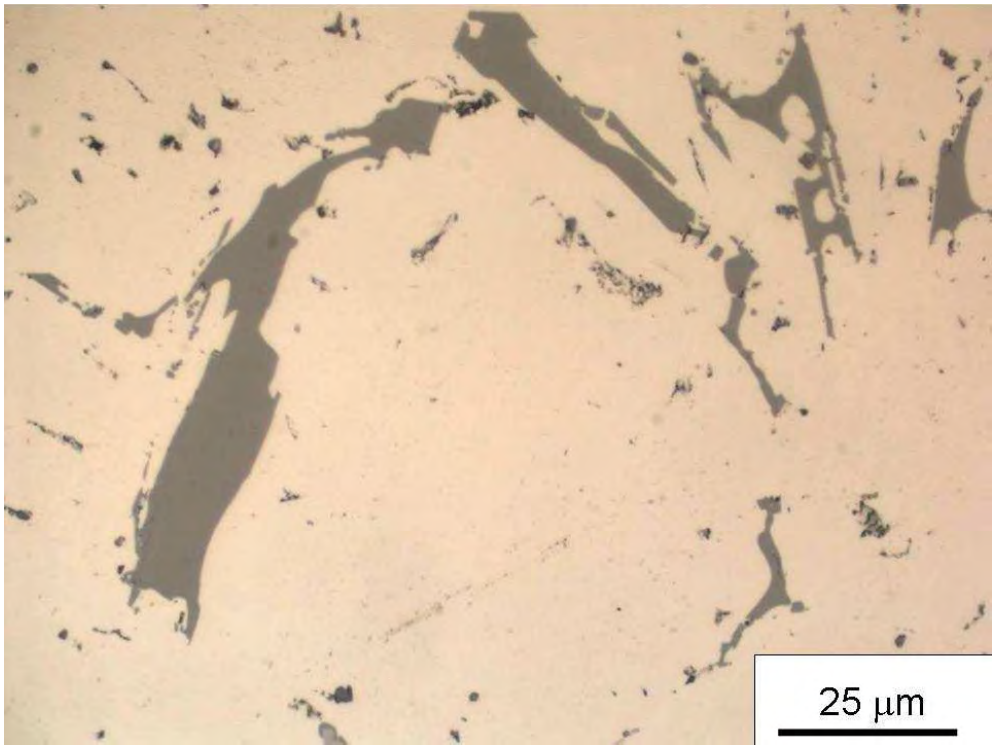

Figure 4.7: Microstructure with MR = 1 (Table 2.2) of rheoprocessed only (not HPDC) alloy with 14 ppm Sr following air cooling from the semi-solid temperature.

Modification of the eutectic component enables rapid spheroidisation of the silicon particles during solution treatment. Figure 4.8 shows microstructures of SSM-HPDC Al-7Si-Mg alloys with 2, 14 and 200 ppm Sr respectively after solution treatment at 540^{o}C for 1 h. Statistical analysis of the eutectic Si-particles in these samples is presented in Table 4.3.

Table 4.3: Statistical analysis of diameter and aspect ratio of eutectic Si in solution treated (540^{o}C-1h) SSM-HPDC Al-7Si-Mg alloys with 2, 14 and 200 ppm Sr.

	Diameter (µm)			Aspect ratio		
	2 ppm	**14 ppm**	**200 ppm**	**2 ppm**	**14 ppm**	**200 ppm**
Mean	1.36	1.13	1.24	1.73	1.58	1.54
Std.Dev	0.83	0.80	0.84	1.5	0.79	1.0
Samples	840	1057	420	840	1057	420

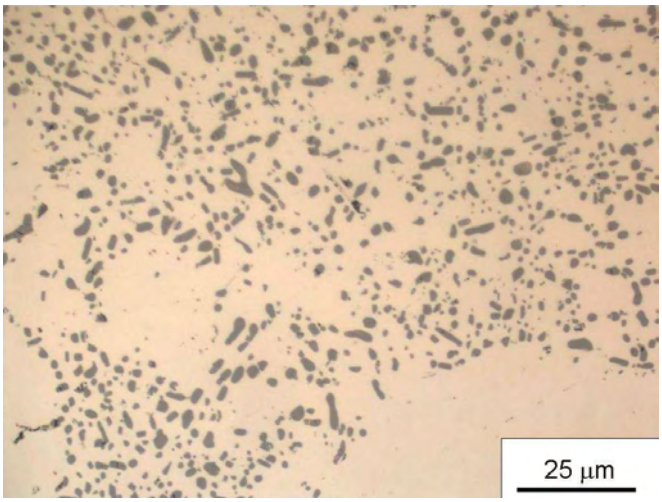

2 ppm Sr

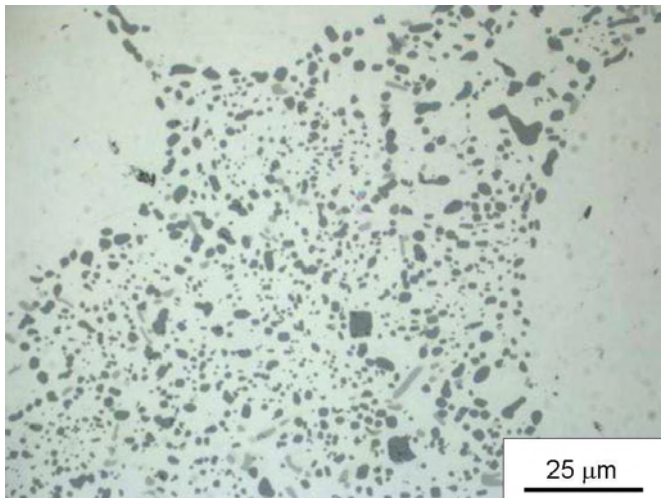

14 ppm Sr

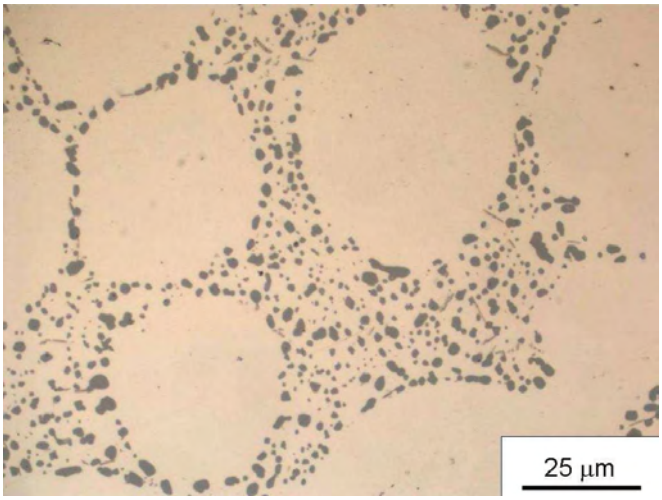

200 ppm Sr

Figure 4.8: Optical micrographs of solution treated (at 540^{o}C for 1 h) SSM-HPDC Al-7Si-Mg alloys with 2 ppm Sr, 14 ppm Sr and 200 ppm Sr.

It is seen that spheroidisation of the eutectic silicon particles occurred in all the alloys with a decrease in the aspect ratio (Table 4.3).

No spheroidisation of the eutectic silicon particles occurred at 540^{o}C in the rheoprocessed-only (no HPDC) alloy with 14 ppm Sr, even after 4 h at 540^{o}C (Fig. 4.9).

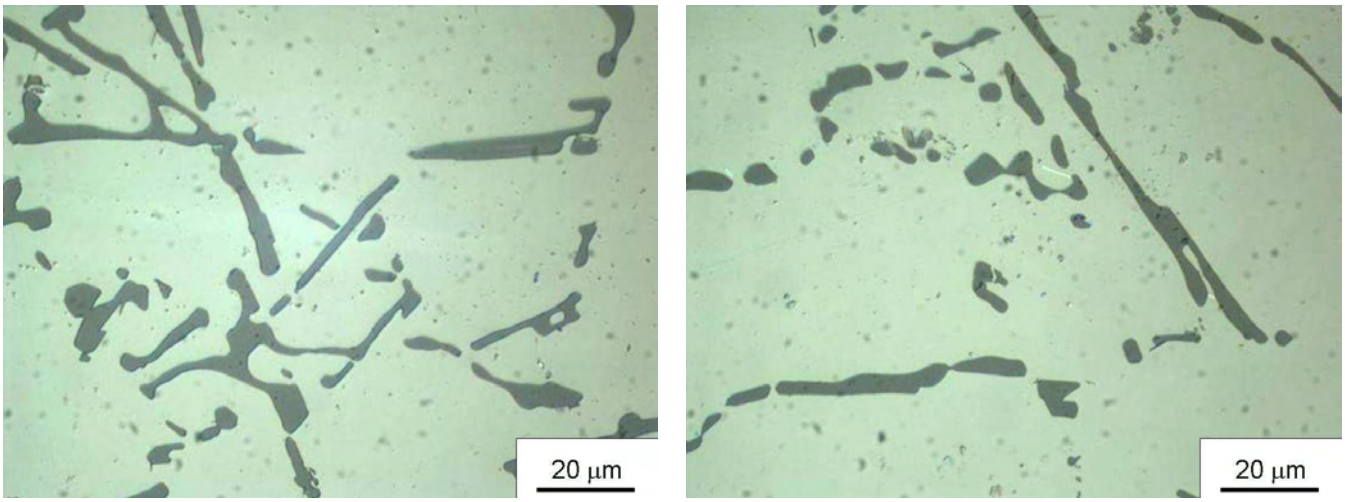

540°C-1h **540°C-4h**

Figure 4.9: Microstructures after solution treatment at 540°C for rheoprocessed-only (no HPDC) alloy with 14 ppm Sr.

The chronology of the spheroidisation of eutectic Si particles of SSM-HPDC Al-7Si-Mg alloys (with 200 ppm Sr) is shown in Fig. 4.10. Statistical analysis of the coarsening of the Si-particles in the eutectic after solution treatment at 540°C is presented in Table 4.4.

Table 4.4: Statistical analysis of the diameter (in µm) of eutectic Si particles after solution treatment at 540°C in SSM-HPDC Al-7Si-Mg alloys

	30 min	1 h	2 h	6 h	24 h
Mean	1.12	1.24	1.41	1.64	2.05
Std. Dev	0.74	0.84	0.89	1.21	1.50
Samples	582	420	278	427	280

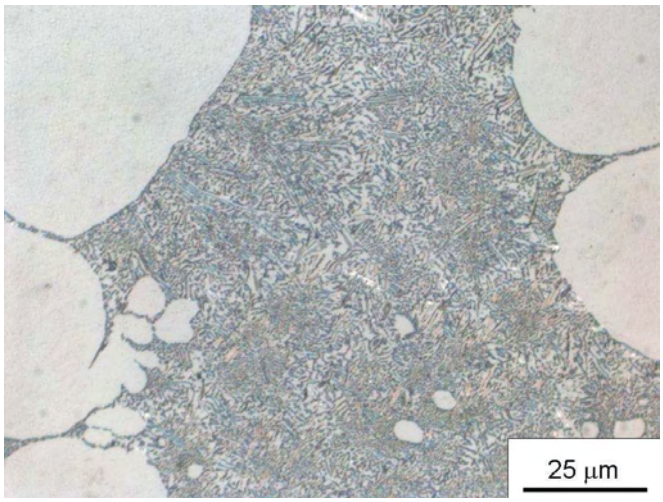

As-cast (MR = 5)

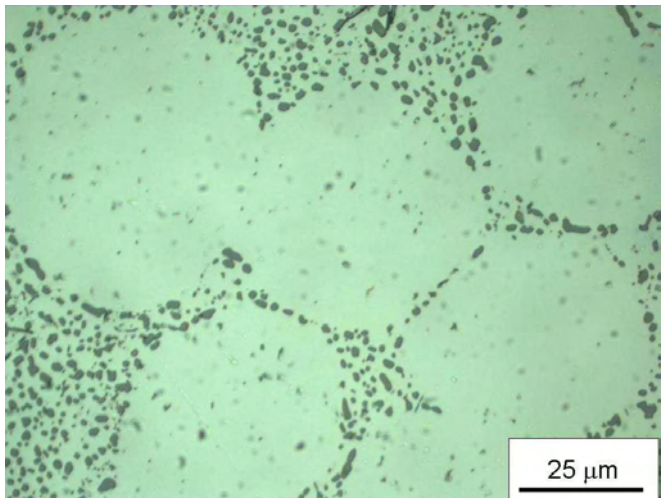

30 min – 540°C

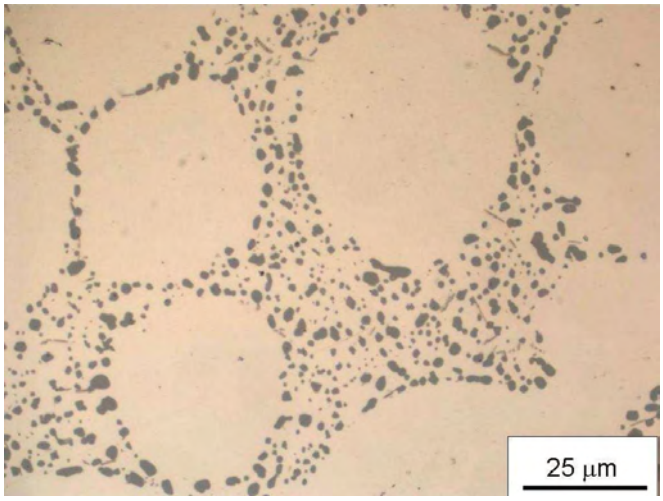

1 h – 540°C

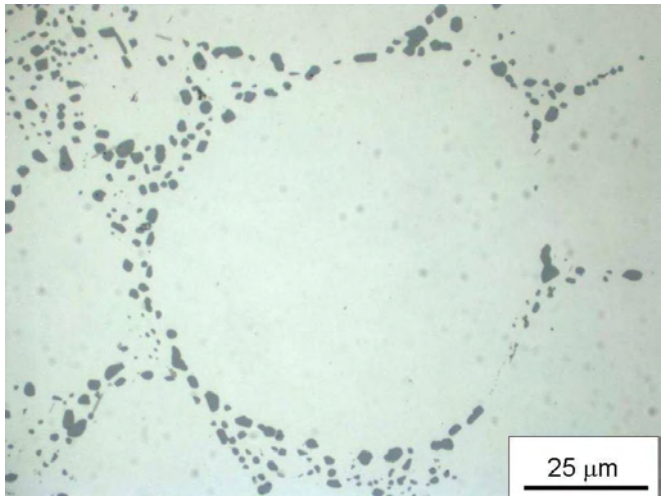

2 h – 540°C

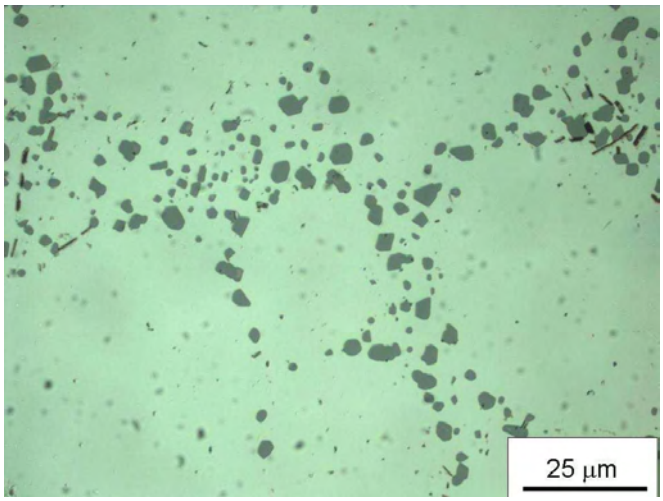

6 h – 540°C

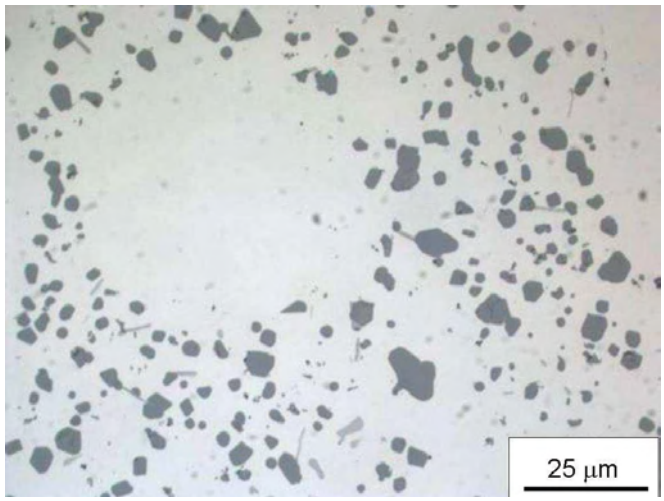

24 h – 540°C

Figure 4.10: Chronology of spheroidisation of the eutectic silicon particles after solution treatment at 540°C of SSM-HPDC Al-7Si-Mg alloys containing ~ 200 ppm Sr.

The cube of the change in mean diameter of the Si eutectic particles (D^3-D_o^3, where D_o = 0.86 μm in Table 4.2) is in reasonable direct proportion to solution treatment time (Fig. 4.11). Therefore, the growth process of the eutectic silicon particles during solution treatment is described by the Lifshitz-Slyozov-Wagner (LSW) theory of Ostwald ripening [6,69,102].

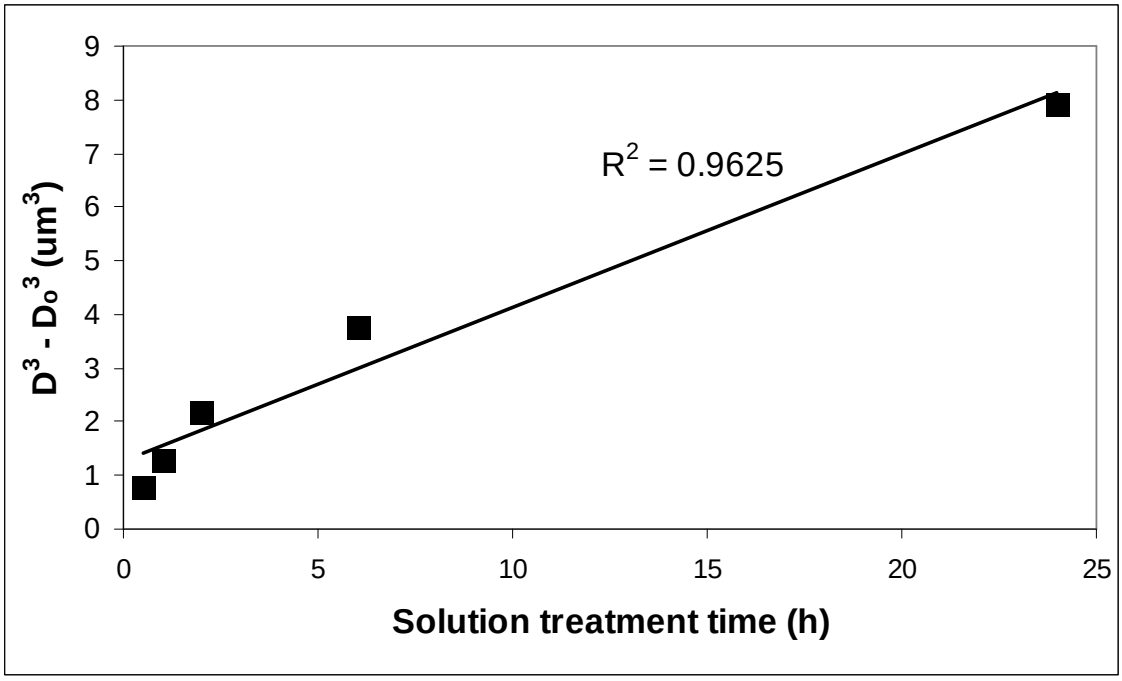

Figure 4.11: The cube of the change in mean diameter of the Si eutectic particles as a function of solution treatment time at 540°C using as starting diameter (D_o) of as-cast fibrous Si.

4.2.2. Dissolution of solutes and reduction of microsegregation

The time necessary to place magnesium in solid solution (dissolve the Mg_2Si in the alloy) is rapid at 540°C and occurs within minutes (section 2.3.1). However, it is frequently specified that solution treatments for these alloys at 540°C should be for 4-10 h (Table 2.8). Artificial aging curves (Fig. 4.12) indicate that similar levels of strengthening can be obtained following solution treatment at 540°C for either 1 or 6 h [HM1-HM3].

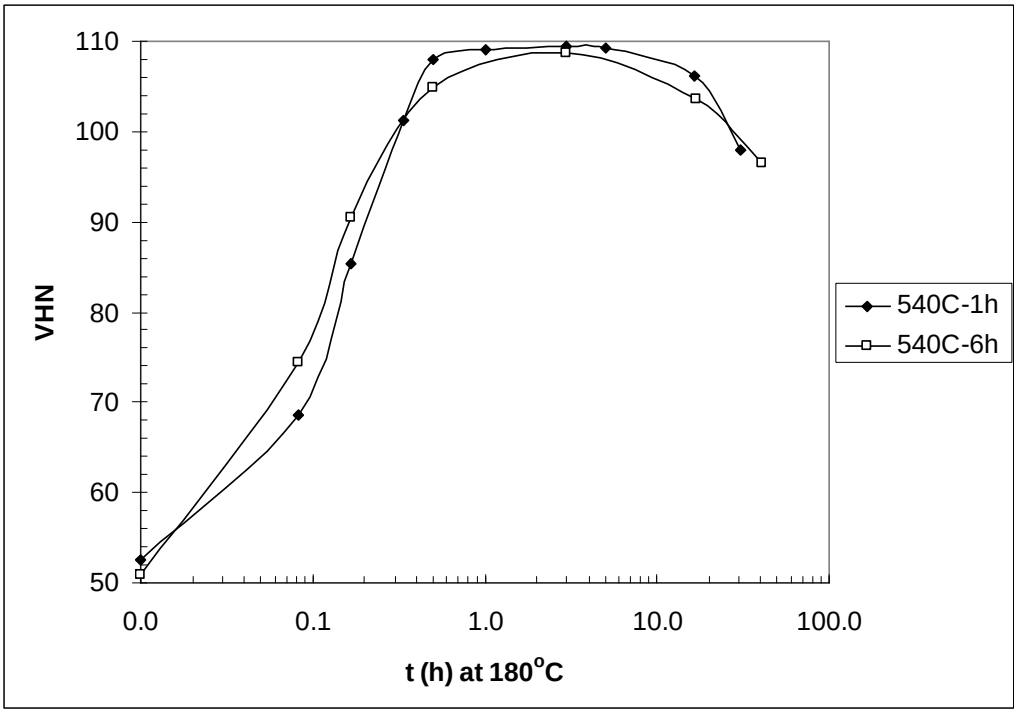

Figure 4.12: Artificial aging curves for SSM-HPDC A356 (0.34% Mg) following solution treatment at 540°C for 1 or 6 h (no natural pre-aging).

Tensile results (Table 4.5) of alloy F357 with 0.62% Mg (Table 3.1) confirm these observations, indicating that even in the higher Mg-containing alloys, a solution treatment of 1 h at 540°C is sufficient to obtain maximum strength [HM8].

Table 4.5: Yield strength (YS), ultimate tensile strength (UTS) and % elongation after fracture of heat treated SSM-HPDC F357 (0.62% Mg) samples. The standard deviation from five values for tensile properties is also indicated in brackets

Heat treatment	YS (MPa)	UTS (MPa)	% Elongation
T4			
540°C-0.5h, 120h NA	170 (3.4)	294 (4.4)	14.6 (2.0)
540°C-1h, 120h NA	172 (4.7)	297 (4.0)	17.0 (2.5)
540°C-6h, 120h NA	172 (1.9)	290 (4.1)	14.2 (0.7)
T6			
540°C-0.5h, 20h NA, 180°C-4 h	304 (2.2)	353 (1.3)	7.8 (1.4)
540°C-1h, 20h NA, 180°C-4 h	312 (4.1)	355 (3.9)	6.0 (1.3)
540°C-6h, 20h NA, 180°C-4 h	317 (4.9)	354 (5.2)	5.6 (1.4)

4.2.3. Impact strength

The impact strength of SSM-HPDC Al-7Si-Mg alloys with different Mg-contents that had been solution treated at 540°C for either 1 or 6 h were determined using a Zwick impact tester with a 40 kpcm hammer [HM3]. The impact strength in the T4 and T6 temper conditions was determined and is shown in Table 4.6. Similar impact properties are obtained after a solution treatment of 1 h rather than 6 h for each composition. There is therefore no advantage to impact strength by employing a longer solution treatment time of 6 h. The strength of the alloy plays a more important role than the solution treatment time on the impact strength in the T4 and T6 temper conditions. Linear relationships are found between impact strength and YS (Fig. 4.13(a) and UTS (Fig. 4.13(b)) regardless of whether the solution treatment was performed for 1 or 6 h. The alloys with lower strength have better impact properties because crack propagation is more difficult in these materials due to blunting, which would suggest that a better correlation between impact strength and UTS (rather than YS) should be found. The reason why a better correlation with UTS is not found in this case is most likely related to the fact that UTS is influenced significantly more by small casting defects than YS [103]. Note that Figure 4.13 is only applicable to alloys in the T4 and T6 temper conditions where spheroidisation of the Si has taken place.

The impact properties of alloys in the F and T5 temper conditions (where the eutectic Si particles are not spheroidised) are discussed later in section 4.8.

Also included in Fig. 4.13 are unit total energies (UTE) for premium strength cast A356/7 alloys obtained using tear testing [94]. Although tear testing is considered a more appropriate technique to measure fracture properties of Al-alloys than Charpy testing [94], the UTE values are reasonably comparable to the impact strength values determined in this study.

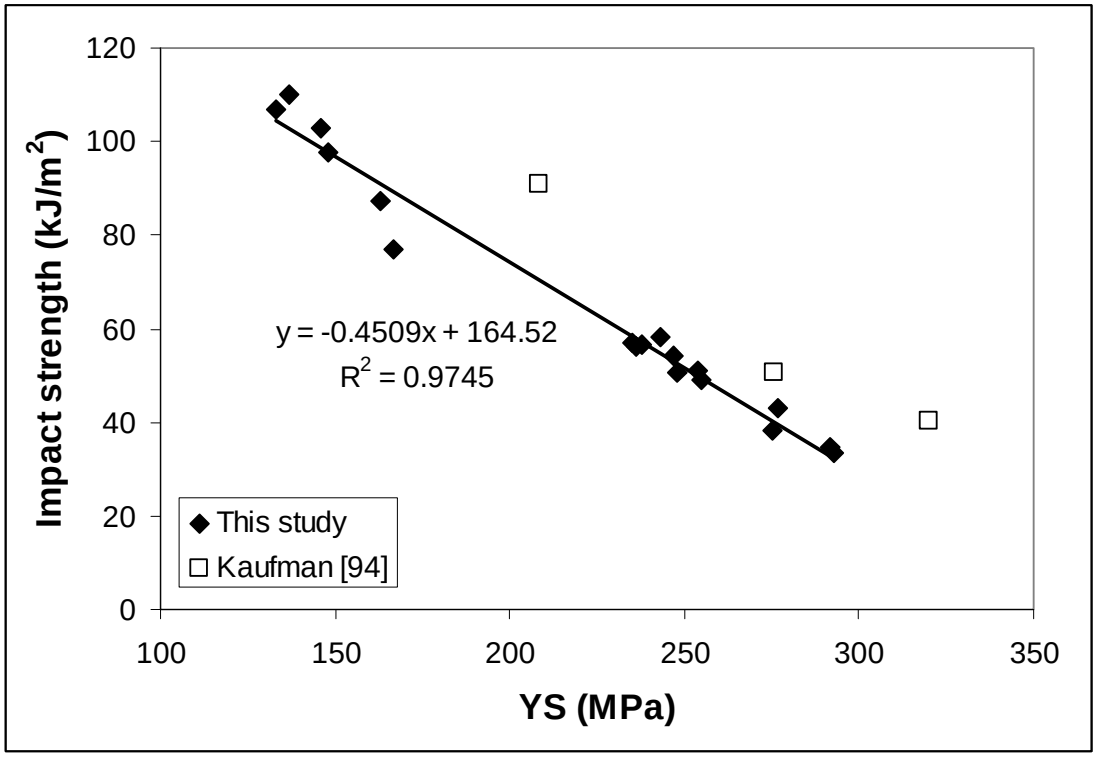

(a)

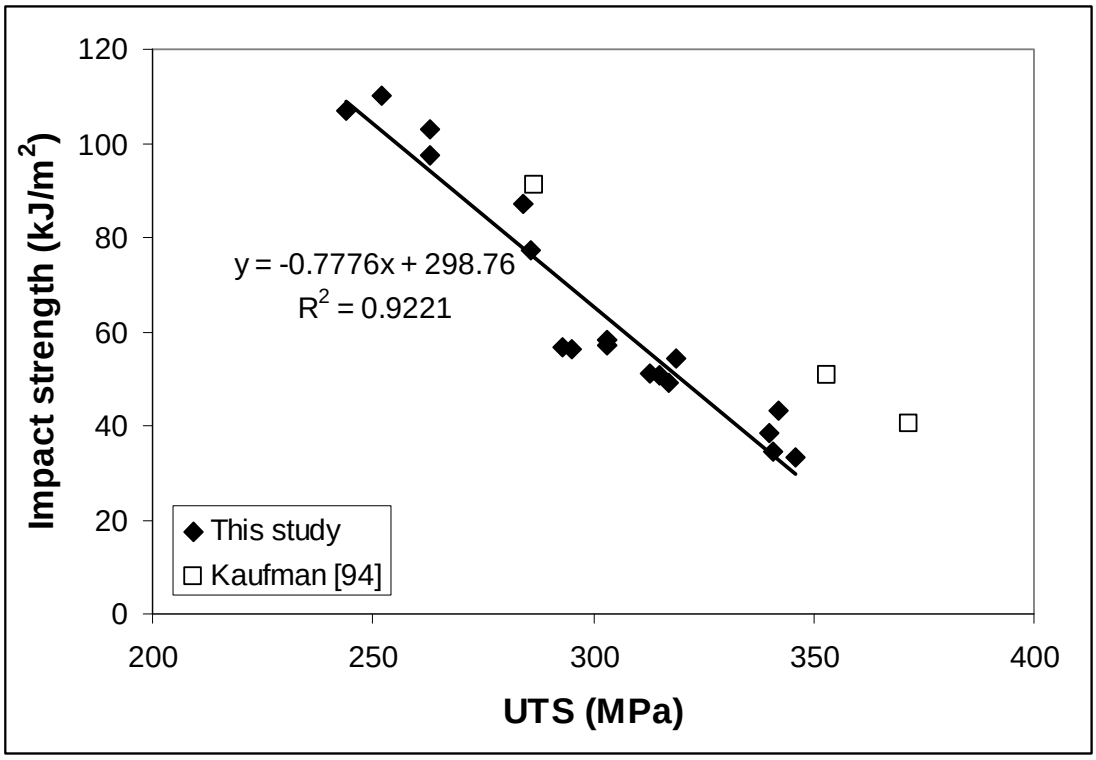

(b)

Figure 4.13: Impact strength of SSM-HPDC Al-7Si-Mg alloys in the T4 and T6 temper conditions as a function of (a) YS and (b) UTS of the alloys. UTE values from tear testing from Kaufmann [94] are also included.

Table 4.6: Impact strength of T4 and T6 heat treated samples of Al-7Si-Mg alloys (standard deviation from five values is also indicated in brackets).

Heat treatment	Impact Strength (kJ/m^2)
T4	
0.25% Mg	
540^{o}C,1 h	110.0 (3.7)
540^{o}C, 6 h	106.9 (9.1)
0.31% Mg	
540^{o}C,1 h	103.0 (5.5)
540^{o}C, 6 h	97.6 (6.0)
0.45% Mg	
540^{o}C,1 h	87.3 (6.4)
540^{o}C,6 h	77.1 (4.7)
T6	
0.25% Mg	
540^{o}C-6h, 0h NA,180^{o}C-1h	56.5 (6.7)
540^{o}C-1h, 0h NA, 180^{o}C-1h	57.0 (2.4)
540^{o}C-6h, 20h NA, 180^{o}C-4h	56.1 (4.1)
540^{o}C-1h, 20h NA, 180^{o}C-4h	58.3 (1.6)
0.31% Mg	
540^{o}C-6h, 0h NA, 180^{o}C-1h	50.6 (2.3)
540^{o}C-1h, 0h NA, 180^{o}C-1h	54.1 (3.0)
540^{o}C-6h, 20h NA, 180^{o}C-4h	49.1 (6.7)
540^{o}C-1h, 20h NA, 180^{o}C-4h	50.9 (4.3)
0.45% Mg	
540^{o}C-6h, 0h NA, 180^{o}C-1h	38.3 (3.8)
540^{o}C-1h, 0h NA, 180^{o}C-1h	43.0 (0.7)
540^{o}C-6h, 20h NA, 180^{o}C-4h	33.4 (2.6)
540^{o}C-1h, 20h NA, 180^{o}C-4h	34.6 (2.0)

4.3. Quench after solution treatment

Slow quench rates after the solution heat treatment can reduce the problems of distortion and residual stresses, but also result in a loss of strength and hardness after artificial aging (section 2.3.2). Natural (Fig. 4.14) and artificial (Fig. 4.15) aging curves for SSM-HPDC A356 with 0.36% Mg (Table 3.1) are shown for samples that were solution treated at 540^{o}C for 1 h and then quenched in water (WQ) at either 25 or 70^{o}C [HM3]. Artificial aging was performed at 180^{o}C.

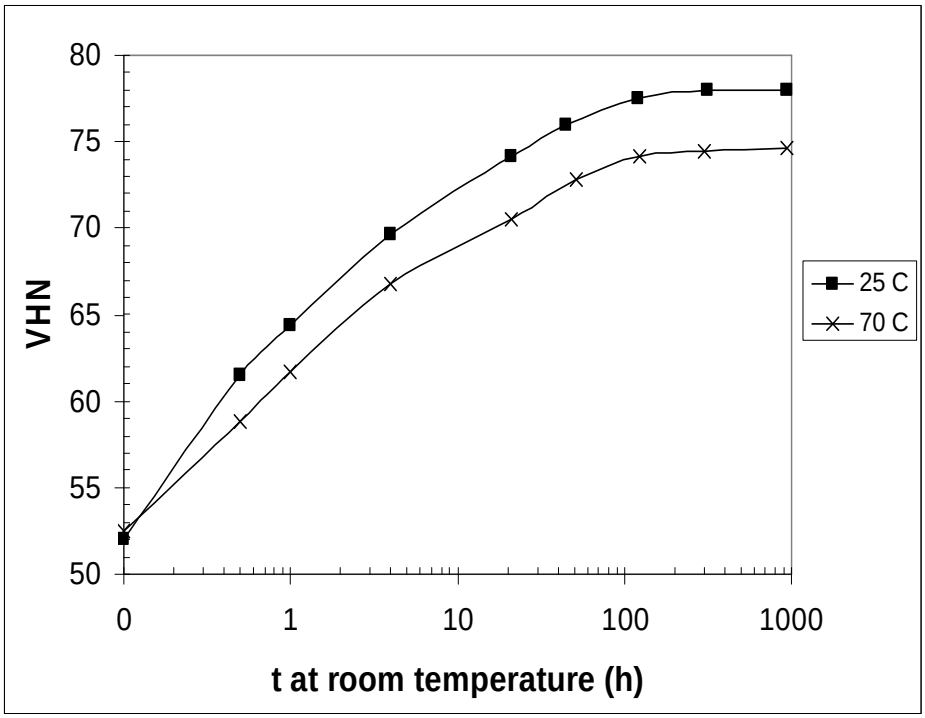

Figure 4.14: Natural aging curves for SSM-HPDC A356 solution treated at 540^{o}C for 1 h, followed by water quenching at 25 and 70^{o}C.

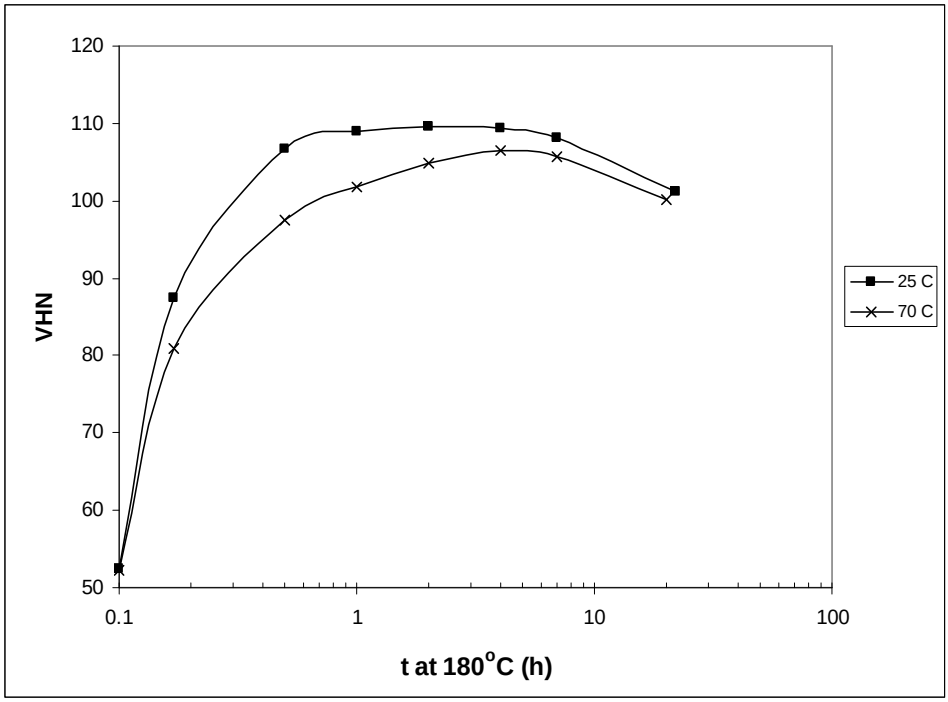

Figure 4.15: Artificial aging curves at 180°C for SSM-HPDC A356 solution treated at 540°C for 1 h, followed by water quenching at 25 and 70°C and artificial aging at 180°C.

It is seen that the higher quench temperature leads to a lower T4 hardness due to less supersaturation (Fig. 4.14). The more sluggish artificial aging response following the 70°C quench is presumably due to less quenched in vacancies (Fig. 4.14). The peak hardness (VHN = 106) is slightly less than when a 25°C water quench is used. This is most likely due to a lower degree of supersaturation obtained after the 70°C water quench. The tensile properties of SSM-HPDC A356 (0.40% Mg) in the T4 and T6 temper conditions are compared in Table 4.7 for samples quenched in 25 and 70°C water respectively. As expected, the YS and UTS of the 70°C water quenched alloys are less than the 25°C water quenched alloys.

Table 4.7: YS, UTS, % elongation after fracture of T4 and T6 heat treated SSM-HPDC samples (0.40wt% Mg-A356). The standard deviation from five values for tensile properties is also indicated in brackets.

Heat Treatment	YS (MPa)	UTS (MPa)	% Elongation
T4			
540°C-1h, 25WQ, 120h NA	152 (3.5)	282 (6.1)	15.8 (3.3)
540°C-1h, 70WQ, 120h NA	138 (2.2)	264 (6.5)	16.5 (2.5)
T6			
540°C-1h,25WQ,0h NA,180°C-4h	276 (8.0)	342 (4.9)	9.1 (1.2)
540°C-1h,70WQ,0h NA,180°C-4h	265 (5.0)	330 (2.7)	9.8 (2.1)
540°C-1h,25WQ,120h NA,180°C-4h	280 (5.2)	337 (6.0)	6.9 (1.8)
540°C-1h,70WQ,120h NA,180°C-4h	265 (3.5)	327 (4.5)	8.6 (0.7)

4.4. Natural aging and the T4 temper

Natural aging time is the time a component is stored at room temperature after the solution heat treatment and quench. The precipitation hardening that result from natural aging alone (no artificial aging) produces the T4 temper. Figure 4.16 shows natural aging curves for SSM-HPDC Al-7Si-Mg alloys after solution treatment at 540°C for 1 h, followed by a water quench (25°C) before natural aging [HM1].

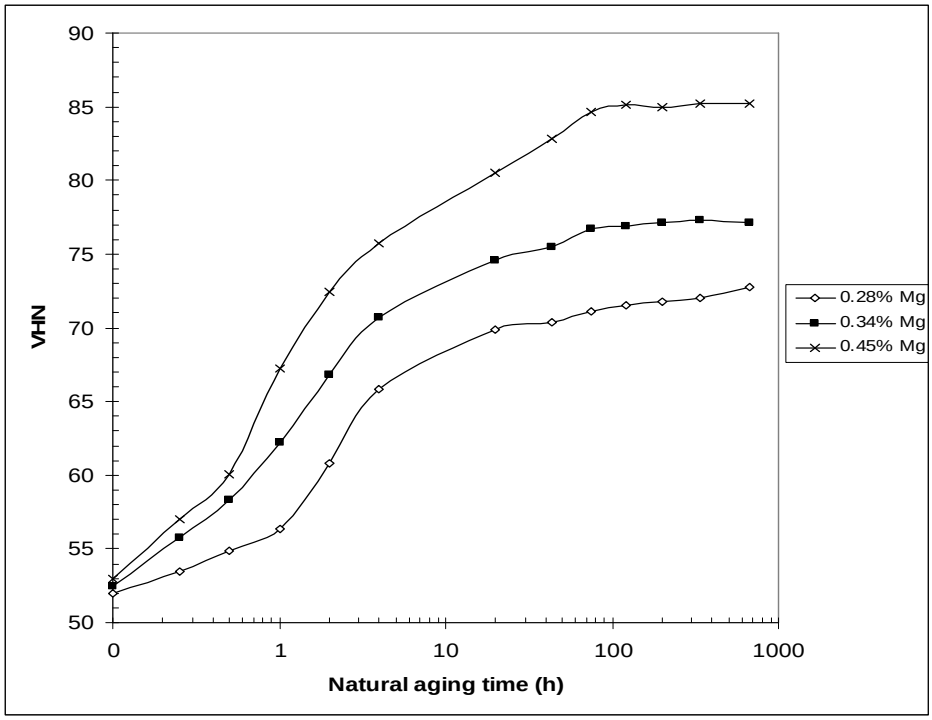

Figure 4.16: Natural aging curves for SSM-HPDC Al-7Si-Mg alloys following solution treatment at 540^{o}C for 1 h and a 25^{o}C water quench.

The alloy is relatively soft immediately after quenching (VHN = ~ 53), but thereafter the hardness increases rapidly and eventually levels out after about 120 h corresponding to the stable T4 temper. The natural aging response of these alloys is considered to be due to the forming of (Mg+Si) clusters (see APT results in section 4.14). The tensile properties of SSM-HPDC Al-7Si-Mg alloys with different Mg-contents are shown in Table 4.8.

Table 4.8: YS, UTS, % elongation after fracture of T4 heat treated SSM-HPDC Al-7Si-Mg alloys (solution treated at 540°C-1 h, 25°C water quench and natural aging for at least 120 h). The standard deviation from five values for tensile properties is also indicated in brackets.

Mg-content (wt%)	YS (MPa)	UTS (MPa)	% Elongation
0.25	137 (4.2)	252 (6.2)	20.2 (0.94)
0.31	146 (7.3)	263 (8.8)	17.4 (1.8)
0.38	152 (2.1)	268 (3.9)	14.5 (1.3)
0.40	152 (3.5)	282 (6.1)	15.8 (3.3)
0.45	163 (1.5)	284 (2.6)	16.5 (1.9)
0.62	172 (4.7)	297 (4.0)	17.0 (2.5)

4.5. Artificial aging and the T6 temper

Artificial aging is performed at temperatures above room temperature to cause precipitation of strengthening phases. Artificial aging curves at artificial aging temperatures of 160, 180 and 190°C are shown in Fig. 4.17 [HM2]. The curves were determined for samples that were solution treated at 540°C for 6 h, water quenched and naturally aged for 20 h before artificial aging. As expected, the maximum hardness is reached in a shorter time as aging temperatures are increased due to higher diffusion rates. However, the maximum hardness achieved simultaneously decreases slightly, due to the higher solubility and hence lower supersaturation, leading to a lower nucleation rate and volume fraction of strengthening phases at higher aging temperatures. The optimum artificial aging parameters depend on the properties required. If a high hardness (strength) is required, a low aging temperature is required (such as 160°C), but this unfortunately takes relatively long times to obtain this high hardness (Fig. 4.17). The best combination of relatively short aging treatments resulting in acceptably high hardness values is obtained by aging at 170-180°C. If a short aging time is, however, a more important factor than maximum hardness (strength), then 185-195°C will give optimum results.

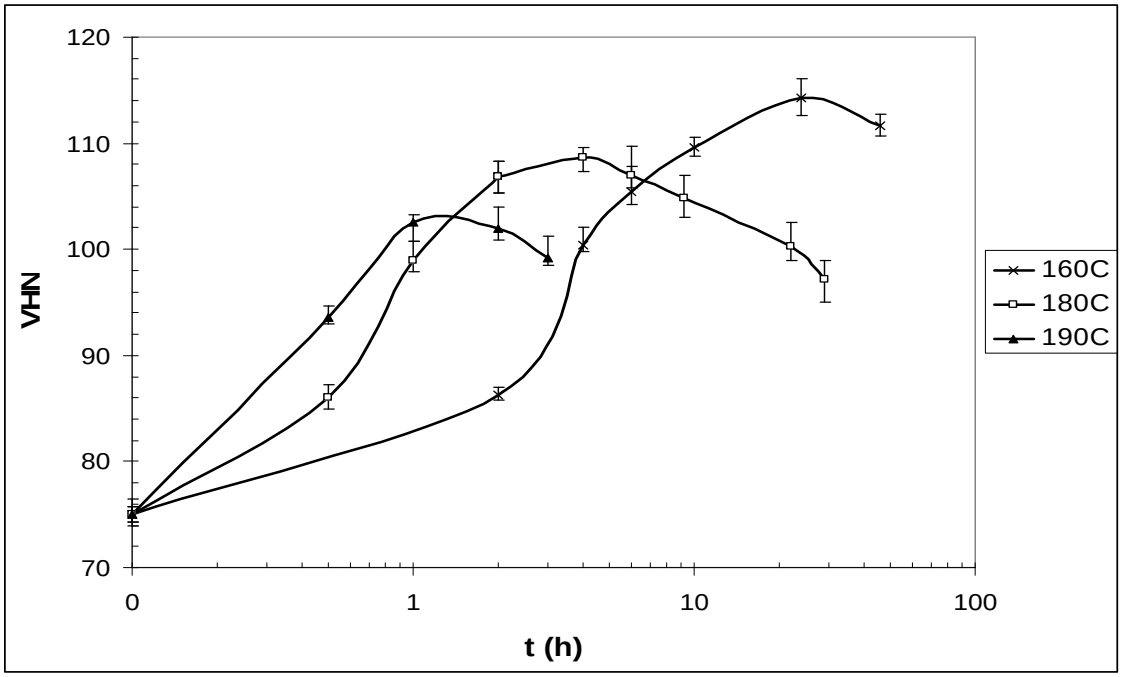

Figure 4.17: Artificial aging curves for alloy A356 (0.36% Mg) after solution treatment at 540°C for 6 h, water quenching, natural aging for 20 h and artificial aging at different temperatures.

Artificial aging curves at 180°C for alloy A356 (with 0.36 wt% Mg), following natural aging periods of either 0, 1, 20 or 120 h, are shown in Fig. 4.18 [HM4]. When no prior natural aging is applied, the initial artificial aging response is rapid. The converse is also true - when natural aging is employed, the subsequent artificial aging response is sluggish. Natural aging of only 1 h decreases the artificial aging response of this alloy significantly.

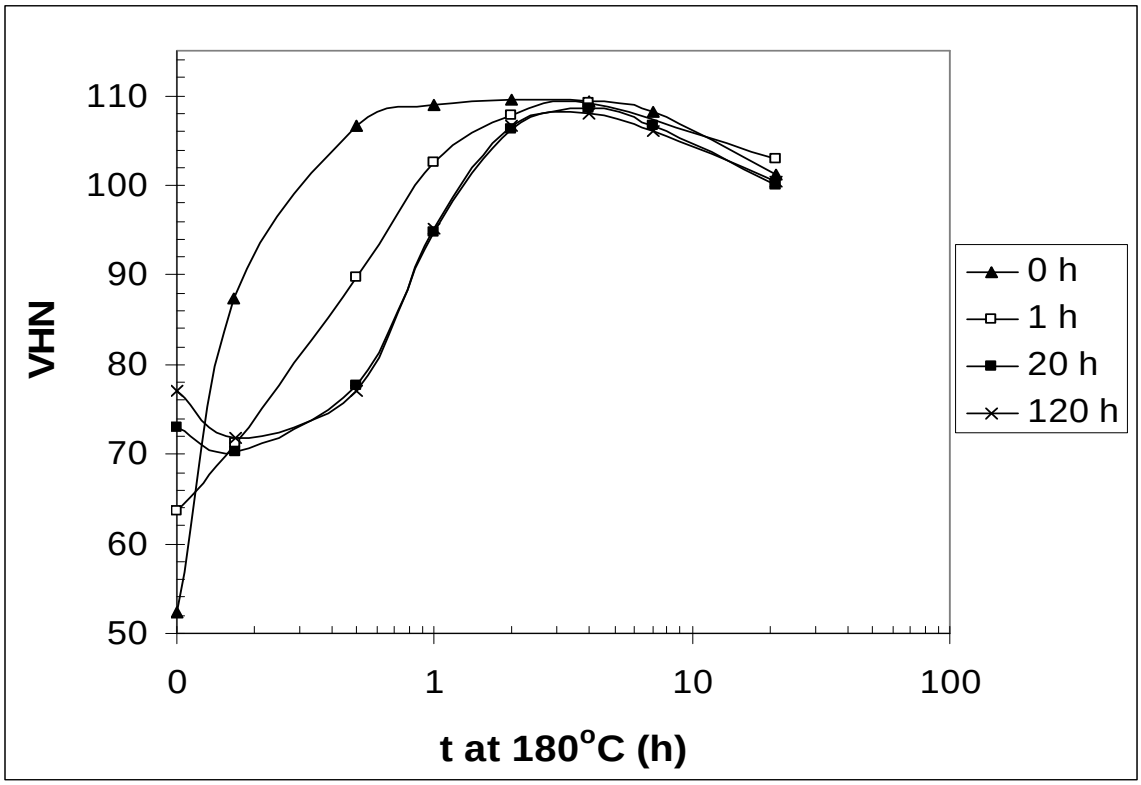

Figure 4.18: Artificial aging curves at 180°C after natural aging for times of 0, 1, 20 and 120 h respectively for A356 with 0.36wt% Mg.

This phenomenon can be explained by two different mechanisms. Firstly, it has been shown that the precipitates which grow during artificial aging from the clusters are coarser than those that develop in certain 6000 series alloys aged immediately after quenching. This results in a reduction of up to 10% in tensile properties for certain alloys [9]. Secondly, it has been shown that natural aging following the solution treatment reduced the age hardenability of Al-Mg-Si wrought alloy 6016, especially in the under-aged condition [104]. This was attributed to solute clustering during natural aging, and the subsequent dissolution of these clusters during artificial aging. The extent of the loss was, however, recovered by precipitation of β″–particles upon further aging.

Considering Fig. 4.18, it is seen that for alloy A356, the hardness values of naturally aged samples are also recovered with further artificial aging. The mechanism of the formation of coarser precipitates that leads to a decrease in tensile properties does not allow for a full recovery in hardness. It is also seen from Fig. 4.18 that the hardness of the sample that did not age naturally increases immediately during artificial aging.

However, the samples that were naturally aged soften during the first 10 minutes at 180^{o}C, before the hardness increases again. The clusters that form during natural aging and their response during artificial aging are shown in detail in the APT results in section 4.14.

When no natural pre-aging occurs, a plateau is maintained once the maximum hardness is reached during artificial aging after about 1 to 5 h (Fig. 4.18). This differs from when natural pre-aging occurs, when a hardness peak is observed after approximately 4 h. The tensile properties (YS and UTS) are shown Table 4.9 as a function of the artificial aging time within the hardness plateau (with no prior natural aging). It is seen that the ultimate tensile strengths of the samples on the hardness plateau are similar. However, the yield strength of the 1 hour artificially aged sample is significantly lower than the rest of the samples with a concurrent higher ductility. The hardness plateau allows more freedom in terms of the artificial aging times that can be used and the dangers of either under-aging or over-aging are therefore minimised. Once natural aging occurs, a hardness plateau is not maintained during the subsequent artificial aging. Instead, a hardness peak is reached after approximately 4 h (Fig. 4.18). This would necessitate stricter control in terms of artificial aging time (i.e. aging for less than 4 h will result in under-aging, and aging for more than 4 h will result in over-aging). The tensile properties after artificial aging for 4 h at 180^{o}C as a function of prior natural aging time are also shown in Table 4.9. In this case, no significant differences are seen in either the yield strength or ultimate tensile strength. The influence of natural aging prior to artificial aging can therefore be removed by a 4 h, 180^{o}C artificial aging treatment. It is seen from Fig. 4.18 that, while artificial aging at 180^{o}C for 1 h causes maximum hardening in SSM-HPDC A356 that was not naturally aged, under-aging is achieved in samples that were naturally aged prior to artificial aging. The tensile properties of 0.40wt% Mg-A356 were determined under these conditions (1 h artificial aging at 180^{o}C for samples that were naturally aged for 0 h, 20 h and 120 h). The negative influence of natural aging on the initial stages of artificial aging can be seen in Table 4.9. Similar effects to those observed for SSM-HPDC A356 in Table 4.9 have also been found for the higher Mg-containing (0.62%) SSM-HPDC alloy F357 and are presented in Table 4.10 [HM8].

Table 4.9: Yield strength (YS), UTS and % elongation after fracture of SSM-HPDC A356. The standard deviation from five values for tensile properties is also indicated in brackets.

Heat treatment	YS (MPa)	UTS (MPa)	% Elongation
0.36wt% Mg			
540°C-1h,0h NA,180°C-1h	255 (4.8)	330 (6.4)	10.4 (2.5)
540°C-1h,0h NA,180°C-2h	269 (8.5)	334 (6.8)	7.5 (1.9)
540°C-1h,0h NA,180°C-4h	273 (6.5)	333 (8.4)	8.4 (2.1)
540°C-1h,0h NA,180°C-5h	273 (3.1)	328 (6.9)	7.7 (3.1)
540°C-1h,1h NA,180°C-4h	269 (5.8)	325 (4.6)	10.3 (3.4)
540°C-1h,20h NA,180°C-4h	270 (4.7)	325 (2.8)	9.3 (1.7)
540°C-1h,120h NA,180°C-4h	270 (5.5)	328 (5.8)	8.0 (2.2)
0.40wt% Mg			
540°C-1h,0h NA,180°C-1h	266 (7.5)	341 (9.5)	7.8 (1.8)
540°C-1h,20h NA,180°C-1h	224 (7.5)	315 (3.4)	12.5 (1.4)
540°C-1h,120h NA,180°C-1h	233 (8.2)	318 (5.2)	10.0 (2.7)
540°C-1h,-18°C for 20h,180°C-1h	266 (6.7)	343 (4.7)	9.1 (1.9)

Table 4.10: Yield strength (YS), ultimate tensile strength (UTS) and % elongation after fracture of SSM-HPDC F357 (0.62% Mg). The standard deviation from five values for tensile properties is also indicated in brackets

Heat treatment	YS (MPa)	UTS (MPa)	% Elongation
540°C-1h,0h NA,180°C-1h	296 (2.9)	358 (3.7)	7.4 (0.7)
540°C-1h,0h NA,180°C-2h	307 (3.1)	364 (2.5)	9.6 (2.4)
540°C-1h,0h NA,180°C-4h	315 (5.2)	360 (5.0)	5.7 (1.1)
540°C-1h,20h NA,180°C-1h	243 (6.2)	320 (7.9)	9.5 (2.6)
540°C-1h,20h NA,180°C-2h	289 (10.7)	346 (4.5)	8.0 (2.4)
540°C-1h,20h NA,180°C-4h	312 (4.1)	355 (3.9)	6.0 (1.3)

To determine whether the process of natural aging could be impeded by low temperatures, SSM-HPDC A356 samples were stored in a freezer at -18°C for 20 h after quenching, before artificial aging at 180°C for 1 h. The tensile properties (Table

4.9) indicate that this treatment was indeed successful. The artificial aging response of the samples that were kept in the freezer was the same as the samples that were not naturally aged at all. However, it would be more practical to remove the influence of natural pre-aging by employing an artificial aging treatment of 180^{o}C for 4 h.

The onset of the hardness plateau (no natural aging) and hardness peak (with natural aging) in Fig. 4.18 as a function of artificial aging temperature follows an Arrhenius-type response (t_{T6} = C EXP (Q/RT)) with C the pre-exponential factor, Q the activation energy in J/mol and R the universal gas constant = 8.314 J/mol K). The equations that describe the time-to-maximum-hardness (t_{T6}) are given by equation 4.2 (with prior natural aging time) and equation 4.3 (for no natural aging time) [HM2]:

$$\mathbf{t_{T6} = 2.3 \times 10^{-15} EXP\ (163000 / 8.314T)} \qquad \mathbf{(4.2)}$$

$$\mathbf{t_{T6} = 4.9 \times 10^{-16} EXP\ (163000 / 8.314T)} \qquad \mathbf{(4.3)}$$

with t_{T6} the time in seconds and T the artificial aging temperature in K.
Arrhenius-type plots are shown in Fig. 4.19 for the artificial aging of SSM-HPDC Al-7Si-Mg alloys with prior natural aging (Equation 4.2) and without prior natural aging (Equation 4.3). Comparing the equations and plots, it is seen that an instantaneous transfer from quench to artificial aging does not have an influence on the activation energy (Q). It does, however, decrease the pre-exponential factor C, thereby resulting in a much faster artificial aging response. These equations are useful for determining how long an SSM-HPDC Al-7Si-Mg component must be artificially aged at a specific temperature to get maximum hardness (for convenience the temperatures and times are shown in Table 4.11).

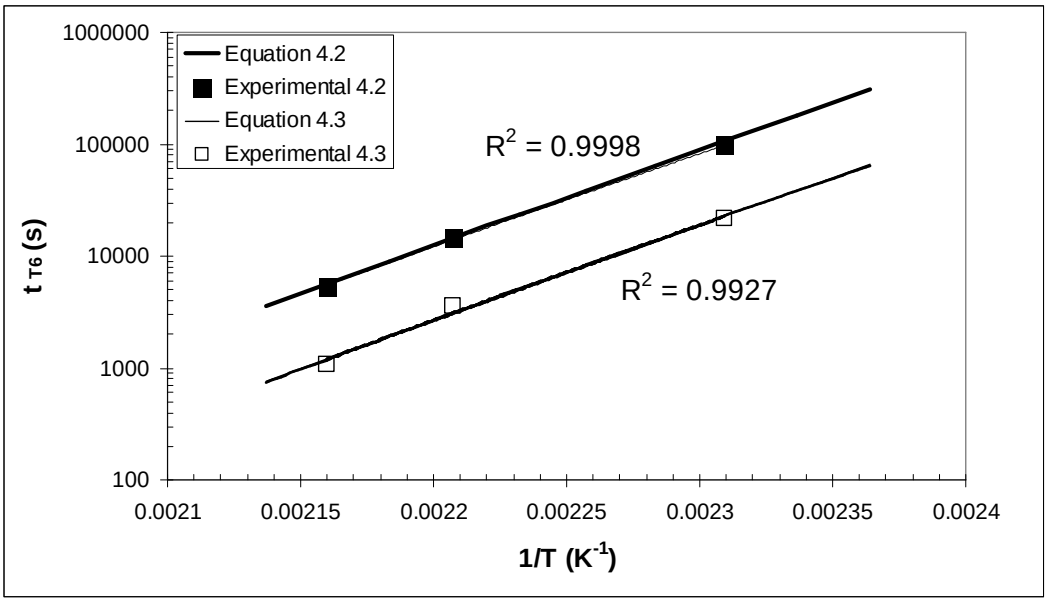

Figure 4.19: Arrhenius-type plots for the artificial aging of SSM-HPDC A356 with prior natural aging (Equation 4.2) and without prior natural aging (Equation 4.3).

The determined activation energy of 163 kJ/mol is higher than those reported by Rometsch and Schaffer [82] (130-138 kJ/mol) and Shercliff and Ashby [15] (130-145 kJ/mol) for Al-Si-Mg alloys. The activation energy for diffusion of Si in Al has been proposed in a range from 118 kJ/mol [105] to 151 kJ/mol [106]. Similarly, the activation energy for diffusion of Mg in Al has been proposed in a range from 111 kJ/mol [107] to 161 kJ/mol [108].

Table 4.11: Time-to-maximum-hardness (t_{T6}) at different artificial aging temperatures (using equations 4.2 and 4.3).

Temperature (^{o}C)	t_{T6} (with natural aging) (h)	t_{T6} (with no natural aging) (h)
160	29	6.5
165	18	4.0
170	10	2.5
175	6.5	1.5
180	4	1.0
185	2.5	0.5
190	1.5	0.3

Note that equation 4.3 (no natural pre-aging) calculates the onset of the hardness plateau (Fig. 4.18). As was shown in Tables 4.9 and 4.10, this does not necessarily result in maximum yield strength (i.e. time-to-maximum-hardness is not the same as time-to-maximum-yield strength). With equation 4.2 (with natural pre-aging), however, time-to-maximum-hardness and time-to-maximum-yield strength are the same. To ensure that maximum yield strength is reached in samples with no prior natural pre-aging, equation 4.2 should rather be used. According to Table 4.11, the traditional artificial aging temperature of 170^{o}C for 6 h (Table 2.7) results in under-aging of naturally pre-aged Al-7Si-Mg alloys, with over-aging of alloys that were not naturally pre-aged. This is not an ideal situation where different properties are obtained as a function of natural pre-aging (see Fig. 2.34). As discussed before, application of equation 4.2 will result in similar tensile properties being obtained regardless of natural pre-aging. Table 4.12 shows tensile properties of alloy F357 (with 0.62% Mg) after artificial aging at 170^{o}C for 6 and 10 h respectively [HM8]. It can be seen that higher strength (especially YS) is indeed obtained as predicted by Table 4.11.

Table 4.12: Yield strength (YS), ultimate tensile strength (UTS) and % elongation after fracture of heat treated F357 samples (0.62% Mg). The standard deviation from five values for tensile properties is also indicated in brackets.

Heat treatment	YS (MPa)	UTS (MPa)	% Elongation
540^{o}C-6h, 20h NA, 170^{o}C-6h	307 (5.7)	356 (4.8)	6.1 (1.5)
540^{o}C-6h, 20h NA, 170^{o}C-10h	320 (4.5)	358 (3.1)	5.8 (1.2)

The tensile properties of SSM-HPDC Al-7Si-Mg alloys heat treated with the traditional heat treatment (540^{o}C-6h, 20h NA, 170^{o}C-6h) are compared with those heat treated with the shortened cycles (540^{o}C-1h, 0-120h NA, 180^{o}C-4h) in Table 4.13. The tensile properties obtained using the traditional and short heat treatment cycles are remarkably similar over a wide range of Mg-compositions. The advantage of the shortened cycles is that it involves only 5 hours at elevated temperatures compared to 12 h with the traditional treatment, with obvious productivity increases and energy savings. The reason why similar properties can be obtained at the higher artificial aging temperature of 180^{o}C compared to 170^{o}C is due to the fact that the

180°C-4h treatment results in peak aging, whereas 170°C-6h results in under-aging (Table 4.11).

Table 4.13: Yield strength (YS), ultimate tensile strength (UTS) and % elongation after fracture of SSM-HPDC Al-7Si-Mg samples heat treated with the traditional or shortened heat treatments. The standard deviation from five values for tensile properties is also indicated in brackets.

Heat treatment	YS (MPa)	UTS (MPa)	% Elongation
0.28% Mg			
540°C-6h, 20h NA, 170°C-6h	243 (4.1)	296 (6.5)	7.2 (1.3)
540°C-1h, 0-120h NA, 180°C-4h	240 (2.8)	301 (3.1)	9.4 (0.9)
0.34% Mg			
540°C-6h, 20h NA, 170°C-6h	261 (4.5)	316 (5.9)	8.3 (2.1)
540°C-1h, 0-120h NA, 180°C-4h	259 (5.2)	317 (7.1)	8.8 (1.4)
0.45% Mg			
540°C-6h, 20h NA, 170°C-6h	297 (5.0)	345 (5.6)	7.3 (2.3)
540°C-1h, 0-120h NA, 180°C-4h	294 (5.8)	344 (3.1)	7.1 (1.4)
0.62% Mg			
540°C-6h, 20h NA, 170°C-6h	307 (5.7)	356 (4.8)	6.1 (1.5)
540°C-1h, 0-120h NA, 180°C-4h	312 (4.1)	355 (3.9)	6.0 (1.3)

4.6. The effects of Mg and Fe in Al-7Si-Mg alloys

The tensile properties of SSM-HPDC Al-7Si-Mg alloys from this study are compared in Fig. 4.20 with SSM-processed Al-7Si-Mg alloys from other researchers [35,89], all heat treated with the traditional T6 heat treatment cycles.

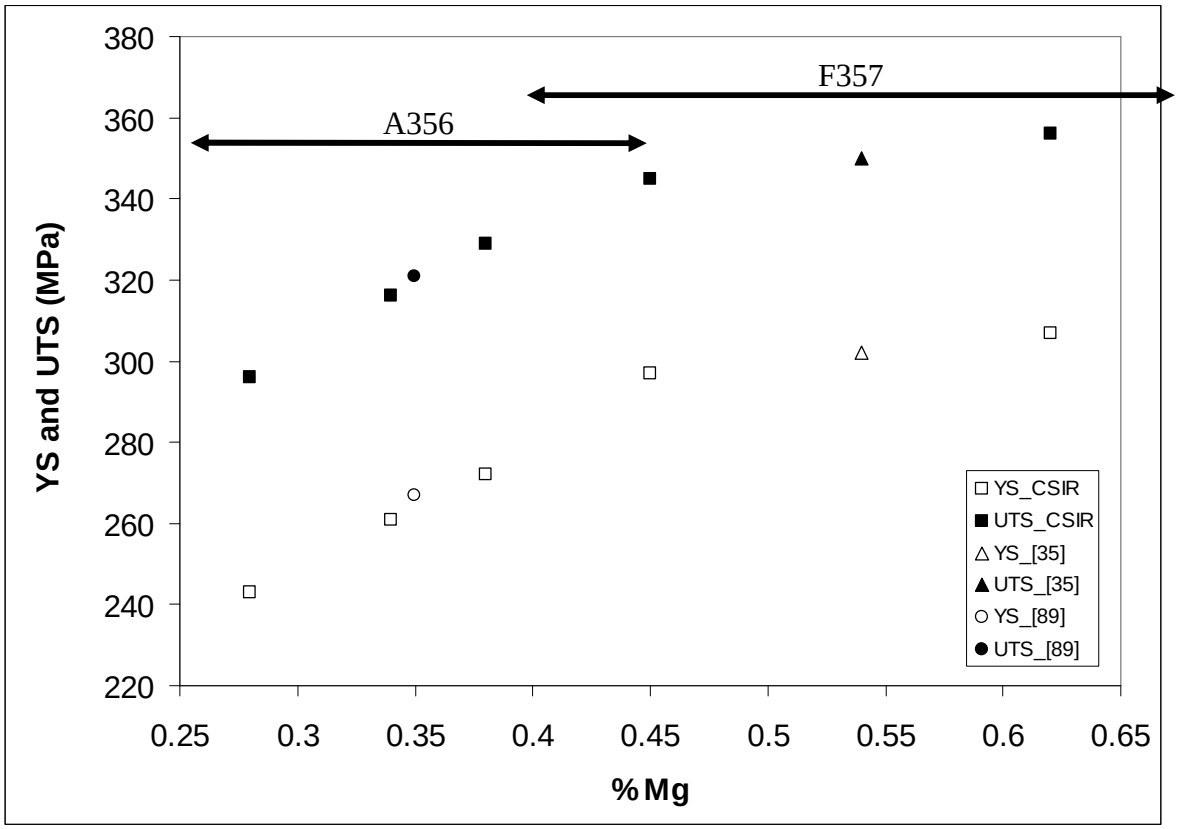

Figure 4.20: YS and UTS as a function of the bulk wt% Mg-content of SSM-processed Al-7Si-Mg alloys heat treated with the traditional heat treatment cycles.

A lower increase in strength with bulk Mg-concentration is observed for alloy F357 when compared to alloy A356. This is in line with the findings of Taylor and co-workers [48] who determined the matrix Mg-content of A356 and F357 alloys (the Mg-concentration in solid solution after solution treatment) by using electron probe microanalysis (EPMA) - as shown in Fig. 2.20. In the low Mg-alloys (A356), it is seen that the final matrix Mg concentration equals the bulk Mg-content of the alloy. This implies that, during solution treatment, all the as-cast Mg_2Si was dissolved, and that the π-$Al_8FeMg_3Si_6$ phase was also dissolved. As the alloy Mg-content increases, the matrix Mg-levels do not reach the bulk values. Since very little Mg_2Si is expected to remain after the solution treatment, this phenomenon is due to the increased stability of the π-phase as the alloy Mg-content is increased. Deviation from full dissolution of Mg in the matrix occurs at approximately 0.4% Mg. The calculated phase equilibria (minor phases) using Thermo-Calc for an Al-alloy with a base composition of alloy F357 with 0.62% Mg (Table 3.1), but with variable Mg, are

shown in Fig. 4.21 [HM8]. In this figure, the liquidus and solidus temperatures are indicated by arrows; "pi" refers to the π phase, "beta" is β–Al_5FeSi, and "alpha" is an Al-Mn-Fe-Si solid solution based on Al_8Fe_2Si (containing approximately equal amounts of Mn and Fe for the cases considered here). In all cases the major phases were liquid, Al-based FCC solid solution (the primary phase upon solidification), and Si (formed by eutectic solidification). In the region of the solution temperature (just below the solidus) the effect is quite clear: higher Mg levels increase the stability range of π to higher temperatures, and suppress β–Al_5FeSi formation at high temperatures. A secondary effect is that the dissolution temperature of Mg_2Si increases (and the equilibrium mass fraction of Mg_2Si at low temperatures increases), as one would expect. The extension of the stability range of the π-phase to high temperatures is in line with the observation that it is not possible to remove π by solution treatment in the high-Mg alloys above 0.4% in Fig. 2.20. According to the Thermo-Calc simulations, the dissolution temperature of π increases linearly with the Mg content of the alloy, and reaches 540°C at a Mg content of 0.40%.

Figs. 4.22(a,b) show scanning electron micrographs of SSM-HPDC A356 and F357 after solution treatment at 540^{o}C for 6 hours. The needle-like phase that is found in both A356 and F357 is tentatively identified by energy dispersive spectroscopy (EDS) (Fig. 4.23(a)) as likely to be β–Al_5FeSi. The blocky intermetallic phase that was mainly found in F357 is tentatively identified with EDS (Fig. 4.23(b)) as likely to be the Mg-containing π-phase ($Al_8FeMg_3Si_6$).

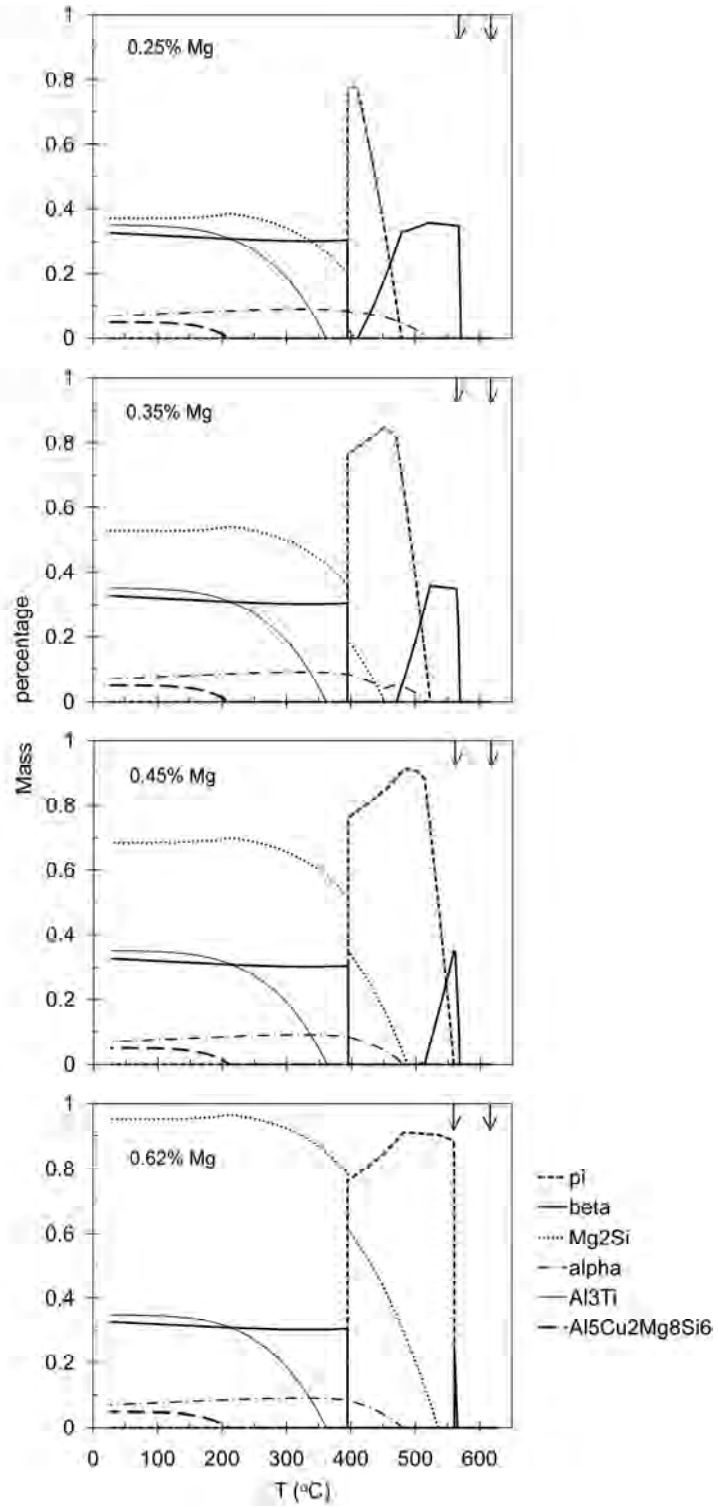

Figure 4.21: Calculated phase equilibria (minor phases) for Al alloy containing 7.01% Si, 0.10% Fe, 0.01% Cu, 0.01% Mn, 0.13% Ti and variable Mg.

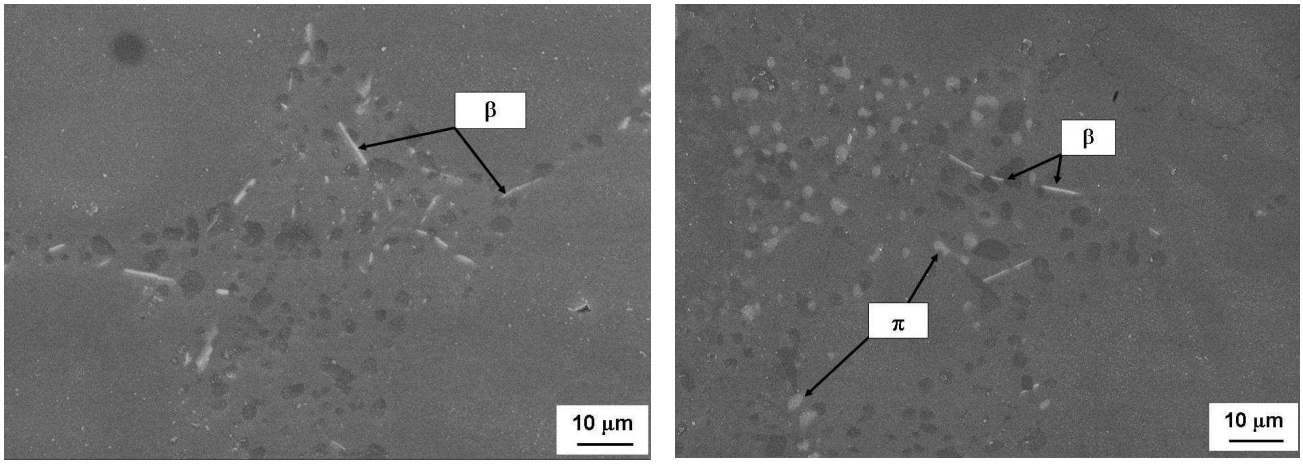

(a) **(b)**

Figure 4.22: Secondary electron images of (a) alloy A356 (with 0.36wt% Mg) and (b) alloy F357 (with 0.62% Mg) after solution treatment at 540°C for 6 h.

The data from Taylor and co-workers [48] as plotted in Fig. 2.20 were used to estimate the Mg-concentration available for precipitation hardening for the bulk compositions used in Fig. 4.20.

Make y = wt% Mg available for precipitation hardening

x = Bulk wt% Mg-content of alloy

For $0.25 \leq$ Bulk Mg ≤ 0.4

$$y = x \qquad (4.4)$$

For $0.4 \leq$ Bulk Mg ≤ 0.7 (see Figure 4.24, deduced from the high Mg-range in Figure 2.20)

$$y = -0.25x^2 + 0.665x + 0.1755 \qquad (4.5)$$

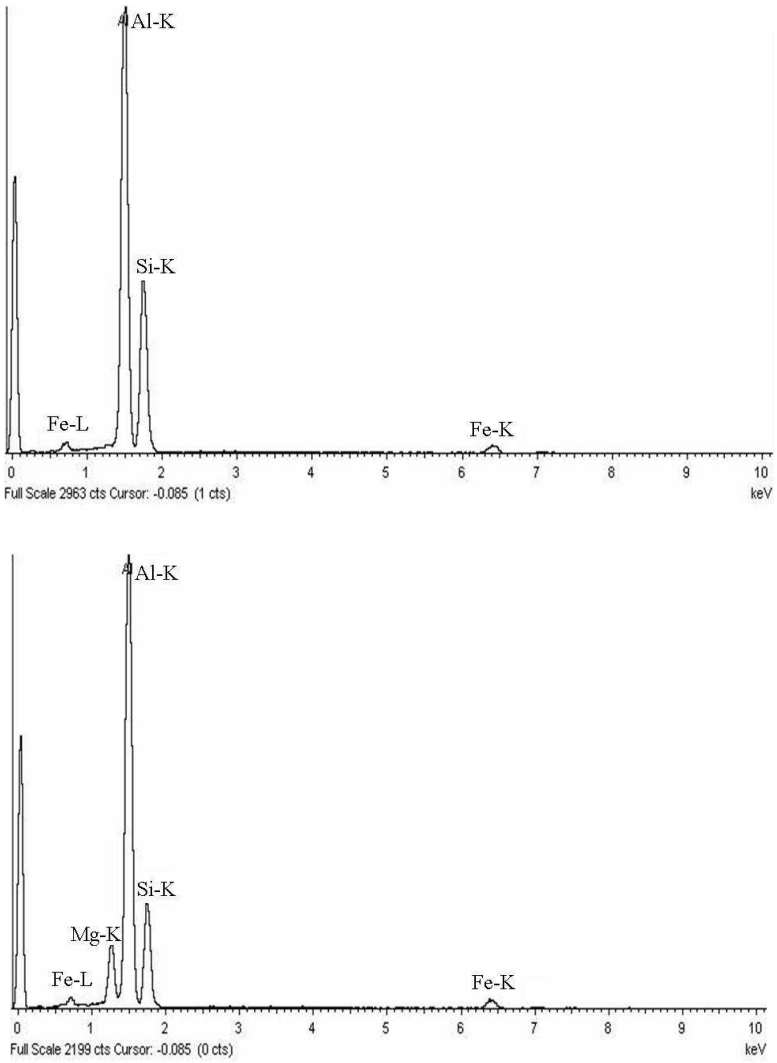

Figure 4.23(a): EDS spectrum for a β–Al_5FeSi-particle. Note the absence of a Mg-peak, (b) EDS spectrum for a π-particle. Note the presence of a Mg-peak.

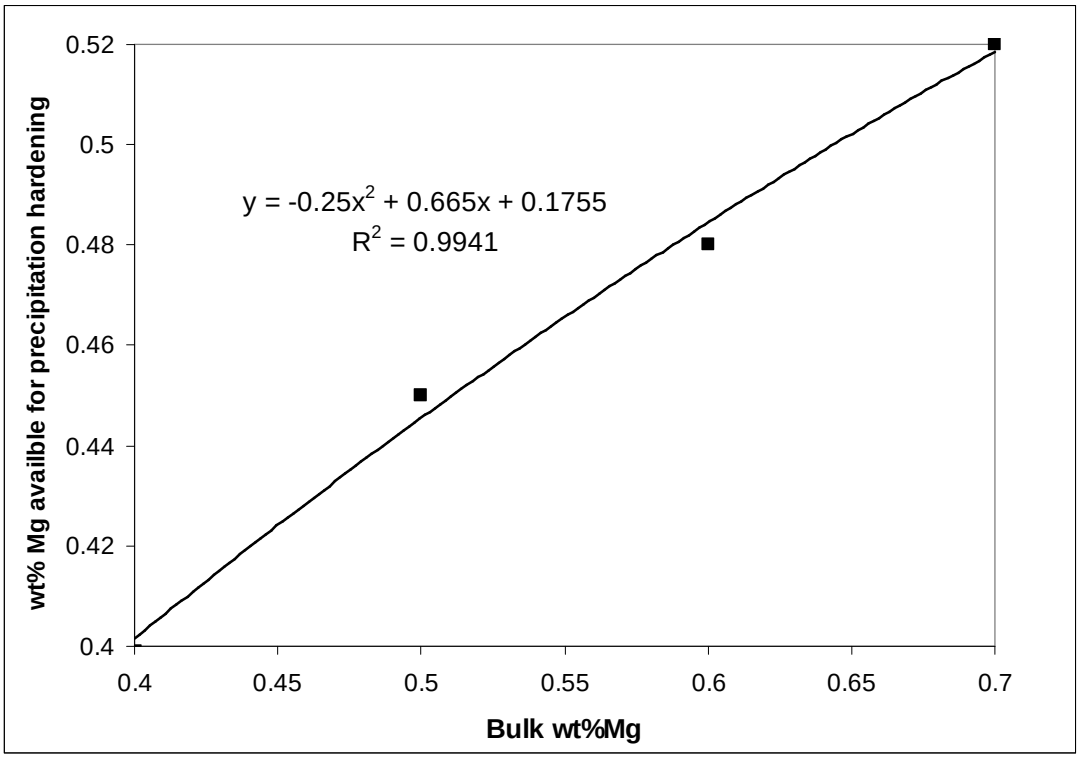

Figure 4.24: Estimation of Mg-content available for precipitation hardening for bulk Mg-contents of between 0.40 and 0.70% (Data points from Fig. 2.20 [48]).

The effects of Mg on the yield strength can be understood in terms of the age-hardening process. It is known [109] that the increment of the yield strength (ΔYS) is determined by the volume fraction (f) of shearable and non-shearable precipitates (eq. 4.6 - also see Chapter 6):

$$\Delta YS = \text{Constant} \times (f)^{1/2} \qquad (4.6)$$

Provided that all the Mg is available for precipitation hardening (i.e. calculated by equations 4.4 and 4.5 and converting from wt% to at% Mg), then ΔYS should be proportional to (at% Mg available for precipitation hardening)$^{1/2}$ – eq. 4.6 [109]. Therefore, taking the same YS data points in Fig. 4.20 and plotting it against (at% Mg available for precipitation hardening)$^{1/2}$, a linear relationship is obtained as shown in Fig. 4.25. Note that a good linear relationship is also found between YS and (at% Mg available for precipitation hardening) - i.e. not the square root of the at% Mg (Fig. 4.26) [HM8]. This occurs due to the fact that the mathematical function of $x^{1/2}$ vs x is almost linear in the composition range of x = 0.28-0.55at% Mg-available for

precipitation hardening in alloys A356/7 (Fig. 4.27). However, the YS-at%$Mg^{1/2}$ relationship in Fig. 4.25 is fundamentally the correct relationship.

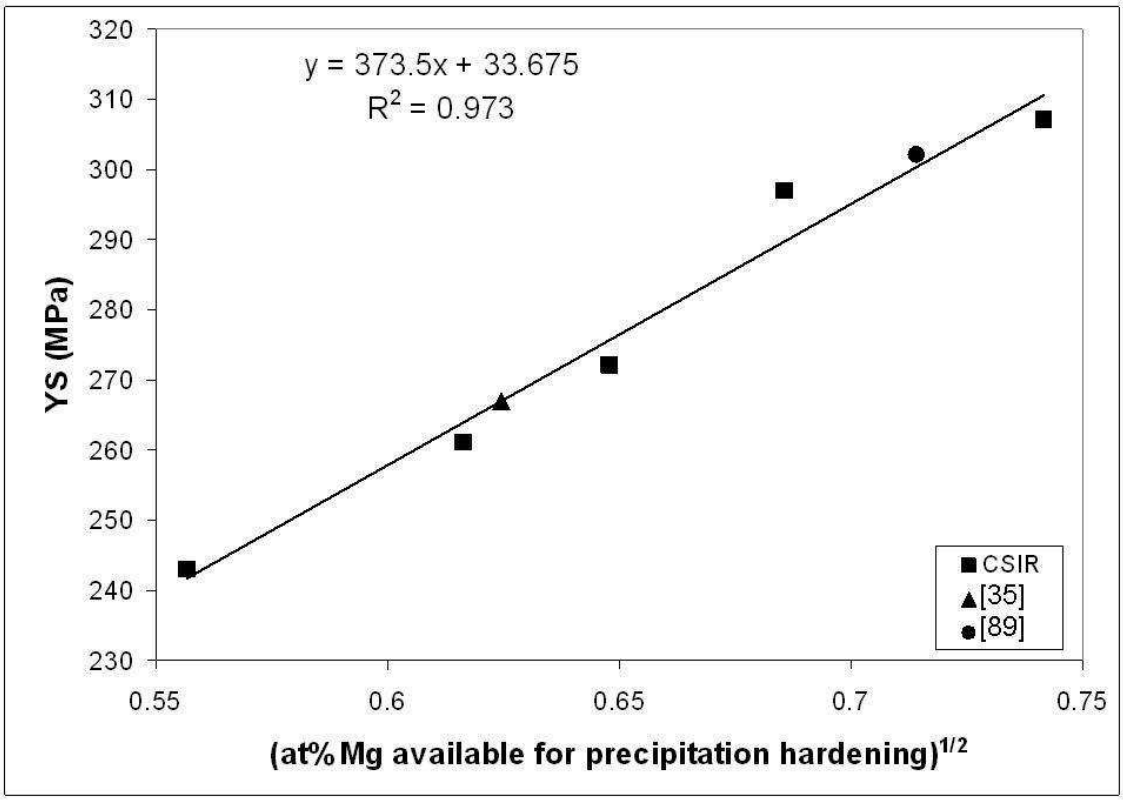

Figure 4.25: YS as a function of (at% Mg-concentration available for precipitation hardening)$^{1/2}$ for the traditional T6 heat treatment - same data points used as in Figure 4.20.

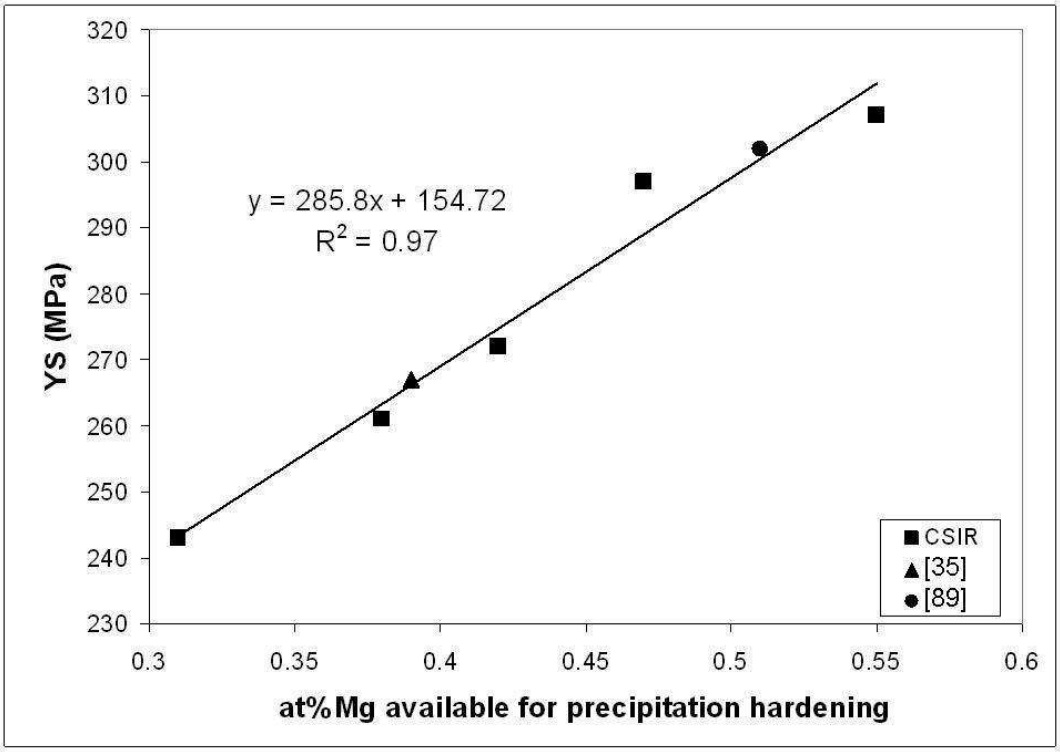

Figure 4.26: YS as a function of at% Mg-concentration available for precipitation hardening for the traditional T6 heat treatment - same data points used as in Figures 4.20 and 4.25.

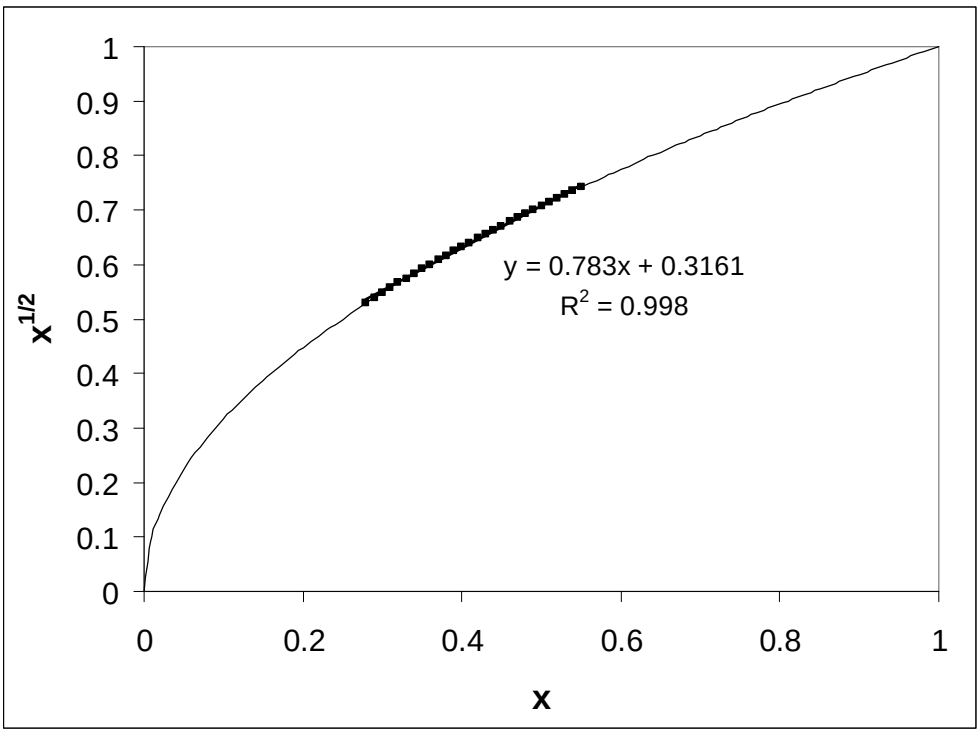

Figure 4.27: $(x)^{1/2}$ vs x mathematical function showing an almost linear relation in the typical range of x = 0.28-0.55at% Mg-available for precipitation hardening for alloys A356/7.

Figure 4.25 is applicable to the traditional T6 heat treatments. A similar approach was followed to determine if the Mg-content has a comparable effect on the CSIR heat treatment cycles (Figs. 4.28 to 4.33) [HM1]. The tensile properties of SSM-HPDC Al-7Si-Mg alloys with different Mg-contents in the CSIR heat treated T6 temper conditions are shown in Table 4.14.

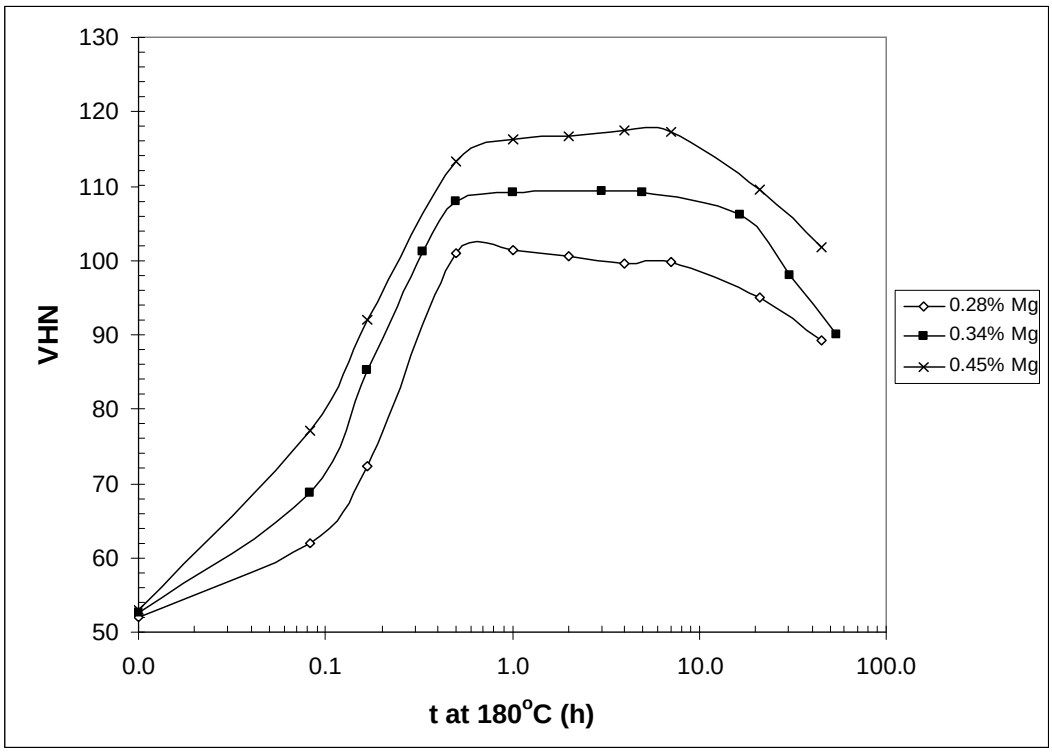

Figure 4.28: Artificial aging curves at 180°C for SSM-HPDC Al-7Si-Mg alloys after 0 h natural pre-aging.

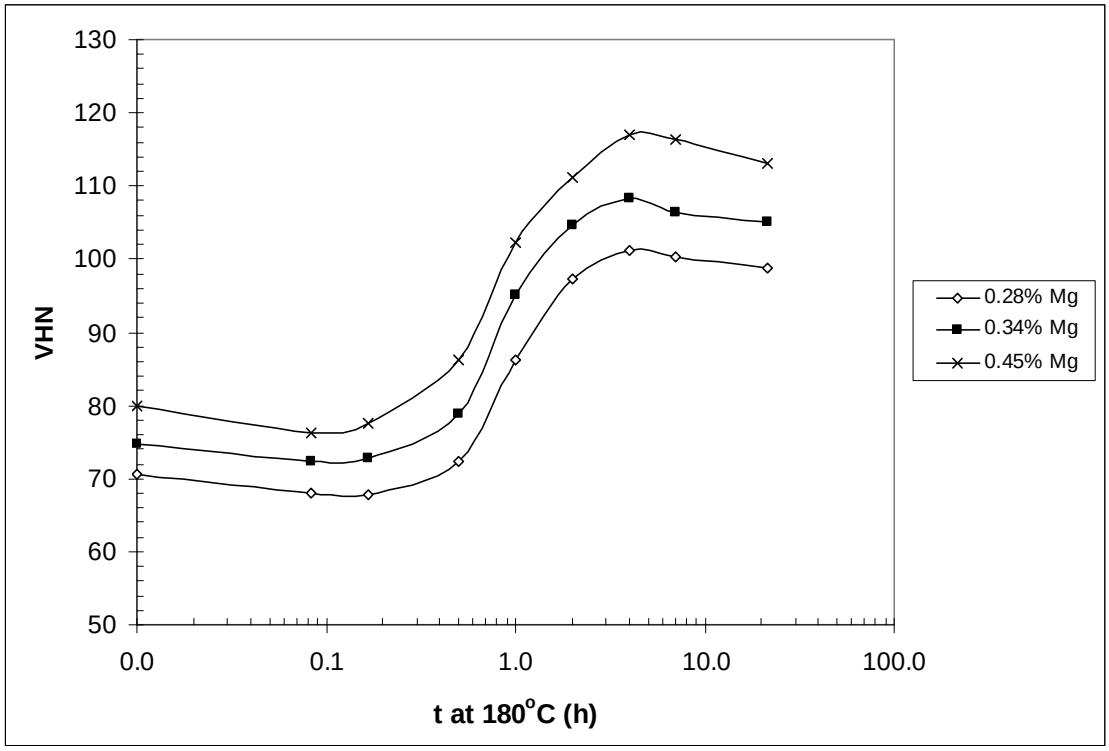

Figure 4.29: Artificial aging curves at 180°C for SSM-HPDC Al-7Si-Mg alloys after 20 h natural pre-aging.

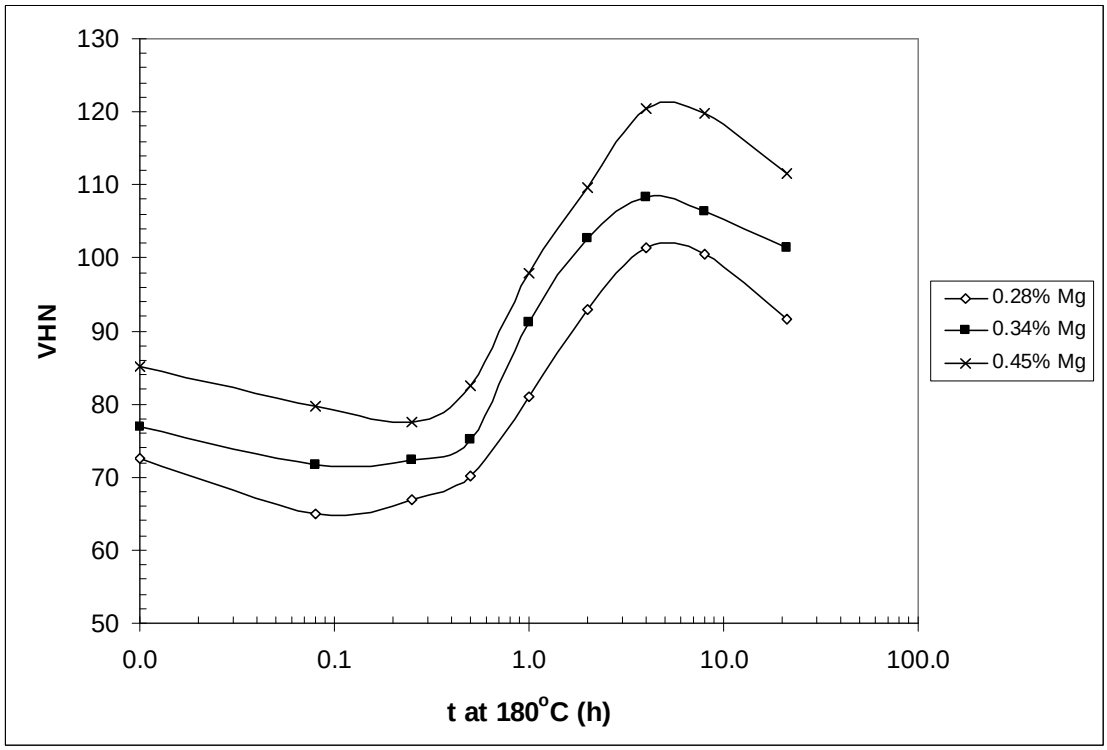

Figure 4.30: Artificial aging curves at 180°C for SSM-HPDC Al-7Si-Mg alloys after 120 h natural pre-aging.

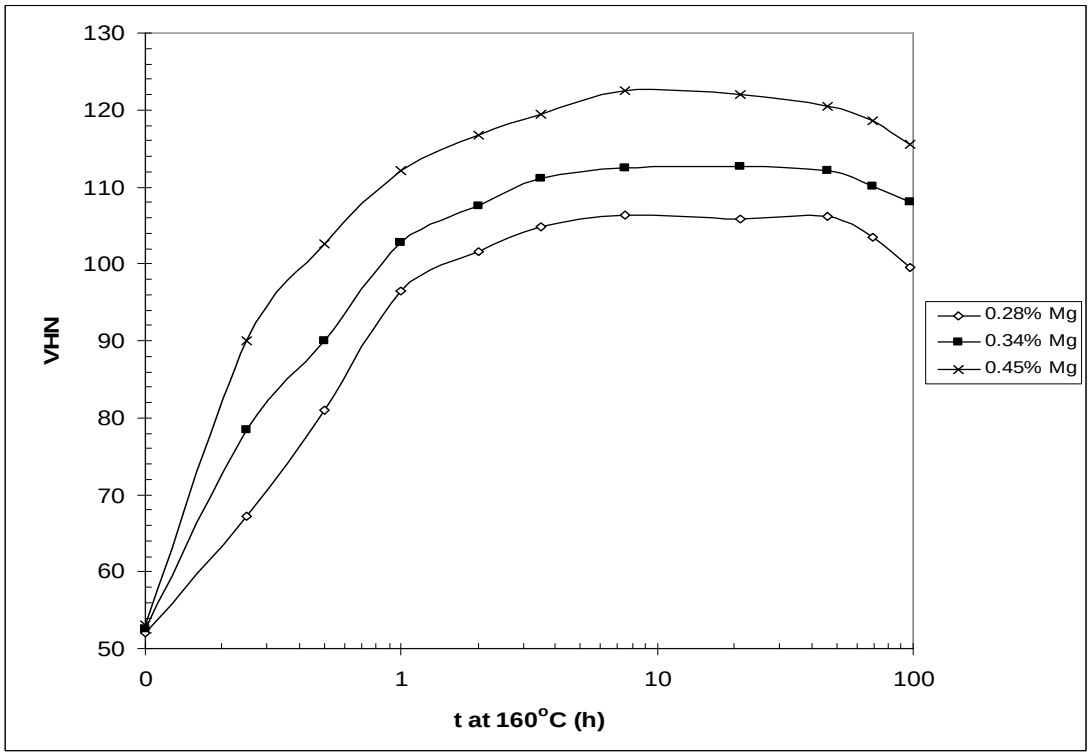

Figure 4.31: Artificial aging curves at 160°C for SSM-HPDC Al-7Si-Mg alloys after 0 h natural pre-aging.

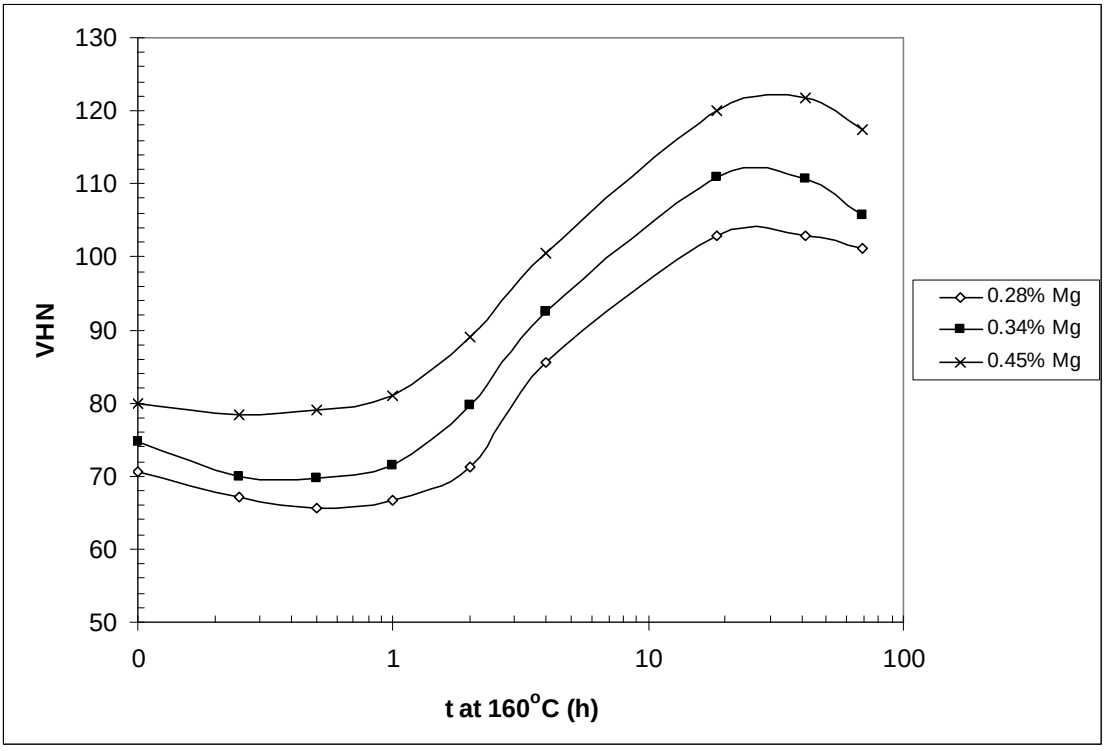

Figure 4.32: Artificial aging curves at 160°C for SSM-HPDC Al-7Si-Mg alloys after 20 h natural pre-aging.

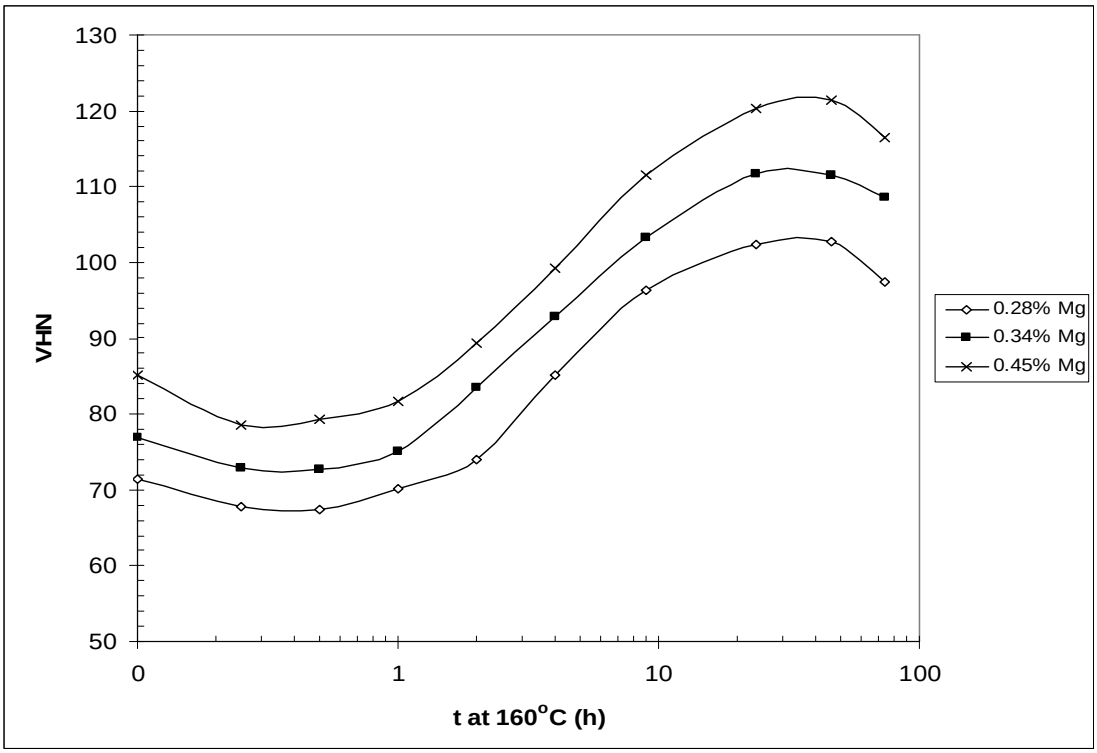

Figure 4.33: Artificial aging curves at 160°C for SSM-HPDC Al-7Si-Mg alloys after 120 h natural pre-aging.

Table 4.14: Yield strength (YS), UTS and % elongation after fracture of SSM-HPDC Al-7Si-Mg alloys (produced with the 50t HPDC machine) in the T6 temper condition (540°C-1h, {20-120}h NA, 180°C-4h). The standard deviation from five values for tensile properties is also indicated in brackets.

Mg-content (wt%)	Mg-content (at%)	YS (MPa)	UTS (MPa)	% Elongation
0.25	0.28	243 (1.4)	303 (1.5)	7.9 (0.7)
0.28	0.31	240 (2.8)	301 (3.1)	9.4 (0.9)
0.31	0.35	254 (6.1)	313 (7.3)	10.5 (0.9)
0.34	0.38	259 (5.2)	317 (7.1)	8.8 (1.4)
0.36	0.40	270 (5.5)	328 (5.8)	8.0 (2.2)
0.38	0.42	272 (5.1)	332 (4.4)	7.9 (1.5)
0.40	0.45	280 (5.2)	337 (6.0)	6.9 (1.8)
0.45	0.50	294 (5.8)	344 (3.1)	7.1 (1.4)
0.62	0.69	312 (4.1)	355 (3.9)	6.0 (1.3)

The data in Table 4.14 were processed in a similar manner to that in Fig. 4.25 to produce YS as a function of (at% Mg-concentration available for precipitation hardening)$^{1/2}$ for the short CSIR T6 heat treatment cycles (Fig. 4.34).

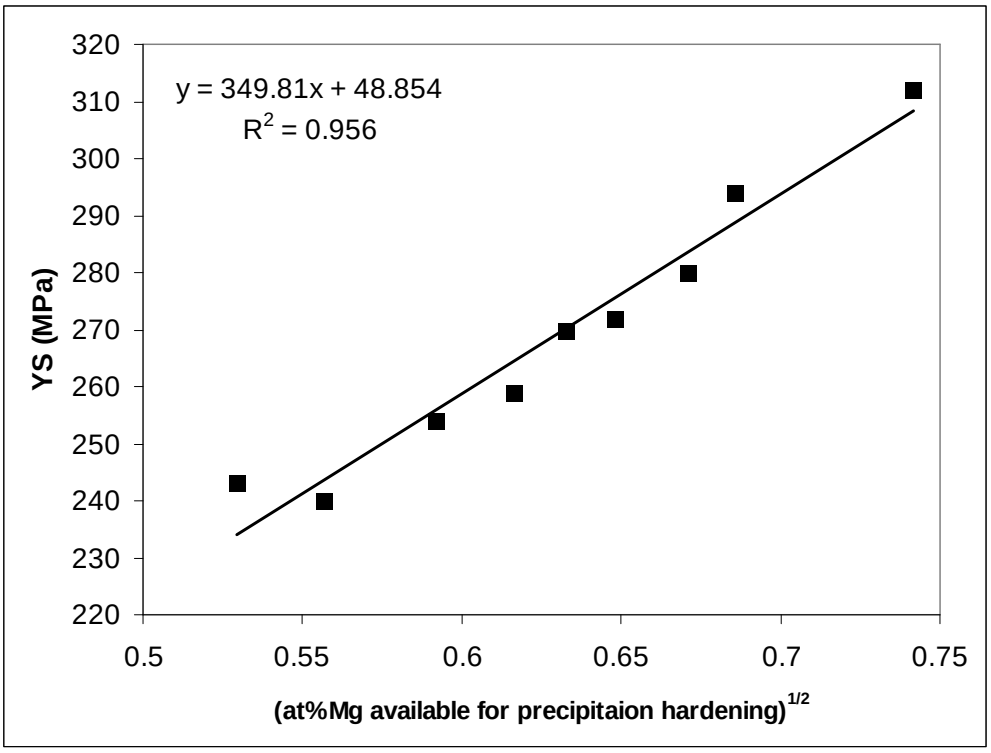

Figure 4.34: YS as a function of (at% Mg-concentration available for precipitation hardening)$^{1/2}$ for the short CSIR T6 heat treatment (540-1,{20-120}NA, 180-4).

As with Fig. 4.25, a reasonable linear relationship is also found in Fig. 4.34. Note that the data points in Figures 4.25 and 4.34 are only applicable for Al-7Si-Mg alloys containing ~ 0.1% Fe. Alloys with more than 0.1% Fe should result in the formation of more of the π-phase and vice versa.

The alloys with 0.62% Mg-0.10% Fe and 0.67% Mg-0.25% Fe in Table 3.1 were used to study the effects of Fe-levels above specification [HM9]. The calculated phase equilibria (minor phases) using Thermo-Calc for these two Al-alloys of alloy F357 are shown in Fig. 4.35. In this figure, the liquidus and solidus temperatures are indicated by arrows; "pi" refers to the π phase, "beta" is β–Al_5FeSi, and "alpha" is an Al-Mn-Fe-Si solid solution based on Al_8Fe_2Si. In all cases the major phases were liquid, Al-based FCC solid solution (the primary phase upon solidification), and Si (formed by

eutectic solidification). Comparing the two diagrams, it is seen that the predicted Mg_2Si content is slightly lower for the 0.62Mg-0.10Fe alloy than the 0.67Mg-0.25Fe alloy. This is to be expected, as the Mg-content of the former is lower than that of the latter. Based solely on the Mg-contents of the two alloys, the expectation is that the strength in the T6 temper of alloys from the 0.67Mg-0.25Fe alloy should be slightly higher (see the discussion on tensile properties later to see why this is not the case here – due to the effects of Fe). The higher Fe and Ni contents of the 0.67Mg-0.25Fe alloy lead to significantly higher predicted quantities of phases such as π-$Al_8FeMg_3Si_6$, β-Al_5FeSi and Al_9FeNi than for the 0.62Mg-0.10Fe alloy. Scanning electron microscopy (coupled with EDS to tentatively identify phases) was used to study the intermetallic phases in the T4 and T6 temper conditions (the intermetallics are similar in both temper conditions). Backscattered electron images of samples from both alloys are shown in Fig. 4.36. For the 0.62Mg-0.10Fe alloy (Fig. 4.36(a)), only β-Al_5FeSi and π-$Al_8FeMg_3Si_6$ could be identified in the eutectic (see typical EDS spectra in Fig. 4.37 for all qualitatively identified phases in the samples). However, for the 0.67Mg-0.25Fe alloy, apart from higher quantities of β-Al_5FeSi and π-$Al_8FeMg_3Si_6$, particles of Al_9FeNi could also be identified (Fig. 4.36(b) and Fig. 4.37(c)). Note that Si was also detected in the EDS of the Al_9FeNi particles. The maximum solubility of Si in this phase has been reported to be 4% [110]. The tensile properties of T4 and T6 heat treated samples were determined and the results are shown in Table 4.15.

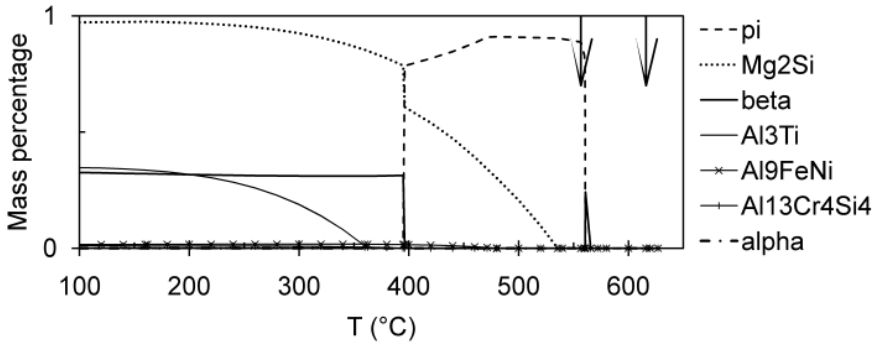

(a)

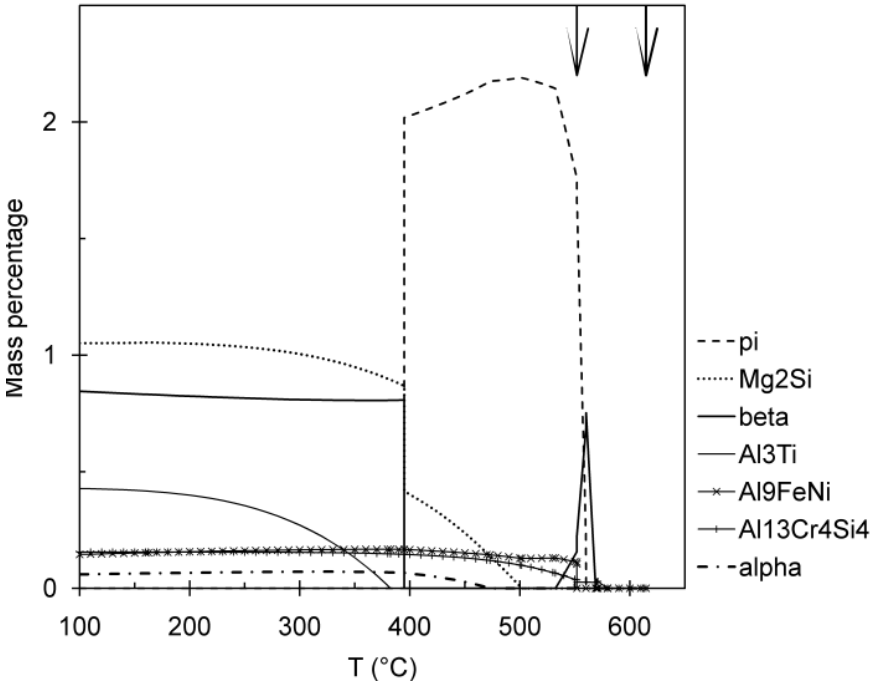

(b)

Figure 4.35: Calculated phase equilibria (minor phases) for Al alloys with compositions given in Table 3.1 corresponding to the (a) 0.62Mg-0.10Fe alloy and (b) 0.67Mg-0.25Fe alloy.

The expectation is that the 0.67Mg-0.25Fe should give higher strength than the 0.62Mg-0.10Fe alloy in both temper conditions based on Fig. 4.34. However, from Table 4.15 it can be seen that the strength (YS and UTS) of the two alloys are fairly similar. This can be related directly to the higher Fe-content of the 0.67Mg-0.25Fe alloy. The presence of high quantities of the Mg-containing π-phase in samples from this alloy (Fig. 4.36(b)) causes a reduction in the amount of magnesium in solid solution, which has a detrimental effect on the aging behaviour of samples from this

alloy. Note that the Mg-free particles such as β-Al_5FeSi and Al_9FeNi particles do not contribute to this effect.

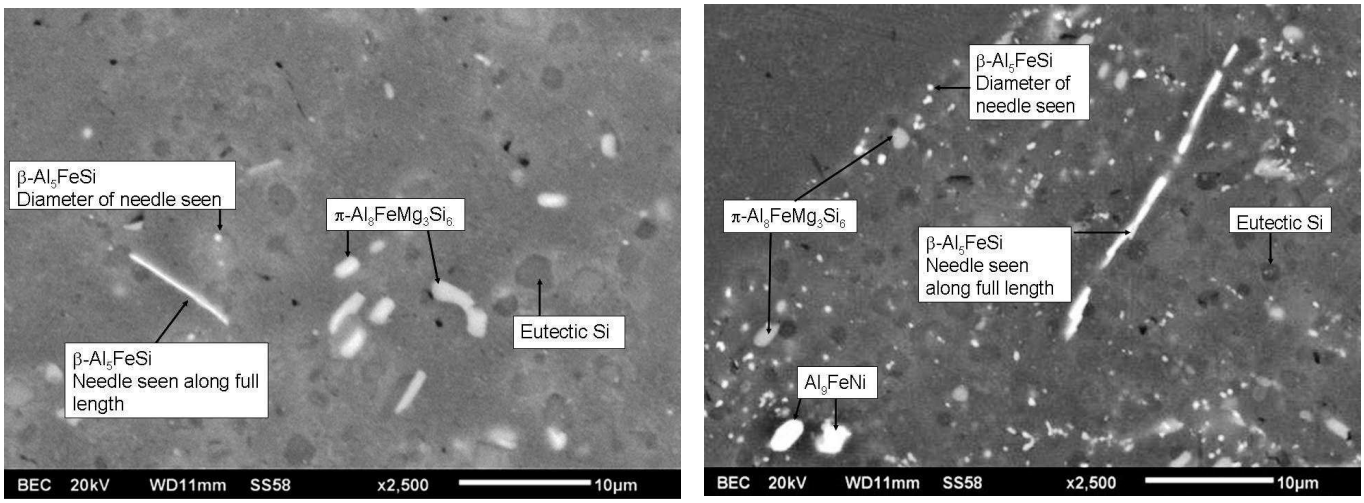

(a) **(b)**

Figure 4.36: Backscattered electron images of T6 samples of (a) 0.62Mg-0.10Fe alloy and (b) 0.67Mg-0.25Fe alloy.

Table 4.15: Yield strength (YS), ultimate tensile strength (UTS) and % elongation after fracture (%A) of T4 and T6 heat treated F357 samples. The standard deviation from five values for tensile properties is also indicated in brackets.

Alloy	YS (MPa)	UTS (MPa)	% A
T4 (540°C-1h, 120 h natural aging)			
0.62Mg-0.10Fe	172 (4.7)	297 (4.0)	17 (2.5)
0.67Mg-0.25Fe	169 (3.6)	285 (5.7)	8.2 (2.0)
T6 (540°C-1h, 20 h natural aging, 180°C-4h artificial aging)			
0.62Mg-0.10Fe	312 (4.1)	355 (3.9)	6.0 (1.3)
0.67Mg-0.25Fe	313 (2.2)	353 (5.0)	3.5 (0.64)

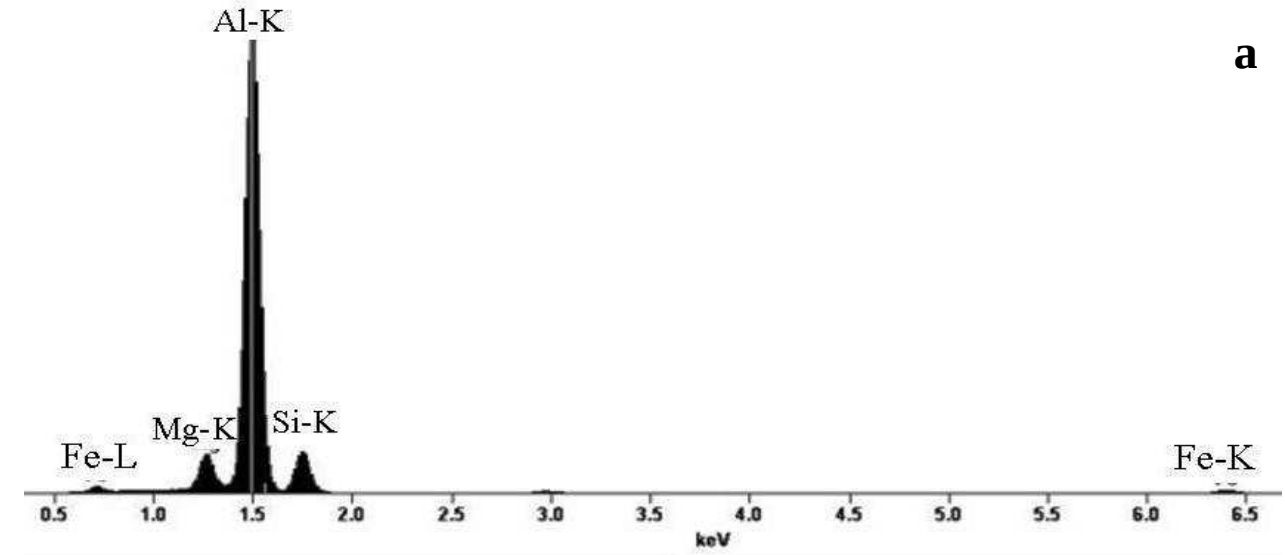
a
Al-K
Mg-K
Si-K
Fe-L
Fe-K
0.5 1.0 1.5 2.0 2.5 3.0 3.5 4.0 4.5 5.0 5.5 6.0 6.5
keV

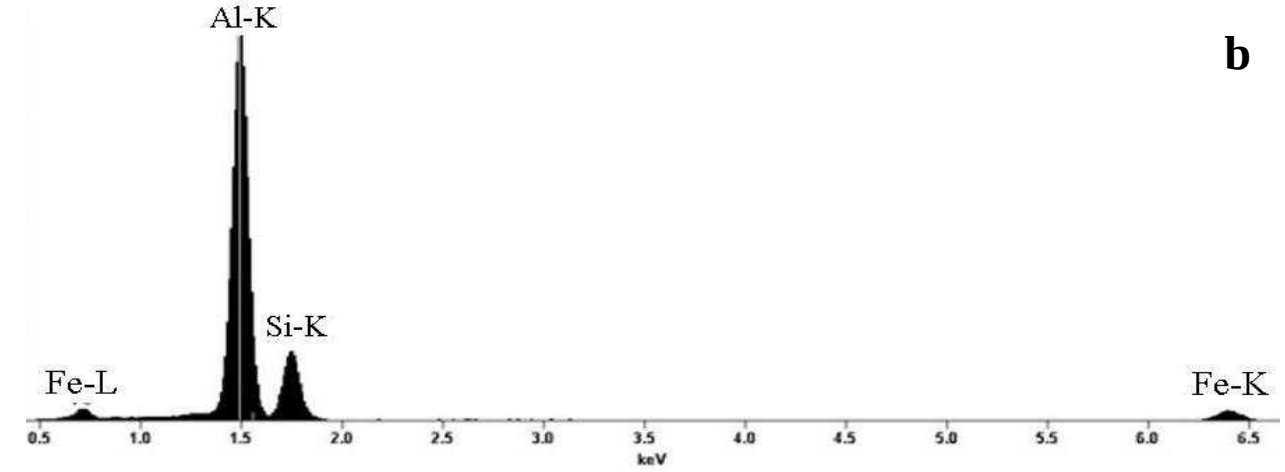
b
Al-K
Si-K
Fe-L
Fe-K
0.5 1.0 1.5 2.0 2.5 3.0 3.5 4.0 4.5 5.0 5.5 6.0 6.5
keV

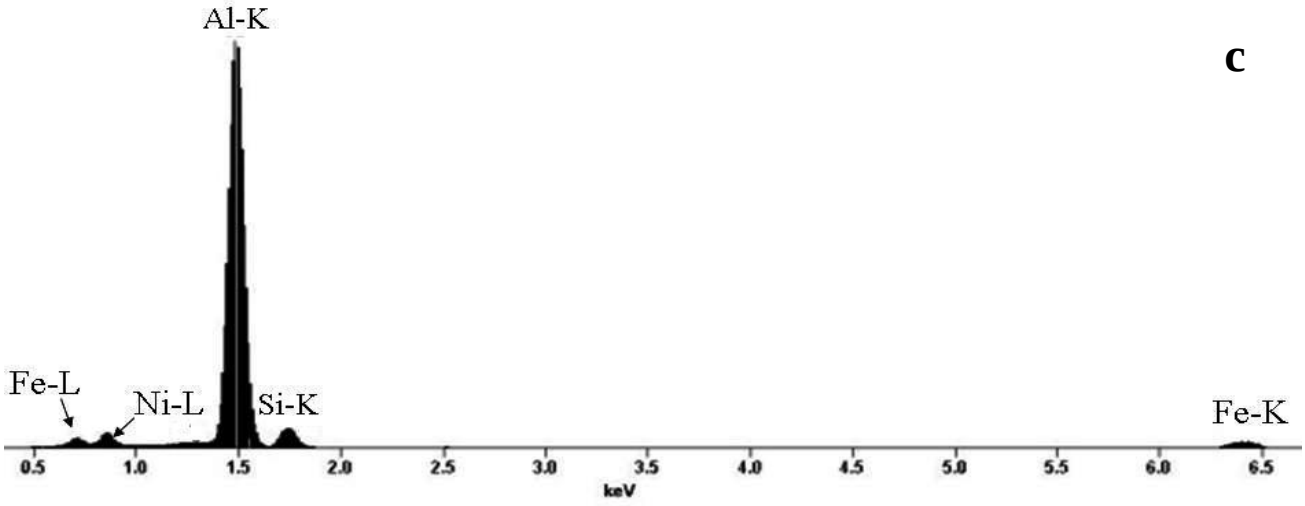
c
Al-K
Fe-L
Ni-L
Si-K
Fe-K
0.5 1.0 1.5 2.0 2.5 3.0 3.5 4.0 4.5 5.0 5.5 6.0 6.5
keV

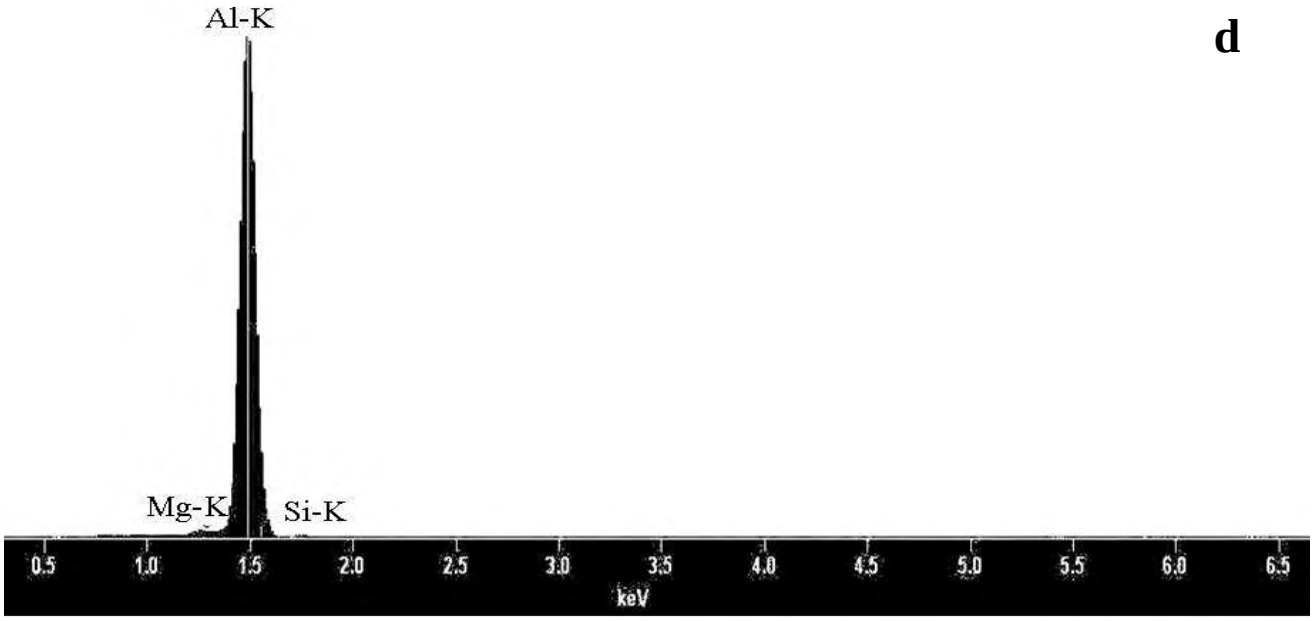

Figure 4.37: EDS spectra of qualitatively identified (a) π-$Al_8FeMg_3Si_6$, (b) β-Al_5FeSi (note the absence of a Mg-peak) and (c) Al_9FeNi particles (note the presence of a Ni-peak). The EDS spectrum in (d) is of a primary α-Al grain from a T4 sample as reference.

Even though the YS and UTS of the two alloys are fairly similar, the ductilities differ significantly (Table 4.15). The % elongation of samples from the 0.67Mg-0.25Fe is considerably lower in both temper conditions. Figure 4.38 shows a backscattered electron image of a sample from the 0.67Mg-0.25Fe alloy in the T6 condition after tensile testing. The fracture occurred to the right of the image and part of the fracture surface can be seen. Micro-cracking of the intermetallics can clearly be seen. Taylor and co-workers [48] also reasoned that any increase in the amount of hard, brittle π-intermetallics would lead to a decrease in elongation to fracture values in this alloy system.

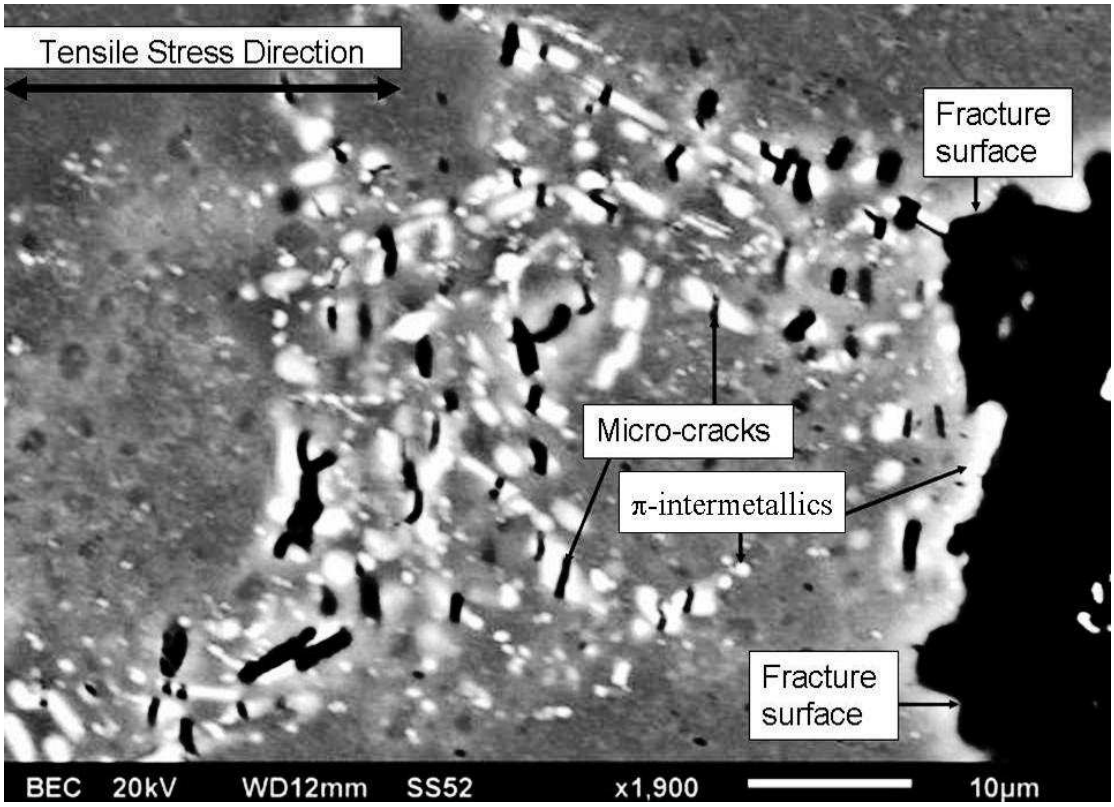

Figure 4.38: Backscattered electron image of T6 sample of the 0.67Mg-0.25Fe after tensile testing showing the fracture surface on the right, as well as micro-cracking of the π-intermetallics.

Another effect of the intermetallics in this alloy system (which was not studied in this work) is their influence on corrosion properties. Yang and co-workers [34] showed that intermetallic compounds play a major role in the pit initiation process of Al–7Si–Mg alloys. Micro-galvanic cells are produced, leading to corrosion attack along the interface between the intermetallic compounds and the aluminium alloy matrix. The 0.67Mg-0.25Fe alloy is therefore expected to have inferior corrosion resistance compared to the 0.62Mg-0.10Fe alloy.

4.7. Artificial aging and the T5 temper

The T5 temper is achieved by artificially aging as-cast material without a solution treatment (as opposed to the T4 and T6 temper conditions where a solution heat treatment is used).

Variables that affect the T5 properties are the cooling rate after casting (air or AQ and water or WQ), the natural aging period after quenching and the artificial aging

temperature and time. The tensile properties of differently T5-treated SSM-HPDC alloy F357 (with 0.63% Mg) are compared in Table 4.16 [HM6]. As expected, higher tensile properties are obtained by water quenching the alloy after SSM-HPDC rather than cooling in air. Also, it can be seen from Table 4.16 that there is a significant difference in tensile properties between the as-cast material that was cooled in air [F357-F(AQ)] and the F357-T5(AQ) sample. This implies that most of the elements are actually placed in solution during cooling with SSM-HPDC, rather than with the quench after SSM-HPDC. It has been shown that the solidification rate during HPDC is relatively high (Fig. 4.4).

Table 4.16: Yield strength (YS), ultimate tensile strength (UTS) and % elongation after fracture (%A) of SSM-HPDC F357 with 0.63% Mg. The standard deviation from 12 values for tensile properties is also indicated in brackets.

Quench after SSM-HPDC	Natural Aging (NA)	Artificial aging (AA)	YS (MPa)	UTS (MPa)	% A
Air (AQ)	25°C-120 h	-	117 (2.2)	229 (4.9)	9.9 (1.7)
Water (WQ)	25°C-120 h	-	124 (2.7)	241 (6.1)	9.4 (1.7)
Air (AQ)	25°C-120 h	180°C-4 h	170 (9.9)	256 (10.9)	7.2 (1.5)
Water (WQ)	-	180°C-4 h	186 (3.6)	273 (3.8)	6.6 (1.1)
Water (WQ)	25°C-120 h	180°C-4 h	188 (1.9)	278 (4.9)	6.4 (1.0)
Water (WQ)	25°C-120 h	160°C-28 h	205 (3.1)	290 (4.9)	6.1 (1.3)

Differences in the morphology of β-Mg_2Si in the F(AQ) and F(WQ) can be observed using backscattered electron imaging (Fig. 4.39(a,b)). The β-Mg_2Si is significantly coarser in the F(AQ) samples than in the F(WQ) samples, which corresponds to a slower cooling rate to room temperature in the former sample.

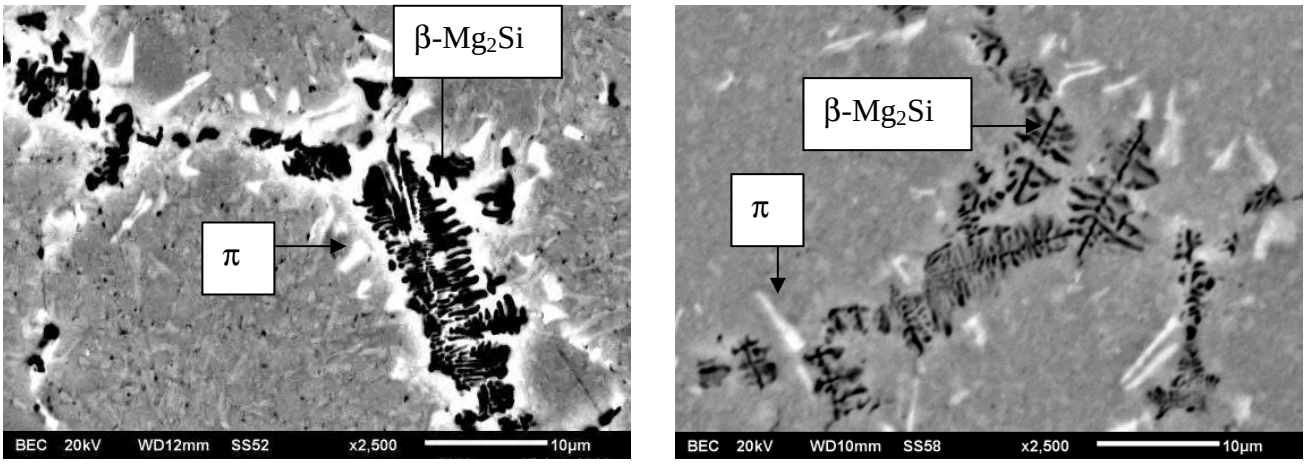

(a) **(b)**

Figure 4.39: Backscattered electron images (BEI) of SSM-HPDC F357 in (a) F(AQ) and (b) F(WQ) conditions.

Figure 4.39 indicates that significant quantities of undissolved β-Mg_2Si are in the F and T5 temper condition samples. The solution treatment of the T4 and T6 temper conditions dissolves the β-Mg_2Si phase and the supersaturation of solute is significantly higher. The artificial aging response for the T6 temper (e.g. Fig 4.18) is therefore considerably more pronounced than for the T5 temper (Fig. 4.40).

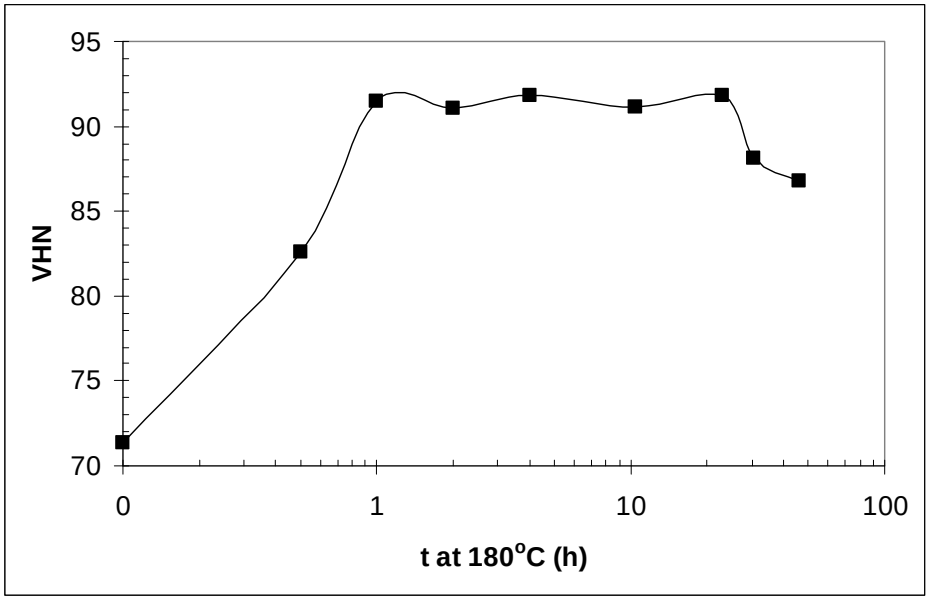

Figure 4.40: T5-artificial aging curve of an SSM-HPDC F357 plate (with 0.63wt% Mg) that was water quenched after casting, naturally aged for 120 h and artificially aged at 180°C.

Natural aging after the quench (0 or 120 h) does not have a meaningful influence on the T5 properties (Table 4.16), but, as already mentioned before, an artificial aging treatment of 180°C for 4 h also resulted in removing the effects of natural pre-aging in the T6 treated alloys (Fig. 4.18). Finally, as with the T6 temper (Fig. 4.17), a lower artificial aging temperature (160 vs 180°C) results in better mechanical properties. Unfortunately, due to the lower diffusion rates at 160°C, the time to attain these properties is reached after much longer times than with artificial aging at 180°C (Table 4.16).

4.8. Comparison between different temper conditions

The properties of SSM-HPDC Al-7Si-Mg alloys in different temper conditions were compared using the alloy with 0.38% Mg in Table 3.1 [HM7]. To make comparisons, solution treatment (for T4 and T6) was performed at 540°C for 1 hour, followed by a water quench (25°C). The T6 treated samples were then naturally aged for 20 hours, before artificial aging for 4 h at 180°C. The T4 treated samples were allowed to naturally age (at 25°C) for at least 120 h. The samples used for the T5 temper condition were quenched in water after SSM-HPDC and naturally aged for 120 h before artificial aging at 180°C for 4 h. Optical micrographs of SSM-HPDC A356 are shown in Figure 4.41 for the as-cast condition or F temper (Fig. 4.41(a)), T4 temper (Fig. 4.41(b)), T5 temper (Fig. 4.41(c)) and the T6 temper (Fig. 4.41(d)). The average Vickers microhardness values (50 g load) of the α-Al and eutectic in all the temper conditions are also shown in Figure 4.41. Heat treatment to the T4, T5 and T6 temper conditions results in an increase in the hardness of the primary α-Al grains and the eutectic regions relative to the A356-F condition. The increase of the hardness of the eutectic component with aging suggests that precipitation hardening also occurs within the α-Al phase of the eutectic. The fibrous silicon particles in A356-F are spheroidised by the solution treatment applied on A356-T4 (Fig. 4.41(b)) and A356-T6 (Fig. 4.41(d)). For A356-T5, no solution treatment is used, and it is seen from Figure 4.41(c) that the artificial aging temperature is too low to cause any spheroidisation of the eutectic silicon particles.

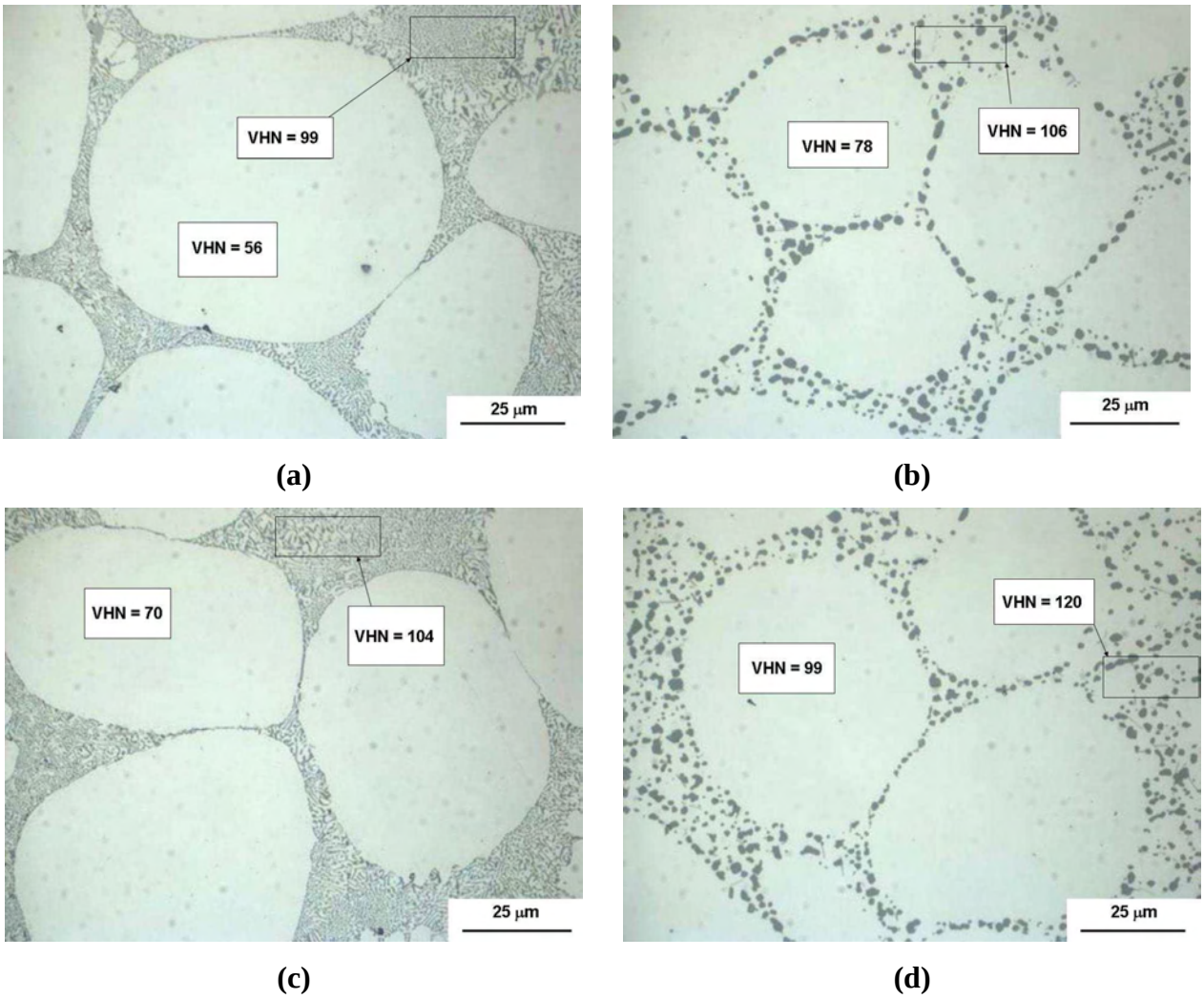

Figure 4.41: Optical micrographs of SSM-HPDC A356 in the (a) F, (b) T4, (c) T5 and (d) T6 temper conditions.

The macrohardness (Fig. 4.42) and tensile properties of this alloy in different temper conditions are shown in Table 4.17. The importance of the solution treatment in dissolving all the solutes for precipitation hardening during artificial aging can clearly be seen by comparing the lower tensile properties of A356-T5 with those of A356-T6. On the other hand, the beneficial effect of artificial aging after solution treatment (A356-T6) rather than natural aging (A356-T4) is also evident. The Quality Index (QI) for SSM-HPDC alloy A356 in different temper conditions is shown in Table 4.17. It is seen that the high ductility of A356-T4 and high strength of A356-T6 result in high QI values for these two temper conditions.

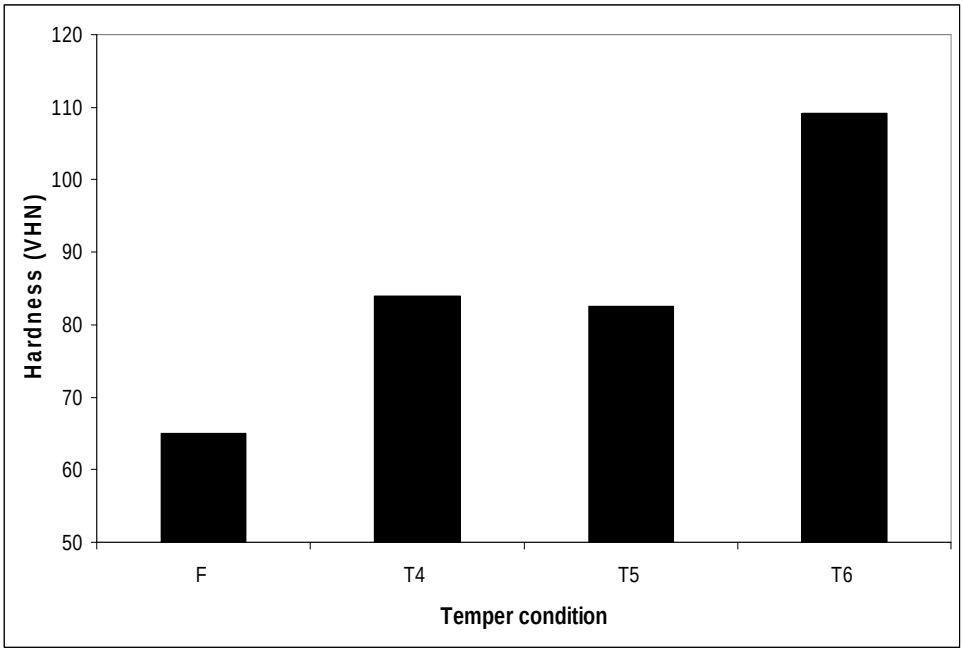

Figure 4.42: Vickers macrohardness (20 kg) of SSM-HPDC A356 in different temper conditions.

Table 4.17: Yield strength (YS), ultimate tensile strength (UTS), % elongation after fracture and Quality Index (QI) of heat treated A356 samples with 0.38% Mg. The standard deviation for tensile properties (from 5 samples/temper condition) is also indicated in brackets.

Temper	YS (MPa)	UTS (MPa)	% Elongation	QI (MPa)
F	113 (3.0)	218 (2.5)	10.6 (1.6)	372 (10.6)
T4	152 (2.1)	268 (3.9)	14.5 (1.4)	442 (7.2)
T5	168 (2.2)	258 (4.0)	8.4 (0.9)	396 (10.2)
T6	272 (5.1)	332 (4.4)	7.9 (1.5)	466 (12.7)

The drop weight impact energies for A356 in different temper conditions are shown in Figure 4.43. Alloy strength (Fig. 4.13) and silicon morphology have the largest effects on the impact properties of this material. The influence of strength of the alloys on the impact properties can be determined by comparing temper conditions in which the silicon morphologies are similar. In both A356-T4 and A356-T6, spheroidised silicon is found. However, the impact strength of the material is slightly higher for A356-T4 than A356-T6. This difference can be related to the lower strength (hardness) of the material in the T4 condition compared to the T6 condition.

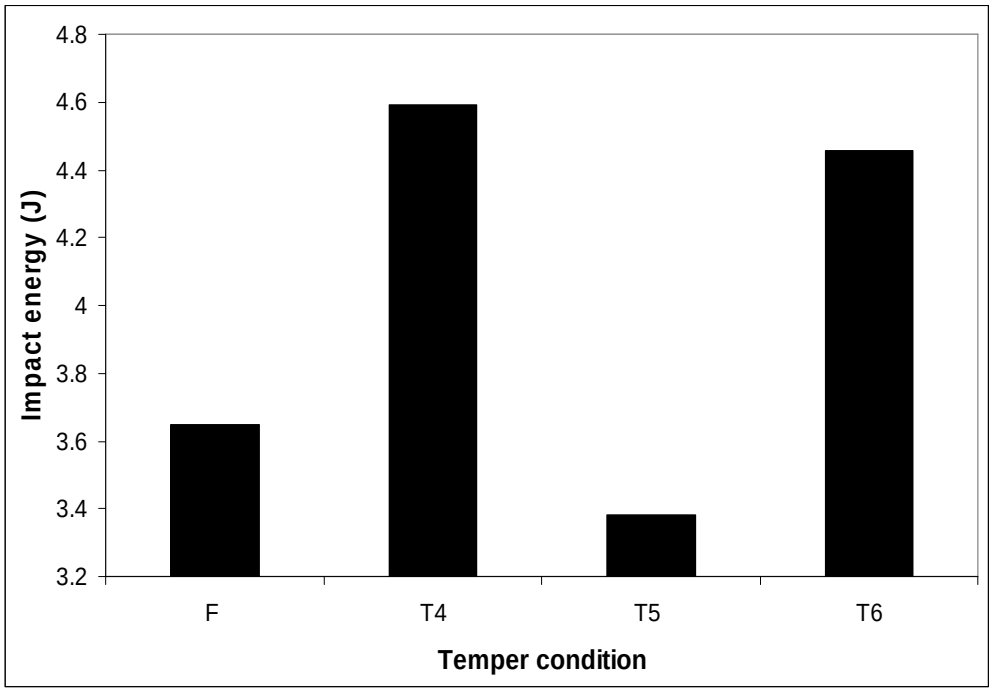

Figure 4.43: Drop weight impact energies for SSM-HPDC A356.

In both A356-F and A356-T5, fibrous silicon is found. Again, the impact strength of the material is slightly higher for the lower strength (hardness) A356-F than A356-T5. The influence of silicon morphology on the impact properties can be determined by comparing temper conditions in which the silicon morphologies are different (and considering the differences in strength too). The impact strength of A356-F and A356-T5 (with fibrous Si) is significantly lower than that of A356-T4 and A356-T6 (with spheroidised Si). The tips of fibrous silicon particles most likely act as stress concentrators causing much lower impact strengths than when the silicon particles are spheroidised.

The impact load as a function of time was measured and is presented in Figure 4.44. The first peak (maximum load) in Figure 4.44 corresponds to crack initiation, whereas the rest of the curve corresponds to crack propagation. The total time to complete fracture (time-to-zero-load in Figure 4.44) is longer for T4 compared to T6 and F compared to T5. This confirms that crack propagation occurs more rapidly in the harder materials.

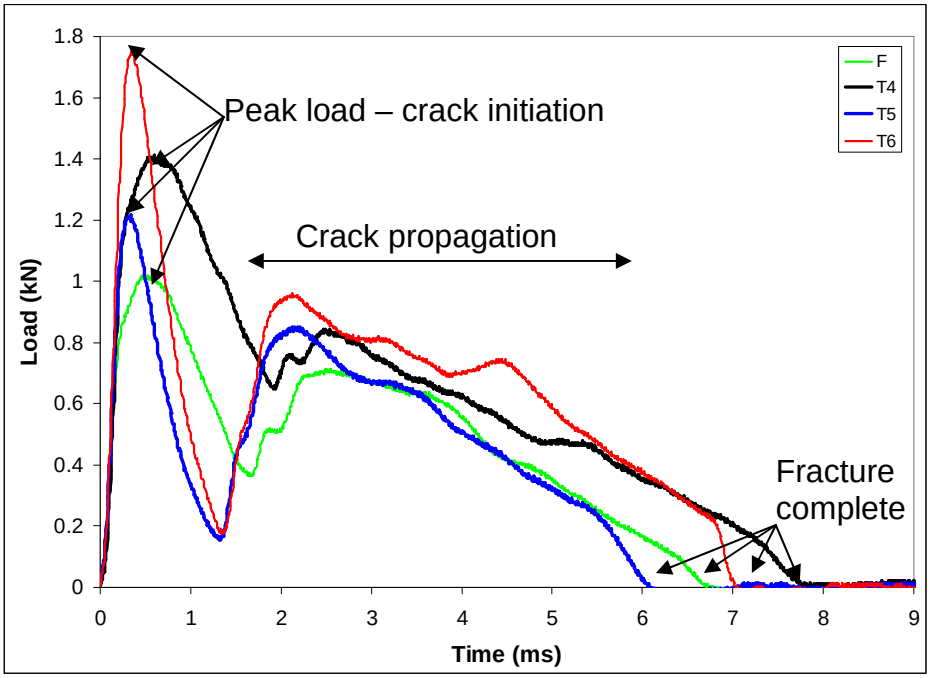

Figure 4.44: Impact load as a function of time during drop weight testing of SSM-HPDC A356.

The impact load as a function of deflection is shown in Figure 4.45. The total energy (in Figure 4.43) is the area beneath this load vs deflection curve.

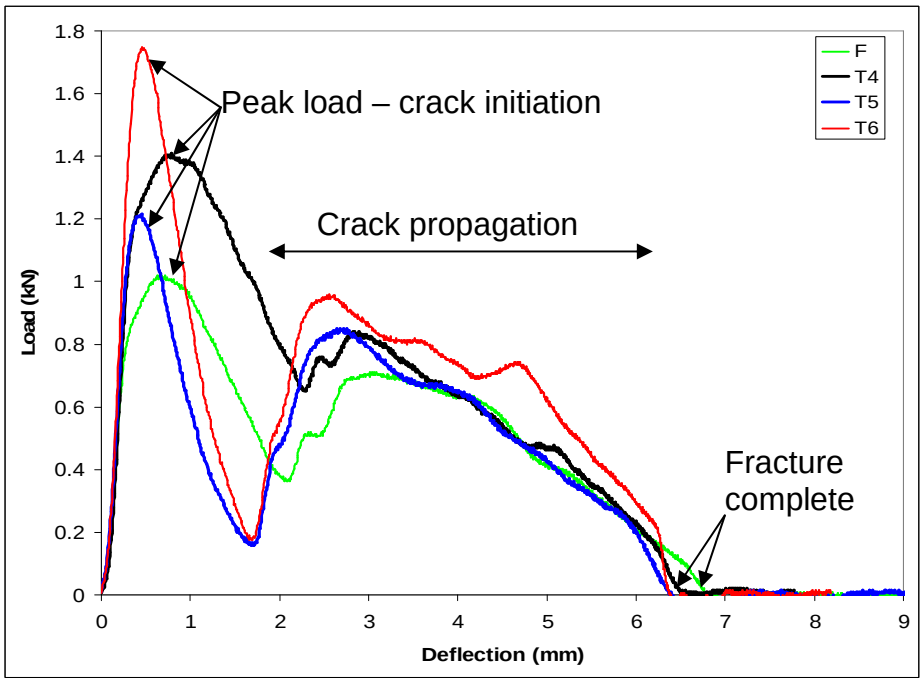

Figure 4.45: Impact load as a function of deflection during drop weight testing of SSM-HPDC A356.

The impact energy as a function of time is shown in Figure 4.46. The narrow peak widths of the T5 and T6 temper conditions (Figures 4.44 and 4.45) result in the inflection points at around 1.5 ms in Figure 4.46.

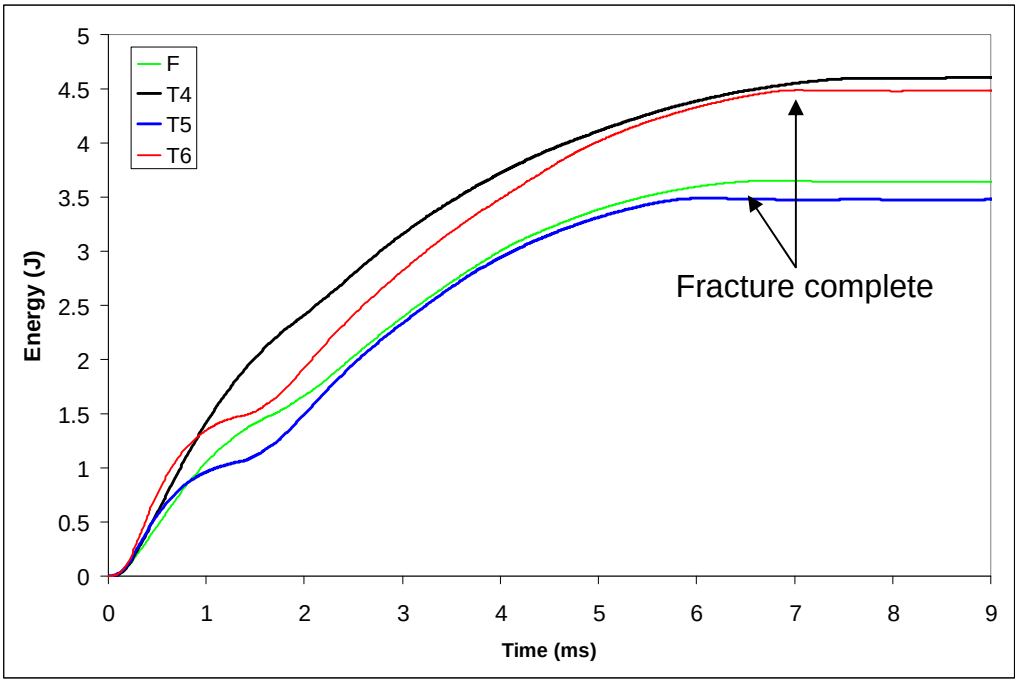

Figure 4.46: Impact energy as a function of time during drop weight testing of SSM-HPDC A356 – fracture is complete once the lines become horizontal.

The peak load value (Figure 4.47) for the T6 condition is higher than for the T4 condition, but the width of the peak is narrower. This is most likely due to the higher strength (hardness) of the T6 material, requiring a higher impact load to initiate the crack. However, after crack initiation, its propagation is much easier through the harder material, causing the narrow peak width compared to the softer T4 material. A similar mechanism is operative when comparing the T5 and F (both with fibrous silicon) temper conditions.

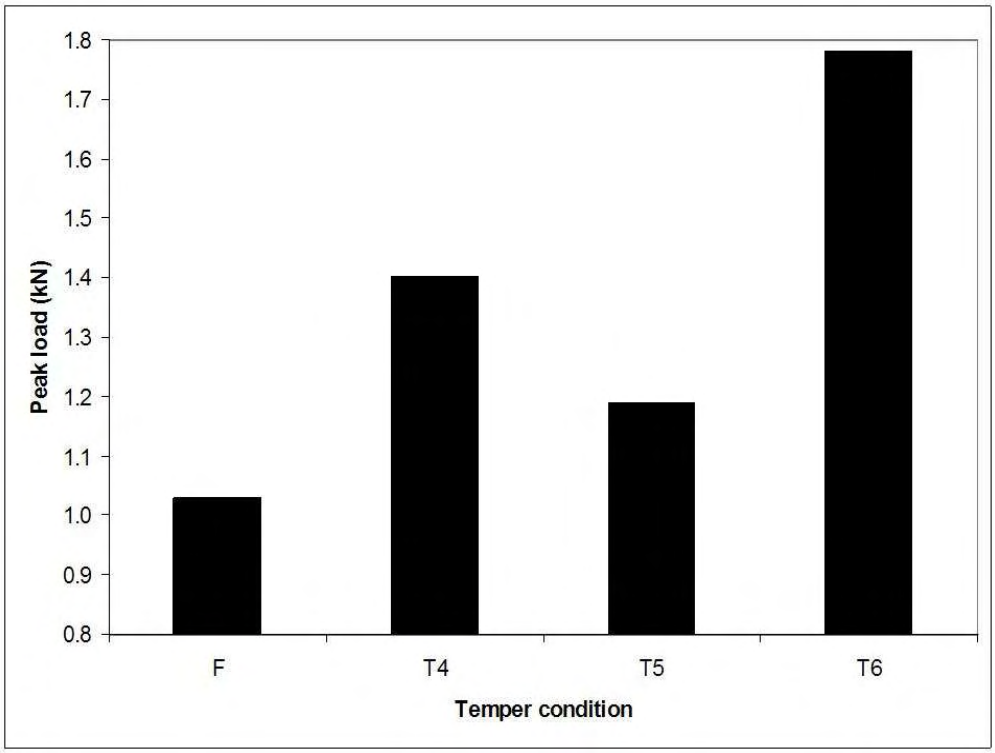

Figure 4.47: Peak load measured during drop weight testing of SSM-HPDC A356.

The cross-section of the fracture surfaces of the tensile and impact tested samples were studied using optical microscopy. It was found that the fracture paths for the different tests in the different temper conditions were similar and, therefore, only the results of A356-T6 are presented. Figure 4.48(a) shows that the crack propagates preferentially through the eutectic regions and not through the softer α-Al globules. Figure 4.48(b) shows a higher magnification micrograph where the fracture completely bypassed an α-Al grain.

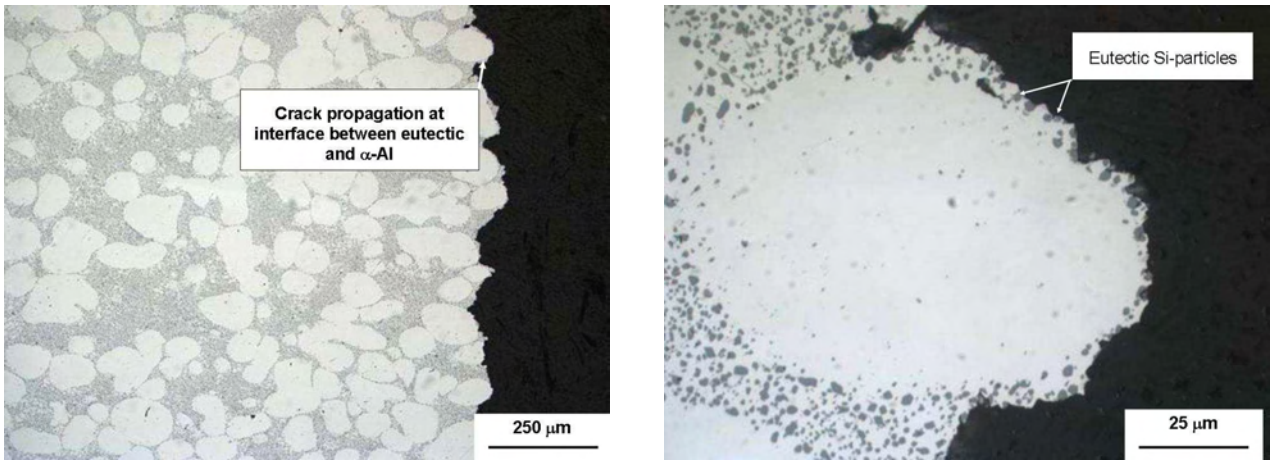

(a) **(b)**

Figure 4.48(a): Fracture path in SSM-HPDC A356-T6 tensile specimen (cross-section of tensile fracture surface) and (b) higher magnification micrograph showing fracture bypassing primary α-Al grain.

Quality Index values of SSM-HPDC A356 (with 0.38% Mg) and F357 (with 0.63% Mg) in different temper conditions are compared in Fig. 4.49. The QI values are higher for alloy F357 than A356 in all the temper conditions. This is due to the higher strengths that can be obtained using the higher Mg-containing alloy F357. The QI values are, however, only marginally higher than for A356. This can be related to the lower ductility achieved for alloy F357 compared to A356 (due, in part, to the higher strength of F357 compared with A356, but also due to the presence of the π-phase in alloy F357 which causes a reduction in ductility).

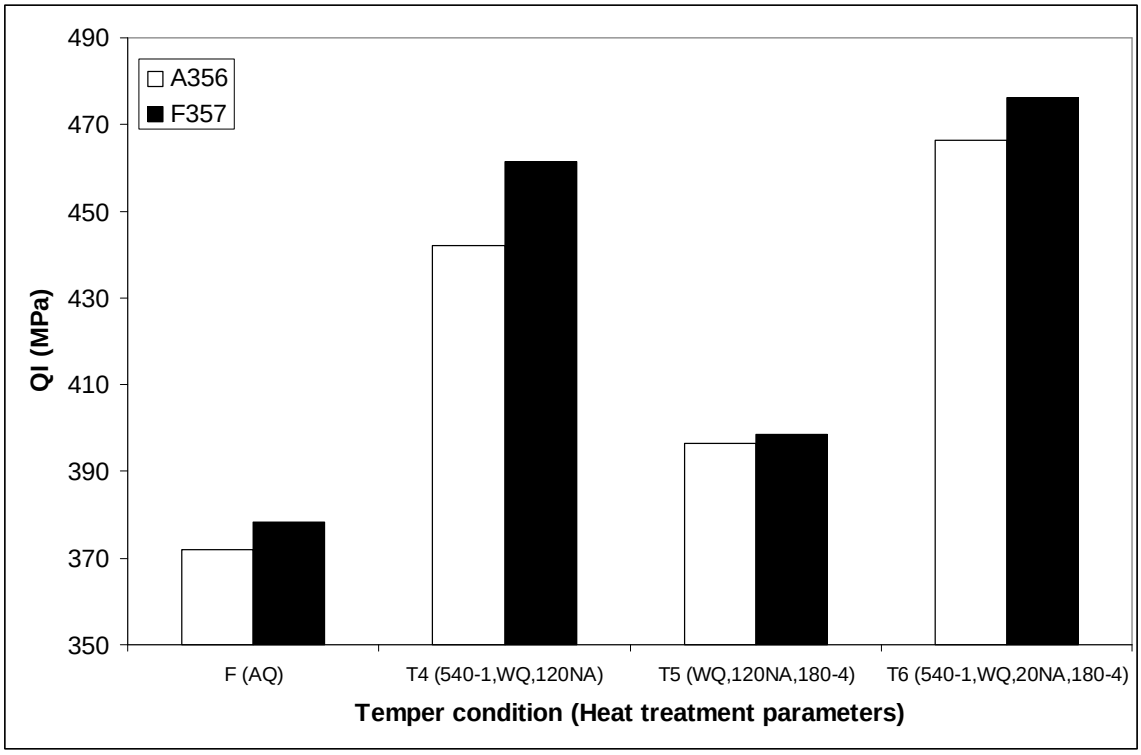

Figure 4.49: Quality index (QI) values for SSM-HPDC Al-7Si-Mg alloys in different temper conditions.

4.9. Surface liquid segregation in SSM-HPDC castings

The surface liquid segregation (SLS) phenomenon in SSM-HPDC castings was studied by using plates with 0.36% Mg in Table 3.1 [HM5]. Chemical analysis depth profiles of the main alloying elements determined using OES, are shown in Figure 4.50. Two regions on the plate were investigated, close to the top of the plate and close to the gate (Fig. 4.51).

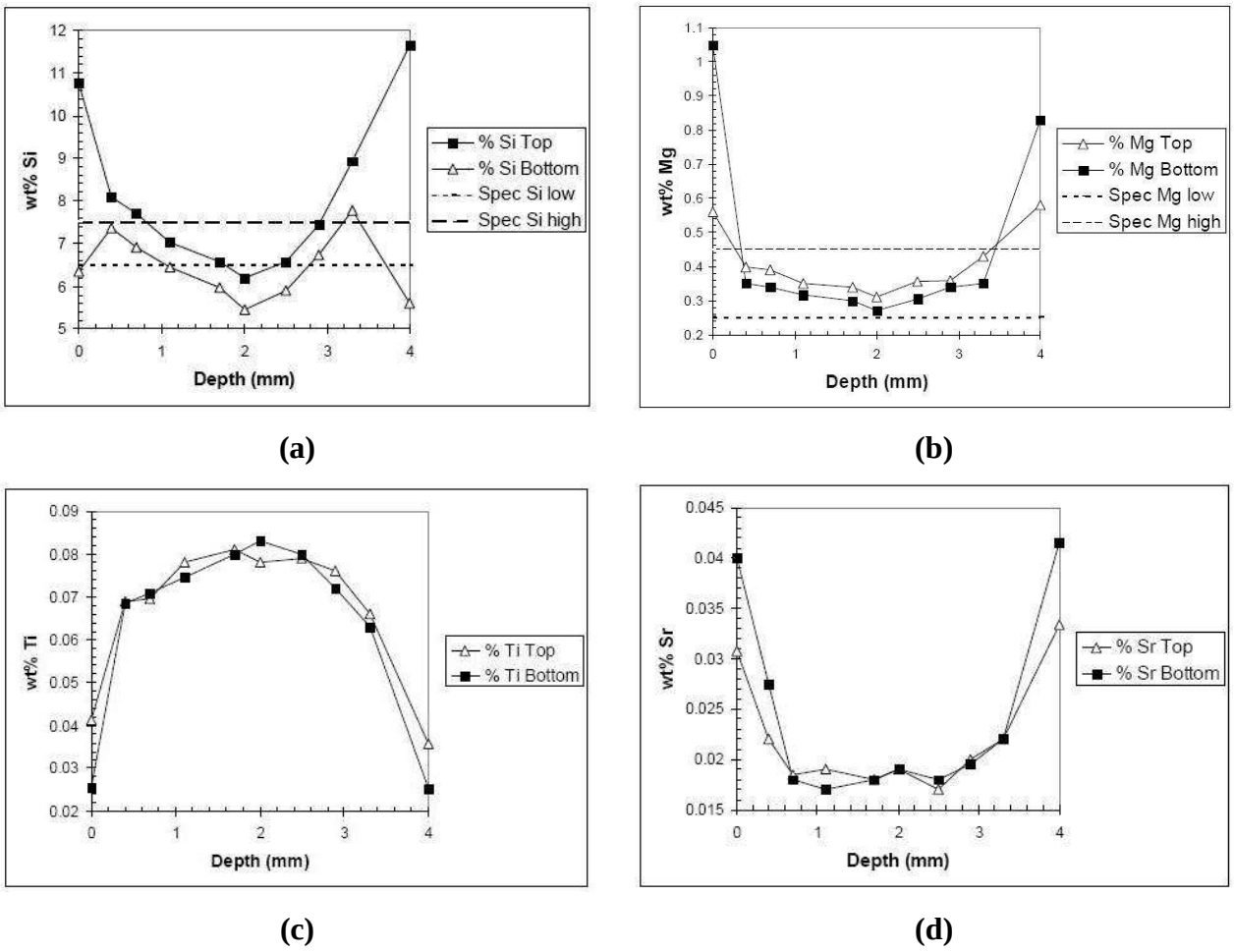

Figure 4.50: OES chemical analyses depth profiles for (a) Si, (b) Mg, (c) Ti and (d) Sr.

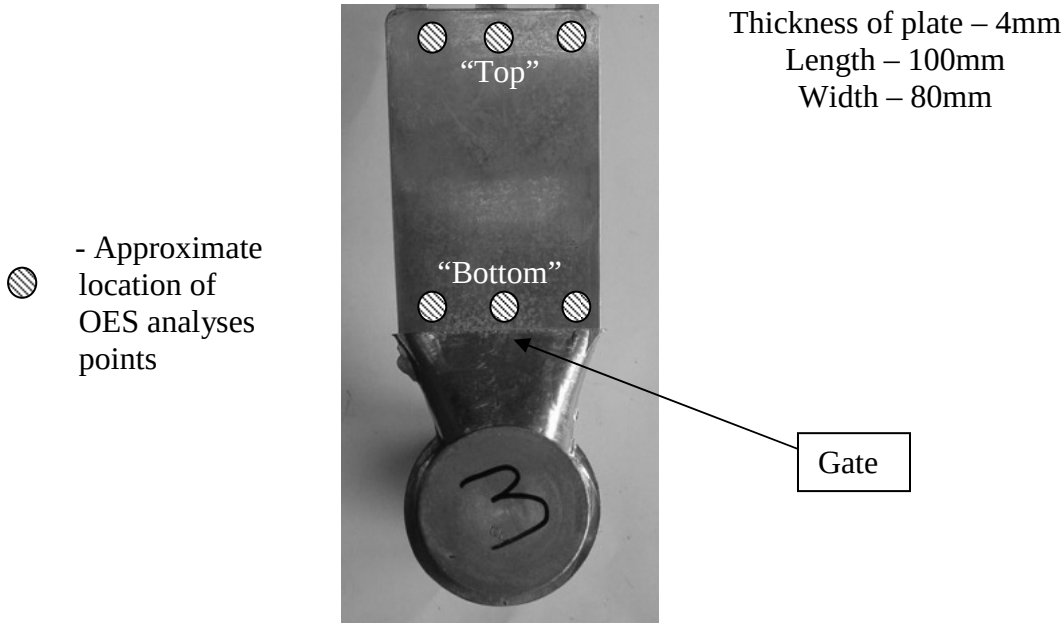

Figure 4.51: Image of a SSM-HPDC plate showing the approximate location for the OES analyses

In the region close to the top of the plate the surface Si, Sr and Mg contents were relatively high while Ti content was relatively low. The Si content drops significantly towards the centre of the plate, dropping below the minimum specification for the alloy. Si, Sr and Mg are typical alloying elements that would be found in the eutectic of the A356 alloy, hence indicating that the regions with high content of these alloying elements were regions of high liquid content. Using the Si high specification as the criteria, it can be seen that the liquid segregation layer can be as high 1.1 mm (measured at the top of the plate). The Ti content displayed the opposite behaviour. This had occurred since Ti was a grain refiner for the primary α-phase and would hence be present where the α grains would be of highest density. At the bottom of the plate, close to the gate, the silicon content was found to be relatively low at the surface, increasing to peak at a depth of approximately 0.4mm on one side of the plate and 0.7mm on the opposite side. The Si content distribution profile through the balance of the cross-section was very similar to that observed at the top. The segregation behaviour observed is as a result of a combination of the gate shape and injection parameters used; these were not optimised for minimising or eliminating liquid segregation for this particular study.

It is evident from these results that the segregation effect is a general phenomenon that occurs on the surface of the component. The region close to the gate shows a slightly different behaviour with a liquid segregation band 0.4-0.7mm below the surface (Fig. 4.50(a)). This had occurred because of a poor gate design resulting in poor filling characteristics around the gate region.

Microstructural analysis of cross-sections close to top and bottom of the castings (Fig. 4.52(a,b)) reveals the presence of the liquid segregation band. The region close to the surface was composed of mainly eutectic while closer to the centre of the casting microconstituents were mainly globular α primary grains and smaller amounts of eutectic. The microstructure at the centre of the casting was more homogenous. It was evident from the solution heat treatments that homogenisation of the surface segregation effects was not possible. Microstructural analysis of the region close to the surface after a T4 heat treatment showed (Fig. 4.52(c)) that there was a structural change in the eutectic structure only, namely spheroidisation of the Si.

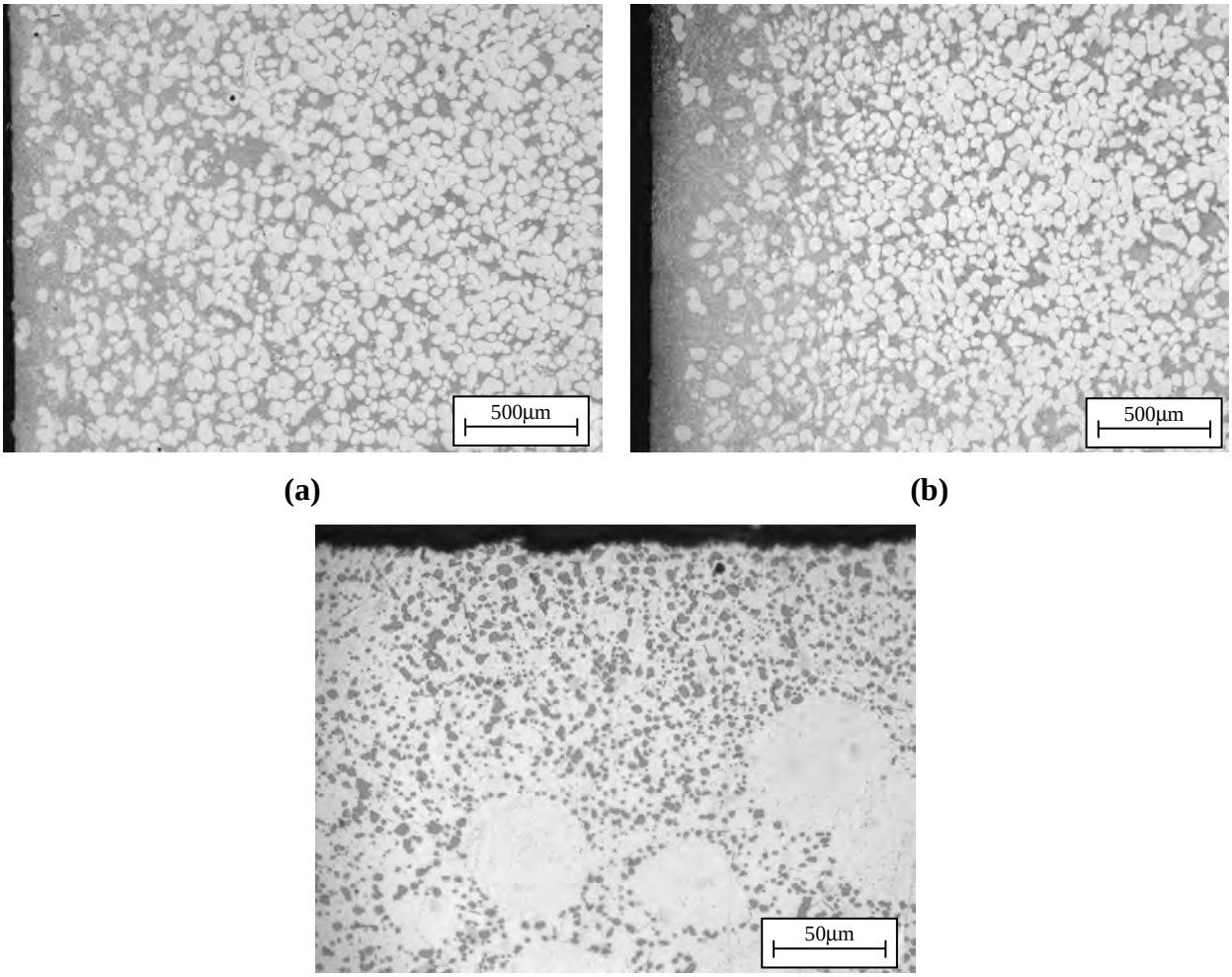

(a) **(b)**

(c)

Figure 4.52: Micrographs of cross-sections (a) close to the top, (b) close to the bottom and (c) after T4 heat treatment (540ºC for 6 h followed by natural aging for 120 h).

It has also been reported that the surface regions of conventional liquid HPDC components is of higher solute content than the centre [111]. This has been ascribed to the presence of externally solidified grains (ESG's). ESG's are large dendritic grains that are formed in the shot sleeve during conventional liquid HPDC, with fine grains solidifying inside the die cavity. These two grain populations mix in dissimilar proportions across the casting cross section, with a prevalence of the fine grains near the surface (skin) and the ESG's at the centre (core) [112]. The distribution of large ESG's at the centre of the cross section of HPDC castings is thought to be due to shear-induced migration of the ESG's during die filling from regions of high to low shear rate (i.e. toward the core of the casting) [111]. The ESG's have a low solute content and their migration to the centre results in surfaces with higher solute content.

Additional macrosegregation in HPDC components has also been ascribed to a combination of inverse segregation and exudation [111]. Inverse segregation is caused by the backflow of enriched liquid through the mushy zone in the dominant direction of heat flow (i.e. to the casting surface) to compensate for solidification shrinkage. With exudation, enriched liquid is drawn to the casting surface due to a pressure differential between the interior and the surface that occurs as the surface pulls away from the die wall during solidification.

With SSM-HPDC, the purpose of rheoprocessing is to form solid globular grains before the billet is transferred to the HPDC machine. In other words, these globular grains can be considered as ESG's that are formed, not in the shot sleeve, but deliberately during the rheopressing step. Additionally, the globular nature of the solid grains should result in a more suitable pathway for enriched liquid to flow to the surface than an interdendritic pathway in conventional HPDC and the surface layer (as shown in Fig. 4.52) is therefore more pronounced in SSM-HPDC components.

Vickers hardness tests of the as-cast surface and core of the casting (Table 4.18) showed a significant difference. This indicates that the mechanical properties of the surface of the casting will be significantly different to the core of the casting and hardness values therefore performed on the surface of a casting does not give a true indication of bulk hardness properties.

Table 4.18: Hardness of the plates without removing the segregation layer and after the surface segregation was removed.

Temper	Surface VHN	Centre VHN
F	80	77
T4	89	80
T6	122	106

4.10. SSM-HPDC of automotive brake callipers

Automotive brake callipers were also produced with SSM-HPDC (Table 3.3) to determine whether the heat treatment cycles that were developed for the small rectangular plates could also be applied successfully to a larger (and more complex) casting [HM10]. The hardness profiles through a cross section of SSM-HPDC brake calliper side-arms (Fig. 3.13) with 0.31% Mg in different temper conditions (F or as-cast, T4, T5 and T6) are shown in Fig. 4.53. The thickness of the side-arm at this selected position is seen to be 20 mm. The hardness values of the surface (at depths of 0 and 20 mm respectively) are significantly higher than the interior (which is constant for all temper conditions from depths of approximately 2-18 mm). The higher surface hardness is due to surface liquid segregation that occurs with SSM-HPDC (Fig. 4.54).

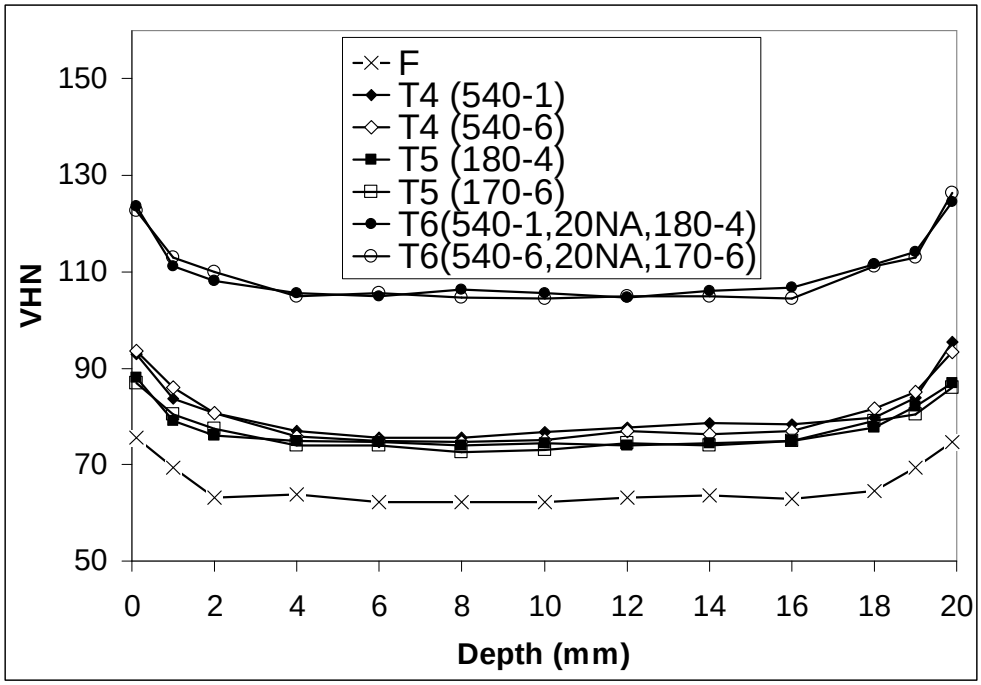

Figure 4.53: Hardness profiles through a cross section of SSM-HPDC brake callipers heat treated to various temper conditions by short cycles and longer "traditional" cycles.

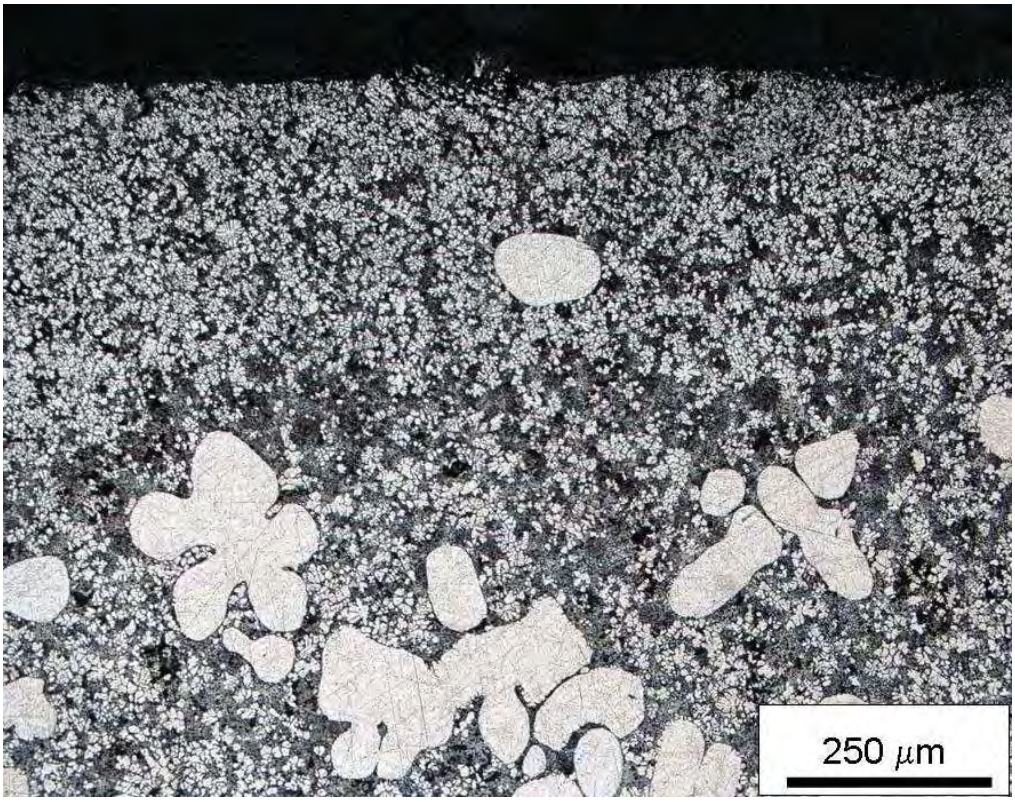

Figure 4.54: Optical micrograph showing the eutectic surface layer found in SSM-HPDC brake callipers.

The hardness profile in the T4 temper condition using the short cycle (540^{o}C for 1 h, quench and natural aging (NA) for 5 days) is very similar to when the longer "traditional" cycle is used (540^{o}C for 6 h, quench and NA for 5 days). Similarly, the shorter T5 cycle (artificial aging (AA) at 180^{o}C for 4 h) results in a comparable hardness profile to the longer "traditional" T5 cycle (AA at 170^{o}C for 6 h). Finally, the short CSIR T6 cycle (540^{o}C for 1 h, quench, NA for 20 h, AA at 180^{o}C for 4 h) results in an almost identical hardness profile than for the "traditional" T6 cycle (540^{o}C for 6 h, quench, NA for 20 h, AA at 170^{o}C for 6 h). Figure 4.53 illustrates that shorter heat treatment cycles can be employed on larger castings to obtain significant energy savings and increased productivity without the loss of properties.

4.11. Comparison of aging response of globular and dendritic Al-7Si-Mg alloys

4.11.1. SSM-HPDC and GDC automotive brake callipers

The investigation entailed comparing SSM-HPDC brake callipers (globular) to gravity die cast (GDC) brake callipers (dendritic) [HM10]. From Table 3.3 it can be seen that the Mg-contents of these brake callipers are similar (0.35 and 0.36% respectively).

The Mg-content controls the response to age hardening (Fig. 4.34), so for direct comparison of strength after heat treatment, the Mg-composition of the different brake callipers needs to be similar. The Fe-content of the SSM-HPDC callipers is, however, lower than for the GDC callipers, which is actually above the upper limit of the specification (Table 3.3). Iron tends to form intermetallics which have a negative influence on ductility (Fig. 4.38). The microstructures achieved with SSM-HPDC and GDC differ significantly. The SSM-HPDC brake callipers have a globular microstructure (Fig. 4.55(a)), whereas the GDC brake callipers have a dendritic microstructure (Fig. 4.55(b)). It is evident from Fig. 4.55 that GDC produces a much finer microstructure than SSM-HPDC. Image analysis revealed an average secondary dendrite arm spacing (SDAS) of 21µm (standard deviation of 3.6 from 30 manual measurements) in the GDC callipers, whereas the average globule size in CSIR SSM-HPDC callipers was 62µm (standard deviation of 21 from 635 measurements using Image–Pro MC v6.0 imaging software).

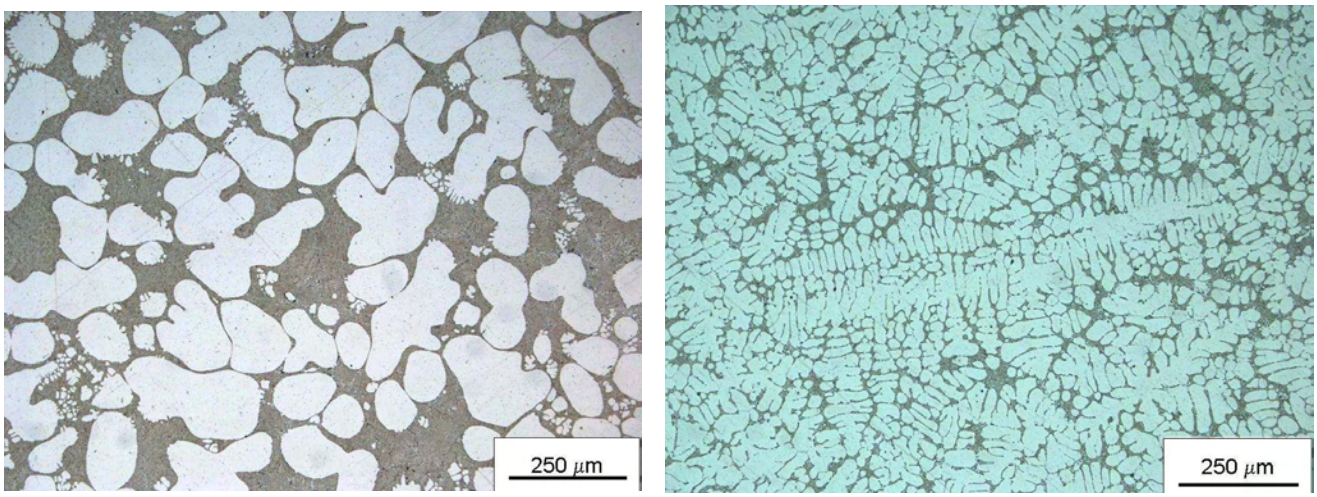

(a) **(b)**

Figure 4.55: Optical micrographs showing the as-cast (F temper) microstructures with MR = 5 (Table 2.2) of automotive brake callipers produced by (a) SSM-HPDC and (b) GDC.

Solution treatment at 540°C for 1 h results in the spheroidisation of the eutectic silicon particles in both the SSM-HPDC and GDC brake callipers (Fig. 4.56).

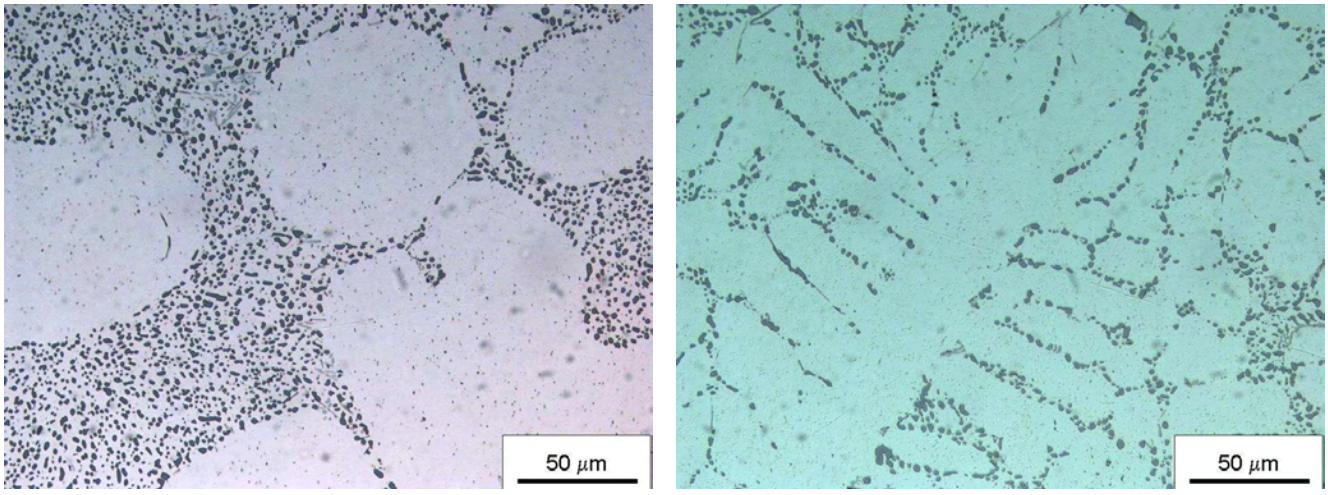

(a) **(b)**

Figure 4.56: Optical micrographs showing the T6 (540°C-1h, 20h NA, 180°C-4h) microstructures of automotive brake callipers produced by (a) SSM-HPDC and (b) GDC.

The Vickers hardness values (VHN) of SSM-HPDC and GDC brake callipers are compared in Fig. 4.57. It can be seen that the hardness values are very similar in both the as-cast (F temper) and T6 temper conditions.

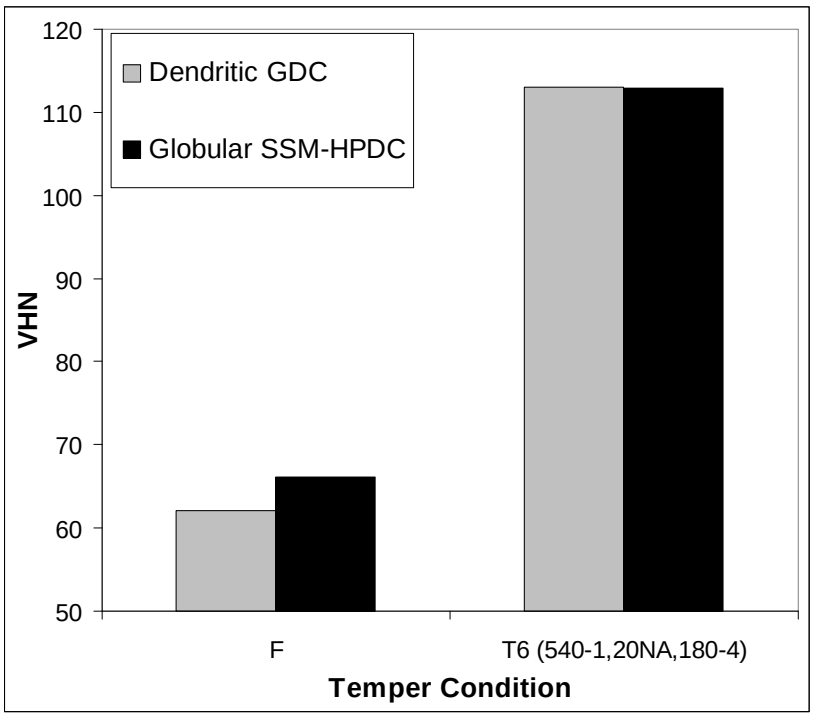

Figure 4.57: Vickers hardness of SSM-HPDC and GDC brake callipers in the as-cast (F temper) and T6 temper conditions.

Also, note that the T6 hardness values are slightly higher than was obtained for the SSM-HPDC brake callipers with 0.31% Mg (Fig. 4.53). This is due to the slightly higher Mg-contents of 0.35 and 0.36% of the alloys in Fig. 4.57.

Comparison of the tensile properties of GDC and SSM-HPDC T6 (540^{o}C-1h,20h NA,180^{o}C-4h) callipers in Table 4.19 confirm the hardness results of Fig. 4.57: the 0.2% yield strengths (YS) and ultimate tensile strengths (UTS) are similar. This result is significant as it shows that dendritic and globular A356 components respond similarly to heat treatment. The lower % elongation after fracture of the GDC calliper as compared to the SSM-HPDC callipers is noteworthy. It is most likely due to the higher Fe-content (Table 3.3) of the GDC calliper, which has an adverse effect on ductility (Fig. 4.38). The differences in Fe-content between the brake callipers make it virtually impossible to determine the effects of globular versus dendritic microstructure on the ductility of A356 in this case.

Table 4.19: Yield strength (YS), ultimate tensile strength (UTS) and % elongation after fracture (%A) of T6 heat treated A356 brake calliper samples. The standard deviation (from 4 values) for tensile properties is also indicated in brackets.

Brake calliper	YS (MPa)	UTS (MPa)	% Elongation
SSM-HPDC (0.35% Mg)	261 (1.4)	317 (3.6)	6.7 (1.9)
GDC (0.36% Mg)	268 (2.1)	315 (4.9)	3.2 (1.6)

Figure 4.34 is redrawn in Fig. 4.58 by also including the data points of the brake callipers in Table 4.19. The data points of the brake callipers correlate well with the data points of the SSM-HPDC plates.

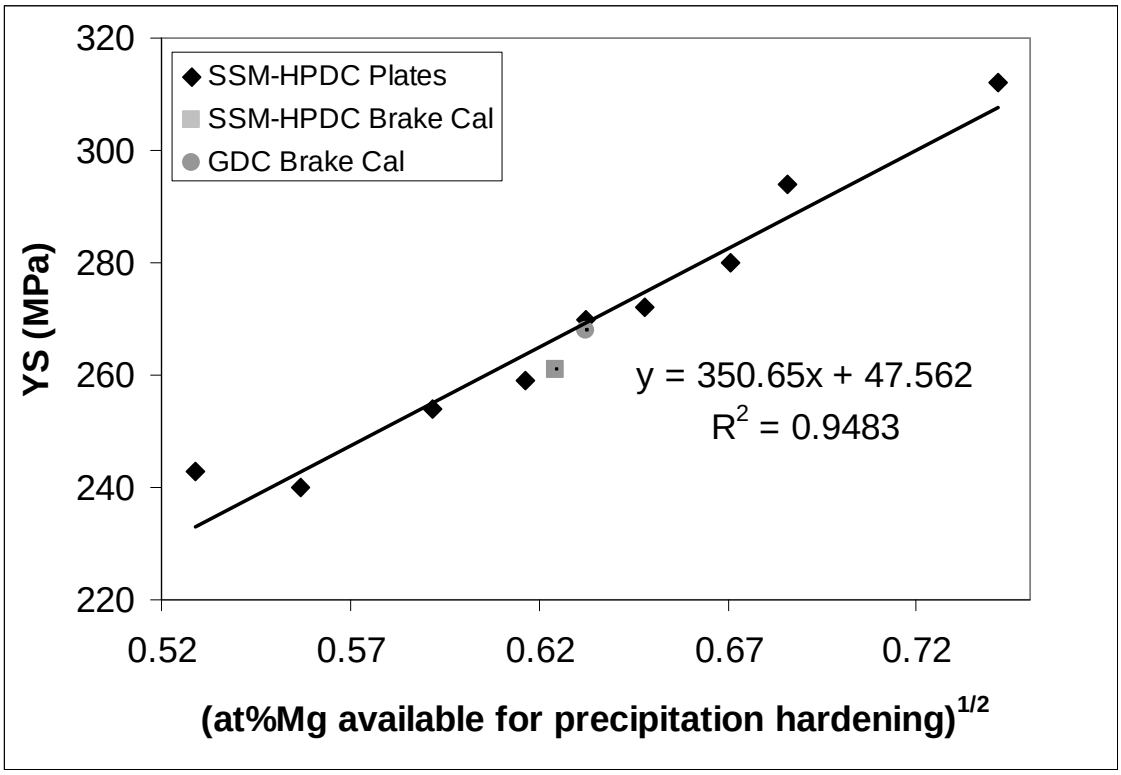

Figure 4.58: YS as a function of (at% Mg-concentration available for precipitation hardening)$^{1/2}$ for the (540-1, {20-120}NA, 180-4) heat treatment applied to SSM-HPDC plates and brake callipers, as well as GDC brake callipers.

4.11.2. Investment cast (IC) plates

Rectangular plates (Fig. 3.10) with composition given in Table 3.4 were cast using investment casting (IC) to obtain a coarser dendritic microstructure than achieved in the brake calliper cast using GDC [HM12]. Optical micrographs for IC-A356 are shown in Fig. 4.59 in the (a) as-cast and (b) T6 temper conditions respectively.

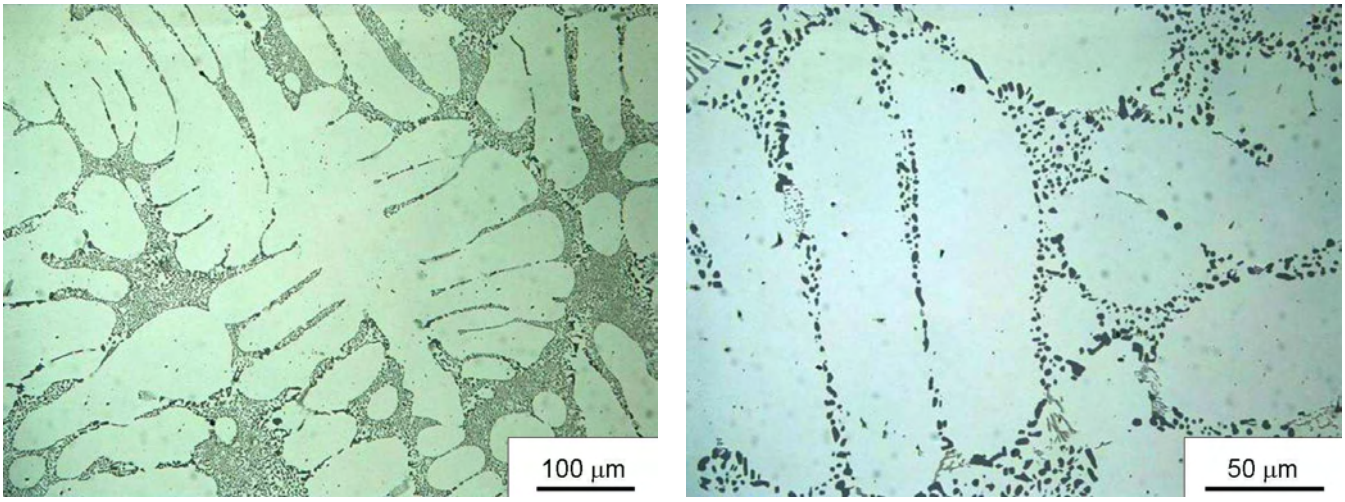

(a) **(b)**

Figure 4.59: Optical micrographs of IC-A356 in (a) the as-cast and (b) T6 temper conditions.

It is evident from Figures 4.55 and 4.59 that IC produced a coarser microstructure than GDC. Image analysis revealed an average secondary dendrite arm spacing (SDAS) of 32µm in the IC callipers (standard deviation of 4.0 from 30 manual measurements), whereas the average SDAS of the GDC plates was 21µm (see section 4.11.1). Solution treatment at 540^{o}C for 1 h resulted in the spheroidisation of the eutectic silicon particles in the IC-A356 (Fig. 4.59(b)). Due to the slow cooling rate during solidification of these plates, a Sr-addition of 300 ppm was necessary to achieve modification of the eutectic Si-particles (Table 3.4). However, the microstructure in Fig. 4.59(a) corresponds to a MR number (Table 2.2) of 4, since some acicular particles are still present.

Figure 4.60 shows artificial aging curves that were determined for SSM-HPDC and GDC brake callipers, as well as IC plates after solution treatment at 540^{o}C for 1 hour, water quenching and no natural pre-aging. The artificial aging response is similar to what was presented in Fig. 4.18 and appears to be independent of whether the microstructure is globular or dendritic. Note that the hardness values are significantly lower for the IC plates than for the brake callipers due to the low Mg-content of the IC plates of only 0.25% (Table 3.4). Artificial aging curves were also determined for these alloys after solution treatment at 540^{o}C for 1 hour, water quenching and 120 hours natural pre-aging, followed by artificial aging (Figure 4.61). Again, the curves are similar to those presented in Fig. 4.18.

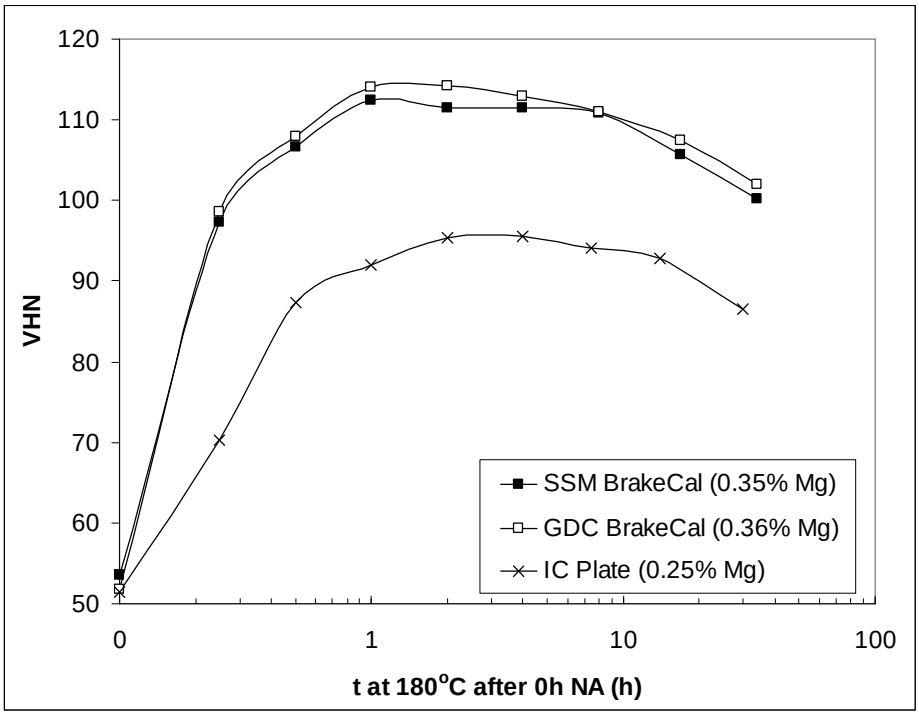

Figure 4.60: Artificial aging curves at 180°C for alloy A356 cast using different casting techniques (after 0 h natural pre-aging time).

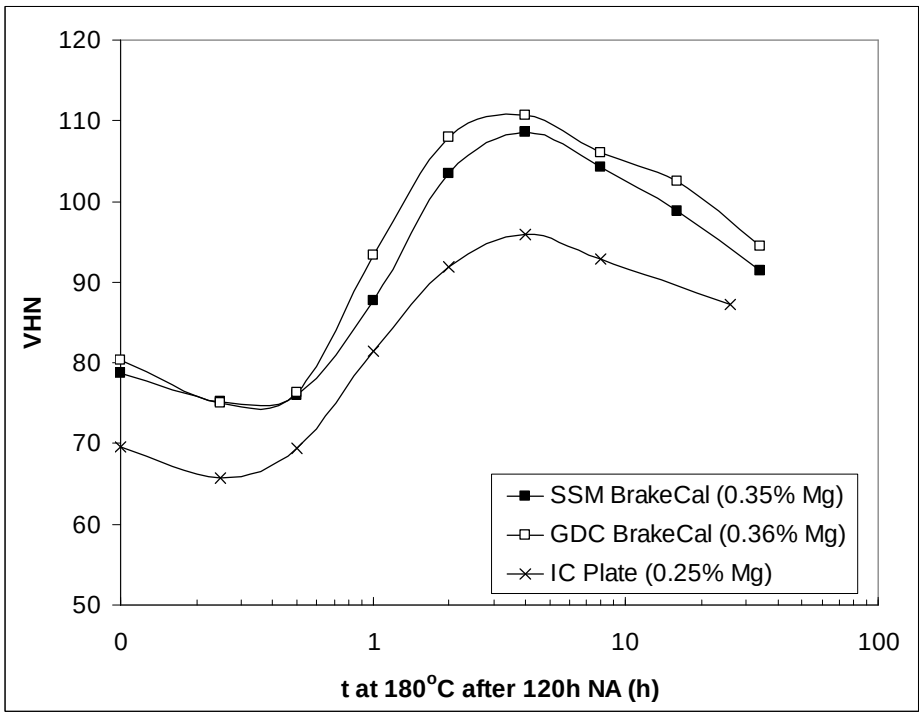

Figure 4.61: Artificial aging curves at 180°C for alloy A356 cast using different casting techniques (after 120 h natural pre-aging time).

No tensile testing could be performed on the IC-A356 plates due to constraints on sample size. In order to make comparisons between the different plates and brake

callipers, hardness was used instead of yield strength (as was done in Fig. 4.58) and the results are shown in Fig. 4.62. Hardness generally correlates better with UTS than with YS since significant plastic deformation occurs with both hardness and UTS determination [82] (see section 4.12). Figure 4.62 is therefore only used as a convenient method of making comparisons of the heat treatment response of Al-7Si-Mg castings produced by different casting techniques. It can be seen that an excellent linear correlation is achieved in Fig. 4.62.

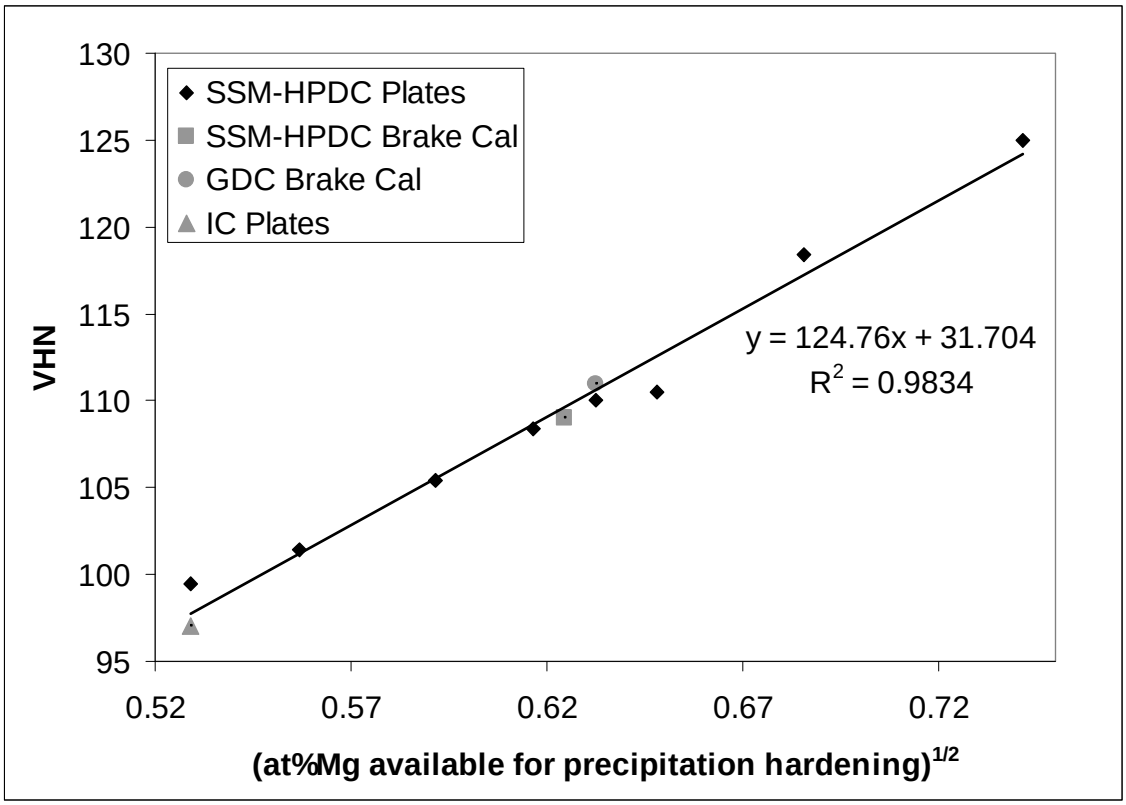

Figure 4.62: VHN as a function of (at% Mg-concentration available for precipitation hardening)$^{1/2}$ for the (540-1, {20-120}NA, 180-4) T6 heat treatment applied to SSM-HPDC plates and brake callipers, as well as GDC brake callipers and IC plates.

4.12. Correlations between hardness, yield strength and UTS in Al-7Si-Mg alloys

As mentioned earlier, direct correlations between yield strength and hardness generally contain an appreciable amount of scatter. This is due to the fact that strain associated with a Vickers indentation is approximately 8% for a variety of strain hardening alloys and hardness therefore generally correlates better with UTS than with YS (where only 0.2% plastic strain has occurred) [82].

The YS and UTS as a function of the Vickers hardness for this work (F, T4, T5 and T6 temper conditions) are plotted in Figures 4.63 and 4.64 respectively.

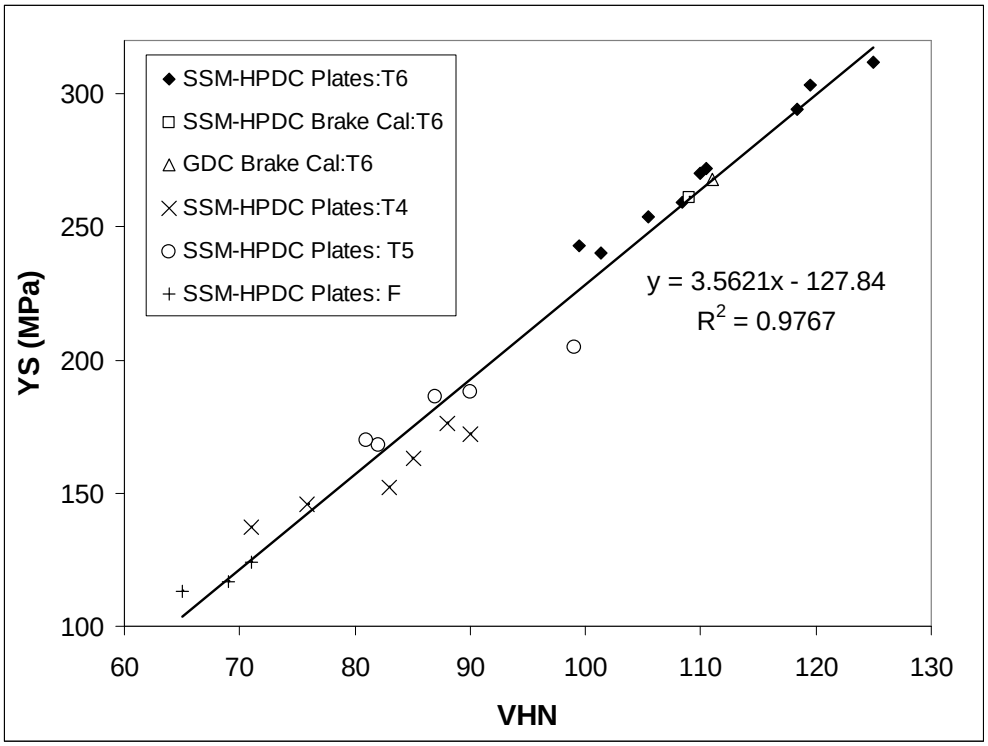

Figure 4.63: Correlation between YS and VHN for Al-7Si-Mg alloys in the F, T4, T5 and T6 temper conditions used in this study.

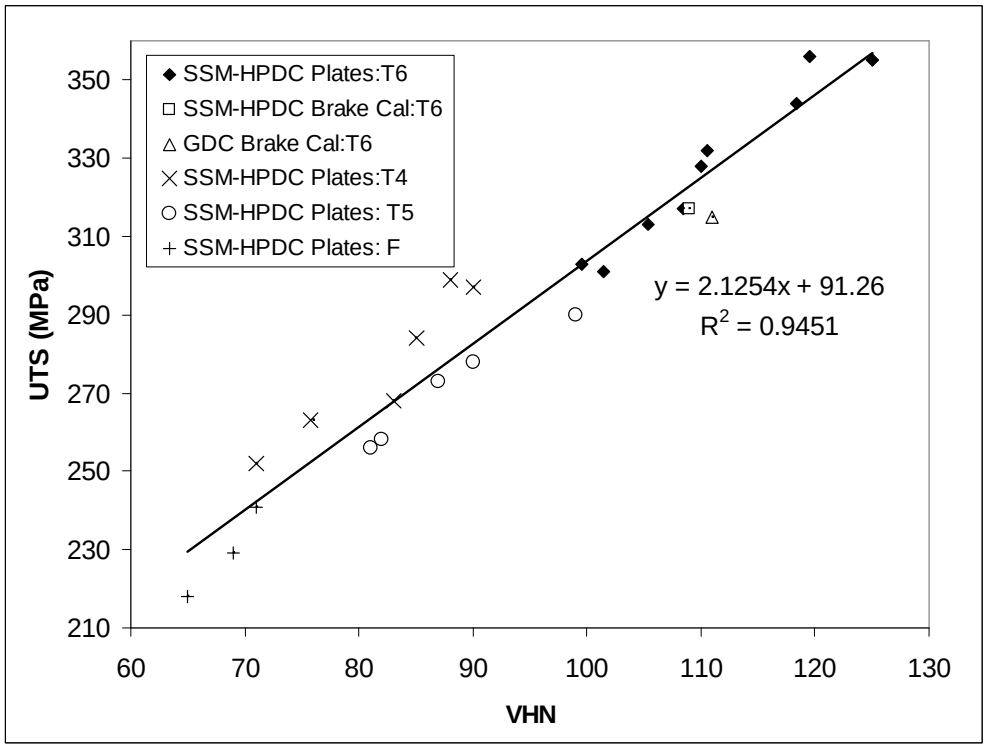

Figure 4.64: Correlation between UTS and VHN for Al-7Si-Mg alloys in the F, T4, T5 and T6 temper conditions used in this study.

From Figure 4.63 it is seen that the correlation between YS and hardness is rather reasonable in the range of hardness and yield strengths tested. From Figure 4.64 it is seen that the correlation between UTS and hardness is comparable to that of YS and hardness in Fig. 4.63. The reason why better correlation with UTS is not obtained with Al-7Si-Mg alloys is most likely due to the fact that UTS is influenced by the degree of spheroidisation of the eutectic Si particles in these alloys. Spheroidised Si-particles tend to result in a higher % elongation, which in turn gives a higher UTS as necking generally does not occur (compare for instance UTS and the % elongation after fracture of the T4 and T5 samples in Table 4.17). The data points in Fig. 4.64 include alloys in which the eutectic Si particles are fibrous (F and T5) and spheroidised (T4 and T6), resulting in a worse-than-expected correlation between UTS and VHN. This suggestion is supported by the fact that most of the F and T5 data points lie below the trend line in Fig. 4.64, whereas the T4 (and to a lesser extent the T6) data points are above the trend line.

Rometsch and Schaffer [82] have proposed an equation (4.7) to convert Brinell hardness (HB) of alloys A356 to A357 to YS by employing the strain hardening exponent (n):

$$\mathbf{YS = 2.95 \times HB \times [0.065]^n} \qquad \mathbf{(4.7)}$$

Accurate n-values from experimental data in this study could not be obtained due to the removal of the extensometer during tensile testing after reaching the 0.2% plastic strain value. However, assuming that the strain hardening exponent is constant over the plastic strain range up to the point of necking during tensile testing of these alloys, an expression for YS/UTS in terms of n alone may be found (eq. 4.8):

$$\mathbf{YS_{0.2\%}/UTS \approx \{(0.002)^n (\exp n)\} /(n)^n} \qquad \mathbf{(4.8)}$$

Equation 4.8 is derived from the Hollomon equation ($\sigma = K\varepsilon^n$), as well as from the conversion equations for engineering strain (e) to true strain (ε) [$\varepsilon = \ln (e+1)$], engineering stress (s) to true stress (σ) [$\sigma = s(e+1)$] and the equivalence of true strain at necking = n [113]. Using the data points in Fig. 4.63 and their respective UTS

values in Fig. 4.64, average n-values for each temper condition can be calculated (Table 4.20).

Table 4.20: Average n-values for Al-7Si-Mg alloys in this study in different temper conditions

Temper condition	Average n-value	Standard deviation
F	0.188	0.0015 from 3 values
T4	0.165	0.0065 from 6 values
T5	0.125	0.0071 from 5 values
T6	0.072	0.0083 from 11 values

The n-values presented in Table 4.20 correspond well to those that could be found in the literature, validating the use of eq. 4.8. Bogdanoff and Dahlström [114] found n-values of 0.17-0.22 for as-cast A356. The evaluated strain hardening exponent for A356/7-T6 according to Wang [115] ranged from 0.045-0.095 depending on the secondary dendrite arm spacing. Rometsch and Schaffer [82] found n-values of 0.088 and 0.078 for their A356 and A357 alloys in the T6 temper condition respectively.

Adapting equation 4.8 slightly to use Vickers hardness rather than Brinell hardness, also minimising $\Sigma(YS_{Measured} - YS_{Predicted})^2$ and ensuring that the intercept of the line of best fit passes through the origin, equation 4.9 is proposed:

$$\mathbf{YS = 3.03 \times VHN \times [0.055]^n} \qquad \mathbf{(4.9)}$$

The predicted YS-values using this equation correlate very well with the measured YS-values (Fig. 4.65).

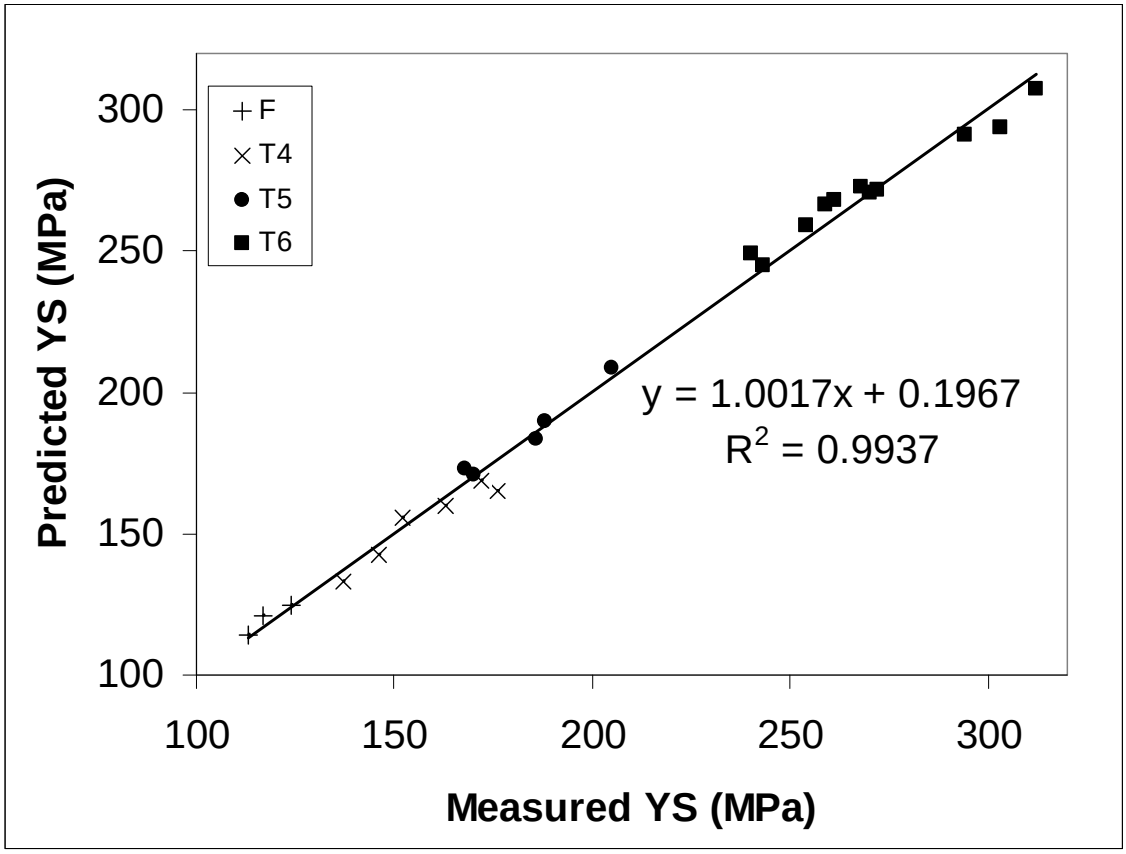

Figure 4.65: Plot of predicted YS (eq. 4.9) against measured YS for Al-7Si-Mg alloys in the F, T4, T5 and T6 temper conditions used in this study.

4.13. Comparison of aging response of SSM-HPDC Al-7Si-Mg alloys with SSM-HPDC 6000 series Al-Mg-Si wrought alloys

Both conventional casting alloys A356/7 and the conventional Al-Mg-Si 6000 series wrought alloys are strengthened by β″, but the influence of especially the high Si content in the casting alloys compared to the wrought alloys is of interest [HM14]. One of the main advantages of SSM-processing is that it is also possible to produce near net-shape components from alloys that are conventionally wrought such as the 6000 series [10,116,117]. By employing SSM-HPDC to A356/7 and the 6000 series alloys, comparable globular microstructures in both series can be obtained. The chemical compositions of alloys 6082 and 6004 can be found in Table 3.6.

Optical micrographs of SSM-HPDC alloys 6082 and 6004 in the as-cast condition are shown in Figure 4.66 (a) and (b) respectively. The globular α-Al that is a prerequisite for SSM-processing is clearly visible in both samples. The inter-globular regions (i.e. the part that was liquid during SSM-processing) of the wrought alloys consist mainly

of fine α-Al (Fig. 4.67), in contrast to the inter-globular regions of the casting alloys which consist mainly of eutectic (α-Al and Si) (Fig. 4.10) due to the high Si content of ~ 7%.

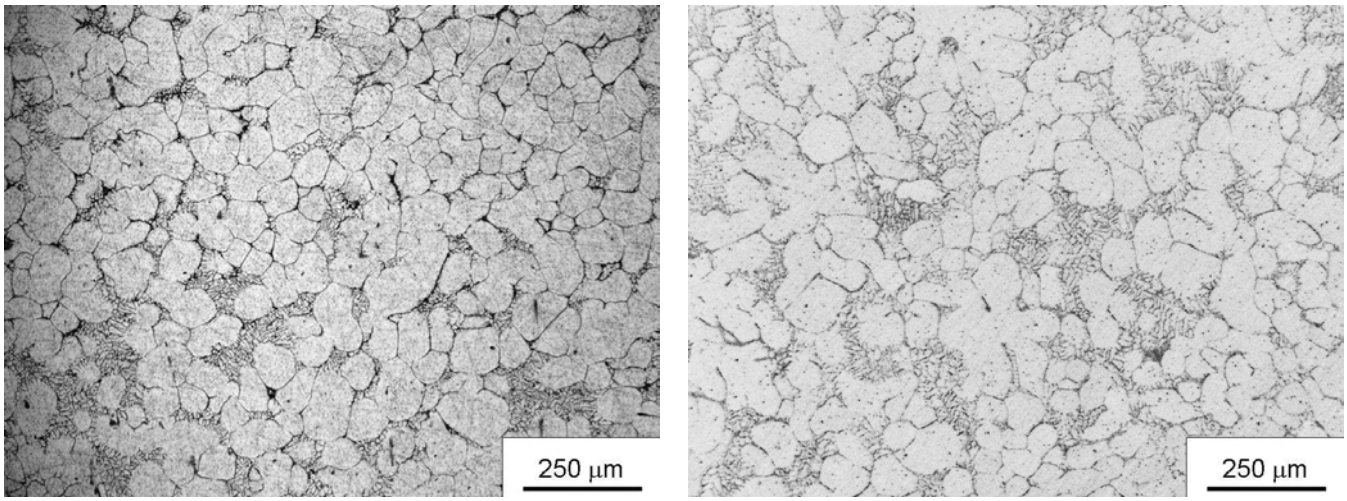

(a) **(b)**

Figure 4.66: Optical micrographs of SSM-HPDC alloys in the as-cast condition for (a) 6082 and (b) 6004.

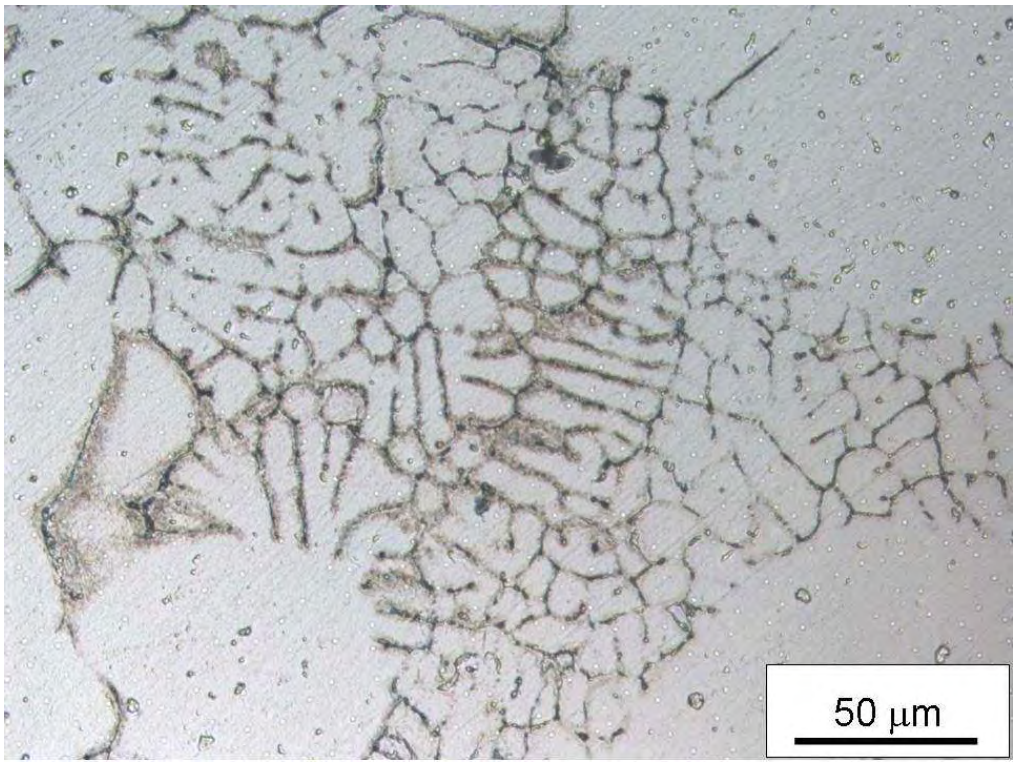

Figure 4.67: High magnification optical micrograph of SSM-HPDC alloy 6004 in the as-cast condition showing the inter-globular regions.

Optical micrographs of SSM-HPDC alloys 6082 and 6004 in the T6 condition are shown in Figure 4.68 (a) and (b) respectively. The globular α-Al structure is retained in the samples during heat treatment.

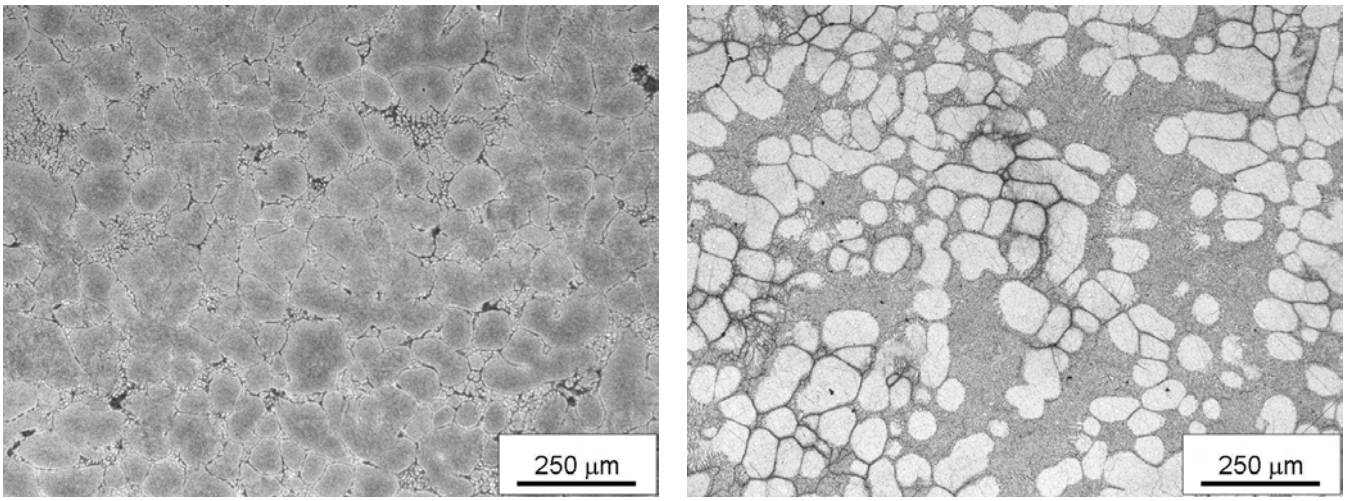

(a) **(b)**

Figure 4.68: Optical micrographs of SSM-HPDC alloys in the T6 temper condition for (a) 6082 and (b) 6004.

As was shown in section 4.9, the nature of the SSM slurry with solid spherical grains suspended in liquid makes it susceptible to liquid segregation during forming processes. An example of the surface liquid segregation (SLS) layer found in alloy 6004-T6 is shown in Figure 4.69. The solution treatment step during the T6 heat treatment has been found to dissolve the majority of the intermetallic phases, however, it does not reduce segregation of elements in the casting [HM11]. As with the A356 and F357 alloys in this study, this surface layer was removed by grinding before all hardness measurements were performed.

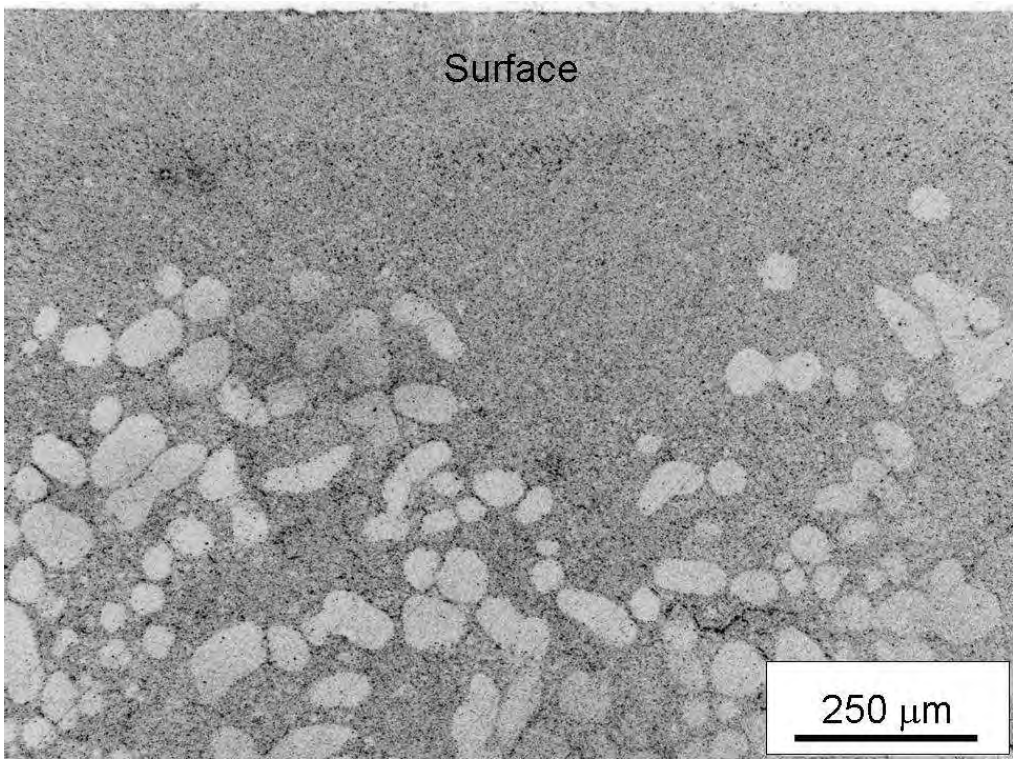

Figure 4.69: Optical micrograph showing the SLS layer in SSM-HPDC alloy 6004-T6.

Figure 4.70 shows artificial aging curves that were determined for the castings at 180^{o}C after solution treatment at 540^{o}C for 1 hour, water quenching and either no or 120 h natural pre-aging. For the casting alloys, aging curves are shown for A356-0.36% Mg (Table 3.1). Considering the effects of prior natural aging on subsequent artificial aging first, it has been shown already that the same maximum hardness can be achieved in A356 regardless of the natural pre-aging time period (Fig. 4.18). Alloy 6082 shows a negative effect of prior natural aging, with the maximum hardness significantly lower when prior natural aging had occurred than without natural aging. This effect is well known for wrought 6082 alloys [84]. Alloy 6004 shows the opposite behaviour, with the maximum hardness being higher when natural aging occurs before artificial aging. This has also been shown to occur before for wrought 6000 series alloys with relatively low Mg and Si contents [85].

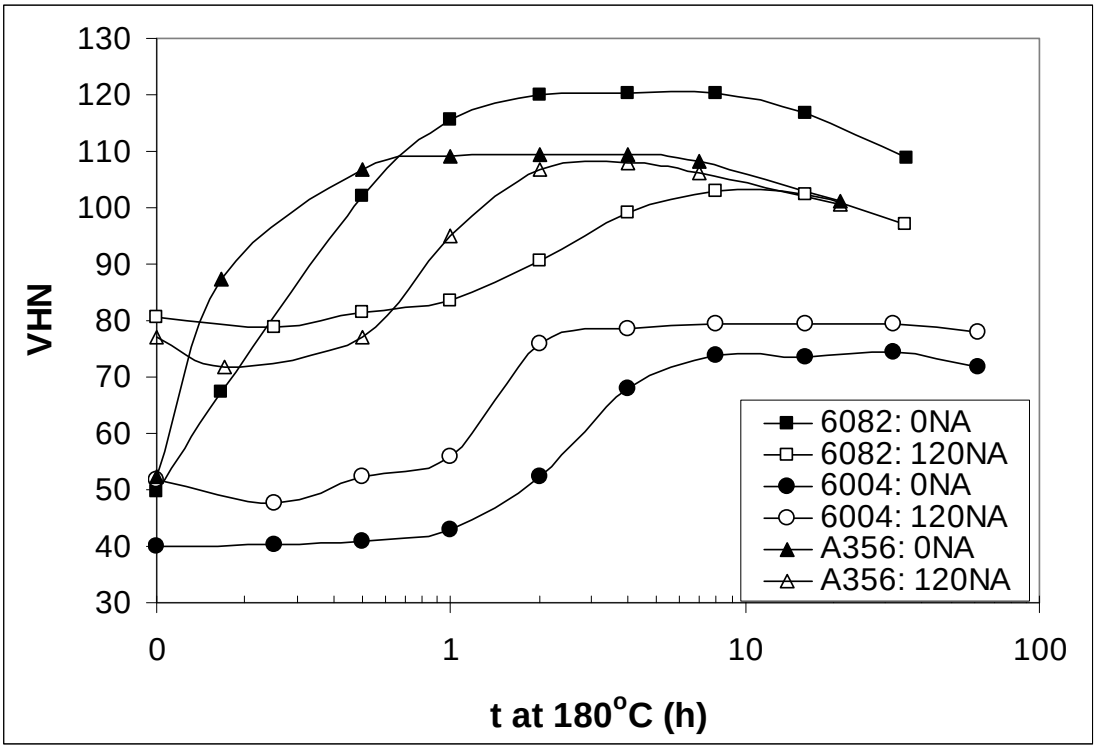

Figure 4.70: Artificial aging curves at 180°C for SSM-HPDC alloys 6082, 6004 and A356 (after either 0 or 120 h natural pre-aging time).

The tensile mechanical properties of SSM-HPDC alloys 6082, 6004 (and A356-0.36% Mg and F357-0.62% Mg for convenience) are shown in Table 4.21. Artificial aging time to peak hardness at 180°C of 4 h was used for A356 and F357 and 8 h for 6082 and 6004 (Fig. 4.70). The tensile mechanical properties are compared for samples that had been naturally aged for 0 or 20-120 h before artificial aging. The tensile results in Table 4.21 are in agreement with the aging curves of Figure 4.70. The strength of SSM-HPDC 6082 is decreased significantly by a prior natural aging period, whereas alloy 6004 displays the opposite behaviour. The strength (YS and UTS) of the casting alloys A356 and F357 are not influenced significantly by a prior natural aging period. It can also be seen from Table 4.21 that alloy 6082 has a strength comparable to alloy F357 when no natural aging of the 6082 occurs and a strength similar to A356 once natural aging occurs. However, this strength is achieved by employing double the artificial aging time at 180°C that was needed for the casting alloys. Also, the Mg requirement to achieve this strength is significantly higher for 6082 than for the casting alloys. The ductility of the 6082 is relatively low if compared to its wrought counterpart and the casting alloys (Table 4.21). Low ductility of SSM-HPDC high performance wrought alloys has been reported before and is related to the distribution

of intermetallic compounds within the coarse eutectic regions [116]. The relatively high ductility of SSM-HPDC 6004 is due to the low strength values that are achieved in this alloy (Table 4.21), in agreement with the low hardness values in Figure 4.70.

Table 4.21: Yield strength (YS), ultimate tensile strength (UTS) and % elongation after fracture (%A) of SSM-HPDC alloys in the T6 temper condition. The standard deviation from at least four values for tensile properties is also indicated in brackets.

	6082		**6004**		**A356**		**F357**	
	0NA	120NA	0NA	120NA	0NA	120NA	0NA	20NA
YS (MPa)	323 (12.9)	278 (6.3)	148 (9.4)	207 (2.2)	273 (6.5)	270 (5.5)	315 (5.2)	312 (4.1)
UTS (MPa)	344 (11.7)	305 (10.3)	189 (5.5)	237 (3.0)	333 (8.4)	328 (5.8)	360 (5.0)	355 (3.9)
%A	4.2 (2.0)	5.4 (2.2)	13.1 (1.0)	12.0 (1.6)	8.4 (2.1)	8.0 (2.2)	5.7 (1.1)	6.0 (1.3)

Bichsel and Ried [87] drew contour plots for 6000 series wrought alloys showing the effect of 24 h natural aging on the change in UTS (MPa) as a function of the Mg and Si content (Fig. 2.32). The contour lines indicate the change in UTS after artificial aging at 165^{o}C for 15 h. This is shown in Figure 4.71, together with the compositions of the 6082 and 6004 used in this study. The change in UTS as a result of prior natural aging is much larger in this case (Table 4.21). The heat treatment cycles and processing techniques (wrought vs. SSM-HPDC) employed in this study are different from the data in Fig. 4.71, which might explain the differences between the two sets of results. The data in Figure 4.71 do not include the Si-composition range of the A356 and F357 alloys of 6.5-7.5% Si. However, the high Si content of these alloys reduces the sensitivity to Mg content – naturally aged alloys A356 and F357 reach the same strength and hardness as the alloys which were not naturally aged before artificial aging for Mg contents covering the whole range of 0.25 to 0.7% (see for example Tables 4.9 and 4.10).

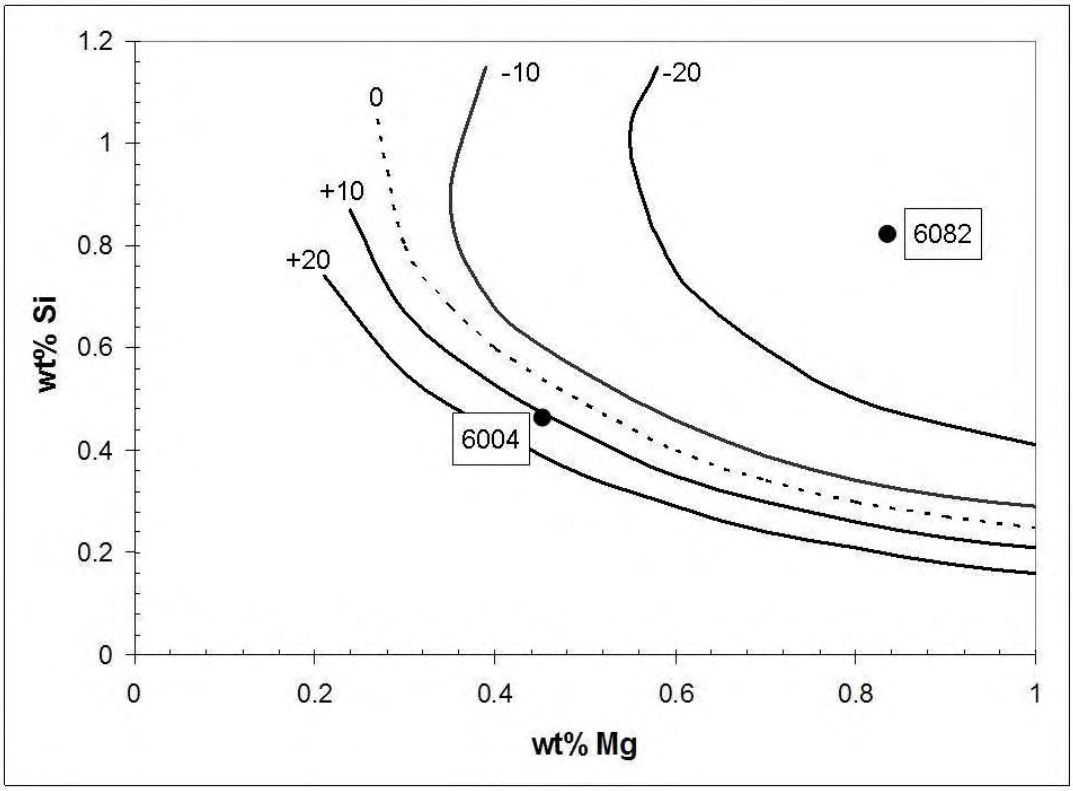

Figure 4.71: Contour plots for 6000 series alloys showing the effect of 24 h prior natural aging on the change in UTS (MPa) after artificial aging at 165°C for 15 h as a function of the Mg and Si content [87]. The present alloy compositions of 6082 and 6004 are also indicated.

4.14. Nanostructural evolution during aging of Al-7Si-Mg alloys

The nanostructural evolution of the 0.49% Mg alloy (Table 3.1) was studied by employing TEM and APT [HM15]. Since APT results are generally presented in terms of at%, the chemical composition in Table 3.1 is presented in Table 14.22 in both wt% and at%.

Table 4.22: Chemical composition of alloy F357 used for TEM and ATP.

	Si	Mg	Fe	Ti	Cu	Mn	Sr	Al
wt%	6.8	0.49	0.13	0.13	0.04	0.01	0.02	Balance
at%	6.6	0.54	0.06	0.07	0.02	0.005	0.006	Balance

4.14.1. Age hardening response and tensile properties

Artificial aging curves following no or 120 h of natural pre-aging for alloy F357 are shown in Figure 4.72. As also shown in Fig. 4.18, a hardness plateau is found between 1 and 4 hours at 180^{o}C following no natural pre-aging. In contrast, a hardness peak is found after 4 h artificial aging following natural pre-aging, with the peak hardness of 120 VHN similar to the plateau hardness. The microhardness values of the primary α-Al and the eutectic components are also indicated in Fig. 4.72. It is seen that the hardness of the primary α-Al is marginally lower than the macrohardness of the alloy, with the hardness of the eutectic being higher. The change of hardness of the eutectic component with aging implies that precipitation hardening also occurs within the α-Al phase of the eutectic. The TEM and APT investigations in this paper relate only to the primary α-Al, but it is seen from Fig. 4.72 that the trends in the aging curves of the alloy (macrohardness) and the primary α-Al are comparable.

Tensile properties of the samples used for TEM and APT investigations are shown in Table 4.23. The results correlate well with the aging curves from Fig. 4.72, with the strength (YS and UTS) of the 120h NA,180^{o}C-10min sample being lower than that of the T4 sample. The strength then increases again for the 120h NA,180^{o}C-1h sample, before reaching peak values for the 120h NA,180^{o}C-4h sample. The samples on the hardness plateau (0h NA,180^{o}C-1h and 0h NA,180^{o}C-4h) have similar UTS values, but different YS values, with the 0h NA,180^{o}C-1h sample having a significantly lower YS than the 0h NA,180^{o}C-4h sample (also see Tables 4.9 and 4.10).

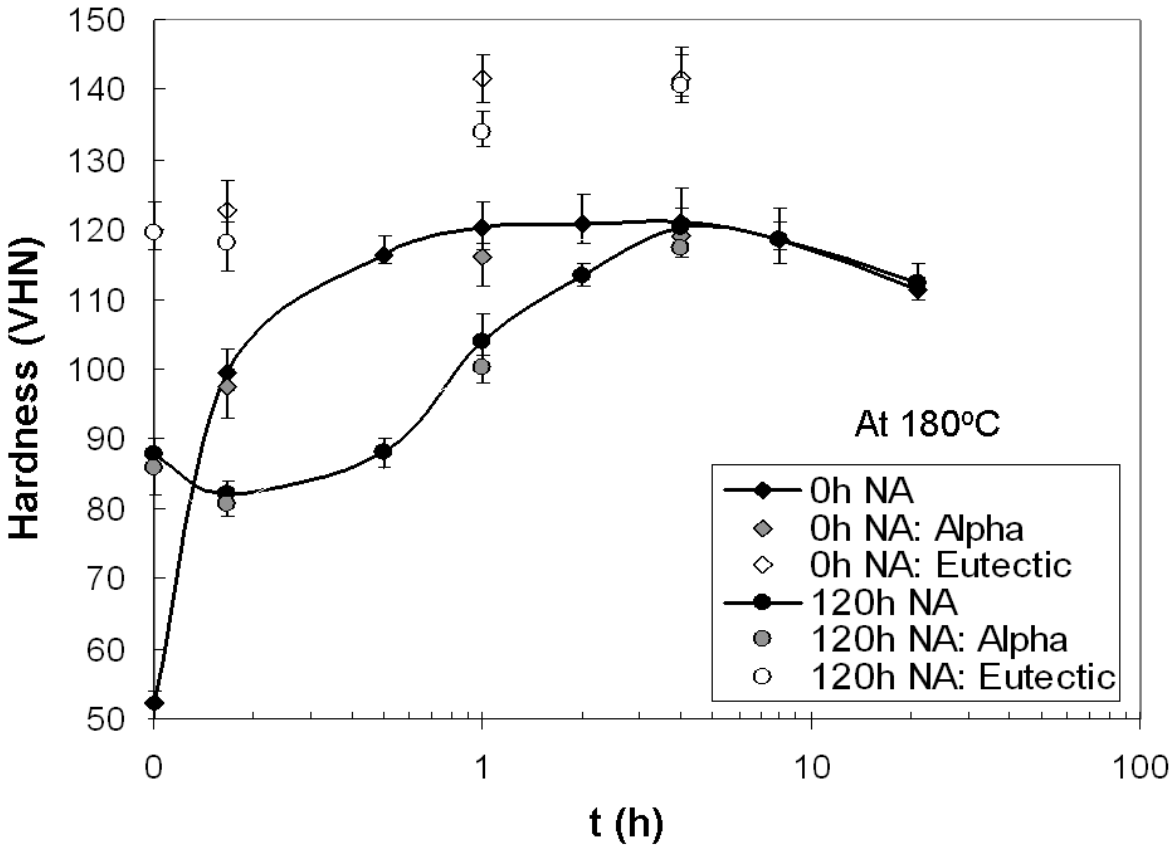

Figure 4.72: Artificial aging curves for alloy F357 following no or 120 h of natural pre-aging (NA), including the microhardness values of the primary α-Al and the eutectic components.

Table 4.23: Tensile properties of SSM-HPDC alloy F357 samples (produced with the 130t HPDC machine) used for TEM and APT analysis. The standard deviation from four values for tensile properties is also indicated in brackets.

	YS (MPa)	UTS (MPa)	% Elongation
T4	176 (4.3)	299 (1.6)	18.0 (2.6)
540°C-1h,120 h NA,180°C-10 min	164 (2.8)	288 (2.6)	20.2 (0.44)
540°C-1h,120 h NA,180°C-1 h	253 (9.5)	335 (3.8)	11.7 (2.6)
540°C-1h,120 h NA,180°C-4 h	303 (3.3)	356 (3.3)	10.6 (1.3)
540°C-1h,0 h NA,180°C-10 min	180 (4.0)	298 (1.6)	19.1 (4.2)
540°C-1h,0 h NA,180°C-1 h	288 (3.0)	362 (1.7)	12.5 (2.4)
540°C-1h,0 h NA,180°C-4 h	304 (1.7)	365 (2.0)	10.6 (1.8)

4.14.2. Nanostructural evaluation

4.14.2.1. Transmission electron microscopy (TEM)

Figure 4.73 shows bright field (BF) images and selected area diffraction patterns (SADPs) recorded with the electron beam near $<001>_{Al}$ for samples that experienced 120 h natural pre-aging before artificial aging at 180°C for up to 4 h, whereas Figure 4.74 shows the same for samples that experienced no natural pre-aging prior to artificial aging at 180°C for up to 4 h. The $<001>_{Al}$ zone axis has been shown to be the best orientation for visualizing the β″ phase [44,118].

There is no indication of precipitation in the bright field images and the SADPs of the T4 sample and the 120h NA,180°C-10min sample in Figures 4.73 (a,b) respectively. The solute clusters that are found in large numbers in Al-alloys in the T4 (Fig. 4.73(a)) and under-aged T6 conditions (Fig. 4.73(b) typically contain only a few to tens of solute atoms [11,78,80]. They are known to be fully coherent with the matrix and are difficult to resolve even by employing high resolution transmission electron microscopy (HRTEM). However, dark contrast arising from GP zones (~ 2 nm diameter) can be seen in the 0 h NA, 180°C-10min sample in Fig. 4.74(a). Faint streaks in the $<100>_{Al}$ SADP of this sample, as shown in Fig. 4.74(a), indicated that there was limited precipitation of β″ [44]. “Cross-shaped” streaks were observed in the $<100>_{Al}$ SADPs of all the samples aged at 180°C for 1 or 4 h, which correspond to weak diffractions produced by the needle β″-precipitates (Figs. 4.73(c,d) and Figs. 4.74(b,c)) [44]. The bright shadows surrounding the needles are reflections of the coherency strains present in the adjoining Al-matrix [44]. The β″-needles increase in size from ~ 2 nm diameter x 10 nm length in the 120h NA, 180°C-1h sample (Fig. 4.73(c)) to ~ 4 nm diameter x 25 nm length in the 120h NA, 180°C-4h sample (Fig. 4.73(d)). Similarly, the β″-needles increase in size from ~ 3 nm diameter x 20 nm length in the 0h NA, 180°C-1h sample (Fig. 4.74(b)) to ~ 4 nm diameter x 25 nm length in the 0h NA, 180°C-4h sample (Fig. 4.74(c)).

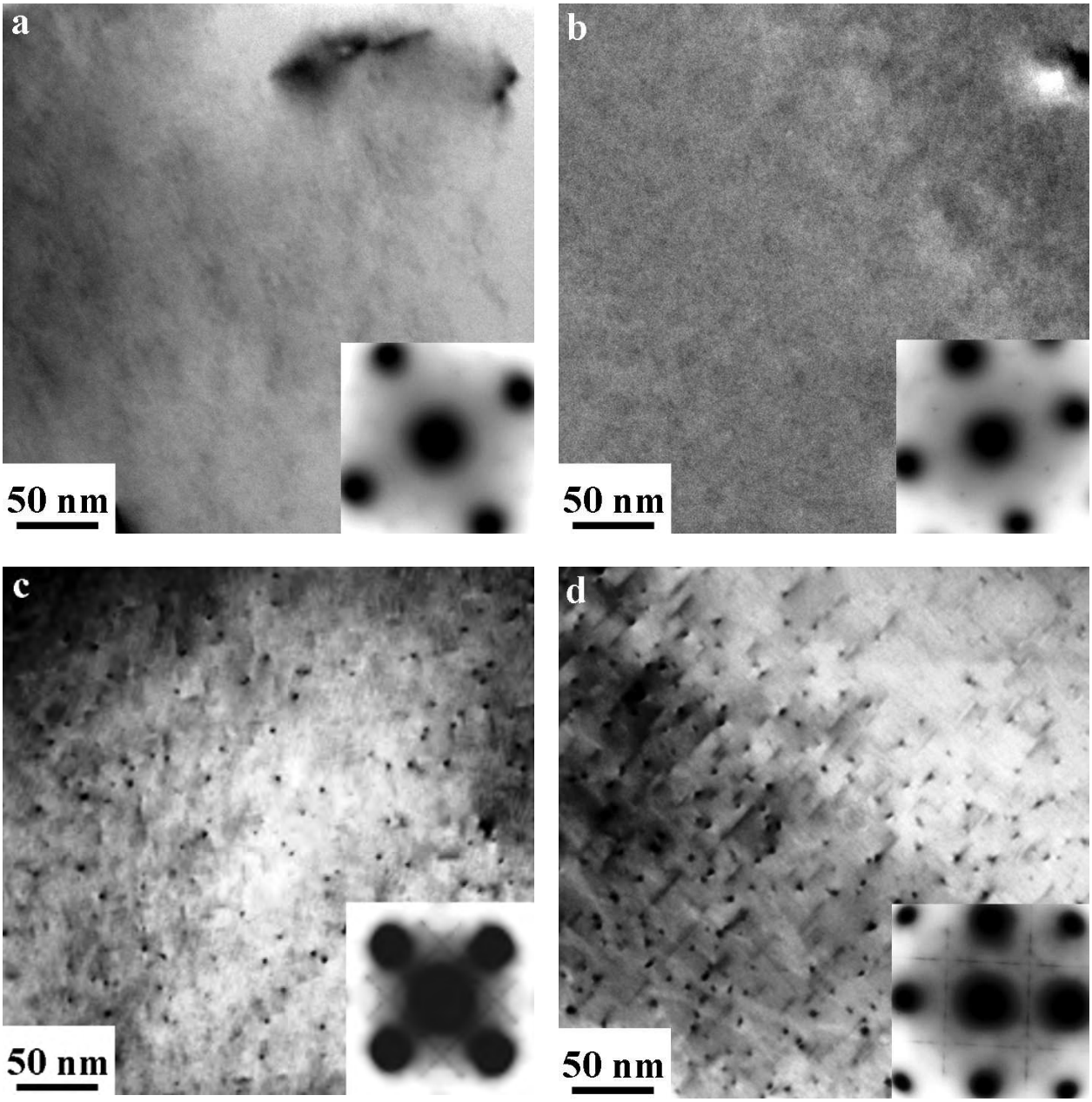

Figure 4.73: Bright field TEM images and SADPs for SSM-HPDC alloy F357 artificially aged at 180^{o}C for (a) 0 min – T4, (b) 10 minutes, (c) 1 h and (d) 4 h after 120 h natural pre-aging.

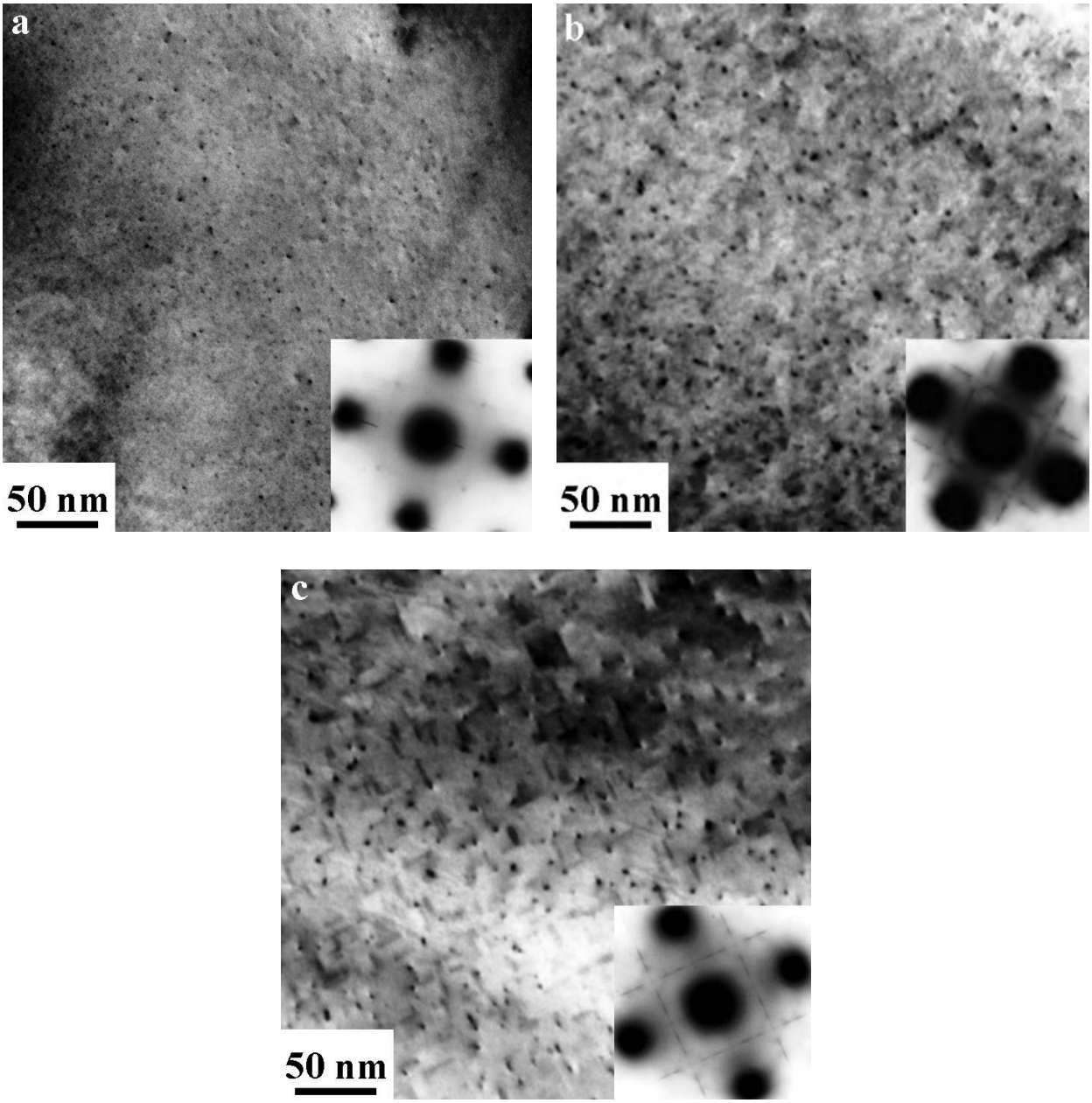

Figure 4.74: Bright field TEM images and SADPs for SSM-HPDC alloy F357 artificially aged at 180^{o}C for (a) 10 minutes, (b) 1 h and (c) 4 h after no natural pre-aging.

4.14.2.2. Atom Probe Tomography (APT)

Figure 4.75 shows three-dimensional (3D) reconstructed Mg atom maps, containing only solute-enriched features of samples that experienced 120 h natural aging before artificial aging at 180^{o}C for up to 4 h, whereas Figure 4.76 shows the same for samples that experienced no natural aging prior to artificial aging at 180^{o}C for up to 4 h. It is difficult to make a scientific distinction between GP zones and clusters of Mg-

Si since they have similar spherical morphologies [39]. GP zones and β″ can be distinguished more readily based on the differences in morphology (spheres vs needles) and also the β″ needles that generally contain more solute atoms than GP zones [42]. Critical sizes of 8 and 30 solutes have been used to distinguish between solute clusters and GP zones in two different wrought Al-Mg-Si alloys [42,78]. The small solute-rich features containing 10-20 detected solute atoms are designated as solute clusters in this study. Considering a detection efficiency of ~55% in APT analysis, a spherical feature of one nm in diameter should contain about 30 atoms. Use of 20 solutes assumes that a third of detected atoms will be Al atoms. Those containing 21-100 solute atoms are GP zones, and elongated β″ contains > 100 solute atoms (Table 4.24). Note that over-aged samples (180°C for > 4 h) were not investigated in this study and that no large β′ rods were detected in any of the analysed volumes (β′ rods typically have diameters of ~ 10 nm and lengths of several hundred nanometers [39]). Thus, even the largest precipitates with n > 1200 in this study refer to β″ rather than β′.

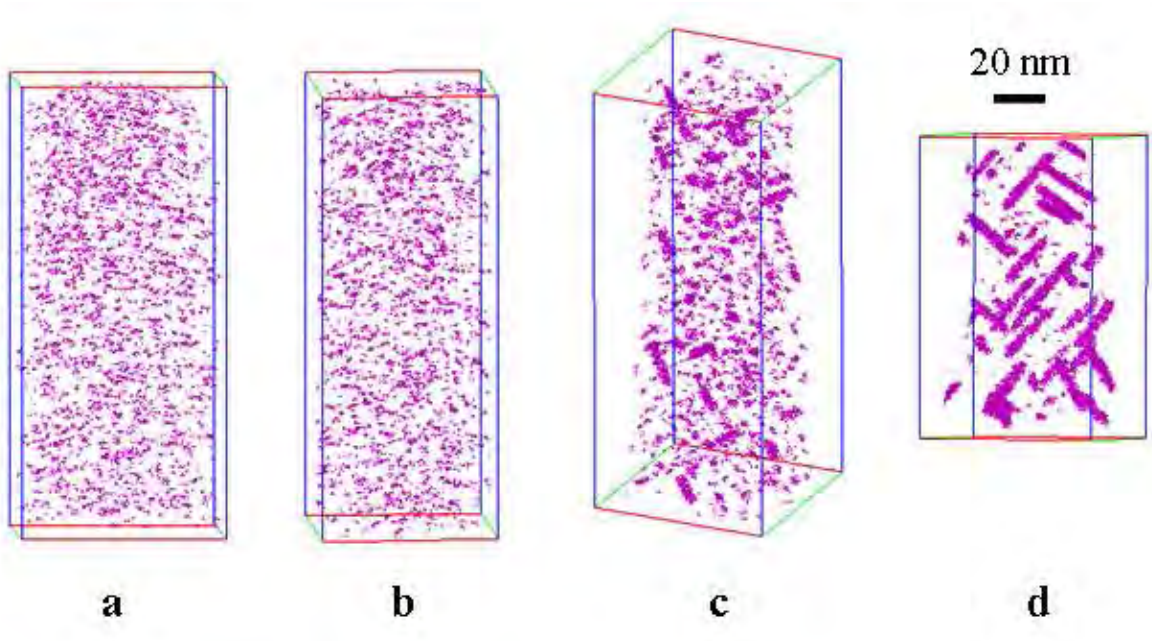

Figure 4.75: 3D Mg atom maps containing only solute enriched features after removing solutes in the matrix of SSM-HPDC F357 alloy samples aged at 180°C for (a) 0 h, (b) 10 min (c) 1 h and (d) 4 h after 120 h prior natural aging.

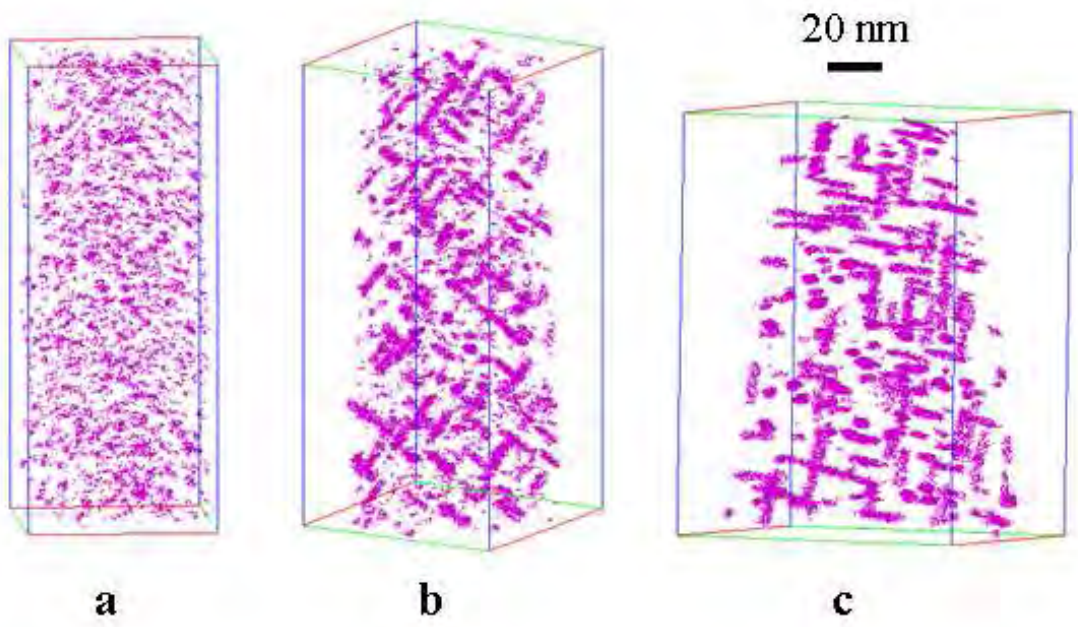

Figure 4.76: 3D reconstructed Mg atom maps containing only solute-enriched features after removing solutes in the matrix of SSM-HPDC F357 alloy samples artificially aged at 180°C for (a) 10 min (b) 1 h and (c) 4 h after no prior natural aging.

Table 4.24: Distinction between solute clusters, GP zones and β″ based on the number of solute atoms (n) detected with APT.

Precipitate	Number of detected solute atoms (n)
Solute clusters	10-20
GP zones	21-100
β″	>100

Only solute clusters and GP zones were observed in the samples in the T4 condition and artificially aged at 180°C for 10 min following 120 h NA, as seen in Figures 4.75 (a) and (b) respectively. In addition to the clusters that were found in Figs. 4.75(a,b), the characteristic needle-shape of the β″-phase was evidenced after artificial aging for 1 h (Fig. 4.75(c)), which corresponds to a significant increase in microhardness of the α-globules (Fig. 4.72). Figure 4.75(d) shows the structure of the peak aged sample, with an apparent higher volume fraction of β″. Figure 4.76(a) shows that more and larger GP zones are found in the sample aged for 10 min at 180°C with no prior NA

compared to Fig. 4.75(b) where 120 h prior NA had occurred, resulting in a higher microhardness value of the former (Fig. 4.72). Continuation of the decomposition of the supersaturated solid solution during artificial aging without prior NA results in a high density network of needle-shape β″ in Figure 4.76(b) after only 1 h, with a significantly higher number density of β″-precipitates compared to Fig. 4.75(c) where 120 h prior NA had occurred. The 0h NA,180^{o}C-1h sample falls within the hardness plateau (Fig. 4.72) and already has the same hardness than that of the 0h NA,180^{o}C-4h sample (Fig.4.76(c)). However, the β″-precipitates appear to be smaller in the 0h NA,180^{o}C-1h sample compared to the 0h NA,180^{o}C-4h (Figs. 4.76(b,c)), in agreement with the TEM micrographs in Figs. 4.74(b,c).

4.14.2.3. Chemical composition evolution of the matrix

The evolution of the Mg- and Si-contents of the matrix during artificial aging is illustrated in Figure 4.77. The Mg and Si contents of the sample in the T4 condition are 0.51 and 1.48at% respectively, which corresponds well with the composition of the alloy (Table 4.22), validating the approach used for sample preparation and analysis. The Si content is in reasonable agreement with a previous study by Taylor and co-workers [48], in which electron probe microanalysis (EPMA) was used to show that the amount of Si in the matrix was ~ 1.3wt% for an Al-7Si-Mg alloy with 0.5wt% Mg. Artificial aging at 180^{o}C for 10 min of the T4 sample does not result in a significant change in the composition of the matrix, measuring 0.52at% Mg and 1.46at% Si. However, further artificial aging causes a gradual decrease in matrix solute content due to precipitation reactions, with the 120h NA,180^{o}C-1h sample containing 0.35at% Mg and 1.41at% Si. Finally, peak aging (120h NA,180^{o}C-4h) results in the lowest matrix solute compositions of 0.12at% Mg and 1.04at% Si. When no natural aging precedes artificial aging, it is seen that the matrix composition decreases more rapidly than when natural pre-aging occurs, with the 0h NA,180^{o}C-10min sample's matrix containing 0.43at% Mg and 1.40at% Si. This decreases further to 0.25at% Mg and 1.23at% Si after 1 h at 180^{o}C, finally reaching values of 0.11at% Mg and 1.13at% Si after 4 h at 180^{o}C. Also, the final matrix compositions of both 180^{o}C-4 h artificially aged samples are similar, regardless of the differences in precipitation sequence caused by natural pre-aging.

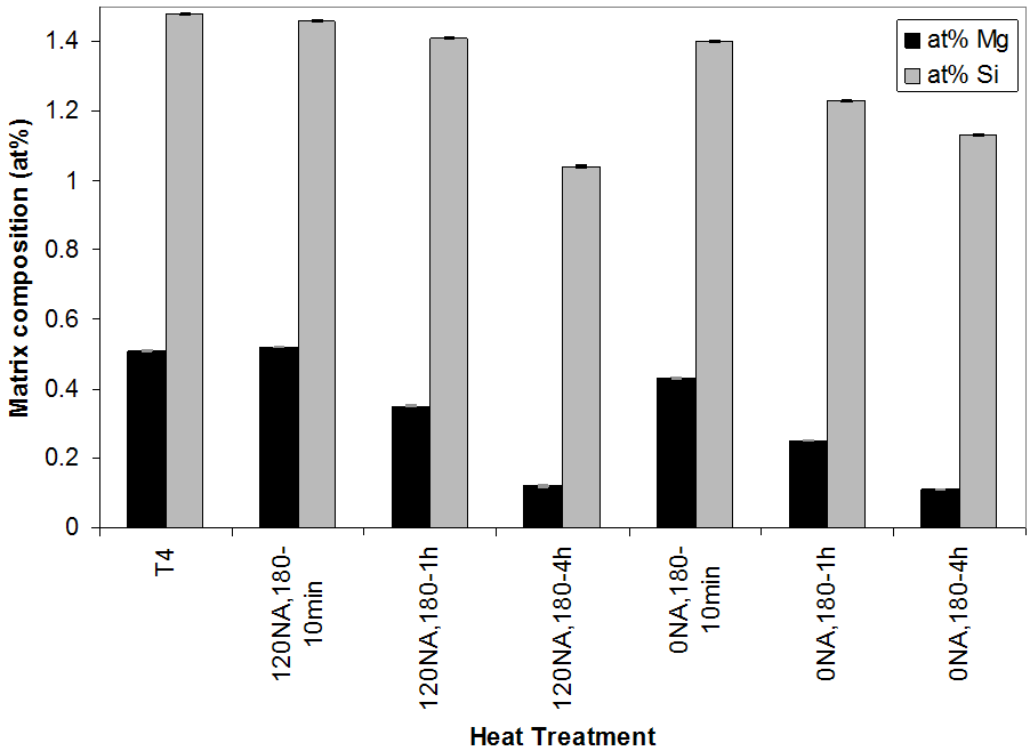

Figure 4.77: The Mg and Si compositions of the F357 matrix in different heat treatment conditions.

4.14.2.4. Number density of precipitates

The number density of precipitates for alloy F357 artificially aged at 180^{o}C for up to 4 h is shown in Figure 4.78(a) following 120 h of natural pre-aging and in Figure 4.78 (b) following no natural pre-aging. Figure 4.78 illustrates that the various precipitates can co-exist during precipitation, which is not discernible from equation 2.1.

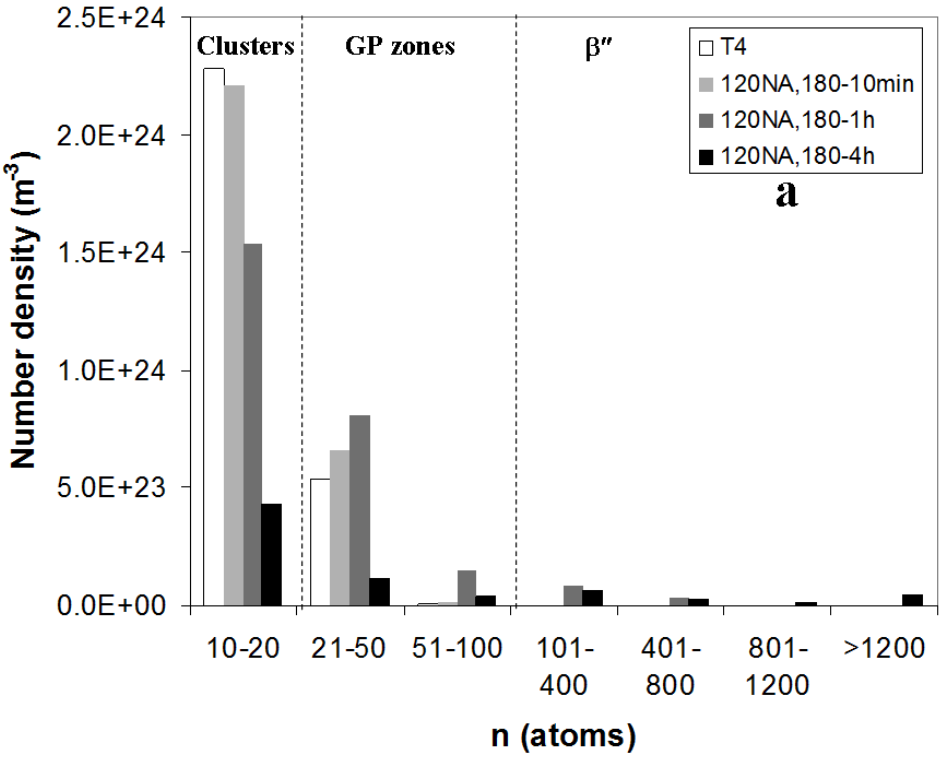

Figure 4.78(a): Comparison of the number density of precipitates for alloy F357 artificially aged at 180°C following 120 h natural pre-aging.

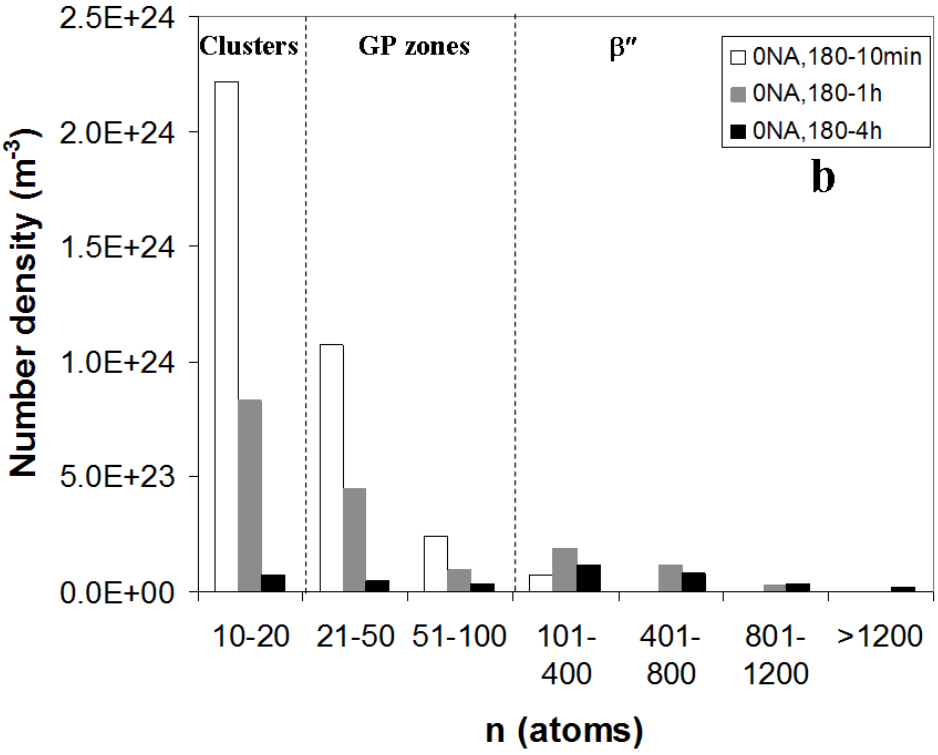

Figure 4.78(b): Comparison of the number density of precipitates for alloy F357 artificially aged at 180°C following no natural pre-aging.

4.14.2.5. The Mg:Si ratio of clusters and precipitates in alloy F357

The composition of the precipitates analysed by APT is normally expressed through the ratio of the main alloying elements, rather than the total quantity of aluminium and solute atoms that are detected in the precipitates [42]. This is due to the issues associated with the acquisition and analysis of atom probe data, especially regarding aberrations in preferential evaporation and ion trajectory [119,120]. Considering the proposed decomposition of the SSS of Al-Si-Mg alloys in equation 2.1, it is seen that the Mg:Si ratio theoretically increases from 0.83 in β″ to 1.7 in β′ to 2 in β. The Mg:Si ratio of solute clusters, GP zones and β″-needles after various stages of artificial aging is shown in Figure 4.79(a) for samples that experienced 120 h natural pre-aging and in Figure 4.79(b) for samples that experienced no natural pre-aging. It is seen that, in general, the Mg:Si ratio increases from ~ 0.6-1.2 with the number of solute atoms within the precipitates.

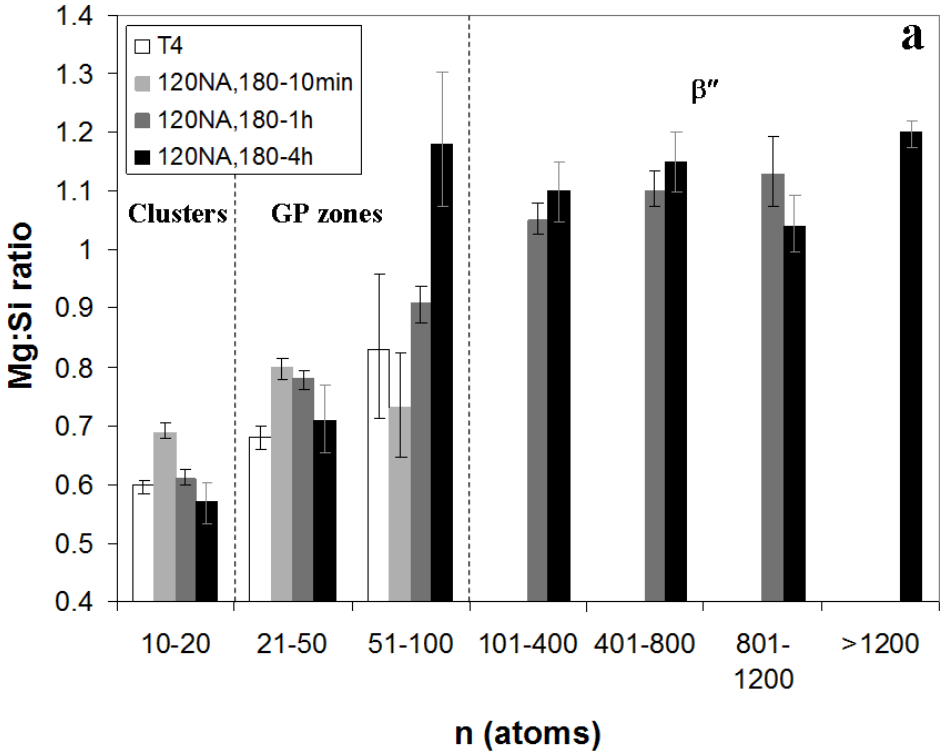

Figure 4.79(a): The Mg:Si ratio of solute clusters, GP zones and β″-needles in F357 samples that were naturally aged for 120 h prior to artificial aging.

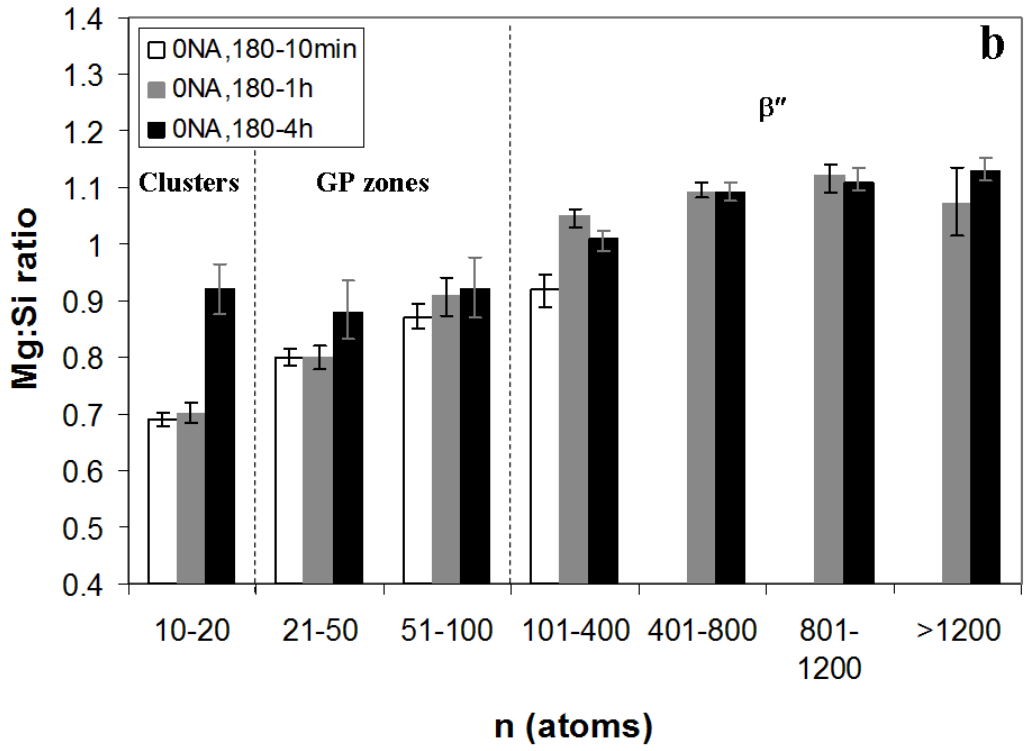

Figure 4.79(b): The Mg:Si ratio of solute clusters, GP zones and β″-needles in F357 samples that were not naturally aged prior to artificial aging.

4.14.2.6. Incorporation of Al into clusters and precipitates of alloy F357

Significant quantities of Al have been detected in all precipitates in this study, despite it being generally accepted that the β″-phase consists of only Mg and Si (Mg_5Si_6) [45]. On average, the solute clusters were found to contain ~ 3.7at% Mg and 5.5at% Si, the GP zones ~ 6.1at% Mg and 6.5at% Si and the β″-needles ~ 10.5at% Mg, and 9.3at% Si. Buha and co-workers [42] also found that the clusters, GP zones and β″-needles in wrought alloy 6061-T6 contained significant amounts of between 65 and 80at% Al. Similar results have also been reported by Vaumousse and co-authors [98] for an Al–Mg–Si–Cu alloy containing an excess of Si. Structural models that accommodate Al atoms in β″-needles and GP zones have been proposed based on TEM studies [118,121].

4.14.2.7. Incorporation of Cu into clusters and precipitates of alloy F357

A few APT precipitation studies have been conducted using pure ternary Al-Mg-Si alloys [50,80]. However, addition of other alloying elements and impurity elements in aluminium alloys can influence precipitation. The addition of Cu for example is

claimed to lead to a higher nucleation rate and refinement of GP zones and β″-precipitates in these alloys [50,51]. The F357 alloy used in this study is a commercial alloy containing numerous alloying elements, with a Cu content of 0.02at% (Table 4.22). The Cu content of the clusters/precipitates is shown in Fig. 4.80(a) for artificial aging with 120 h prior NA and in Fig. 4.80(b) for artificial aging without prior NA.

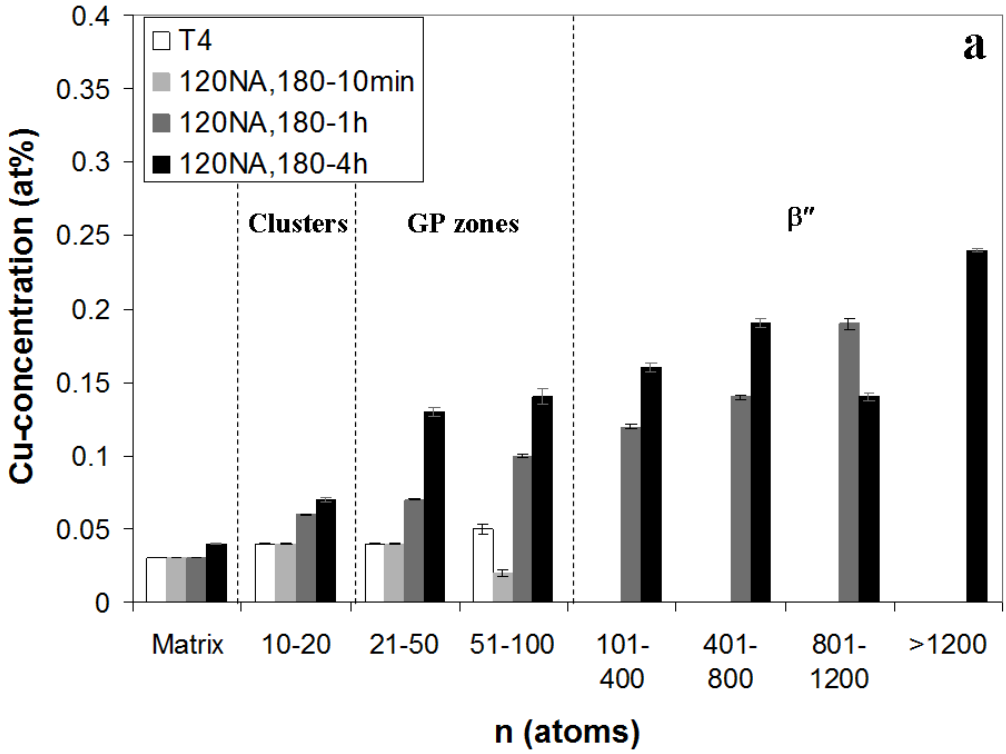

Figure 4.80(a): The Cu content in at% of the clusters/precipitates after artificial aging of alloy F357 with 120 h prior NA.

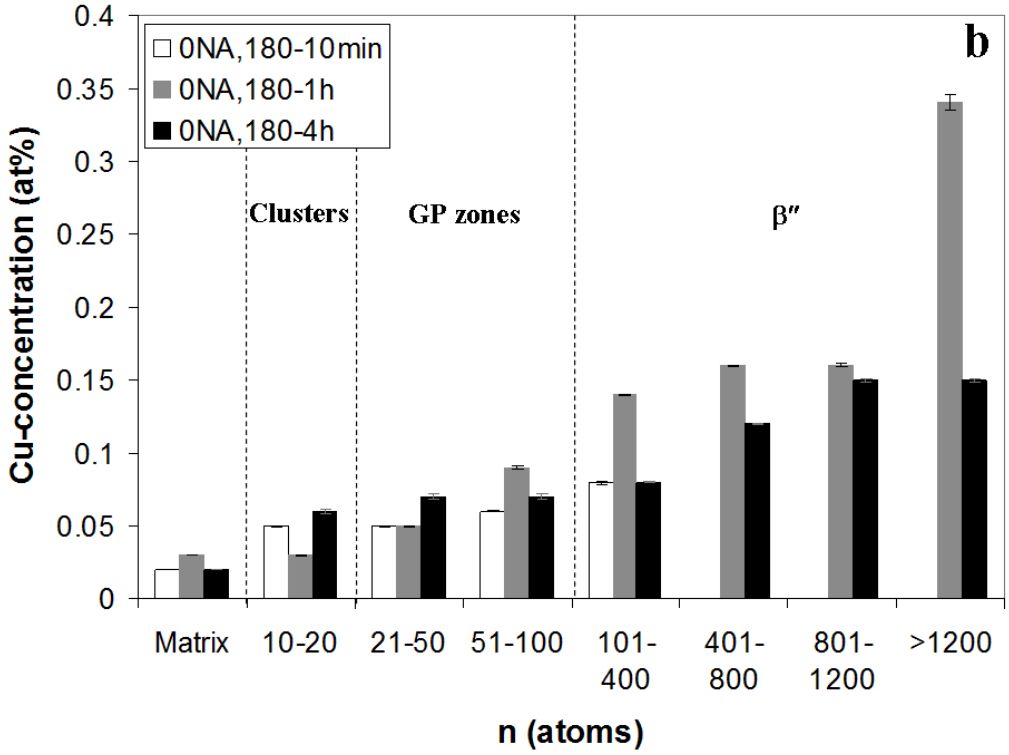

Figure 4.80(b): The Cu content in at% of the clusters/precipitates after artificial aging of alloy F357 without prior NA.

The matrix content of Cu analysed by APT is generally similar to the nominal Cu composition of the alloy, namely 0.02at%. In general, the Cu-content of the particles increases with artificial aging time and as the decomposition of the SSS progresses from clusters to GP zones to β″. Buha and co-workers [42] also found in a 6061-T6 wrought alloy that all precipitates classified as GP zones and β″ were enriched in Cu, whereas no Cu was associated with the solute clusters. Considering Table 4.22, it is seen that Fe and Ti are the other main alloying elements in this alloy. However, neither Fe nor Ti was detected in noteworthy quantities within any of the precipitates in this study and they were detected in the matrix only as trace elements. These elements are rather incorporated into intermetallic particles of which π-$Al_8FeMg_3Si_6$, β-Al_5FeSi and Al_3Ti are the most common in this alloy [HM8].

5. DISCUSSION

5.1. SSM-HPDC

5.1.1. Rheoprocessing

The rheoprocessing step during SSM-HPDC produces relatively coarse globular primary α-Al grains (Fig. 4.5). The coarse α-Al primary globular structure of 60-70μm diameter (Table 4.1 and Fig. 4.55(a)) is typical for SSM-processed A356/7 alloys – see for instance Fig. 2.15 from Nafisi et al [56]) where even coarser average globule circular diameters of 81μm in A356 without Ti and B, and with a diameter of 78μm in A356 with Ti and B, was found. Birol [13,14] postulated that the favourable impact of the globular structure (presumably lower surface area/volume) of the globular primary α-Al is offset by this relatively coarse structure in SSM-processed alloys and that this is the main cause of the comparable heat treatment response between globular and dendritic A356/7 alloys. However, this study has considered the effects of both fine (Fig. 4.55(b)) and relatively coarse (Fig. 4.59) dendritic microstructures in comparison with the globular SSM-processed microstructure and found that the strength (or hardness) in the T6 temper condition is controlled primarily by the Mg-content of the alloy (see Fig. 4.62), rather than primary α-Al microstructure.

5.1.2. High pressure die casting

The relatively high cooling rates that are achieved with HPDC (Fig. 4.4) play an important role in the microstructural evolution and heat treatment response of these alloys. Figure 4.4 illustrates that cooling rates of ~ 18^{o}C/s are estimated during the initial stages of solidification of SSM-HPDC castings and this results in modification of the eutectic component, even at low Sr levels of only 14 ppm (Fig. 4.6). It also enables rapid spheroidisation of the eutectic silicon particles during solution treatment (Fig. 4.8 and also see section 5.2.1).

The high cooling rates additionally retain a relatively high quantity of solutes in solid solution which causes a decrease in the time needed for solution treatment (see section 5.2.2) and allows a relatively high aging response for the T5 temper condition (see section 5.5).

5.2. Solution heat treatment

5.2.1. Spheroidisation of eutectic Si

The purpose of modification is to enable rapid spheroidisation of the silicon particles during solution treatment, with the advantage of high cooling rates during SSM-HPDC being that low Sr levels of only 14 ppm are required (Fig. 4.8) as compared to about 200 ppm that is necessary in permanent mould and investment cast A356/7 [9].

The cube of the change in mean diameter of the Si eutectic particles is in reasonable direct proportion to the solution treatment time (Fig. 4.11) as predicted by Lifshitz-Slyozov-Wagner (LSW) for the diffusion controlled coarsening of a second phase. Ogris has also shown that coarsening of the eutectic Si-particles follows the Lifshitz-Slyozov-Wagner (LSW) theory of Ostwald ripening [6]. However, in the study of Ogris [6], the mean diameter of Si-particles was incorrectly plotted as a function of $t^{1/3}$. This implies that the initial diameter (D_o) in the LSW theory is zero, which is obviously not the case (Fig. 4.10). The Si-particles are not spheroidised at the start of solution heat treatment, but they do not have a zero size. The slight deviation from linearity at short solution treatment times in this study in Fig. 4.11 is therefore most likely related to the fact that the Si particles do not commence growth immediately as spherical particles, but firstly have to undergo spheroidisation before growth can continue through LSW coarsening. This observation is supported by the better linear fit in Fig. 5.1, by rather starting the LSW-graph only at t = 30 minutes where it is known that spheroidisation has occurred (Fig. 4.10), and using D_o = 1.12 μm from Table 4.4. Further support for this argument can be found in the work of Parker and co-workers [69], who also did not consider spheroidisation as part of the coarsening process.

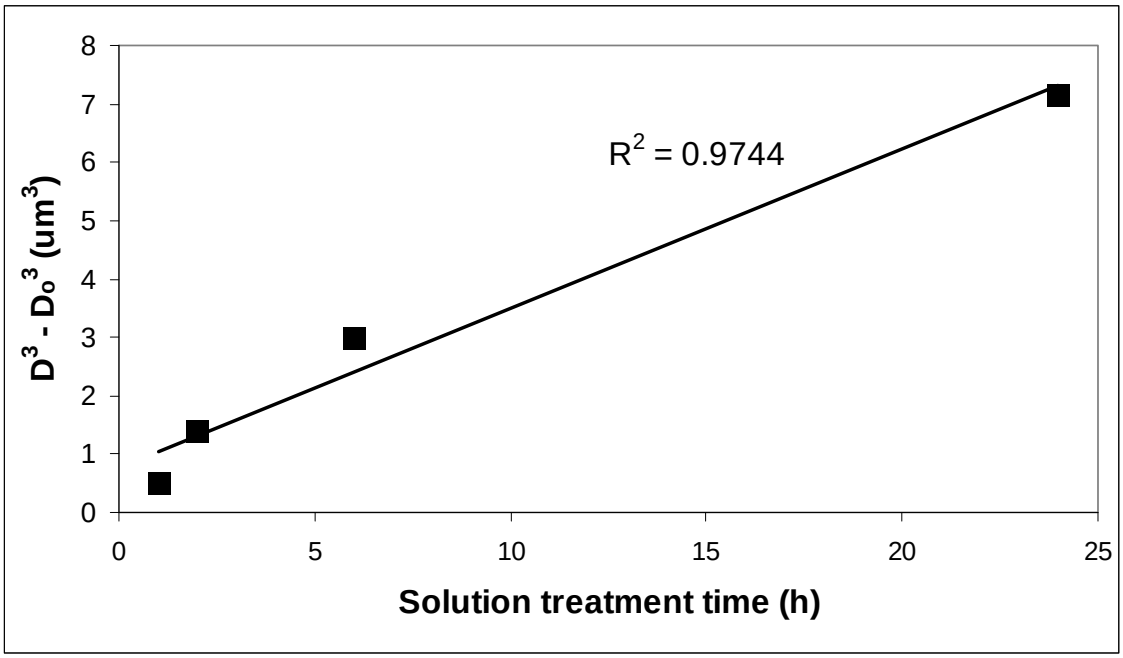

Figure 5.1: The cube of the change in mean diameter of the Si eutectic particles as a function of solution treatment time at 540°C using a starting diameter (D_o) of spheroidised Si after 30 minutes of solution treatment.

Spheroidisation of the eutectic Si occurs rapidly at 540°C (Fig. 4.10), with Parker and co-workers [69], as well as Ogris [6] suggesting that it is complete in less than 10 minutes. The eutectic Si-particles in unmodified alloys do not spheroidise, even after long times at 540°C (Fig. 4.9). The long solution treatment times (4-10 h) frequently specified for these alloys (Table 2.6) most likely cater for unmodified alloys and would be an energy and production restriction for modified alloys, provided that complete solutionising of solutes can also occur in shorter times [58].

5.2.2. Dissolution of solutes and reduction of microsegregation

Taylor et al [47] and Rometsch et al [68] showed that dissolution of Mg_2Si particles and homogenisation of the concentration profiles are complete within one hour at 540°C for both A356 and A357. In spite of these short reported times (and the rapid spheroidisation of the Si-particles in modified alloys), times of 4-10 h are specified for these alloys at 540°C (Table 2.6). Rosso and Actis Grande [90] proposed that a solution heat treatment of 1 hour at 540°C is sufficient to obtain a high level of properties in the T6 temper of SSM-processed A356. According to Dewhirst [12], the optimum solution treatment time for SSM-processed A356 at 540°C is 4 h. Birol [13]

suggested that a solution treatment time of at least 2 h at 540^{o}C is required to obtain maximum hardness after artificial aging in the SSM-processed alloy F357 (Fig. 2.36). A large variation in suggested solution treatment times is therefore found in the literature for SSM-processed alloys A356/7. The tensile results in Table 4.5 of SSM-HPDC alloy F357 with a high Mg-content of 0.62% Mg in this study show that a high level of properties in the T6 temper condition can be obtained after only 30 minutes of solution treatment at 540^{o}C. This is in contradiction to the results of Birol in Fig. 2.36 [13] and is most likely caused by the fact that HPDC was used in this study, resulting in higher cooling rates during solidification (Fig. 4.4) than achieved by Birol in his study. These high cooling rates achieved with HPDC promotes enhanced solutionising before heat treatment commences and result in shorter times being required.

5.2.3. Impact strength

Another important consideration to optimise solution treatment time is the impact strength of the alloys that can be achieved (Table 4.6). Zhang et al [67] found that shorter solution treatments than the standard 6 hours resulted in lower impact strengths for permanent mould cast A356-T6. This was attributed to the smaller interparticle Si-spacing after shorter solution treatments, which assisted with crack growth. However, Ogris [6] showed that the impact strength for thixoformed A357-T6 was better using only 3 minutes solution treatment compared to 12 hours. This was postulated to be due to the fact that the Si was three dimensionally separated after 3 minutes at 540^{o}C, whereas longer times caused the silicon to agglomerate and form large interconnected silicon crystals. This hypothesis seems unlikely as the agglomeration of the Si should rather form large crystals that are not interconnected as the Si- interparticle spacing increases due to coarsening. Similar impact properties were obtained after a solution treatment of 1 h rather than 6 h for each composition in this study in the T4 and T6 temper conditions (Table 4.6). However, it was also shown in Fig. 4.13 that the strength of the alloy plays a more important role in the impact strength in the T4 and T6 temper conditions than the solution treatment time. The higher impact strength for thixormed A357-T6 found by Ogris [6] using only 3 minutes solution treatment time rather than 12 h, is therefore most likely a “strength effect” rather than a “Si-interparticle spacing effect”. Solution treatment for only 3 minutes does not allow complete dissolution of strengthening solutes, resulting in a lower strength in the T6 temper condition (YS = 240 MPa, UTS = 325 MPa) than

after 12 h solution treatment (YS = 312 MPa, UTS = 358 MPa) [6]. The lower strength of the 3 minute solution treated sample will, however, improve the impact properties of the alloy according to Fig. 4.13.

In addition, Figure 4.53 also indicates that good mechanical properties in the T4 and T6 temper conditions can be achieved in a larger, more complex casting such as an automotive brake calliper by using shorter solution treatment times.

Conclusion: Considering the processes of spheroidisation of eutectic Si-particles, dissolution of solutes, reduction of microsegregation, achieving the optimum tensile and impact properties, as well as the size of the casting, the optimum solution treatment parameters for SSM-HPDC alloys A356 and F357 are suggested to be 540^{o}C for 1 h.

5.3. Quench after solution treatment

Slow quench rates after the solution heat treatment can reduce the problems of distortion and residual stresses, but also result in a loss of strength after artificial aging (Table 4.7). To get an estimate of the quench rate in water at 70^{o}C, the data of Zhang and Zheng [73] (Table 2.5) were plotted as shown in Fig. 5.2.

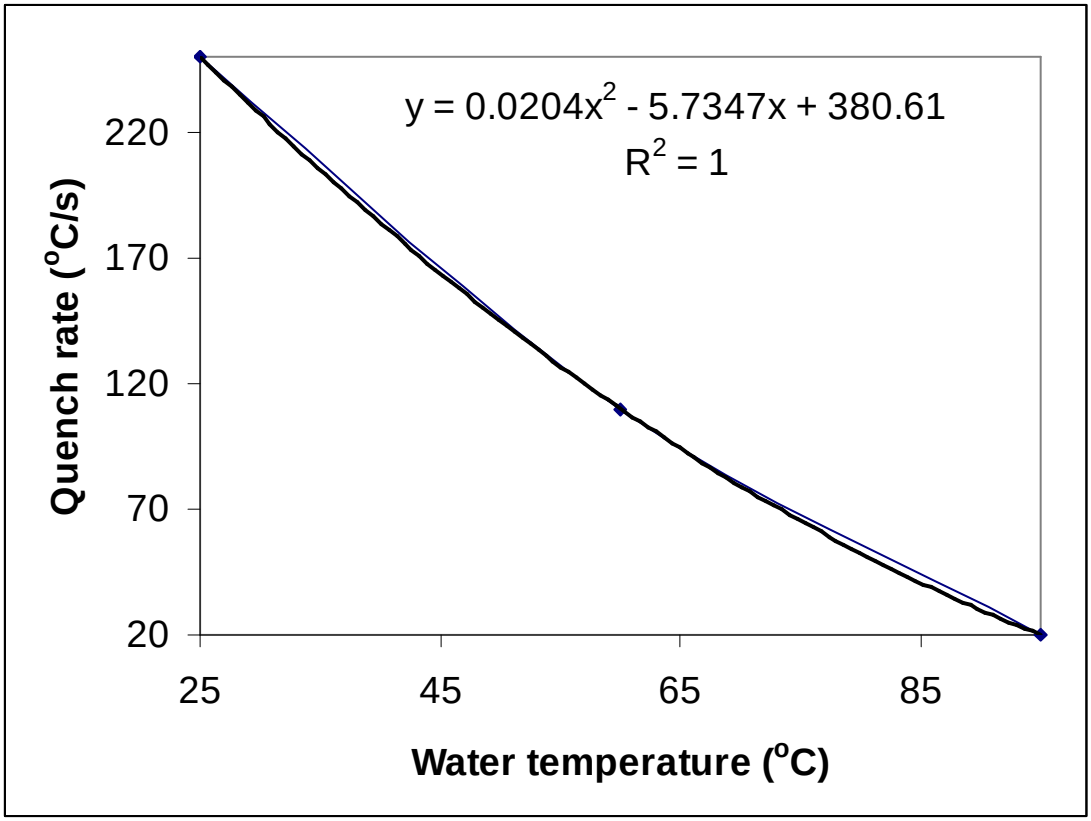

Figure 5.2: Quench rate as a function of water temperature (from [73]) for A356 samples of 14x14x55 mm^3 size.

Using the equation of the trend line in Fig. 5.2 it can be estimated that the quench rate in water at 70°C is ~ 80°C/s (note that the geometry of the plates used in this study (6x55x100mm^3) is reasonably comparable to the 14x14x55mm^3 samples used in [73]). The YS and UTS of the peak aged A356 in this study, as a function of quench rate (Table 4.7) are compared in Fig. 5.3 with those presented by Zhang and Zheng in their Fig. 2.24 [73].

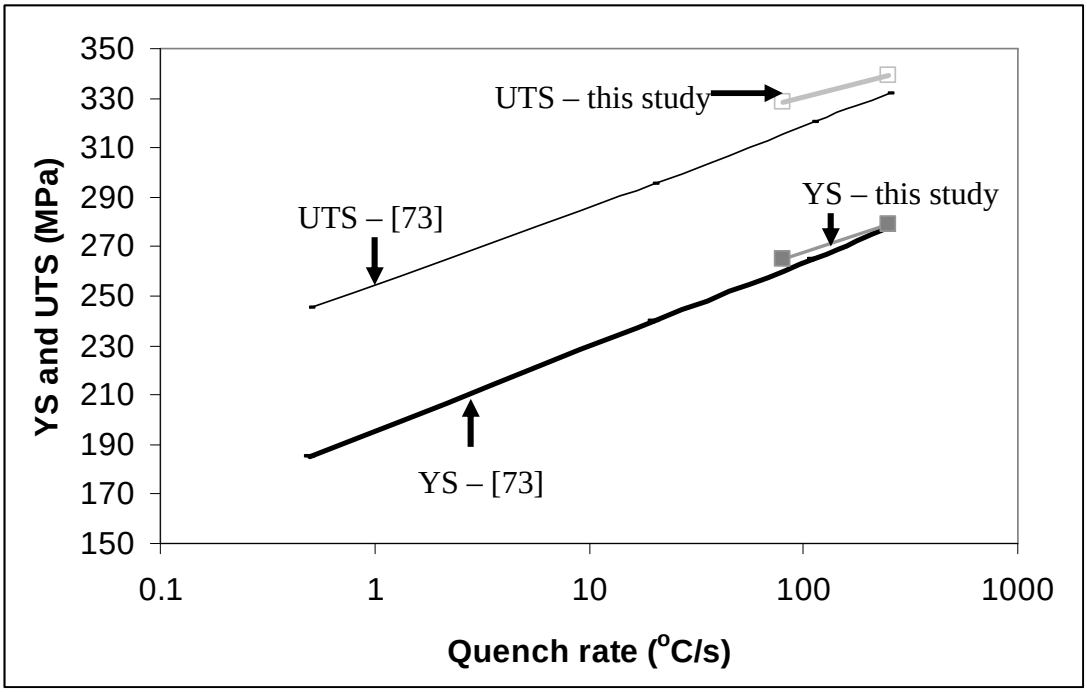

Figure 5.3: Strength of peak-aged alloy A356 as a function of the average quench rate from this study in comparison with data from Zhang and Zheng [73].

Despite the differences in microstructures (globular in this study and dendritic in [73]), the geometry of samples and artificial aging parameters (180°C-4h in this study and 170°C-6h in [73]), the effects of quench rate are very similar: the values of YS and UTS and the slopes of the curves in Fig. 5.3 correspond well. In both this study and in ref. [73] a solution treatment temperature of 540°C was used, resulting in similar solute supersaturation (the 0.40% Mg in this study and 0.38% Mg in [73] are similar) and vacancy concentration after quenching.

5.4. The T6 temper condition

It was shown that the onset of the hardness plateau (no natural aging) and hardness peak (with natural aging) in Fig. 4.18 as a function of artificial aging temperature follows an Arrhenius-type response (t_{T6} = C EXP (Q/RT)) and is described by equations 4.2 and 4.3.

$$t_{T6} = 2.3 \times 10^{-15} \text{ EXP } (163000 / 8.314T) \qquad (4.2)$$

$$t_{T6} = 4.9 \times 10^{-16} \text{ EXP } (163000 / 8.314T) \qquad (4.3)$$

An instantaneous transfer from quench to artificial aging does not have an influence on the activation energy Q of 163 kJ/mol, which is used in Chapter 6 where the artificial aging curves are modelled mathematically. However, the pre-exponential factor (C) is lower with no natural pre-aging, thereby resulting in a much faster artificial aging response. The total t_{T6} time is a complex sum of the "incubation time"+ "time of nucleation of GP zones"+ "time of growth/coarsening of GP zones"+ "time of transformation of GP zones to β″ + "time for growth and coarsening of β″. The reasons for the lower C value (and hence lower t_{T6} times) in samples that had experienced no natural pre-aging are discussed in more detail in the section on APT results (section 5.8), but in short is due to the much faster formation of GP zones and β″ owing to a high concentration of quenched-in vacancies.

The main advantage of equation 4.2 (Table 4.11) is that artificial aging times at temperature can be calculated that will result in similar tensile properties being obtained, regardless of the natural pre-aging time period. For instance, ASTM Standard B969-10 specifies that SSM-processed A356 should be artificially aged at 160^{o}C for 3-6 h to obtain the T6 temper condition (Table 2.6). However, Table 4.11 of this study (equation 4.2) shows that at 160^{o}C, a time of 29 h would be required to obtain peak properties, which also simultaneously gives similar properties in this alloy regardless of natural pre-aging. This is illustrated graphically in Figure 5.4, which shows artificial aging curves of SSM-HPDC alloy A356 (0.34% Mg) at 160^{o}C following no or 120 h natural pre-aging. Using the specified times of 3-6 h according to ASTM B969-10 will result in a large variation in tensile properties in the different naturally pre-aged alloys, in contrast to when a time of 29 h (according to Table 4.11) is used. According to this study, the specified times to achieve the T6 condition at 160°C in ASTM B969-10, probably need to be revised.

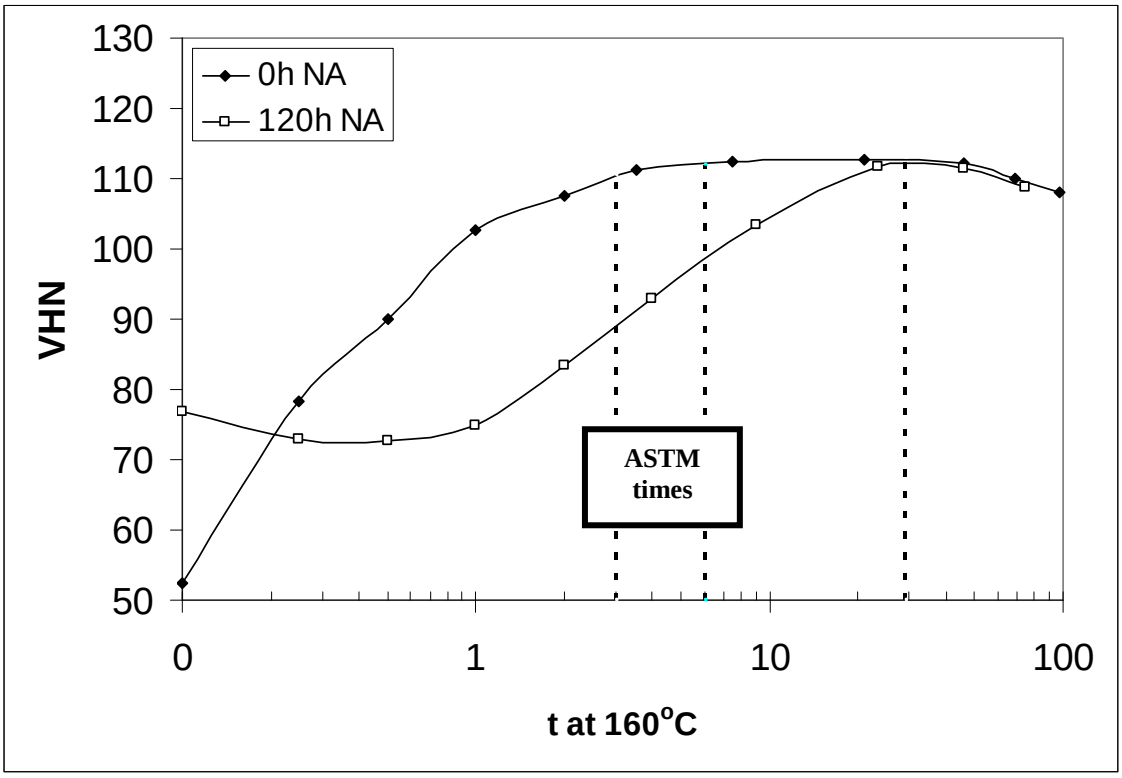

Figure 5.4: Artificial aging curves of SSM-HPDC alloy A356 (0.34% Mg) at 160°C following no or 120 h natural pre-aging, showing specified aging times of 3-6 h according to ASTM B969-10, as well as 29 h according to Table 4.11.

An artificial aging time of 29 h may be prohibitively long and therefore artificial aging parameters of 180°C for 4 h (Table 4.11) are suggested as the optimum for SSM-HPDC alloys A356 and F357 (Fig. 4.18) and for dendritic A356 and F357 (Figs. 4.60 and 4.61). The tensile properties that can be obtained using these parameters are compared with those specified by ASTM B969-10 (Table 2.9) for mid-range compositions of SSM-processed alloys A356 and F357 in Table 5.1. It is seen that the specified tensile properties are met or in most cases exceeded by using the suggested 180°C-4h T6 heat treatment cycles.

Table 5.1: Mid-range mechanical properties for rheocast A356 (0.35% Mg) and A357 (0.55% Mg) in T6 temper condition according to ASTM B969-10 and the results found in this study for SSM-HPDC A356/F357.

Alloy	Temper	0.2% YS (MPa)	UTS (MPa)	% Elongation
A356	T6-ASTM B969-10	235	310	11
A356-0.31% Mg	540^{o}C-1h, (20-120)h NA,180^{o}C-4h	254	313	10.5
A357	T6-ASTM B969-10	290	345	6
F357-0.49% Mg	540^{o}C-1h, (20-120)h NA,180^{o}C-4h	303	356	10.6

The high %elongation after fracture of the SSM-HPDC alloy F357-0.49% Mg in Table 5.1 merits further discussion. In general, the ductility of F357 is lower than that of similarly heat treated A356 (Table 4.14) due to the presence of the π-phase (Fig. 4.22). The F357 alloy in Table 5.1 used in this study was produced with a 130 ton clamping force HPDC machine, whereas the A356 was produced with a 50 ton clamping force machine. The higher intensification pressures that could be applied with the bigger machine most likely caused a reduction in microporosity compared with the smaller machine. Microsporosity in these alloys are known [103] to have a significant influence on ductility and UTS, but not much on YS and therefore the good linear graph in Fig. 4.58 is still found regardless of the casting machine used.

5.5. The T5 temper condition

The tensile properties of differently T5-treated samples of SSM-HPDC alloy F357 (with 0.63% Mg) are compared in Table 4.16. From this Table it can be seen that slightly better T5 tensile properties are obtained by water quenching the alloy after SSM-HPDC rather than cooling in air. For these experiments, a 50 ton clamping force Edgewick HPDC machine was used and a relatively long intensification time of 30s was applied before the plate castings could be quenched in water or cooled in air. The average cooling rates achieved within different parts of the plate-casting between 0-10s, 10-20s and 20-30s are shown in Fig. 4.4. Even though fast cooling rates are achieved within the plates during the first ten seconds of intensification, the cooling

rate drops significantly thereafter. Ideally, to have achieved the maximum effects of water quenching after casting, an intensification time of only 10s should rather have been used, especially considering that solidification within the plate is predicted to be complete after only ~ 5.5 s (Fig. 4.2(a)).

From Table 4.16 it can also be seen that the air-cooled T5 sample's tensile properties have significantly higher standard deviations than the water quenched T5 samples. For example, the standard deviations for the YS, UTS and %elongation for the AQ, 120h NA,180^{o}C-4h samples are 9.9, 10.9 and 1.5 respectively. This is significantly higher than the standard deviations for the YS, UTS and %elongation for the WQ, 120h NA,180^{o}C-4h samples of 1.9, 4.9 and 1.0 respectively. Considering Fig. 4.3, it can be seen that the large volume of the biscuit causes a heterogeneous temperature distribution throughout the plate casting, which would be present for longer times in the air-cooled T5 sample. This is most likely the cause of the high variation in tensile properties for this sample in Table 4.16.

The presence of β-Mg_2Si in both the F(AQ) and F(WQ) samples are shown in Fig. 4.39. The solution treatment of the T6 temper condition dissolves this β-Mg_2Si phase and the supersaturation of solute is significantly higher, which results in the artificial aging response for the T6 temper (e.g. Fig 4.18) being considerably more pronounced than for the T5 temper (Fig. 4.40). According to Fig. 2.23, the "nose" of the T-t quenching diagram for alloy F357 lies at approximately 350^{o}C and 10 s. The ProCAST simulation of Fig. 4.3 reveals that a temperature of 350^{o}C is only reached in the plate after approximately 15 s (Fig. 5.5), resulting in the precipitation of β-Mg_2Si as shown in Fig. 4.39.

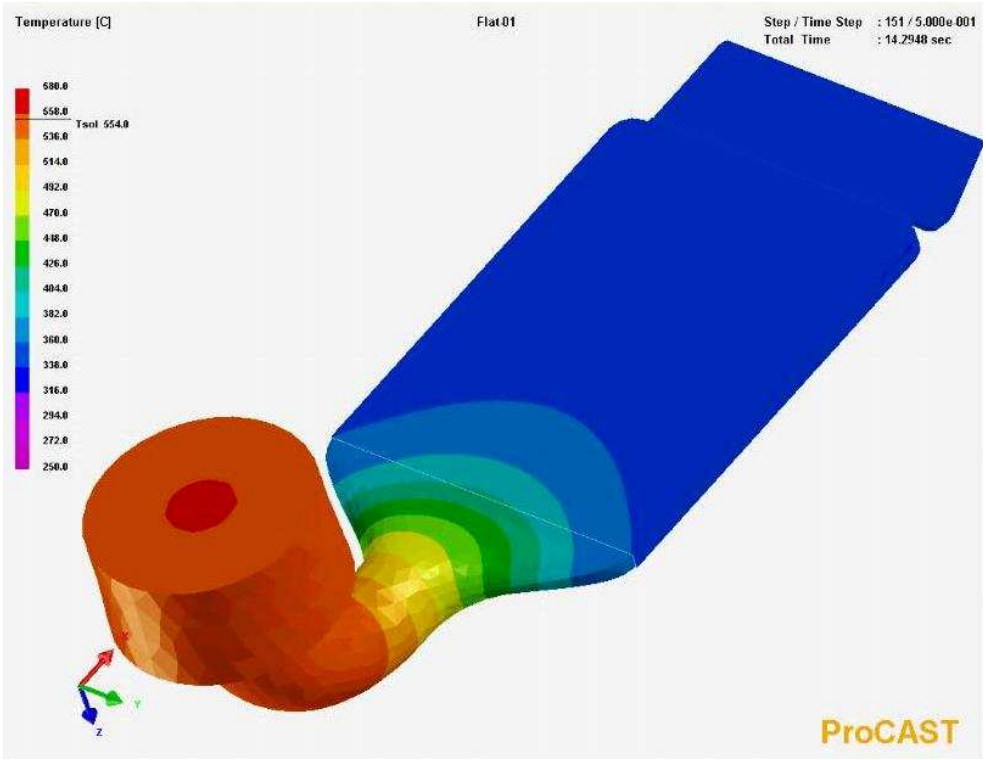

Figure 5.5: ProCAST simulation showing that the critical temperature of 350°C (Fig. 2.23) is reached in the plate during SSM-HPDC after ~ 15 s.

5.6. Comparison of aging response of globular and dendritic Al-7Si-Mg alloys

Birol [13,14], using DSC (Fig. 2.35) and artificial aging curves (Fig. 2.36), showed that there are no differences between the age hardening response of dendritic and globular Al-7Si-Mg alloys. The artificial aging curves of dendritic and globular A356 in this study (Figs. 4.60 and 4.61), as well as tensile results in Table 4.19 corroborate this conclusion. Plotting the Vickers hardness in the T6 temper condition as a function of the (at% Mg available for precipitation hardening)$^{1/2}$ in Fig. 4.62 results in an excellent linear correlation with R^2 = 0.9834. The data points in Fig. 4.62 include hardness values of A356 and F357 SSM-HPDC plates (cast with 50 ton and 130 ton clamping force HPDC machines), SSM-HPDC brake callipers (cast with a 630 ton clamping force HPDC machine), gravity die cast brake callipers with a relatively fine dendritic microstructure (Fig. 4.55(b)) and investment cast plates with a relatively coarse dendritic microstructure (Fig. 4.59). The Si-contents of the alloys used in Fig. 4.62 varied between 6.6-7.3% (Tables 3.1, 3.3, 3.4), i.e. covering almost the whole range of 6.5-7.5% allowed in the specification (Table 2.1). Figure 4.62 therefore implies that the hardness of Al-7Si-Mg alloys in the T6 temper condition is controlled

primarily by the Mg-content available for precipitation hardening after solution treatment and is independent of the casting technique used (i.e. dendritic or globular primary α-Al microstructure). The insignificant influence of Si-content variation is due to the fact that these Al-7Si-Mg casting alloys contain an excess Si that is required to form the strengthening β″–precipitates, which has a Mg:Si ratio of 1.1-1.2 (Fig. 4.79). The other important alloying element controlling the age-hardening capacity of (dendritic and globular) Al-7Si-Mg alloys is in fact iron (section 4.6). The data points in Fig. 4.62 are all for alloys containing ~ 0.1% Fe. Higher Fe-contents (especially in alloys containing > 0.40% Mg) will result in a reduced response to age-hardening due to the stability of the π-$Al_8FeMg_3Si_6$ phase (Fig. 4.22(b)). Therefore, provided that the maximum quantity of the alloy's Mg is placed into solid solution during solution treatment (which might take longer than 1 h at 540^{o}C for dendritic alloys with a very coarse dendritic microstructures such as in large sand castings), and the alloy's Fe content is within specification (but preferably ~ 0.1%), the response to age hardening of Al-7Si-Mg alloys should be independent of the processing technique used.

5.7. Comparison of aging response of SSM-HPDC Al-7Si-Mg alloys with SSM-HPDC 6000 series Al-Mg-Si wrought alloys

Both conventional casting alloys A356/7 and the conventional Al-Mg-Si 6000 series wrought alloys are strengthened by β″, but the high Si content in the casting alloys compared to the wrought alloys has a significant influence on the age-hardening response (Fig. 4.70). The solute clusters that are formed during natural aging in alloy 6082 are known to be relatively stable at the artificial aging temperature [9]. This claim is supported by the small initial decrease in hardness during artificial aging of the naturally aged 6082 sample compared to the naturally aged A356 sample in Fig. 4.70. Natural pre-aging of 6082 has an important effect on the precipitation of GP zones and β″ [84]. The atomic clusters, which formed during natural pre-aging, and the low concentration of the quenched-in vacancies in the naturally pre-aged samples, have a delaying effect upon the nucleation of GP zones. As a result, the final β″ structure developed in these 6082 samples is coarse. However, the large number of GP zones formed in the 6082 samples artificially aged without natural pre-aging, transform into a dense structure of small β″ particles, with the number density of β″

precipitates being five times higher in samples that were artificially aged immediately after solution treatment compared to samples that were naturally aged for a week before artificial aging (i.e. 200 000 vs 40 000 particles/μm^3) [84]. The opposite of these processes is believed to occur in alloys such as 6004 [9]. Chang and co-workers [50] described the positive effect of natural pre-aging on precipitation hardening in a wrought alloy with a composition similar to the 6004 in this study. They showed, in an Al-0.44at% Mg-0.38at%Si alloy, that artificial aging of naturally aged samples increased the level of the peak hardness. This was attributed to the increase in the number density of needle-like precipitates (β″) as compared to the samples without prior natural aging.

It can also be seen from Figure 4.70 that the hardening response of alloy A356 is very rapid compared to that of the wrought alloys (with the response of 6004 being the slowest). Gupta and co-workers [88] studied the precipitation hardening in wrought 6000 series alloys with and without excess Si that is required to form stoichiometric Mg_2Si. They found that excess Si (which is most pronounced in the casting alloys in this study) reduced the time to initiate strengthening, possibly due to a higher driving force for nucleation which will lead to a finer particle size and shorter diffusion distances. They also found that excess Si increases strength in both the T4 and artificially aged tempers (T6), most likely due to a higher volume fraction of strengthening precipitates as well as from a finer particle size from the higher driving force for nucleation. This is also applicable to Fig. 4.70, where alloy A356 has higher hardness values than alloy 6004, even though A356 contained 0.36% Mg compared to the 0.45% Mg of the 6004. Low hardness values for wrought alloy 6004 upon aging have been reported before [122]. Gupta and co-authors [88] claimed that the improvements to the aging response due to excess Si were caused by enhanced precipitation of fine, uniformly distributed β″ particles. They also claimed that excess Si reduced the Mg/Si ratio in the zones/clusters and β″-precipitates, thus allowing higher levels of precipitation and strengthening. From Figure 4.70 it is evident that over-aging also occurs faster in A356 than the wrought 6000 series alloys. Especially alloy 6004 maintained its maximum hardness for a long time at 180^{o}C. Gupta and co-workers [88] determined that excess Si reduced the peak strength stability in the over-

aged conditions. The reduced Mg/Si ratio is believed to make the β″ phase less stable, and as a result, the stability in strength beyond the peak aging condition is reduced.

5.8. Nanostructural evolution during aging of Al-7Si-Mg alloys

The nanostructural evolution of Al-7Si-Mg alloys as studied by means of APT and TEM (section 4.14) allows the quantification of the precipitation sequence of Al-7Si-Mg alloys, while also considering the effects of natural pre-aging.

5.8.1. Artificial aging with natural pre-aging

The T4 sample (Fig. 4.75(a)) has a large number density (2.3 x 10^{24} m^{-3}) of solute clusters containing n = 10-20 solute atoms with few GP zones (5.4 x 10^{23} m^{-3}) and no β″-needles (Fig. 4.78(a)). Figure 4.78(a) also shows that the 120h NA,180^{o}C-10min sample has a slightly lower number density (2.2 x 10^{24} m^{-3}) of solute clusters than the T4 sample, but also a marginally higher number density of GP zones (6.7 x 10^{23} m^{-3}) and no β″-needles. This suggests that the 10 min artificial aging at 180^{o}C may have resulted in the dissolution of some of the solute clusters (< 20 solute atoms), with concurrent nucleation of some new and growth of all of the GP zones (> 20 solute atoms), which results in a small decrease in macrohardness (Fig. 4.72), YS and UTS (Table 4.23). Dissolution of room temperature clusters with artificial aging has been inferred from DSC before (Fig. 2.33). However, dissolution of a large number of clusters should result in an increase in Mg and Si concentrations of the matrix after 10 min at 180^{o}C. As shown in Fig. 4.77, however, no significant changes were measured with Mg and Si essentially remaining constant at 0.51 to 0.52at% and 1.48 to 1.46at% respectively. Therefore, it is more likely that the observed nanostructural change may be due to coarsening of some small solute clusters as was also postulated before for alloy 7050 [123]. The 120h NA,180^{o}C-1h sample has less clusters (1.5 x 10^{24} m^{-3}) and more GP zones (9.5 x 10^{23} m^{-3}) than the 120h NA,180^{o}C-10min sample (2.2 x 10^{24} m^{-3} clusters and 6.7 x 10^{23} m^{-3} GP zones respectively), indicating further growth of clusters to GP zones during this artificial aging time period. Also, in contrast to the T4 and 120h NA,180^{o}C-10min samples where no β″-needles were found, the 120h NA,180^{o}C-1h sample has 1.2 x 10^{23} m^{-3} small β″-needles with n = 100 – 1200 solute atoms, but no β″-needles with n > 1200 solute atoms (Fig. 4.78(a)). This corresponds to a higher hardness and strength, as seen in Fig. 4.72 and Table 4.23. Further

artificial aging to peak hardness (Fig. 4.72) after 4 h at 180°C results in a significant decrease in solute clusters (4.3 x 10^{23} m^{-3}) and GP zones (1.6 x 10^{23} m^{-3}) compared to the 120h NA,180°C-1h sample. However, the number density of β″-needles needles is concurrently increased, with large needles containing > 1200 solute atoms (4.3 x 10^{22} m^{-3}) found in this sample resulting in peak strength (Table 4.23). Heterogeneous nucleation of β″-needles from GP zones has been postulated before [43,84].

5.8.2. Artificial aging without natural pre-aging

The 0h NA,180°C-10min sample has a high number density of solute clusters (2.2 x 10^{24} m^{-3}) and GP zones (1.3 x 10^{24} m^{-3}), with a lower number density of small β″-needles with n = 100-400 solute atoms (7.6 x 10^{22} m^{-3}) (Fig. 4.78(b)). This is in good agreement with the faint streaks observed in the <001> SADP of the sample (Fig. 4.74(a)) as discussed previously. Further artificial aging to 1 h at 180°C caused a decrease in the number density of both solute clusters (8.3 × 10^{23} m^{-3}) and GP zones (5.4 × 10^{23} m^{-3}), with a concurrent increase of this number in small β″-needles containing 101-1200 solute atoms (3.3 × 10^{23} m^{-3}) and large β″-needles with n > 1200 in a low number density of 2.4 × 10^{21} m^{-3}. With the increase in aging time from 1 h to 4 h at 180°C, the number density of solute clusters decreases almost 12 times to 7.3 × 10^{22} m^{-3} and that of GP zones more than 6 times to 8.5 × 10^{22} m^{-3}. Concurrently, the number density of large β″-needles with > 1200 solute atoms increased almost 8 times to 1.9 × 10^{22} m^{-3} (Fig. 4.78(b)). This coincides with the hardness plateau as shown in Fig. 4.72. During coarsening of the β″-precipitates within the hardness plateau, both the UTS and macrohardness values remain relatively constant, but the YS increases (Table 4.23).

5.8.3. Comparison of artificial aging with and without natural pre-aging

The 120h NA,180°C-10min and 0h NA,180°C-10min samples have similar number densities of solute clusters, but the latter sample has a significantly higher number density of GP zones and also contains small β″-needles with n = 100-400 solute atoms (Fig. 4.78). The vacancy-rich solute clusters that are formed during natural aging diminish the matrix of quenched-in vacancies [84,124]. The lower concentration of quenched-in vacancies in the 120h NA,180°C-10min sample compared to the 0h NA,180°C-10min sample most likely had a delaying effect on precipitation of GP

zones by limiting diffusion. This also agrees with the model for GP zone growth postulated by Herman [125]. The clusters are vacancy-rich due to lattice strains caused by the differences in atom radii of Al, Mg and Si of 0.143, 0.160 and 0.117 nm respectively [126], which results in misfits of +11.9% for Al-Mg and -18.2% for Al-Si. The higher number densities of GP zones and small β″-needles in the 0h NA,180^{o}C-10min sample compared to the 120h NA,180^{o}C-10min sample causes a marked increased hardness (Fig. 4.72) and strength (Table 4.23)

The 120h NA,180^{o}C-1h sample has a higher number density of solute clusters and GP zones than the 0h NA,180^{o}C-1h sample, with a concurrent lower number density of β″-needles (Fig. 4.78), which results in lower hardness (Fig. 4.72) and strength (Table 4.23).

The 120h NA,180^{o}C-4h sample has similar hardness, YS and UTS than the 0h NA,180^{o}C-4h sample (Table 4.23). However, the 120h NA,180^{o}C-4h sample has a significantly higher number density of solute clusters and GP zones than the 0h NA,180^{o}C-4h sample (Fig. 4.78). The presence of a larger number of small clusters and GP zones in the naturally pre-aged sample is most likely due to remnants of clusters and GP zones that had formed during natural aging. These would have been the room temperature clusters and GP zones that were durable during artificial aging and which did not undergo reversion. Such stability of room temperature clusters during artificial aging at 180^{o}C of Al-Mg-Si alloys has been reported before [50,86]. Yamada and co-workers [86] postulated that these clusters are Si and –vacancy rich (see section 5.9.1) and are durable at 180^{o}C due to the strong covalent bonds between the Si atoms within these clusters. The 120h NA,180^{o}C-4h sample also has a higher number density of large β″-needles with n > 1200 solute atoms than the 0h NA,180^{o}C-4h sample and a correspondingly lower number density of smaller β″-needles with n = 100-1200 solute atoms. Whereas the 0h NA,180^{o}C-4h sample therefore relies mostly on a relatively high volume fraction of comparatively small β″-needles for its hardness and strength, the 120h NA,180^{o}C-4h sample relies more on a combined presence of solute clusters, GP zones and large β″-needles.

After aging for 4 h at 180°C, the relative reductions of the matrix solute concentrations detected in the two samples reached the same level, which indicates that the decomposition of the supersaturated solid solution in the two respective microstructures has developed to a similar stage (Fig. 4.77). The initial vacancy concentration difference between the two samples therefore has little influence on the long-term precipitation process after 4 hour aging. After 1 h aging at 180°C, the vacancy concentrations of the two samples appear to have quickly evolved to the stable concentration at that temperature.

5.9. Characteristics of precipitates in Al-7Si-Mg alloys

5.9.1. Solute clusters

The solute clusters are fully coherent with the matrix and cannot be resolved by TEM (Fig. 4.73(a)). They are Si-rich with a Mg:Si ratio of less than the theoretical 0.83 of β″ (Fig. 4.79). Rinderer and co-workers [11] showed that the clusters in under-aged A356 have a Mg:Si ratio of 0.7, which is in good agreement with the results in this study. The clusters are enriched in Si [80,86] due to its higher diffusion rate and lower solubility than Mg in Al [39,50]. The strong covalent bonds between the Si atoms in the clusters presumably make them durable at artificial aging temperatures of 180^{o}C, even at a time of 4 h that corresponds to the peak aged condition.

5.9.2. GP zones

The GP zones are approximately 2 nm in diameter and can be resolved by TEM in Fig. 4.74(a). GP zones are fully coherent with the matrix and do not have a distinct structure and therefore their SADP's (Fig. 4.74(a)) do not show extra reflections nor diffuse scattering. The Mg:Si ratio of GP zones of 0.8-1.1 (Fig. 4.79) is higher than those of the solute clusters and are close to the theoretical value of 0.83 of β″. The increase in Mg-content of the GP zones compared to clusters indicates that Mg-diffusion is rate limiting during precipitation [80]. Using the Arrhenius parameters from Du and co-authors [105], it can be calculated that the diffusivity of Mg in Al at 180^{o}C is half of that of Si in Al (1.9 x 10^{-19} and 3.8 x 10^{-19} m^2/s respectively).

5.9.3. β″-needles

The β″-needles range in size from ~ 2 nm diameter x 10 nm length early during artificial aging (Fig. 4.73(c)) to ~ 4 nm diameter x 25 nm in the peak aged condition (Fig. 4.73(d)). The β″-needles have the highest Mg:Si ratio of all the precipitates due to the precipitation process being controlled by Mg-diffusion (Fig. 4.79). The needles with > 1200 solute atoms for instance have a Mg:Si ratio of ~ 1.0–1.2 (more than 0.83 of β″ but less than 1.7 of β′) - in excellent agreement with the ratio of 1.2 found by Rinderer and co-workers [11] for peak aged β″-needles in alloy A356. Recent first principle calculations suggest that the lowest formation enthalpy configuration of β″ has a Mg:Si ratio of 1.25 [127].

5.10. Precipitation sequence of Al-7Si-Mg alloys

By considering the results obtained by employing TEM and APT in this study, the precipitation sequence can be expressed as follows, while also elucidating the co-existence of precipitates during precipitation.

- **During natural aging (T4)**: Formation of a high number density of vacancy- and Si-rich Si-Mg clusters with a significantly lower number density of GP zones and no β″-needles.
- **During artificial aging after natural pre-aging**: Coarsening of the room temperature clusters → spherical GP zones → β″-needles, coinciding with a decrease of the matrix Mg and Si content and an increase in Mg:Si ratio of the precipitates, while retaining a relatively high number density of room temperature Si-rich clusters and GP zones that remain durable during artificial aging.
- **During artificial aging without natural pre-aging**: A high concentration of solute and quenched-in vacancies leads to rapid formation of clusters and GP zones → relatively small β″-needles at the start of the hardness plateau → coarsening of β″-needles during the hardness plateau depleting the matrix from Mg and Si, increasing the Mg:Si ratio of the precipitates, whilst retaining only a few clusters and GP zones, which results in constant hardness and UTS, but increasing YS.

Summary: SSS → solute clusters → solute clusters + GP-zones → solute clusters + GP-zones + $\beta''_{needles.}$

A natural pre-aging treatment has a significant influence on the precipitation kinetics during initial 1 h artificial aging of alloy F357. Natural pre-aging, however, has no influence on the precipitation sequence, but it affects the relative proportion of solute clusters, GP zones and β″-needles.

6. AGE HARDENING MODEL FOR Al-7Si-Mg ALLOYS

6.1. Age hardening models

Since the precipitation of strengthening phases is critical to the properties of age-hardenable alloys, modelling of precipitation and strengthening has gained considerable interest among researchers. Various age hardening models have been developed, especially for wrought aluminium alloys [15,128-130]. In contrast to the wrought aluminium alloys, little modelling work on the age-hardening of casting aluminium alloys has been performed [82,131]. In the work of Rometsch and Schaffer [82], the methodology used by Shercliff and Ashby [15] was applied to model aging curves of Al-7Si-Mg alloys. In the work by Wu and Ferguson [131], the methodology used by Kampmann and Wagner was applied [132]. Wu and Ferguson [131] also summarised the modelling approaches of both Shercliff-Ashby and Kampmann-Wagner. The Shercliff-Ashby process model draws together established knowledge of the kinetics of microstructure evolution with dislocation behaviour in order to determine the mechanical properties. In the Kampmann-Wagner model, a numerical approach capable of describing the particle size distribution in the time domain, while dealing with the nucleation-growth-coarsening phenomena within the same formulation, is used. A strength model is then used to evaluate the resulting change in hardness or yield strength.

For the purposes of this study, the Shercliff-Ashby process model approach was used, firstly due to its relative simplicity compared to the Kampmann-Wagner approach and secondly, to allow comparison with the work of Rometsh and Schaffer on alloys A356 and A357 [82], as well as comparison with the original work of Shercliff and Ashby on alloy 6082 [15].

6.2. The Shercliff-Ashby model

Shercliff and Ashby [15] developed a process model to describe the changes in hardness or yield strength due to age hardening of heat treatable alloys. The model was successfully applied to the isothermal aging curves of wrought Al-alloys 6061 and 6082.

Included in the model are expressions for:

- the decrease in solute concentration and growth in volume fraction of precipitates during the early stages of precipitation;
- the effect of aging temperature on the equilibrium volume fraction of precipitates;
- the coarsening of precipitates by LSW ripening;
- the strength contribution from solute atoms; and
- the strength contribution from both shearable and non-shearable precipitates.

Equations describing these events are kept as straightforward as possible by combining unknown constants into physically or empirically meaningful parameters and by using dimensionless variables where possible. Only the most necessary variables to describe the microstructure and strengthening are incorporated. The methodology is consistent across the sub-models and is calibrated using experimental aging curves (i.e. making it a “mechanistic” model). Aging curves for hardness and yield strength may be calibrated equally well as some of the constants have the dimensions of yield strength and may take values in any appropriate units. As described in section 4.12, it is fundamentally more correct to make a comparison between hardness and UTS, rather than YS. However, in Fig. 4.63 it was shown that the correlation between VHN and YS in the ranges found in these alloys is acceptable.

The total Vickers hardness (VHN_t) of an Al-7Si-Mg alloy is given by equation 6.1 [15]:

$$\mathbf{VHN_t = VHN_o + \Delta VHN_{Si} + \Delta VHN_{Fe} + \Delta VHN_{ss,Si} + \Delta VHN_{ss,Mg} + \Delta VHN_{ppt,Si} + \Delta VHN_{ppt,Mg-Si}} \quad \mathbf{(6.1)}$$

where VHN_o is the hardness of pure aluminium, ΔVHN_{Si} is the contribution to the hardness due to eutectic Si particles, ΔVHN_{Fe} from the eutectic Fe-phase particles, $\Delta VHN_{ss,Si}$ from the Si in solid solution, $\Delta VHN_{ss,Mg}$ from the Mg in solid solution, $\Delta VHN_{ppt,Si}$ from the Si precipitates and $\Delta VHN_{ppt,Mg-Si}$ due to Mg–Si precipitates.

Equation 6.1 may be simplified because ΔVHN_{Si}, ΔVHN_{Fe} and $\Delta VHN_{ss,Si}$ are expected to remain reasonably unchanged during aging. Although $\Delta VHN_{ss,Si}$ may fluctuate with aging time and temperature, these effects are expected to be negligible

since changes in the Si concentration from 0.5 to 1.2 wt.% in solid solution in a binary Al–Si alloy are known to increase YS in the annealed condition by not more than 2–3 MPa [9,82]. For simplicity, it is also assumed that $\Delta VHN_{ppt,Si}$ is negligibly small, particularly in relation to the large strengthening contribution due to Mg–Si type precipitates. Accordingly, Eq. (6.1) may be simplified to:

$$\mathbf{VHN_t = VHN_i + \Delta VHN_{ss,Mg} + \Delta VHN_{ppt,Mg-Si}} \qquad \mathbf{(6.2)}$$

where VHN_i is the intrinsic strength of the alloy, which may be defined as being the sum of VHN_o and those strengthening contributions which remain invariable during aging. Potential differences in age hardening characteristics between primary α-Al and the eutectic regions are assumed as being insignificant since the α-Al phase is mostly homogenised during the solution treatment. This assumption is supported by the aging curves in Fig. 4.72 which showed that both the hardness of the eutectic and primary α-Al components increased during artificial aging.

When precipitates are small and coherent they are sheared by moving dislocations (Fig. 2.25(a)). Their contribution to the strength of the alloy involves a convolution of the resistance to shear of one particle, their population and the flexibility of the dislocations with which they interact – known as the Friedel effect [15]. It is normally accepted that the contribution to VHN by shearable precipitates (ΔVHN_s) is approximately related to the precipitate volume fraction (f) and the precipitate radius (r) through a constant c_1:

$$\mathbf{\Delta VHN_s = c_1 f^{1/2} r^{1/2}} \qquad \mathbf{(6.3)}$$

The spacing of precipitates increases during coarsening and there becomes a spacing at which the stress required to bend a dislocation (so that it bows between neighbouring particles in its slip plane, known as the Orowan mechanism) becomes less than that required to shear through them (Fig. 2.25(b)). The contribution to VHN due to the bypassing of dislocations around non-shearable precipitates (ΔVHN_b) is approximately related to the precipitate volume fraction and the precipitate radius through a constant c_2:

$$\Delta VHN_b = c_2 f^{1/2}/r \qquad (6.4)$$

Shercliff and Ashby [15] have shown that single-peak aging curves are satisfactorily described by taking the harmonic mean of eqs. (6.3) and (6.4):

$$\Delta VHN_{ppt,Mg-Si} = [2S(P^*)^{1/6}]/[1+(P^*)^{1/2}] \qquad (6.5)$$

where S is the precipitate strength and P* = P/P_p. The term P is the "normalised temperature-corrected time", in s/K.

$$P = t/T \exp(-Q_A/RT) \qquad (6.6)$$

where t is the aging time, T the aging temperature, Q_A the activation energy for volume diffusion of atoms through the matrix and R the gas constant (8.314 J/mol K). The parameter P_p is the value of P at the peak in the aging curve and is a constant for a given set of aging conditions.

The assumption of a single-peak aging curve is an important consideration, because it implies that only the contribution of β″-precipitation is considered. It has been shown in section 4.14 that β″-needles are mostly responsible for peak aging, with solute clusters and GP zones mainly occurring in the under-aged condition. Even though β_{rods}' was not investigated in this study, it is known that these precipitates are found in Al-7Si-Mg alloys in the over-aged condition (Fig. 2.30). By therefore only considering β″-precipitation, the expectation is that peak aging will be predicted more accurately than under- and over-aging.

The precipitate strength, S, as a function of aging time (t) and temperature (T) is expressed as follows [82]:

$$S^2(t,T) = (S_o)^2_{max}\left[1 - \exp\frac{-Q_s}{R}\left(\frac{1}{T} - \frac{1}{T_s}\right)\right]\left[1 - \exp\left(\frac{-t}{\tau_1}\right)\right] \qquad (6.7)$$

where the strength parameter $(S_o)_{max}$, the solvus enthalpy (Q_s) and the metastable solvus temperature (T_s) are determined from experimental aging data. The constant τ_1 is related to the aging time corresponding to the peak t_p by the constant K_1:

$$\tau_1 = K_1\, t \qquad (6.8)$$

The solid solution hardening component $\Delta VHN_{ss,Mg}$ in Eq. (6.2) has been described to vary with aging time as follows:

$$\Delta VHN_{ss,Mg} = [(\Delta VHN_{ss0})^{3/2} + [(\Delta VHN_{ssi})^{3/2} - (\Delta VHN_{ss0})^{3/2}]\exp(-t/\tau_1]^{2/3} \qquad (6.9)$$

where the subscripts refer to initial ΔVHN_{ssi} and final ΔVHN_{ss0} solid solution strengthening contributions. The initial solid solution strengthening contribution is the difference between the as-quenched hardness (VHN_q) and the intrinsic hardness (VHN_i), whereas the final solid solution strengthening contribution is the difference between the over-aged hardness (VHN_{oa}) at that aging temperature and VHN_i. VHN_{oa} may be determined from known values of VHN_q and VHN_i:

$$VHN_{oa} = VHN_i + (VHN_q - VHN_i)\exp(-2Q_s/3R)(1/T - 1/T_s) \qquad (6.10)$$

The contribution to the strength (or hardness) of all 3 sub-models in equation 6.2 is shown schematically in Fig. 6.1 [15]. Note that the effective mechanism of precipitation hardening is the one requiring the least shear stress, with a smooth transition between the two.

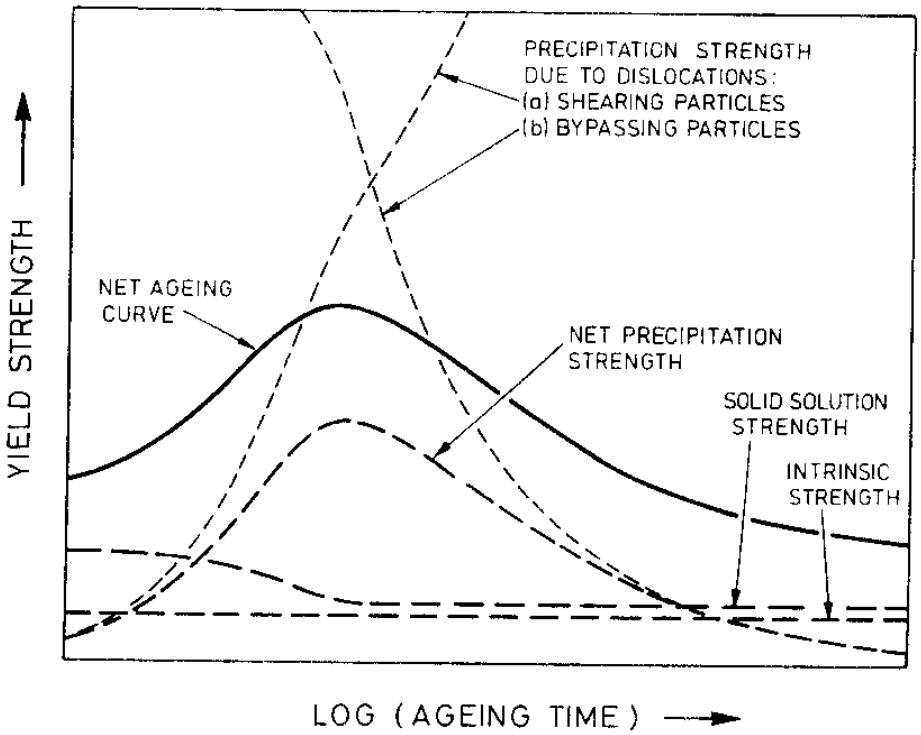

Figure 6.1: A schematic diagram of the relative contributions to the full aging curve of the intrinsic strength, solid solution strength and the precipitation hardening due to shearable and non-shearable precipitates [15].

Finally, the employment of the as-quenched hardness VHN_q implies that this model is only applicable to aging curves where no natural pre-aging has taken place, for example, it is valid for Figs. 4.28 and 4.31, but not for Figs. 4.29, 4.30, 4.32 and 4.33 of this study.

6.2.1. Calibration of the model

The steps in the calibration procedure have been summarised by Shercliff and Ashby [15]:

1) Choose values for the as-quenched hardness (VHN_q) and the intrinsic hardness (VHN_i) to calculate the first estimate of VHN_{oa} midway between the two.
2) Examine the aging curves and determine the time to reach the peak (t_p) and the peak hardness for as many different temperatures as possible.
3) Plot $\ln(t_p/T)$ vs $1/T$ and measure the gradient (Q_A/R) to find the activation energy Q_A.

4) Calculate P_p using the average of the values of the peak temperature-corrected-time.
5) For each temperature, evaluate the peak precipitation hardening increment $(\Delta VHN_{ppt,Mg-Si,})_{peak}$ and hence experimental values for S_o.
6) Plot S_0^2 vs temperature as in Fig. 6.2 and estimate T_s.
7) Estimate $(S_0)_{max}$ from the low temperature plateau in Fig. 6.2 and solve for Q_s using all the data.
8) For each temperature calculate VHN_{oa} more accurately using Eq. 6.10, then $(\Delta VHN_{ppt,Mg-Si,})_{peak}$ $(=S_0^2)$; adjust T_s, $(S_0)_{max}$ and Q_s and replot S_0^2 vs T. Repeat until the fit between theory and data is satisfactory.
9) Adjust the constant K_1 such that the solid solution part decays with an appropriate time constant τ_1 (scaled by P_p and T).

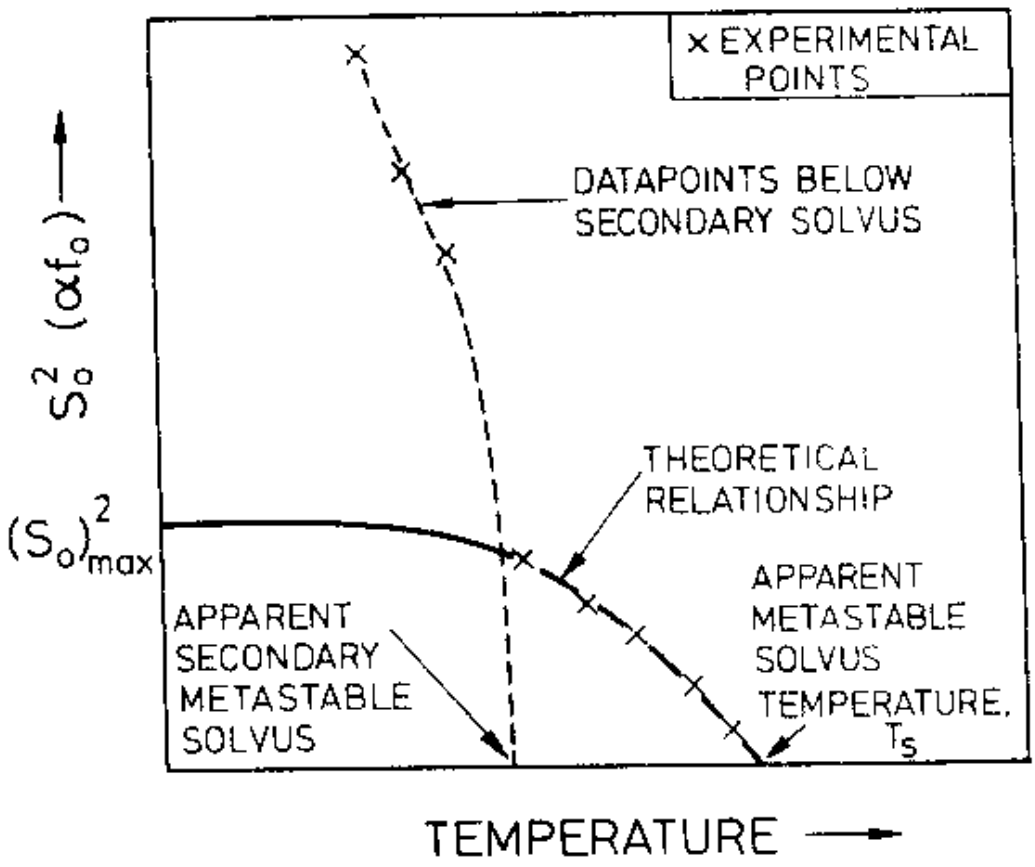

Figure 6.2: The variation of S_0^2 (which is proportional to the equilibrium volume fraction) with temperature. Typical experimental data points are shown, some of which lie at T below a secondary solvus. The solid line is the theoretical curve used to model the relationship [15].

6.2.2. Application of the model in the literature

Shercliff and Ashby [15] have applied the model to predict artificial aging hardness curves for Al-Mg-Si wrought alloy 6082 (Fig. 6.3). The agreement between theory and experimental values are good throughout, with the model fitting experimental data to within 10%.

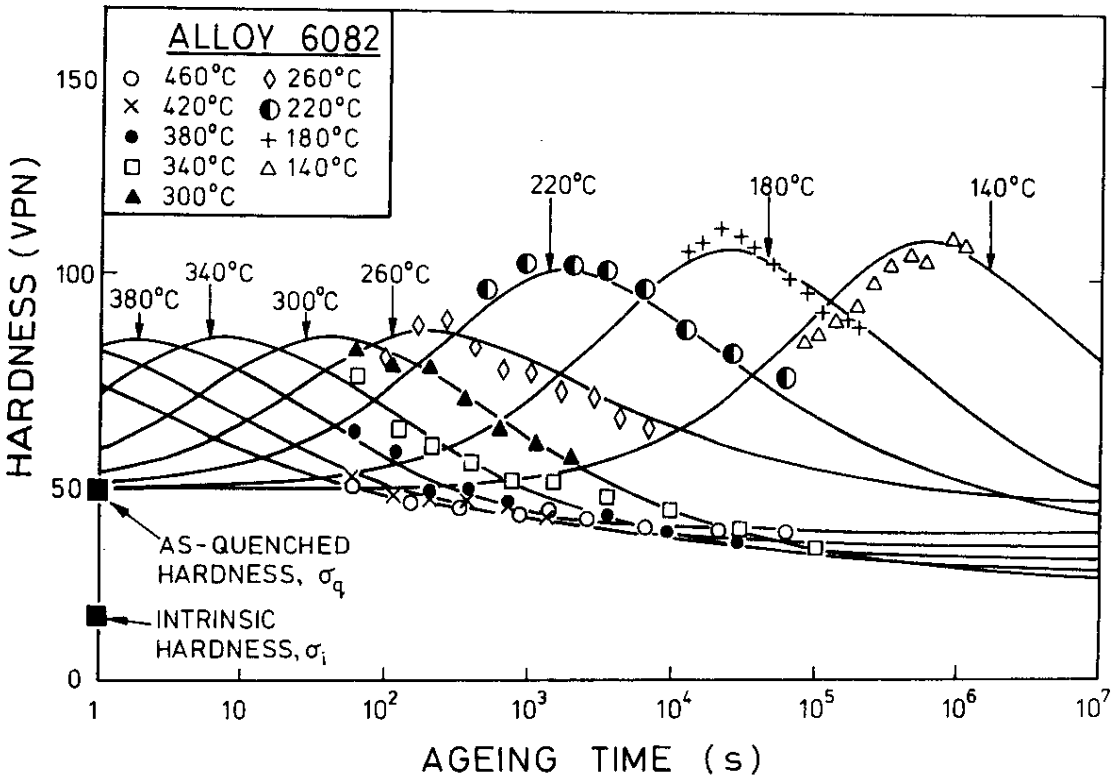

Figure 6.3: Experimental data for alloy 6082 compared with the model for nine aging temperatures [15].

Rometsch and Schaffer [82] applied the model to predict YS-aging curves for dendritic Al-7Si-Mg alloys A356 (Fig. 6.4(a)) and A357 (Fig. 6.4(b)). The modelled YS_t aging curves have more sharply defined peaks than the experimental aging curves do. The authors postulated that the broadness of the peaks in the experimental A356 and A357 aging curves suggests that under-aged and over-aged precipitates may cause more hardening than is normally assumed [82]. It is likely that, by also considering the contributions by GP zones and β′, better correlation between experimental and predicted values will be obtained.

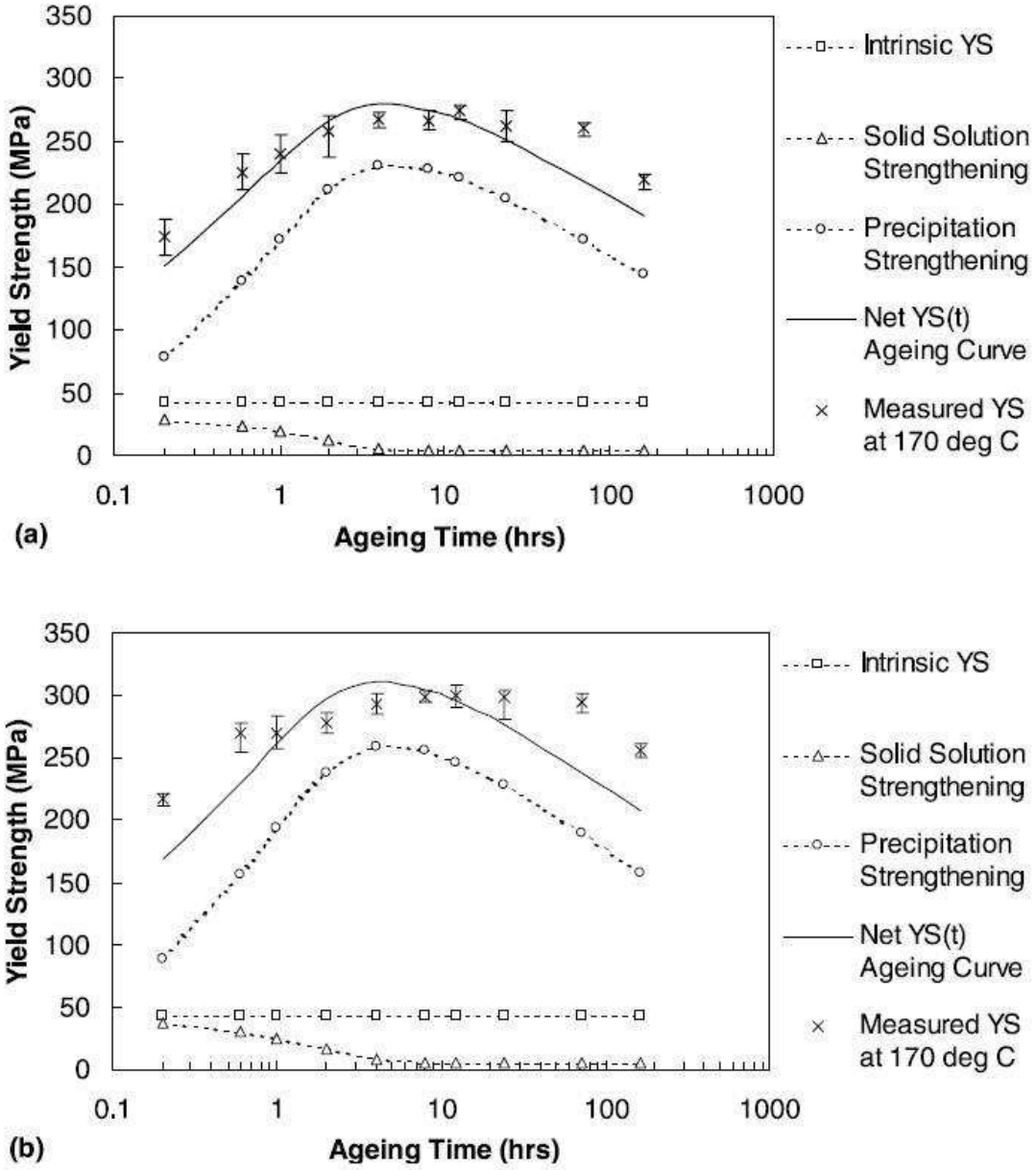

Figure 6.4: Strengthening contributions that produce the net YS_t aging curves for (a) A356 and (b) A357 at 170°C. Error bars are shown for measured YS values at 170°C [82].

6.3. Application of the model in this study

The CSIR recently successfully processed SSM-HPDC of high purity Al, even though it does not possess a solidification temperature range – Fig. 6.5 [HM13].

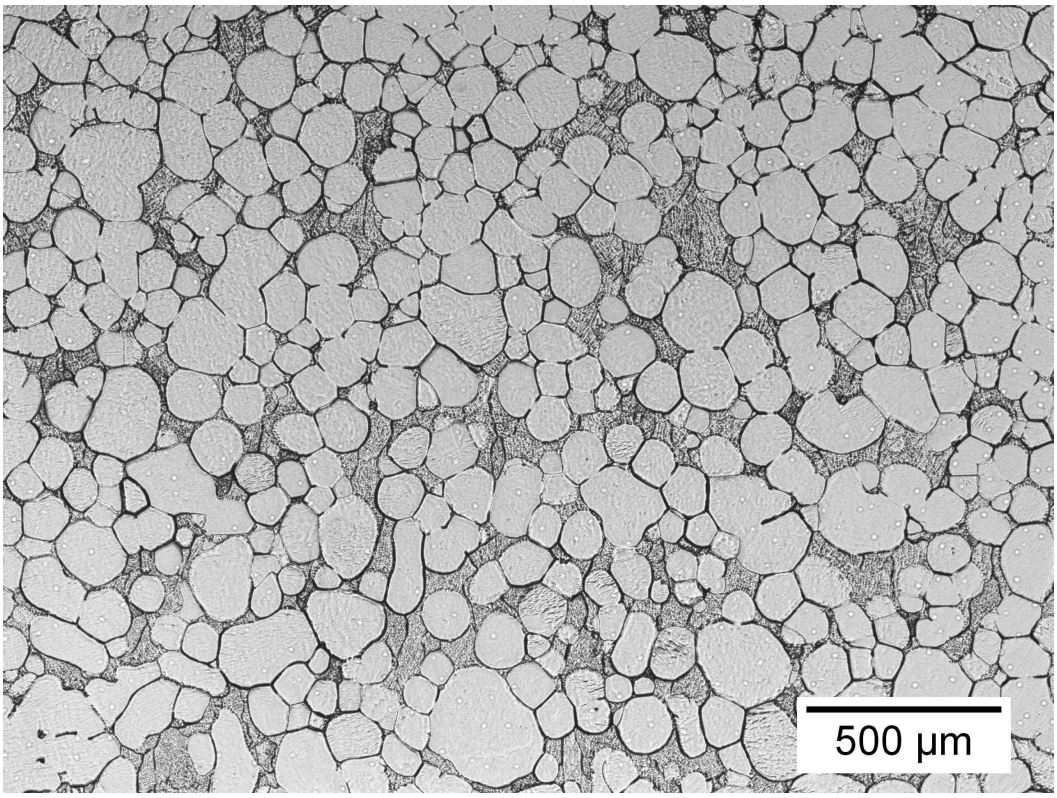

Figure 6.5: Optical micrograph of SSM-HPDC high purity Al [HM13].

The hardness of the pure Al (with globular microstructure) was measured as 19.5 VHN and this value was used as VHN_o. It corresponds reasonably well with the hardness of pure Al of 15 VHN used by Shercliff-Ashby [15]. However, the value needed for eq. 6.2 is VHN_i and not VHN_o. VHN_i is defined as being the sum of VHN_o and those strengthening contributions which remain invariable during aging. Rometsch and Schaffer [82] estimated their YS_i value from the results of Erginer and Gurland [133] who determined the YS of solution treated (100 h at 538°C) and air cooled binary Al–Si alloys containing different amounts of Si. For alloys containing 5.3% Si, the average YS was 40 MPa, whereas for alloys containing 8.5% Si, the average YS was 46 MPa; the YS_i was therefore estimated to be 43 MPa for Al–7Si alloys. To convert this YS_i to VHN_i, eq. 4.9 is used with n = 0.188 (Table 4.20) to give $VHN_i = 25$, which by definition must be > $VHN_o = 19.5$.

From Fig. 6.6, it can be seen that the as-quenched hardness VHN_q = ~ 53.

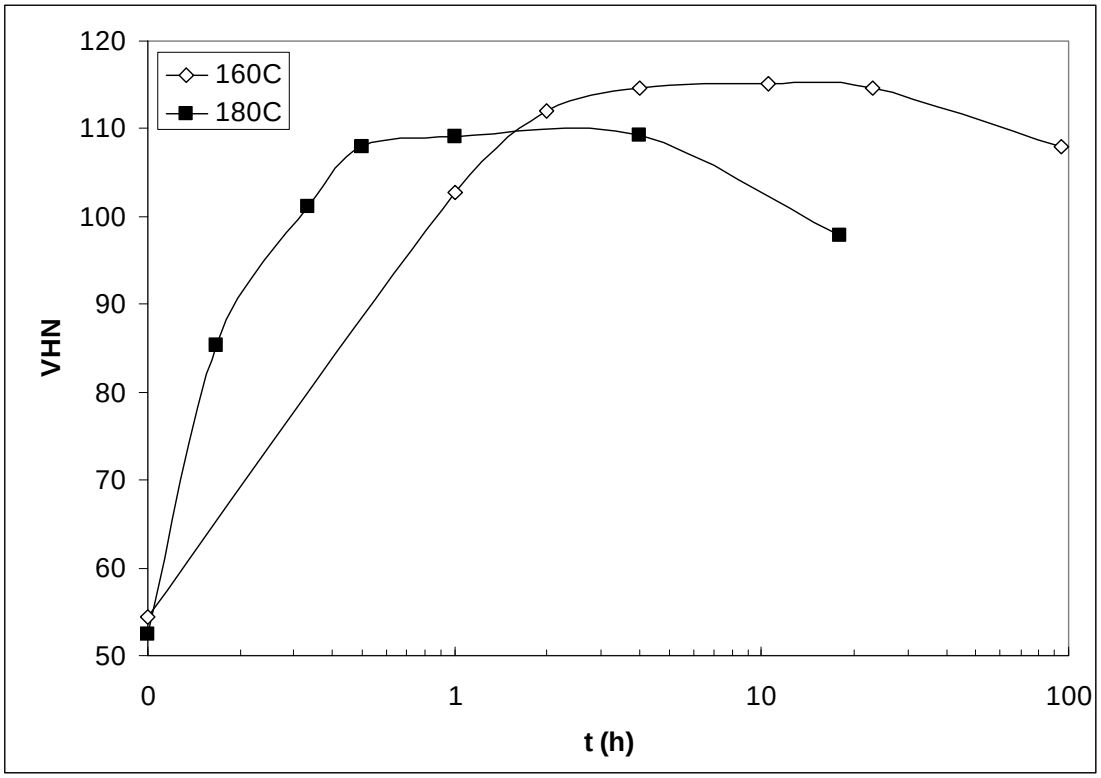

Figure 6.6: Artificial aging curves at 160 and 180°C for SSM-HPDC alloy A356 (with 0.36%Mg) showing VHN_q = ~ 53.

The first estimate of the over-aged hardness is then made midway between VHN_i and VHN_q i.e. VHN_{oa} = 39.

The activation energy (Q_A), has been determined in Fig. 4.19 as Q_A = 163 kJ/mol.
The average value of P_p is determined by using the values summarised in Table 6.1 and the initial value for S_o is determined by subtracting the estimated over-aged hardness from the peak hardness. Note that "peak time" was calculated by means of eq. 4.2 and not eq. 4.3. Eq. 4.3 gives time to maximum hardness, but not maximum YS (Table 4.23), whereas eq. 4.2 gives time to "peak" properties in terms of hardness, YS and UTS.

Table 6.1: Data for peak time and hardness, and evaluated parameters at various artificial aging temperatures.

Temperature (^{o}C)	Time to peak (s) – eq. 4.2	P_p (s/K)	Peak VHN	S_o (VHN)
160	106200	5.32×10^{-18}	115	76
180	14400	5.09×10^{-18}	109	70
190	5400	4.75×10^{-18}	104	65
Average		**5.05×10^{-18}**		
Standard deviation		2.83×10^{-19}		

The first plot of S_o^2 vs temperature is shown in Fig. 6.7 and this gives an estimate of the metastable solvus temperature T_s = 278^{o}C.

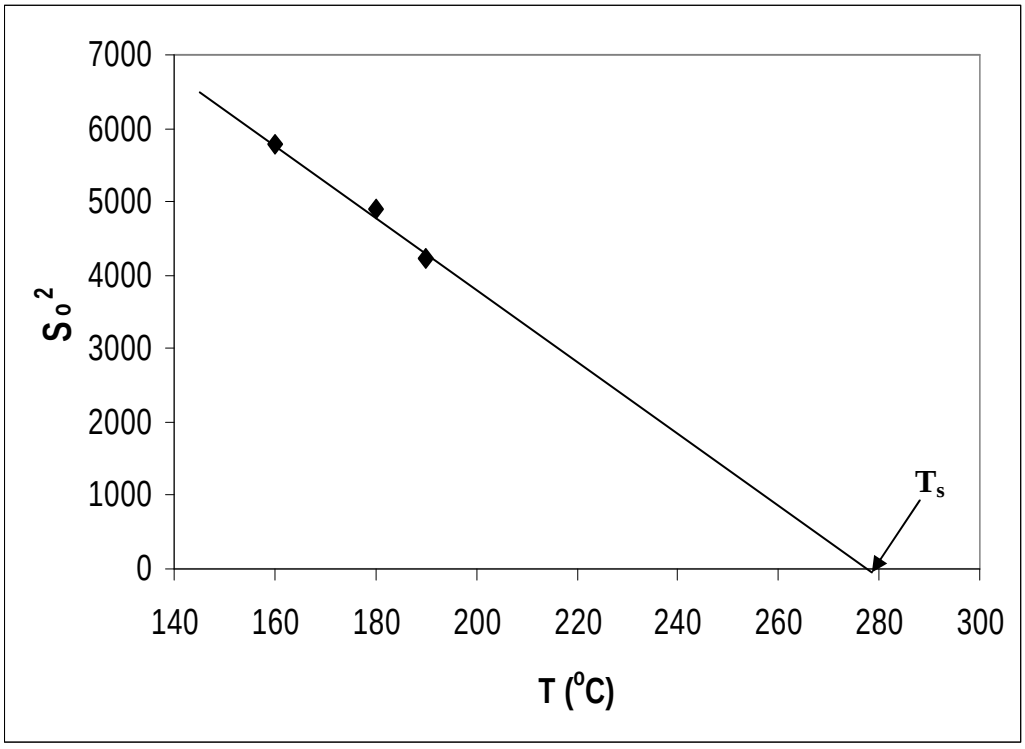

Figure 6.7: First graph of S_o^2 with temperature used to estimate T_s.

The limited number of data points in Figure 6.7 makes the determination of an accurate value for $(S_0)_{max}$ virtually impossible. The value determined by Rometsch and Schaffer [82] of 228 MPa is therefore used, which converts to VHN = 93 using eq. 4.9 with n = 0.072 (Table 4.20).

Solving equation 6.7 gives an average estimated Q_s = 18 kJ/mol. This allows a more accurate determination of VHN_{oa} = 36.2 using eq. 6.10 and a second plot of S_o^2 vs temperature can be drawn as shown in Fig. 6.8, giving an unchanged metastable solvus temperature of T_s = 278°C implying that further iterations to get a best fit of S_o^2 vs temperature are not necessary.

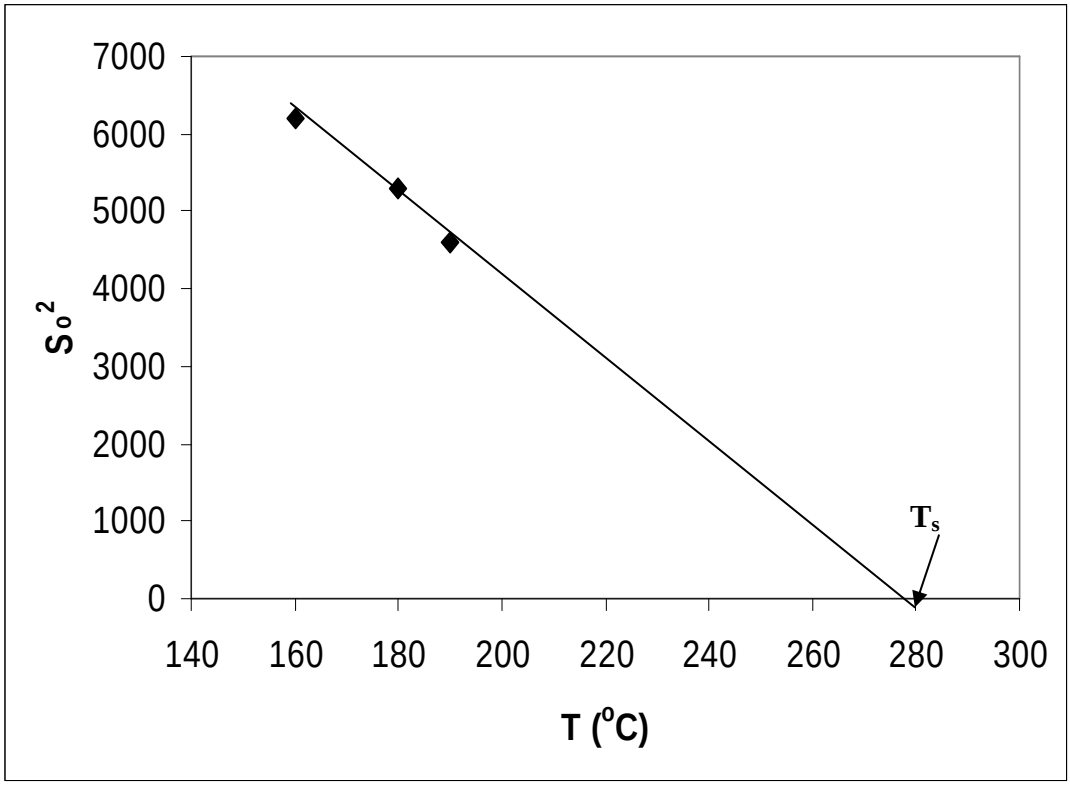

Figure 6.8: Second graph of S_o^2 with temperature used to estimate T_s.

The required decay of the solid solution component is achieved using a value of K_1 = 0.08.

A summary of the constants and calibration parameters used to model the aging curves are presented in Table 6.2. Application of the model to predict the artificial aging curves in Fig. 6.6 are shown in Fig. 6.9 for 180°C and in Fig. 6.10 for 160°C. The agreement between predicted and measured values are good, with the greatest deviation occurring at over-aged conditions, in agreement with what was also reported by Rometsch and Schaffer [82]. It needs to be recognised, however, that any model that uses experimental hardness data to set up the model and then uses that same model to compare with the same hardness data, is bound to give a good fit.

Table 6.2 Values of constants and calibration parameters used to model the aging curves.

Parameter	This study: A356
Intrinsic hardness (VHN_i)	25
As-quenched hardness (VHN_q)	53
Activation energy for aging in kJ/mol (Q_A)	163
Metastable solvus temperature in ^oC (T_s)	278
Solvus boundary enthalpy in kJ/mol (Q_s)	18
Strength parameter in VHN $(S_o)_{max}$))	93
P_p in s/K	5.05×10^{-18}
K_1	0.08

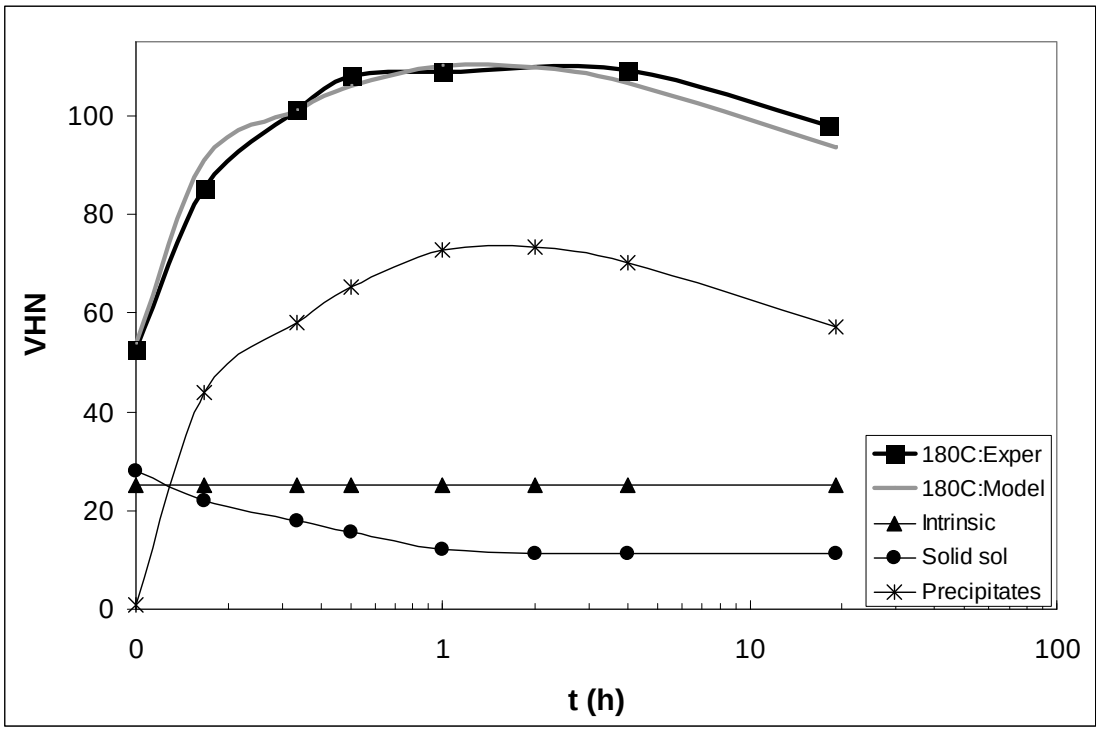

Figure 6.9: Strengthening contributions that produce the net aging curves for SSM-HPDC alloy A356 (0.36%Mg) at 180^{o}C.

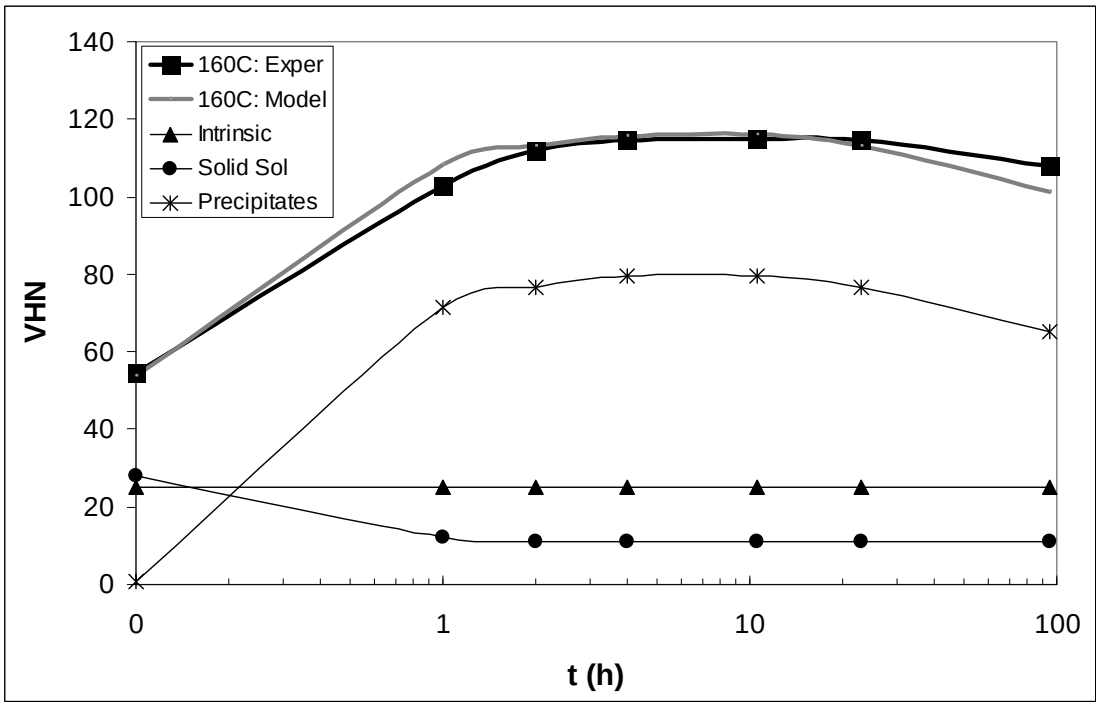

Figure 6.10: Strengthening contributions that produce the net aging curves for SSM-HPDC alloy A356 (0.36%Mg) at 160°C.

6.4. Comparison of Al-7Si-Mg casting alloy A356 to the wrought alloy 6082

Table 6.3 compares the values of constants and calibration parameters used in this study with those used by Rometsch and Schaffer [82] for alloy A356 and Shercliff and Ashby for alloy 6082 [15]. The main differences between the values found in this study and those of Rometsch and Schaffer are for Q_A and P (which are related through equation 6.6) and Q_s. As mentioned in section 4.5, the activation energy for diffusion of Mg in Al has been proposed in a range from 111 kJ/mol to 161 kJ/mol. Therefore, the experimentally determined value for Q_A of 163 kJ/mol in this study lies close to the upper limit of the range that has been proposed, with the value of 130 kJ/mol found by both [15] and [82] in Table 6.3 being within this range. The higher Q_A value in this study results in a lower P_p-value, due to their relation through equation 6.6. The Q_s value found in this study of 18 kJ/mol differs significantly from that found by Rometsch and Schaffer for A356 of 64 kJ/mol, which in turn also differs from the value found for alloy 6082 of 30 kJ/mol. These differences in Q_s might be due to the relation of Q_s with the over-aged hardness VHN_{oa} in eq. 6.10, which has been shown in Figs. 6.9 and 6.10 to be the least successfully predicted part of the aging curves.

Table 6.3 Comparison of values of constants and calibration parameters used to model the aging curves in this study with references [15] and [82].

Parameter	This study: A356	Rometsch-Schaffer: A356 [82]	Shercliff-Ashby: 6082 [15]
Activation energy for aging in kJ/mol (Q_A)	163	130	130
Metastable solvus temperature in ^oC (T_s)	278	271	282
Solvus boundary enthalpy in kJ/mol (Q_s)	18	64	30
Strength parameter in VHN $(S_o)_{max}$))	93	93	94
P_p in s/K	5.05×10^{-18}	3.71×10^{-14}	5.50×10^{-14}
K_1	0.08	0.11	0.50

The solvus temperatures found in Table 6.3 ranges from 271-282^{o}C, which corresponds well with the peak for β″-precipitation in the DSC curve shown in Fig. 2.33. In addition, Rometsch and Schaffer [134] have also shown by means of DSC that the β″ solvus occurs at about 270-280^{o}C. The strength parameter $(S_o)_{max}$ of 93 VHN was derived from the values found by Rometsch and Schaffer [82] and also corresponds well with the value of 94 VHN found for alloy 6082 in Table 6.3. This would suggest that similar precipitation strengthening occurs in alloys A356 and 6082. The constant $K_{1,}$ which relates τ_1 to t_p through eq. 6.8, is similar for this study and the A356 of Rometsch and Schaffer (~0.1), but significantly lower than the 0.5 for alloy 6082. The decay of the solid solution component therefore occurs faster in alloy A356 than in alloy 6082, a conclusion that is supported by the artificial aging curves presented in Fig. 4.70. As discussed in section 5.7, the excess Si in the casting alloys in this study is believed to reduce the time to initiate strengthening, presumably due to a higher driving force for nucleation which will lead to a finer particle size and shorter diffusion distances.

6.5. Modelling of artificial aging curves of SSM-HPDC Al-7Si-Mg alloys with varying Mg-contents

The parameters derived in Table 6.2 for the artificial aging curves of Figs. 6.9 and 6.10 are only applicable for a single composition – in this case the 0.36wt% Mg alloy in Table 3.1. Theoretically, to model the aging curves of the other compositions listed

in Table 3.1, new parameters must be derived by determining artificial aging curves at as many temperatures as possible. This would be a very time consuming process and a simple, but accurate method to convert the aging curves of one composition to that of another composition would be beneficial.

From Fig. 4.62 it is seen that the peak hardness of Al-7Si-Mg alloys is linearly related to the (at% Mg-concentration available for precipitation hardening)$^{1/2}$. In addition, from Figs. 4.28 to 4.33 it can be seen that the shape of the aging curve is not influenced by the Mg-content of the alloy and the curve is shifted either upwards or downwards depending on the Mg-content. Therefore, using the 0.36wt% Mg alloy as a reference alloy, artificial aging curves of other alloys can be predicted using the following procedure by employing the 0.49wt% Mg alloy (Fig. 4.72) as example:

- Calculate the wt% Mg available for precipitation hardening by employing either eq. 4.4 or 4.5. For the 0.49wt% Mg alloy, eq. 4.5 must be used and the wt% Mg available for strengthening is then 0.44wt% (also ensure that the Fe-content of the alloy is ~0.1%, otherwise eq. 4.5 becomes invalid).
- Convert the wt% Mg to at% Mg. For the specific alloy in question, the at% Mg available for strengthening is calculated as 0.49at%.
- Estimate the peak hardness at 180^{o}C of this alloy by using the equation of the trend line in Fig. 4.62 (after converting the at% to at%$^{1/2}$). For the alloy in question the estimated peak hardness is 119 VHN.
- The peak hardness of the reference alloy at 180^{o}C is 109 (Fig. 6.6). Take the ratio of the peak hardness of the alloy in question to the peak hardness of the reference alloy giving 1.092.
- Keep the intrinsic hardness value VHN_i unchanged at 25, but scale the contribution of solid solution strengthening and precipitation hardening with the ratio of 1.092. The actual and predicted aging curves for the 0.49wt% Mg alloy are compared in Fig. 6.11.

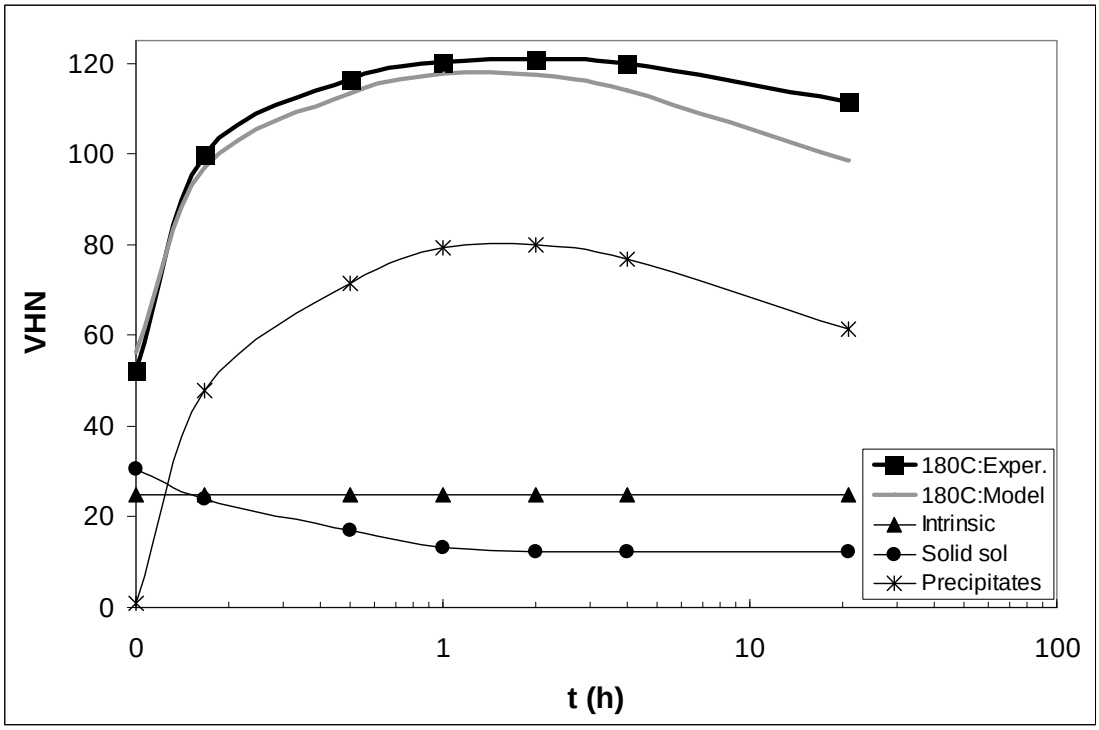

Figure 6.11: Strengthening contributions that produce the net aging curves for SSM-HPDC alloy F357 (0.49wt% Mg) at 180°C.

As before, the agreement between predicted and measured values is reasonable, with most deviation again occurring at the over-aged condition.

Artificial aging curves of alloys with less Mg than the reference alloy can also be predicted using a similar approach e.g. by employing the 0.28wt% Mg alloy (Fig. 4.28) as example:

- Calculate the wt% Mg available for precipitation hardening by employing eq. 4.4 in this case giving 0.28wt% Mg.
- Convert the wt% Mg to at% Mg which is 0.31at%.
- Estimate the peak hardness at 180°C of this alloy by using the equation of the trend line in Fig. 4.62 (after converting the at% to at%$^{1/2}$). For the alloy in question the estimated peak hardness is 101 VHN.
- The peak hardness of the reference alloy at 180°C is 109 (Fig. 6.6). Take the ratio of the peak hardness of the alloy in question to the peak hardness of the reference alloy giving 0.9266.
- Keep the intrinsic hardness value VHN_i unchanged at 25, but scale the contribution of solid solution strengthening and precipitation hardening with

the ratio of 0.9266. The actual and predicted aging curves for the 0.28wt% Mg alloy are compared in Fig. 6.12.

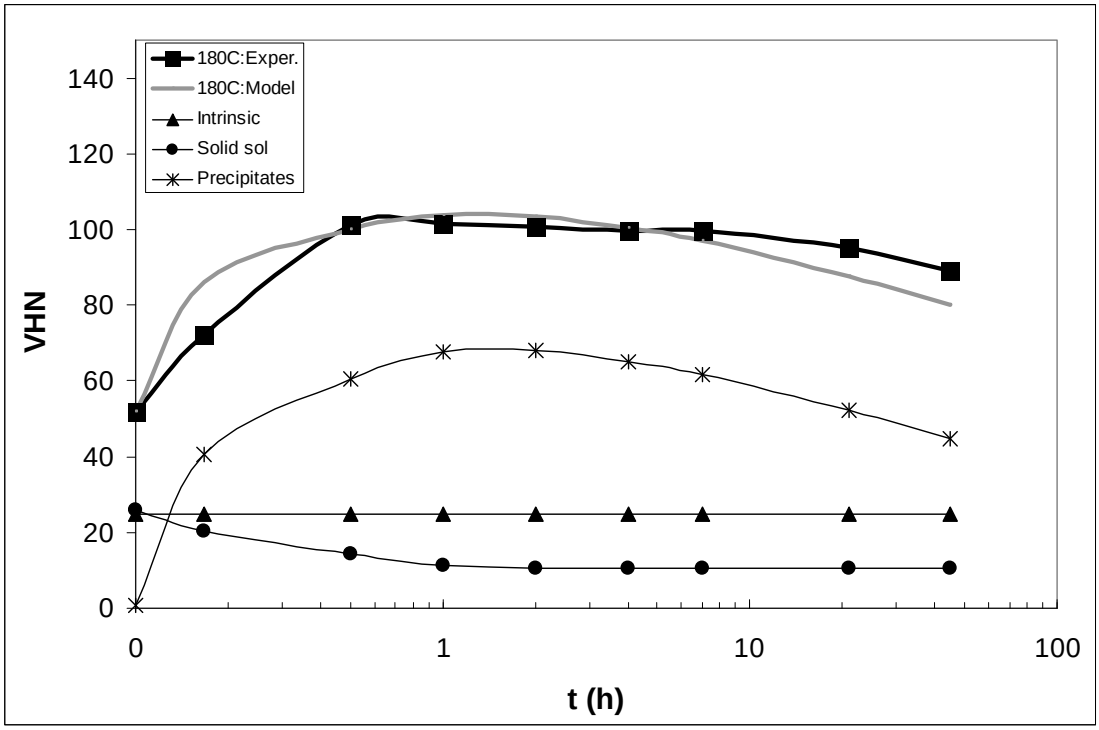

Figure 6.12: Strengthening contributions that produce the net aging curves for SSM-HPDC alloy A356 (0.28wt% Mg) at 180°C.

The agreement between predicted and measured values is good, with slight deviation again occurring in the over-aged condition, but in this case also in the under-aged condition as well. As discussed before, by only considering single peak β″-precipitation, peak aging is predicted more accurately than under- and over-aging.

7. CONCLUSIONS

7.1. SSM-HPDC

- Rheoprocessing of Al-7Si-Mg alloys with the CSIR rheocasting system results in a globular microstructure with primary α-Al globule diameters of 60-70 μm.
- High cooling rates of ~ 18^{o}C/s are achieved during the initial stages of the HPDC step, resulting in predicted solidification being completed within 5.5s in the plate castings.
- The eutectic component in these alloys is modified by the high cooling rates achieved during HPDC, with levels of Sr as low as 14 ppm being sufficient, as opposed to about 200 ppm Sr necessary for conventional casting techniques such as permanent mould casting and investment casting.

7.2. Solution heat treatment

- The solution treatment of Al-7Si-Mg alloys has a dual beneficial effect – it causes spheroidisation of the eutectic silicon particles (improved ductility and impact properties) and it causes complete dissolution of the strengthening solutes (maximum strength after artificial aging).
- Spheroidisation of the eutectic Si particles occurs rapidly at 540^{o}C, with their coarsening being described reasonably well by means of LSW-coarsening.
- The high cooling rates achieved during HPDC result in a high concentration of solute being retained in solid solution after casting. A solution treatment time at 540^{o}C for only 1 h is therefore sufficient to obtain a high level of mechanical properties in the T4 and T6 temper conditions.
- The impact strength of the alloys in the T4 and T6 temper conditions is not influenced significantly by the solution treatment time (and hence the Si-interparticle spacing), but rather by the strength of the alloy.

7.3. Quench after solution treatment

- Slow quench rates after the solution heat treatment can reduce the problems of distortion and residual stresses, but also result in a loss of strength and hardness after natural- and artificial aging.

7.4. Natural aging and the T4 temper condition

- Al-7Si-Mg alloys are relatively soft directly after quenching (VHN = ~ 53), but thereafter, the hardness increases rapidly at room temperature, eventually levelling out after 4-5 days at 70-95 VHN, depending on the Mg-content of the alloy.
- Natural aging of Al-7Si-Mg alloys result in the formation of a high number density of vacancy- and Si-rich Si-Mg clusters with a significantly lower number density of GP zones and no β″-needles.
- The solute clusters are fully coherent with the matrix and they have a low Mg:Si ratio of ~ 0.6-0.7.

7.5. Artificial aging and the T5 temper condition

- The relatively fast cooling rates achieved with HPDC result in an adequate quantity of solutes remaining in solid solution after casting, which allows a reasonable response to age hardening in the T5 temper condition.
- No spheroidisation of the eutectic Si occurs in the T5 condition due to the lack of a solution treatment step, causing relatively low elongation and impact strength.

7.6. Artificial aging and the T6 temper condition

- Artificial aging at lower temperatures (e.g. 160^{o}C) produces slightly higher peak hardnesses compared to artificial aging at higher temperatures (e.g. 180^{o}C), but the time-to-peak hardness is significantly increased.
- The time required to obtain maximum hardness at different artificial aging temperatures can be predicted using Arrhenius-type equations.
- When no natural pre-aging occurs, a hardness plateau is maintained once the maximum hardness is reached during artificial aging at 180^{o}C after about 1 to 5 hours. This differs from when natural pre-aging occurs when a hardness peak is observed after approximately 4 hours.
- The effects of any natural aging can largely be removed by an artificial aging treatment of 180^{o}C for 4 hours.

7.6.1. Artificial aging without natural pre-aging

- A high concentration of solute and quenched-in vacancies leads to rapid formation of clusters and GP zones → transformation to relatively small β″-needles at the

start of the hardness plateau → coarsening of β″-needles during the hardness plateau. This depletes the matrix from Mg and Si, while increasing the Mg:Si ratio of the precipitates, whilst retaining only a few clusters and GP zones. This results in constant hardness and UTS, but increasing YS.

7.6.2. Artificial aging with natural pre-aging

- Coarsening of the room temperature clusters → spherical GP zones → β″-needles, coinciding with a decrease of the matrix Mg and Si content and an increase in Mg:Si ratio of the precipitates, while retaining a relatively high number density of room temperature Si-rich clusters and GP zones that remain durable during artificial aging.

7.6.3. Characteristics of precipitates found in Al-7Si-Mg alloys

- **Solute clusters**

  The Si-rich room temperature clusters are durable at artificial aging temperatures of 180^{o}C, even at a time of 4 h that corresponds to the peak aged condition.

- **GP zones**

  The GP zones are approximately 2 nm in diameter and are fully coherent with the matrix. The Mg:Si ratio of GP zones of 0.8-1.1 is higher than those of the solute clusters, which indicates that Mg-diffusion is rate limiting during precipitation.

- **β″-needles**

  The β″-needles range in size from ~ 2 nm diameter x 10 nm length early during artificial aging to ~ 4 nm diameter x 25 nm in the peak aged condition. The β″-needles have the highest Mg:Si ratio of all the precipitates due to the precipitation process being controlled by Mg-diffusion with the needles with > 1200 solute atoms having a Mg:Si ratio of ~ 1.0 – 1.2.

7.7. Influence of chemical composition fluctuations

- The strength and macrohardness values of Al-7Si-Mg alloys show good linear relationships to (at% Mg-concentration available for precipitation hardening)$^{1/2}$.
- Higher Mg-levels (> 0.4wt%) in Al-7Si-Mg alloys increase the stability range of the Mg-containing π–phase to higher temperatures, and suppress the Mg-free β–$FeSiAl_5$ phase at high temperatures.

- The stability of the π-phase in alloy F357 causes a reduction in the amount of magnesium in solid solution. This has a detrimental effect on the aging behaviour of this alloy compared to alloy A356.
- High Fe-levels above specification (> 0.20%) in alloy F357 result in the formation of high volume fractions of intermetallics such as π-$Al_8FeMg_3Si_6$ and β-Al_5FeSi. Micro-cracking of these intermetallics during tensile testing causes a marked reduction in ductility.

7.8. Comparison of the aging response of globular and dendritic Al-7Si-Mg alloys

- The natural aging (T4) and artificial aging (T6) responses of Al-7Si-Mg alloys are not influenced by having a globular or dendritic microstructure.
- Provided that the maximum quantity of the alloy's Mg is placed into solid solution during solution treatment, and that the alloy's Fe content is within specification, the response to age hardening of Al-7Si-Mg alloys should be independent of the processing technique used.
- The frequently specified artificial aging parameters of 160^{o}C for 3-6 h or 170^{o}C for 6 h for both dendritic and globular Al-7Si-Mg alloys will result in large variations in properties depending on the natural pre-aging period. Parameters of 180^{o}C for 4 h are proposed as an alternative to overcome this shortcoming.

7.9. Comparison of the aging response of Al-7Si-Mg alloys with 6000 series wrought alloys

- Conventional casting alloys A356 and F357 obtain the same level of strength (hardness) in the T6 temper regardless of the prior natural aging period employed over a relatively wide range of Mg compositions. Alloy 6082 (with relatively high Si and Mg contents for a 6000 series alloy) displays a much reduced strength and hardness in the T6 condition following natural aging. Alloy 6004 (with relatively low Mg and Si) displays the opposite behaviour.
- The high Si content of the conventional casting alloys compared to the 6000 wrought series alloys results in a faster artificial aging response (shorter T6 aging cycles), higher strength for comparable Mg contents and less sensitivity to prior natural aging on peak strength. However, over-aging occurs earlier in the casting alloys than for the wrought alloys.

7.10. Age hardening model for Al-7Si-Mg alloys

- The Shercliff-Ashby methodology was followed to successfully predict artificial aging curves (with no natural pre-aging) of Al-7Si-Mg alloys.
- A method to allow prediction of artificial aging curves with Mg-contents different from that of the reference alloy has been proposed.

8. RECOMMENDATIONS

Based on the results of this study, the following recommendations for future research are made:

8.1. SSM-HPDC

- The surface liquid segregation (SLS) layer found in castings produced by means of SSM-HPDC has been noted during this study. The effects of this SLS layer on mechanical properties, but especially surface-sensitive properties such as fatigue and corrosion, need to be investigated.

8.2. Solution heat treatment

- Even though the impact strength of the alloys in the T4 and T6 temper conditions is not influenced significantly by the solution treatment time, the effects on other properties such as fatigue, creep and corrosion (which also includes stress corrosion cracking and corrosion fatigue), must be characterised.

8.3. Quench after solution treatment

- More data points at lower cooling rates during quenching of SSM-HPDC Al-7Si-Mg alloys after solution heat treatment would be beneficial, as well as quantification of distortion and the development of residual stresses.

8.4. Artificial aging and the T5 temper condition

- The relatively fast cooling rates achieved with HPDC has not been utilised to the full for the T5 temper condition in this study due to too long intensification times being employed during HPDC. Optimisation of intensification parameters and subsequent quenching should result in a more improved response to age hardening in the T5 temper condition.
- APT was done only on samples in the T4 and T6 temper conditions in this study. APT analyses of samples in the T5 temper condition (i.e. air cooled or water quenched after HPDC, with or without natural pre-aging and artificially aged at different temperatures and times) would reveal the influence of different levels of supersaturation on the nanostructural evolution during aging.

8.5. Artificial aging and the T6 temper condition

- APT was done only on samples artificially aged at 180°C for times up to 4 h in this study. APT analyses revealing the transformation of $\beta_{needles}''$ to β_{rods}' to β_{plates} in over-aged samples (t > 4 h at 180°C) would be beneficial.
- APT analyses of samples artificially aged at lower and higher temperatures than 180°C would quantify how the differences in solubility and hence supersaturation would lead to different nucleation rates and volume fractions of strengthening phases.

8.6. Influence of chemical composition fluctuations

- The strength and macrohardness values of Al-7Si-Mg alloys show good linear relationships to (at% Mg-concentration available for precipitation hardening)$^{1/2}$. The APT analysis in this study was only performed for a single Al-7Si-Mg alloy. APT analyses on alloys with varying Mg-contents (but constant Fe-contents) should quantitatively reveal the origin of this linear relation.

8.7. Age hardening model for Al-7Si-Mg alloys

- The Shercliff-Ashby methodology can be improved by not only considering the $\beta_{needles}''$ (peak aging), but also considering the effects of solute clusters and GP zones (under-aging) and β_{rods}' and β_{plates} (over-aging).

10. REFERENCES

1. Metals Handbook Volume 15: Casting, Metals Park, Ohio, ASM International, 1988.
2. Spencer DB, Mehrabian R, Flemings MC. *Metallurgical Transactions*, vol. 3, 1972, pp. 1925-1932.
3. Wilm A. *Metallurgie*, vol. 8, 1911, pp. 225-227.
4. Guinier A. *Nature*, vol. 142, 1938, pp. 569-570.
5. Preston GD. *Nature*, vol. 142, 1938, p. 570.
6. Ogris E. Development of Al-Si-Mg Alloys for Semi-Solid Processing and Silicon Spheroidization Treatment (SST) for Al-Si Cast Alloys. Doctoral dissertation, Swiss Federal Institute of Technology, 2002.
7. Pacz A. U.S. patent 1387900, 1921.
8. Archer RS, Jeffries Z. *Transactions of AIME*, vol. 71, 1925, p. 828.
9. Polmear I. Light alloys: from traditional alloys to nanocrystals. 4th ed. Oxford: Butterworth-Heinemann; 2006.
10. Liu D, Atkinson HV, Kapranos P, Jirattiticharoean W, Jones H. *Materials Science and Engineering A*, vol. 361, 2003, pp. 213-224.
11. Rinderer B, Couper M, Xiong X, Gao S, Nie J-F. *Materials Science Forum*, vols. 654-656, 2010, pp. 590-595.
12. Dewhirst BA. Optimization of the heat treatment of semi solid processed A356 aluminum alloy. Masters Thesis, Worcester Polytechnic Institute, 2005.
13. Birol Y. *International Journal of Materials Research*, vol. 101, 2010, pp. 439-444.
14. Birol Y. *Journal of Alloys and Compounds*, vol. 484, 2009, pp. 164-167.
15. Shercliff HR, Ashby MF. *Acta Metallurgica et Materialia*, vol. 38, 1990, pp. 1789-1802.
16. Atkinson HV. *Progress in Materials Science*, vol. 50, 2005. pp. 341-412.
17. Proc. 1st Int. Conf. on Semi-Solid Processing of Alloys and Composites, Ecole Nationale Superieure des Mines de Paris, Societe Francaise de Metallurgie, Cemef, Sophia-Antipolis, France, 1990.
18. Brown SB, Flemings MC, editors. In: Proc. 2nd Int. Conf. on Semi-Solid Processing of Alloys and Composites, Cambridge, MA, USA, June 1992. Warrendale: TMS; 1992.

19. Kiuchi M, editor. In: Proc. 3rd Int. Conf. on Semi-Solid Processing of Alloys and Composites Tokyo, Japan, June 1994. Tokyo Institute of Industrial Science, 1994.
20. Kirkwood DH, Kapranos P, editors. In: Proc. 4th Int. Conf. on Semi-Solid Processing of Alloys and Composites, Sheffield, UK, June 1996, University of Sheffield, 1996.
21. Bhasin AK, Moore JJ, Young KP, Midson S, editors. In: Proc. 5th Int. Conf. on Semi-Solid Processing of Alloys and Composites, Golden, Colorado, USA, June 1998. Golden, CO: Colorado, School of Mines, USA; 1998.
22. Chiarmetta GL, Rosso M, editors. In: Proc. 6th Int. Conf. on Semi-Solid Processing of Alloys and Composites, Turin, Italy, Sept 2000, Brescia. Italy: Edimet Spa; 2000.
23. Tsutsui Y, Kiuchi M, Ichikawa K, editors. In: Proc. 7th Int. Conf. on Advanced Semi-Solid Processing of Alloys and Composites, Tsukuba, Japan, Sept 2002. Japan: National Institute of Advanced Industrial Science and Technology and the Japan Society for Technology of Plasticity; 2002.
24. Proc. 8th Int. Conf. on Semi-Solid Processing of Alloys and Composites, Limassol, Cyprus, September 2004.
25. Kang CG, Kim SK. Lee SY, editors. In: Proc. 9th Int. Conf. on Semi-Solid Processing of Alloys and Composites, Busan, Korea, September 2006, Pusan National University, Trans Tech Publications; 2006.
26. Hirt G, Rassili A, Buhrig-Polaczek A, editors. In: Proc. 10th Int. Conf. on Semi-Solid Processing of Alloys and Composites, Aachen, Germany and Liege, Belgium, Trans Tech Publications; September 2008.
27. Huang W, Kang Y, Yang X, editors. In: Proc. 11th Int. Conf. on Semi-Solid Processing of Alloys and Composites, Beijing, China, Elsevier; September 2010.
28. Winterbottom WL. *Metallurgical Science and Technology,* vol. 18, 2000. pp. 5-10.
29. Quaak CJ, Katgerman L, Kool WH. *Proceedings of the 4th International Conference on Semi-solid processing of alloys and composites,* Sheffield, United Kingdom, June 1996, pp. 35-39.
30. Bruwer R, Wilkins JD, Ivanchev LH, Rossouw P, Damm OFRA. US Patent No. 7368690, 2008.

31. Ivanchev LH, Wilkins JD, Govender G. *Proceedings of the 8th International Conference on Semi-solid Processing of Alloys and Composites*, Limassol, Cyprus, 2004, Paper # 152.
32. Massalski TB, Okamoto H, Subramanian PR, Kacprzak L. *Binary Alloy Phase Diagrams*, ASM International, Materials Park OH, 1990.
33. ASM Specialty Handbook: Aluminium and Aluminium Alloys, Materials Park, Ohio, ASM International, 1993.
34. Yang CY, Lee SL, Lee CK, Lin JC. *Materials Chemistry and Physics*, vol. 93, 2005, pp. 412-419.
35. Rosso M, Romano E, Giordano P, Chiarmetta GL. *Proc. 7th Int. Conf. on Advanced semi-solid processing of alloys and composites*, Tsukuba, Japan, Japan Society for Technology of Plasticity, 2002, pp. 151-156.
36. Forn A, Baile MT, Martin E, Goni J, Sarries I. *Solid State Phenomena*, vols. 116-117, 2006, pp. 181-184.
37. Zhao H, Bai H, Wang J, Guan S. *Materials Characterization,* vol. 60, 2009. pp. 377-383.
38. Kaufmann H, Fragner W, Galovsky U, Uggowitzer PJ. *Proceedings of the 2nd International Light Metals Technology Conference*, St. Wolfgang, Austria, 2005, pp. 169-177.
39. Vissers R, van Huis MA, Jansen J, Zandbergen HW, Marioara CD, Andersen SJ. *Acta Materialia*, vol. 55, 2007, pp. 3815-3823.
40. Zander J, Sandström, R. *Materials & Design,* vol. 29, 2008, pp.1540-1548.
41. Abdulwahab M, Madugu IA, Yaro SA, Hassan SB, Popoola API. *Materials & Design*, vol. 32, 2011, pp. 1159-1166.
42. Buha J, Lumley RN, Crosky AG. *Philosophical Magazine*, vol. 88, 2008, pp. 373-390.
43. Murayama M, Hono K. *Acta Materialia,* vol. 47, 1999, pp. 1537-1548.
44. Yang W, Wang M, Zhang R, Zhang Q, Sheng X. *Scripta Materialia,* vol. 62, 2010, pp. 705-708.
45. Zandbergen HW, Andersen SJ, Jansen J. *Science*, vol. 277, 1997, pp. 1221-1225.
46. Li C, Wu YY, Li H, Liu XF. *Acta Materialia*, vol. 59, 2011. pp. 1058-1067.
47. Taylor JA, StJohn DH, Zheng LH, Edwards GA, Barresi J, Couper MJ. *Aluminum Transactions*, vols. 4-5, 2001, pp. 95-110.

48. Taylor JA, StJohn DH, Couper MJ. *Aluminum Transactions*, vols. 4-5, 2001, pp. 111-124.
49. Muller-Quernheim J. Chronic beryllium disease, Orphanet Encyclopedia, Nov. 2005, pp. 1-10.
50. Chang CST, Wieler I, Wanderka N, Banhart J. *Ultramicroscopy*, vol. 109, 2009, pp. 585-592.
51. Eskin DG, Kharakterova ML. *Materiali in Technologije*, vol. 35, 2001, pp. 5-8.
52. Caceres CH, Djurdjevic MB, Stockwell TJ, Sokolowski JH. *Scripta Materialia*, vol. 40, 1999, pp. 631-637.
53. Ye, H. *Journal of Materials Engineering and Performance*, vol. 12, 2003, pp. 288-297.
54. Kim HY, Han SW, Lee HM. *Materials Letters*, vol. 60, 2006, pp. 1880-1883.
55. Castillo LD, Lavernia EJ. *Metallurgical and Materials Transactions A*, vol. 31, 2000, pp. 2287-2298.
56. Nafisi S, Ghomashchi R. *Materials Characterization*, vol. 57, 2006, pp. 371-385.
57. Nafisi S, Ghomashchi R. *Materials Science and Engineering A*, vol. 415, 2006, pp. 273-285.
58. Sigworth GK. *International Journal of Metalcasting*, vol. 2, 2008, pp. 19-40.
59. Hegde S, Prabhu KN. *Journal of Materials Science*, vol. 43, 2008, pp. 3009-3027.
60. Lumley RN, Polmear IJ, Curtis PR. *Metallurgical and Materials Transactions A*, vol. 40, 2009, pp. 1716-1726.
61. Lumley RN, O'Donnell RG, Gunasegaram DR, Givord M. *Metallurgical and Materials Transactions A*, vol. 38, 2007, pp. 2564-2574.
62. Funatani K. *Proc. 1st Automotive Heat Treating Conf.*, Puerto Vallata, Mexico, 13-15 July, 1998, pp. 283-290.
63. Apelian D, Shivkumar S, Sigworth G. *AFS Transactions*, vol. 97, 1990, pp. 727-742.
64. Dahle AK. Heat Treatment of Aluminium Alloys, *Encyclopedia of Material Science and Technology*, vol. 3, 2001, pp. 1-3.
65. Ohnisi N, Takaai T, Nakayama Y, Ohmori M. *Journal of the Japan Institute of Light Metals*, vol. 45, 1995, pp. 447-452.
66. Shivkumar S, Ricci S, Steenhoff B, Apelian D, Sigworth G. *AFS Transactions*, vol. 138, 1989, pp. 791-810.

67. Zhang DL, Zheng LH, StJohn DH. *Journal of Light Metals*, vol. 2, 2002, pp. 27-36.
68. Rometsch PA, Arnberg L, Zhang DL. *International Journal of Cast Metals Research*, vol. 12, 1999, pp. 1-8.
69. Parker BA, Saunders DS, Griffiths JR. *Metals Forum*, vol. 5, 1982, pp. 48-53.
70. Shabestari SG, Shahri, F. *Journal of Materials Science*, vol. 39, 2004, pp. 2023-2032.
71. Otarawanna S, Gourlay CM, Laukli HI, Dahle AK, *Metallurgical and Materials Transactions A*, vol. 40, 2009, pp. 1645-1659.
72. Emadi D, Whiting LV, Sahoo M, Sokolowski JH, Burke P, Hart M. *Light Metals* 2003, pp. 983-989.
73. Zhang DL, Zheng LH. *Metallurgical and Materials Transactions A*, vol. 27, 1996, pp. 3983-3991.
74. Tiryakioglu M, Shuery RT. *Metallurgical and Materials Transactions B*, vol. 38, 2007, pp. 575-582.
75. Sjölander E, Seiffedine S. *Journal of Materials Processing Technology*, vol. 210, 2010, pp. 1249-1259.
76. Gerold V. Precipitation hardening. In: Nabarro, F.R.N. (Ed.), *Dislocations in Solids*. North-Holland, 1979, p. 222.
77. Buha J, Lumley RN, Crosky AG, Hono K. *Acta Materialia*, vol. 55, 2007, pp. 3015-3024.
78. Wanderka N, Lazarev N, Chang CST, Banhart J. *Ultramicroscopy*, 2010; doi:10.1016/j.ultramic.2010.11.022.
79. Edwards GA, Stiller K, Dunlop GL, Couper MJ. *Acta Materialia*, vol. 46, 1998, pp. 3893-3904.
80. Banhart J, Chang CST, Liang Z, Wanderka N, Lay MDH, Hill AJ. *Advanced Engineering Materials*, vol. 12, 2010, pp. 559-571.
81. Govender G, Ivanchev L, Jahajeeah N, Bëan R. *Solid State Phenomena*, vols. 116-117, 2006. pp. 501-504.
82. Rometsch PA, Schaffer GB. *Materials Science and Engineering A*, vol. 325, 2002. pp. 424-434.
83. Eskin DG. *Journal of Materials Science*, vol. 38, 2003, pp. 279–290.
84. Marioara CD, Andersen SJ, Jansen J, Zandbergen HW. *Acta Materialia*, vol. 51, 2003, pp. 789-796.

85. Royset J, Stene T, Saeter JA, Reiso O. *Materials Science Forum*, vols. 519-521, 2006, pp. 239-244.
86. Yamada K, Sato T, Kamio A. *Materials Science Forum*, vols. 331-337, 2000, pp. 669-674.
87. Bichsel H, Ried A, *Warmebehandeling*, D. Gesellsch. Fur Metallkunde e.V. 1973, p. 173.
88. Gupta AK, Lloyd DJ, Court SA. *Materials Science and Engineering A*, vol. 316, 2001, pp.11-17.
89. Badiali M, Davidson CJ, Griffiths JR, Zanada A. *Proceedings of the 6th International Conference on Semi-solid Processing of Alloys and Composites*, Turin, Italy, 2000, pp. 349-354.
90. Rosso M, Actis Grande M. *Solid State Phenomena*, vols. 116-117, 2006, pp. 505-508.
91. Reed-Hill RE, Abbaschian R. Physical Metallurgy Principles. Boston: PWS Publishing Compony; 1994.
92. Curle UA, Wilkins JD, Govender G. *Advances in Materials Science and Engineering*, vol. 2011, 2011, Article ID 195406.
93. Drouzy M, Jacob S, Richard M. *International Cast Metals Research Journal*, vol. 5, 1980, pp. 43-50.
94. Kaufman JG. Fracture resistance of aluminium alloys: notch toughness, tear resistance and fracture toughness, ASM International, 2001.
95. Miller MK. Atom probe tomography: analysis at the atomic level. New York: Kluwer Academic/Plenum Publishers; 2000.
96. Gault B, Moody MP, de Geuser F, Tsafnat G, La Fontaine A, Stephenson LT, et al. *Journal of Applied Physics*, vol. 105, 2009, Article no. 034913.
97. Moody MP, Gault B, Stephenson LT, Haley D, Ringer SP. *Ultramicroscopy*, vol. 109, 2009, pp. 815-824.
98. Vaumousse D, Cerezo A, Warren PJ. *Ultramicroscopy*, vol. 95, 2003, pp. 215-221.
99. Marceau RKW, Sha G, Ferragut R, Dupasquier A, Ringer SP. *Acta Materialia*, vol. 58, 2010, pp. 4923-4939.
100. Cabibbo M, Spigarelli S, Evangelista E. *Materials Characterization*, vol. 49, 2003, pp. 193-202.

101. Su JF, Nie X, Stoilov V. *Materials Science and Engineering A*, vol. 527, 2010, pp. 7168-7175.

102. Lifshitz IM, Slyozov VV. *Journal of Physical Chemistry of Solids*, vol. 19, 1961, pp. 35-50.

103. Lee CD. *Materials Science and Engineering A*, vol. 464, 2007, pp. 249-254.

104. Gupta AK, Lloyd DJ, Court SA. *Materials Science and Engineering A*, vol. 301, 2001, pp. 140-146.

105. Du Y, Chang YA, Huang B, Gong W, Jin Z, Xu H, et al. *Materials Science and Engineering A*, vol. 363, 2003, pp. 140-151.

106. Fricke WG in: van Horn KR (Ed.), *Aluminum*, vol. 1, Properties Physical Metallurgy and Phase Diagrams, American Society for Metals, Metals Park, OH, 1967.

107. Doig P, Edington JW, *Philosophical Magazine*, vol. 28, 1973, p. 961.

108. Brick RM, Phillips A, *Transactions of AIME*, vol. 124, 1937, p. 331.

109. Caceres CH, Griffiths JR, Wang QG, Davidson CJ. *Metallurgical and Materials Transactions A*, vol. 30, 1999, pp. 2611-2618.

110. Chen C-L, Thomson RC. *Journal of Alloys and Compounds*, vol. 490, 2010, pp. 293−300.

111. Gourlay CM, Laukli HI, Dahle AK. *Metallurgical and Materials Transactions A*, vol. 38A, 2007, pp. 1833-1844.

112. Nagasekhar AV, Caceres CH, Kong C. *Materials Characterization*, vol. 61, 2010, pp. 1035-1042.

113. Dieter GE. Mechanical Metallurgy. Boston: McGraw-Hill; 1986.

114. Bogdanov T, Dahlström J. *The influence of copper on an Al-Si-Mg alloy A356 - Microstructure and mechanical properties*. Bachelor's thesis, Jönköping University, Sweden, 2009.

115. Wang QG. *Metallurgical and Materials Transactions A*, vol. 35, 2004, pp. 2707-2718.

116. Curle UA. *Transactions of the Nonferrous Metals Society of China*, vol. 20, 2010, pp. 1719-1724.

117. Birol Y. *Journal of Alloys and Compounds*, vol. 455, 2008, pp.178-185.

118. Marioara CD, Andersen SJ, Jansen J, Zandbergen HW. *Acta Materialia*, vol. 49, 2001, pp. 321-328.

119. Miller MK, Cerezo A, Hetherington MG, Smith GDW. *Atom Probe Field Ion Microscopy*, Oxford: Oxford University Press; 1996.
120. Blavette D, Vurpillot F, Pareige P, Menand A. *Ultramicroscopy*, vol. 89, 2001, pp. 145-153.
121. Matsuda K, Naoi T, Fujii K, Uetani Y, Sato T, Kamio A, Ikeno S. *Materials Science and Engineering A*, vol. 262, 1999, pp. 232-237.
122. Bryantsev PY, Zolotorevskiy VS, Portnoy VK. *Materials Science Forum*, vols. 519-521, 2006, pp. 401-406.
123. Sha G, Cerezo A. *Acta Materialia*, vol. 53, 2005, pp. 907-917.
124. Cuniberti A, Tolley A, Castro Riglos MV, Giovachini R. *Materials Science and Engineering A*, vol. 527, 2010, pp. 5307-5311.
125. Herman H. *Metallurgical Transactions*, vol. 2, 1971, pp.13-22.
126. Smith WF. Principles of Materials Science and Engineering, New York: McGraw-Hill; 1996.
127. Hasting HS, Froseth AG, Andersen SJ, Vissers R, Walmsley JC, Marioara CD, Danoix F, Lefebvre W, Holmestad R. *Journal of Applied Physics*, vol. 106, 2009, Article number 123527.
128. Myhr OR, Grong O. *Acta Metallurgica et Materialia*, vol. 39, 1991, pp. 2693-2702.
129. Deschamps A, Brechet Y. *Acta Materialia*, vol. 47, 1999, pp. 293-305.
130. Starink, MJ, Wang P, Sinclair I, Gregson PJ. *Acta Materialia*, vol. 47, 1999, pp. 3855-3868.
131. Wu L, Ferguson WG in: Aluminium Alloys: Theory and Applications, INTECHopen, 2011, pp. 307-330.
132. Kampmann R, Wagner R. GKSS-Forschungszentrum, Inst fuer, Physik, Geesthacht, West Ger, GKSS-Forschungszentrum, Inst fuer Physik, Geesthacht, West Germany, 1984.
133. Erginer E, Gurland J. *Zeitschrift für Metallkunde*, vol. 61, 1970, p. 606.
134. Rometsch PA, Schaffer GB. *International Journal of Cast Metals Research*, vol. 12, 2000, pp. 431-439.

HM1: Möller H, Govender G, Stumpf WE. *International Journal of Cast Metals Research*, vol. 20, 2007, pp. 340-346.

HM2: Möller H, Govender G, Stumpf WE. *Open Materials Science Journal*, vol. 2, 2008, pp. 6-10.

HM3: Möller H, Govender G, Stumpf WE. *Open Materials Science Journal*, vol. 2, 2008, pp. 11-18.

HM4: Möller H, Govender G, Stumpf WE. *Solid State Phenomena*, vols. 141-143, 2008, pp. 737-742.

HM5: Govender G, Möller H. *Solid State Phenomena*, vols. 141-143, 2008, pp. 433-438.

HM6: Möller H, Govender G, Stumpf WE. *Materials Science Forum*, vols. 618-619, 2009, pp. 365-368.

HM7: Möller H, Govender G, Stumpf WE, Knutsen RD. *International Journal of Cast Metals Research*, vol. 22, 2009, pp. 417-421.

HM8: Möller H, Govender G, Stumpf WE, Pistorius PC. *International Journal of Cast Metals Research*, vol. 23, 2010, pp. 37-43.

HM9: Möller H, Govender G, Stumpf WE. *Transactions of the Nonferrous Metals Society of China*, vol. 20, 2010, pp. s842-s846.

HM10: Möller H, Govender G, Stumpf WE. *Transactions of the Nonferrous Metals Society of China*, vol. 20, 2010, pp. 1780-1785.

HM11: Möller H, Curle UA, Masuku EP. *Transactions of the Nonferrous Metals Society of China*, vol. 20, 2010, pp. s847-s851.

HM12: Möller H, Govender G, Rossouw P, Stumpf WE. *Advances in Materials Science and Engineering*, vol. 2011, 2011, Article ID 375150.

HM13: Curle UA, Möller H, Wilkins JD. *Scripta Materialia*, vol. 64, 2011, pp. 479-482.

HM14: Möller H, Govender G, Stumpf WE. *Materials Science Forum*, vol. 690, 2011, pp. 53-56.

HM15: Sha G, Möller H, Stumpf WE, Xia JH, Govender G, Ringer SP. Submitted to *Acta Materialia*, 2011.